Dirk Feldmann

Real-Time Rendering and Synthesis of Digital Surface Models Using Textures of Time-Varying Extension

Münster ✦ 2013

Informatik

Real-Time Rendering and Synthesis of Digital Surface Models Using Textures of Time-Varying Extension

Inauguraldissertation zur Erlangung des akademischen Grades eines Doktors der Naturwissenschaften durch den Fachbereich Mathematik und Informatik der Westfälischen Wilhelms-Universität Münster

vorgelegt von

Dirk Feldmann

aus Hamm

2013

Westfälische
Wilhelms-Universität
Münster

Dekan:	Prof. Dr. Martin Stein
Erster Gutachter:	Prof. Dr. Klaus H. Hinrichs
Zweiter Gutachter:	Prof. Dr. Achim Clausing
Tag der mündlichen Prüfung:	25. Juni 2013
Tag der Promotion:	25. Juni 2013

Abstract

Digital surface models represent surfaces by finite sets of sampling points based in some plane of reference together with associated sampled values such as elevation and color. These models can be stored as texture data and are used in many applications to create three-dimensional renderings of the underlying surface. Due to advances in data processing and data transmission, it has become possible to already render these surface models while the data acquisition is still in progress. However, the texture data required for rendering will not only vary in content, but also in extension in the course of time during data acquisition, and thus pose a challenge to real-time rendering. This dissertation addresses the problem of creating digital surface models by means of aerial photographs, as well as managing and rendering such data by using textures of time-varying extension, while the acquisition of the data about the underlying surface is still proceeding.

Table of Contents

Preface

This dissertation is the result of the work and research which was conducted from February 2010 to December 2012 at the Department of Computer Science at the University of Münster. Many thanks go to Prof. Dr. Klaus Hinrichs for giving me the opportunity to conduct my research and for his kind support and guidance. I also thank Prof. Dr. Frank Steinicke for introducing me to the "AVIGLE" project and his support at the beginning of my work, as well as my colleagues at the Visualization and Computer Graphics Research Group for our pleasant on- and off-topic conversations. Furthermore, I would like to give thanks to Aerowest GmbH in Dortmund, Germany, for their kind provision of elevation data and orthophoto images of the city of Münster, and the numerous people who were involved in the acquisition and provision of the original data of the data sets "Blue Marble", "ETOPO1" and "Mars" which are used throughout this dissertation.

This work was developed in the context of the project "AVIGLE" which is funded by the state of North Rhine-Westphalia, Germany, and the European Union, European Regional Development Fund, "Europe – Investing in your future".

Münster, December 2012 *Dirk Feldmann*

1 Introduction

In many application scenarios it is often required to render surfaces which are given as a finite set of point-sampled data. The sampling points, which are assumed to be based in some plane of reference, together with the sampled values form a *digital surface model (DSM)* of the surface. An important property of a surface is the *elevation* which denotes the deviation from the plane of reference (*ground plane*). The sampling positions and the corresponding elevations form a *digital elevation model (DEM)* of the surface which can be considered as a part of the DSM. If the DSM contains no other information about the surface than elevation, the DEM and the DSM of a surface are identical. However, a DSM may contain any kind of information about a surface and does not necessarily have to provide surface elevation data. In the context of this thesis, we assume that a DSM contains at least elevation data and consider a DSM as a DEM which may provide in addition to elevation data further information about the surface. In other words, we consider a DEM as a minimal DSM so that we can use the term *DSM* in situations in which the term *DEM* is used, but not vice versa.

Digital surface models allow to produce three-dimensional (3D) renderings of the surfaces for many different purposes. For instance, 3D terrain models of rural and urban areas are useful for landscape planing, surveying, field mapping and navigation. Further applications can be found, for instance, in the field of bathymetry where the elevation of the ocean floor is used to create maps and depth profiles, or in material science, where surfaces of materials and components are examined at microscopic scales to find structures or defects.

The creation of a DSM requires to sample the surface and to register the resulting values with their corresponding sampling positions in the ground plane. Since it is convenient for many applications to organize point samples on rectangular regular grids, DSM values are often represented as 2D arrays. Such arrays can be visualized as shown in figure 1.1 and may be used directly as *texture maps (textures)* for rendering.

Depending on the underlying application, different technologies for surface scanning are available, e. g., radar based techniques, echo sounding, laser scanning devices or scanning tunnel microscopes. Another possibility to obtain surface elevation information is to employ photogrammetric methods which under certain conditions allow to recover 3D information from two-dimensional images. These methods are used very often in conjunction with orthographic aerial photographs acquired from airplanes or satellites. In particular, aerial photographs captured from airplanes can be used to create high resolution DSMs of large areas like entire cities. The data shown in figure 1.1 are an example of a DSM generated by means of photogrammetric methods from aerial photographs. The field of photogrammetry has benefited from developments in digital photography and from the increased performance

(a) *elevation data* **(b)** *color data*

Figure 1.1: *A visualization of two kinds of DSM data which are represented as two 2D arrays. The elevation data (left) are also called* height map *in which brighter areas are more elevated than darker ones.*

of computers, and it has become possible to extract accurate elevation data automatically from aerial images.

A widely used method for surface rendering is to derive a polygonal mesh from the elevation data contained in a DSM and to use traditional rendering techniques based on triangle rasterization. A triangular mesh is an alternative representation of a surface and can be created by triangulating the original point-sampled data. If the DSM contains additional data about the surface, it is common practice to represent this information in textures and to map them onto the mesh. As the generation of high quality meshes and matching textures can be a time-consuming task, this is preferably done when the data acquisition has finished and no further data are added to the DSM. Otherwise the shape and the size of the corresponding mesh and additional textures may have to be modified each time the underlying data change. Furthermore, a DSM may become very large and may have sizes of several hundred gigabytes, which makes it necessary to partition the data in order to make the model manageable by graphics hardware with its limited physical memory. The task of finding an appropriate partitioning can be dealt best with after the final extensions of the domain covered by the DSM are known. Therefore the creation of meshes and textures is usually postponed until after the data acquisition has finished.

Rendering digital surface models during their creation and while the acquisition of the underlying surface data is still proceeding has the advantage that the creation process can be monitored and instant feedback can be given about the acquired data and the underlying surface. This requires that the source data are directly available for further processing. In the case of traditional aerial photography, the airplane usually has to land before the storage devices with the acquired images can be accessed for further processing. By exploiting advances in wireless communication, which enable the transfer of even large amounts of data over greater distances, the creation of digital surfaces models with matching textures and their rendering can already be started while the image acquisition is still in progress. The creation of DSMs which contain elevation data and matching color textures by means

of photogrammetric methods is not restricted to a certain image acquisition technique. It is sufficient if the images look like aerial images and have similar properties. For instance, appropriate photographs can be captured by suitable unmanned aerial vehicles (UAVs) instead of airplanes. Small UAVs offer an attractive alternative for this task, because they are less expensive and can capture images from a wider range of perspectives and at even higher resolutions due to their potentially lower operational altitudes. A drawback of such UAVs is their sensitivity to drift and that they may be less capable of following strict routes above the ground, which is important in traditional aerial photography. A rendering of a DSM which is directly derived from the acquired images can provide an operator with additional information for controlling the flight or for directing a UAV to an area of interest.

Another problem specific to the rendering of digital surface models in a virtual 3D environment arises when using *orthophoto textures* only. Orthographic images depict surfaces from an orthographic point of view and intentionally do not provide any information about (lateral) surfaces which are perpendicular or near-perpendicular to the plane against which the elevation is measured, e. g., frontages of buildings in urban areas or canyon walls. Figure 1.1(b) contains an example of such an orthophoto texture. Such images are amongst others very useful for creating schematic maps or for enhancing traditional maps with photographic details. In virtual 3D environments, however, a digital surface model is frequently not shown from an orthographic point of view, and the lack of color information on lateral surfaces becomes clearly visible to the viewer. The problem is mitigated, for example, in case of rendering certain kinds of *digital terrain models*, in which any elevation information resulting from vegetation, buildings or structures other than terrain has been removed. However, in virtual 3D views of cliffs or canyons, the missing color information is still apparent. In order to provide color information for lateral surfaces, *oblique aerial photographs* can be captured from airplanes by means of specially arranged camera systems or from suitable UAVs, and the images can be incorporated into 3D renderings.

This thesis addresses the problem of creating digital surface models and matching color texture maps from images similar to aerial photographs and managing and rendering such DSMs. But instead of waiting with the processing of a static set of images until after their acquisition has been completed, our goal is to process a dynamically changing set of images in order to enable the rendering of the corresponding surface already during the acquisition. The rendering poses a challenge since not only the sampled elevation and color data may change during acquisition, but also the domain covered by the digital surface model and thus the extension of the textures may vary over time. We assume vertical and oblique aerial photographs as source images which are captured by UAVs at low altitudes and immediately transferred by wireless networks to a ground station for processing. However, our methods are not confined to a certain image acquisition technique. The requirements for the source data and detailed background information about the underlying concepts of our work as well as definitions of important terms are given in chapter 2. Chapter 3 describes our work on managing growing texture data by means of a *Flexible Clipmap (FCM)*. This data structure was developed in order to provide partitioning and level-of-detail concepts for very large

texture data sets that can vary in size during the course of time. By design, the FCM is also capable of accelerating our DSM rendering process which is based on ray casting and is explained in chapter 4. The method we use to obtain elevation data from appropriate source images by means of photogrammetric techniques is presented in chapter 5 and relies on a 3D space sweep. In chapter 6 we present a solution to the problem of missing color information on lateral surfaces in DSMs which utilizes projective textures and some features specific to ray casting. The framework of implemented data structures and algorithms with its main components and properties is described in chapter 7. Our work concludes with a discussion and summary in chapter 8.

The following papers which have been published previously contain parts of the contributions of this thesis: The FCM as described in chapter 3 has been presented at the International Conference on Computer Graphics Theory and Applications (GRAPP) [28]. The work on managing and rendering texture maps of time-varying sizes by means of the FCM is part of papers presented at the Joint Virtual Reality Conference (JVRC) [75] and at the International Symposium on VR innovation (ISVRI) [74]. Chapter 4 is a detailed presentation of the DSM rendering method that has been published in the digital proceedings of the Computer Graphics International (GGI) conference [27].

2 Background

This chapter serves as an introduction into various topics that are essential for the remainder of this dissertation. The terms *digital surface model*, *image* and *texture* are important and used throughout this work, but their meaning in the field of computer graphics is to a certain degree context-sensitive. Hence in sections 2.1 and 2.2 we discuss these terms and specify how we understand them. Since aerial images form the basic input to the methods presented within this thesis their most important properties and aspects of their acquisition are covered in section 2.3. In section 2.4, we present the different coordinate systems that are used throughout this thesis and how they are related to each other. Section 2.5 introduces the basic principles of photogrammetry and the underlying mathematical formulations.

2.1 Digital Surface Models

The term *digital surface model (DSM)* is not clearly defined, because it depends on the context of its usage within the different sciences and applications, as well as the underlying data. In geoscience and photogrammetry, several closely related terms are used, which are sometimes considered to be synonyms, but may also refer to distinct types of models in different disciplines. According to Li et al. [46, pp. 6–9], common terms are

- digital terrain model (DTM)
- digital elevation model (DEM)
- digital terrain elevation model (DTEM)
- digital height model (DHM)
- digital ground model (DGM)

The authors consider DTMs as more complex models that may have additional information about the terrain, such as land-use plans, road networks and natural features, and they view a DEM as a special case of a DTM where the only available information is the elevation. DTEM, DHM and DGM are taken as synonyms for DEM, but interestingly, Li et al. do not use the term *digital surface model* at all.

In contrast, Kraus [42, p. 354], who discusses the earth surface from a photogrammetric point of view, distinguishes DTMs, which contain only elevation information about the terrain, but not about other structures like vegetation or buildings, from DSMs, which contain elevation data for these additional structures.

For the mere purpose of rendering and managing, the actual semantics of the underlying surface data is less important and our methods are not limited to terrains or applications in

geoscience. Most of the methods presented in this work can be applied to data acquired from surfaces at microscopic scales, e. g., by means of a scanning tunnel microscope, or to other complex surfaces such as reliefs and friezes on buildings or works of art. Therefore we prefer the general term *surface* and formally define a DSM within the context of this thesis as follows:

Definition: *Digital Surface Model (DSM)*

A *digital surface model (DSM)* is a finite set of n-tuples

$$\mathcal{DSM} = \{(t_1, t_2, t_3, \ldots, t_n) \in \mathbb{R}^n\}$$

for which $t_1 = x$ and $t_2 = y$ denote the position of a point $p = (x, y)$ in a section $D \subset \mathbb{R}^2$ of the zero plane, and $t_3 = h$ denotes a deviation at p from the zero plane, i. e., an elevation or depression. Any two distinct n-tuples in the DSM have to correspond to different points in D, i. e.

$$\forall s = (s_1, \ldots, s_n), t = (t_1, \ldots, t_n) \in \mathcal{DSM} : s_1 = t_1 \wedge s_2 = t_2 \Rightarrow s = t$$

This definition allows the tuples of a DSM to contain further scalar values besides the spatial position information (x, y, h). In case of $n = 3$ the DSM is identical to a DEM, but if $n > 3$, other information about the surface may be part of the DSM. A DEM is formed by projecting the n-tuples of the DSM to their first three components. When indicated, we will use attributes like *color textured* or simply *textured* DSM, if the additional information is color, for example, in order to emphasize the presence of additional surface information and its meaning. Otherwise the terms DSM and DEM are used interchangeably and the respective distinction can be inferred from the context or is not relevant at that point. In addition, the zero plane of a DSM will also be called *ground plane* within this thesis.

Though our comprehension of a DSM is very similar to the one of a DTM by Li et al. in [46], the difference is that our definition does not force the kind of surface to be terrain. Furthermore, it requires at least one scalar value to be present in every DSM that has the semantics of elevation or depression at point p relative to the ground plane in which p is located (*height value*). The latter aspect is more important for the interpretation of the renderings generated by our methods than for the techniques themselves. It is also intended to make our definition somewhat distinct from the concept of fields as used in physics, although the difference may be rather subtle. For example, a finite set $\mathcal{T}$ of triples $(x, y, h) \in \mathbb{R}^3$ may be interpreted as a DSM and treated in the same way. But if h denoted, e. g., air pressure or some kind of density instead of a height value at location (x, y), the interpretation of $\mathcal{T}$ as a DSM and the resulting renderings might be less reasonable.

2.1.1 Representing DSMs

From a mathematical point of view, there is no reason to confine a DSM to be a *finite* set of n-tuples as in the definition given above. But most surfaces in real-world applications, especially in geoscience, are too complex for creating analytical models by means of mathematical methods, and therefore surfaces are usually sampled at discrete locations, which

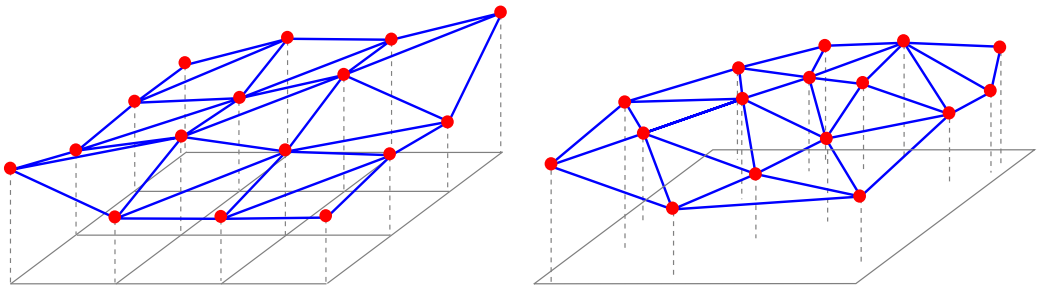

(a) *triangular regular network (TRN)* **(b)** *triangular irregular network (TIN)*

Figure 2.1: *Illustration of two different types of triangular networks for representing DEMs having 16 samples on a regular grid (left) and with an irregular distribution (right).*

results in a representation as finite sets of *sampling points* (cf. Li et al. [46]). The size of these sets is limited by the spatial resolution of the employed sampling technique and the time spent on sampling, and furthermore by the amount of available physical memory when the data are stored for processing by computers. Depending on the sampling method, the sampled values are distributed either irregularly, or arranged on a regular orthogonal grid.

According to our definition, the first three components of each sample correspond to a point in 3D Euclidean space. Sets of such points can be represented as *triangular regular networks (TRNs)* or *triangular irregular networks (TINs)*. Depending on the sampled data and the application, one may prefer to create either TRNs or TINs, but both types of networks can be converted into each other by means of re-sampling and sample selection. An illustration of DEMs represented as triangular networks is given in figure 2.1. The generation of TRNs from DSM samples given on a regular grid is straightforward, but not necessarily unique, whereas TINs are frequently generated by a process called *triangulation*, like Delaunay triangulation, for example. The Delaunay triangulation for a set of points in Euclidean space is the dual graph of its Voronoi diagram, which is also known as Dirichlet tessellation or Thiessen polygons [46, pp. 75–85], and it is unique, if and only if all points are in general position [17, pp. 189–190]. More details on triangulation can be found in [17], for instance.

Triangular networks are the most basic polygonal meshes that can be used for rasterization based rendering, and many algorithms for their creation are available. Due to the requirements of graphics hardware, triangular meshes are very common in computer graphics and used exclusively in numerous applications. However, if these meshes are used for rasterization-based rendering in a virtual 3D environment, triangles which are small, e. g., because they are distant from the viewer, may become projected to less than one screen pixel and therefore will cause aliasing. This effect is usually avoided by using level-of-detail techniques in order to generate meshes in which the size of triangles increases with the distance from the viewer. Since the creation of appropriate triangular meshes requires extra processing of the DSM samples, this representation is less appropriate for our application in which the DSM may frequently change. We prefer to directly employ the DSM

samples and refer to [46] for further details on the representation of DSMs respectively DTMs as triangular networks.

If the sampled DSM values are given on a regular rectangular grid, they are prevalently stored as arrays for processing by computers. The whole DSM may be stored as one *interleaved array* where each element of the array corresponds to one complete n-tuple. As an alternative, the DSM can be stored in multiple arrays all having the same number of elements where each element corresponds to one or more components of the DSM n-tuple. The individual arrays may be stored in sequence in a contiguous block of memory and can be interpreted as a two-dimensional (2D) array where the second index is limited by the number k of arrays which store the data. The two different possibilities for splitting one array of 4-tuples are depicted in figure 2.2. The array in figure 2.2(a) is split into $k = 4$ arrays of single values. In figure 2.2(b), the same array is divided into $k = 2$ arrays, where the first array contains single values and the second one contains triples. By splitting the DSM data with respect to their semantics into k different arrays, we can consider each of these arrays as a *layer* of the DSM, and each layer depicts a certain feature of the surface, e. g., the DEM layer which contains elevation data and is present in all of our DSMs.

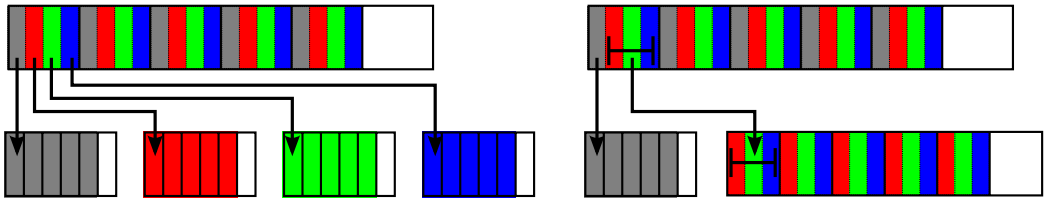

(a) $k = 4$ *arrays* **(b)** $k = 2$ *arrays*

Figure 2.2: *Interleaved arrays which store n-tuples may be split up into $1 < k \leq n$ arrays that can be treated as 2D arrays. Each of the arrays has the same number of elements, but the elements themselves may have different sizes.*

If a DSM given on a regular rectangular grid in Cartesian coordinates is stored in an array, random access to individual DSM values for a given location in Euclidean space or a certain grid position $(i, j) \in \mathbb{N}^2$ is very efficient[1]. On a regular rectangular grid, which will be called *grid* for simplicity for the remainder of this dissertation, the spacings between each two samples are uniform and fixed, and each sample position $p = (x, y) \in \mathbb{R}^2$ can be represented as

$$p = (x, y) = (i \cdot g_x, j \cdot g_y) + p_0$$

where $g = (g_x, g_y) \in \mathbb{R}^2$ denotes the grid spacings in x- respectively y-direction and $p_0 = (x_0, y_0)$ is the offset of the grid in the reference coordinate system of the DSM at grid position $(i = 0, j = 0)$. (i, j) is the grid position within the grid of size $W \times H$, and

[1] Throughout this thesis, $\mathbb{N}$ will be considered to include zero, i. e., $\mathbb{N} = \mathbb{N}_0$.

$W, H \in \mathbb{N}$ denote the grid size[2] in x-direction respectively in y-direction in terms of sample points so that $0 \leq i < W$ and $0 \leq j < H$.

Usually p_0, W, H and g are constant for DSMs and hence can be stored separately. This allows to drop the original sample positions $p = (x, y)$ from the DSM representation and to reduce the amount of memory that is required for storage, because at grid position (i, j), p can be restored by means of the grid spacings g and a reference position p_0. Note that this reduction of data cannot be achieved for irregularly sampled data and the TIN representation, and p is therefore made a part of a DSM in our definition. As the arrays in both layouts described above are contiguous sections of linear computer memory, grid samples are conceptually stored either row- or column-wise.

Within this thesis, we use the layered and reduced representation of DSMs as 2D arrays. The employed DSMs either consist of only a single DEM layer or have a second *color texture layer* which contains color information about the surface. We use row-wise storage and index the n^{th} element of a DSM array by $n = j \cdot W + i$ where i and j denote the column and the row of the grid, respectively. The rows and columns of a grid are indexed starting with zero and grid position $(i = 0, j = 0)$ is conceptually located at the left lower corner.

2.2 Images, Photographs and Texture Maps

The terms *image* and *texture map*, or *texture* in short, have already been used several times and are important in the context of our work[3]. In the area of computer graphics, these two terms can be well differentiated, but their synonymous usage is acceptable if a distinction is not required or only of minor importance. This is justified by the fact that a large number of textures which are used in computer generated renderings are images. Since we make use of textures that are not images in the proper sense in order to handle DSMs, we want to distinguish *images* from *textures* and assign different meanings to the two words.

2.2.1 Images

A digital 2D raster image can be defined as a mapping I of spatial locations (x, y) given on a raster $D \subset \mathbb{R}^2$ to a finite set Q of values:

$$I : D \subset \mathbb{R}^2 \rightarrow Q, \quad (x, y) \mapsto I(x, y)$$

Q may be either a finite set of discrete scalar values or a finite set of tuples of discrete scalar values. In the former case, the images are frequently called *monochrome*, and in the latter case they are called *color images* (see section 2.2.3). The elements of a digital image are called *pixels* and the values from the co-domain Q of I are often referred to as *intensities* [34, pp. 1]. This definition allows to interpret any such function I as an image.

[2] In this dissertation, we use the notation $x \times y$ with scalar quantities x and y to emphasize the 2D character of sizes of 2D structures such as grids, textures, matrices and 2D arrays. The notation $x \cdot y$ is used in situations where the actual result obtained by the multiplication of the two values x and y is meant.

[3] Within this dissertation, the terms *image* and *texture* always refer to digital data in the field of computer graphics and not to any analog photographic images or physical objects.

But within this thesis, we use the term *image* to imply that the pixels are associated with real-world objects or scenes in the sense of a *photographic image*. In addition, we assume that the domain D of I is always a Cartesian grid. The actual image acquisition is less important than the *content* of an image and its property that the pixels are related to real-world objects. According to our interpretation, the term *image* therefore comprises photographs acquired by still image cameras, as well as, for instance, computer generated renderings of real-world objects.

2.2.2 Texture Maps

According to Shreiner [71, p. 390], we consider a *texture map*, or simply *texture*, as a rectangular array of *texels*. For a long time, these arrays have been used in computer graphics prevalently for adding properties such as color, surface normals, reflectance or roughness to surfaces in order to reproduce a certain texture in the proper sense (cf. [83, pp. 223]). Because of the evolution of graphics processing units (GPUs), and in particular due to their increasing employment for general purpose computing (GPGPU computing), the interpretation of these arrays as textures according to their original meaning has become imprecise in many cases, but the term *texture* is still prevailing [59].

By the term *texture* within the scope of this thesis, we only imply that these arrays can be handled by graphics hardware in the same way like traditional texture maps. The texels are not limited to a certain kind of semantics, in contrast to our interpretation of pixels in images. Texels normally need to have a certain format (see section 2.2.3) in order to be suited for processing by graphics hardware. In addition, the maximal extension of a texture which can be employed by graphics hardware, i. e., its lateral sizes in terms of texels along each direction, is confined by some manufacturer specific limits. Typically, textures are conceptually two-dimensional arrays (2D textures), but one-dimensional (1D textures) or three-dimensional (3D textures) arrays are also common. If nothing else is stated, we use the term *texture* as an abbreviation for *2D texture*.

2.2.3 Representing Images and Textures

Depending on the co-domain Q of the mapping I which defines an image, a single pixel may be a single scalar value or a tuple of scalar values. A single texel from a texture may likewise be either a single scalar value or a tuple of scalar values. The number of bits required to store one pixel or one texel is called *depth*. The *pixel format* respectively *texel format* is defined by the depth and, if there is more than a single value, by the order of values, i. e., the order of the elements of the tuple. Pixel and texel values are in most cases related to (discretized) intensities from the visual electromagnetic spectrum [34, pp. 1], and we call them *grayscales* if there is only one value per pixel respectively texel. If there are multiple values for different wavelengths, e. g., red, green and blue in the RGB color model, the values are called *colors*. The different pixel and texel formats, which are frequently used in the context of our work, and their respective labels, properties and short descriptions are given in table 2.1.

label	depth [bits]	no. values	data type	description
I8	8	1	BYTE	unsigned 8-bit intensity values, primarily used for grayscale images and textures
F32	32	1	float	32-bit IEEE 754 floating point values, mainly used for storing elevation data of a DSM
R8G8B8	24	3	BYTE	triple of unsigned 8-bit values, one each for the red, green and blue components in the RGB color model
R8G8B8A8	32	4	BYTE	quadruple of unsigned 8-bit values, same as R8G8B8 but with an additional alpha channel for controlling the opacity

Table 2.1: *Description of pixel and texel formats that are used within this thesis. The column* data type *denotes the interpretation of the bit pattern of a single value.*

Conceptually textures and images are 2D arrays of size $T_u \times T_v$ where $T_u, T_v \in \mathbb{N}$ denote the number of elements in each row respectively column and $T_u, T_v > 0$. Their elements are stored in linear computer memory and are accessed in the same way as the elements of DSM layers (see section 2.1.1). In contrast to the prevalent convention in the field of image processing, we assume the first row of an image (resp. texture) to be located at the bottom of the image (resp. texture) rectangle instead of at its top, so that the first pixel (resp. texel) is located at the bottom left. In this way, we can interpret the data from any DSM which is given in the reduced layered array representation as described in section 2.1.1 as a set of textures and the DSM samples of each layer can be identified with texels. Layers which hold DEM data are interpreted as F32 textures (*DEM textures*), and layers with color information as R8G8B8 or R8G8B8A8 *color textures*. If necessary, the data types of DSM layers are converted in order to match the required texel format.

We can summarize the differences between *images* and *textures* according to our definitions as follows: if a pixel format is compatible with a texel format, or if it can be converted accordingly, we can take any image for a texture. A texture, however, cannot be taken for an image in general, because even if a texel format is a valid pixel format, texels may not be associated with real-world objects, in contrast to the pixels of an image. This is a common case in GPGPU computing, for instance, but it already appears somewhat odd to us if we interpret a DEM texture as a grayscale image, because the content of the image may not be comprehensible without any further explanation.

2.3 Aerial Images

In this thesis we focus on DSMs which are derived from aerial images by means of photogrammetric methods. The most common source of aerial images are digital photographs which are traditionally captured from airplanes. Miniature UAVs (mUAVs) have become a less expensive alternative to conventional airplanes [25] and are increasingly used for civil purposes, e. g., for surveying archaeological sites [8, 21, 22, 68]. The actual image acquisi-

tion is less important for our methods than the fact that the images look like aerial images, but we intend to employ primarily aerial images captured by mUAVs.

This section gives a classification of aerial images and outlines the differences in image acquisition by means of mUAVs and airplanes. According to our interpretation of images, the terms *photograph* and *image* are used interchangeably in this section (cf. section 2.2).

2.3.1 Classification of Aerial Images

According to Paine and Kiser [60, pp. 28], we use the attribute *aerial* in contrast to *terrestrial* to refer to all kinds of images that are captured from an arbitrary platform in the air, including scaffolds or cranes, for example, and classify them likewise into *vertical* and *oblique* images.

The ground plane is the virtual plane which is oriented in such a way that the normal $\vec{n}_g$ of this plane has the opposite direction as the vector of gravity which points towards the Earth's center. Let $\vec{n}_I$ denote the normal of the image plane of an aerial image I in world space as illustrated in figure 2.3. $\varphi = \measuredangle(\vec{n}_I, -\vec{n}_g) \in \left[-\frac{\pi}{2}, \frac{\pi}{2}\right]$ denotes the angle enclosed between $\vec{n}_i$ and $-\vec{n}_g$. According to [60], an aerial photograph is called *vertical* if $0 \leq |\varphi| < \varphi_{\text{max}}$, and *oblique* if $\varphi_{\text{max}} \leq |\varphi| \leq \frac{\pi}{2}$ where $\varphi_{\text{max}} = \frac{\pi}{60} = 3°$. Paine and Kiser call a vertical aerial photograph *true vertical* if $|\varphi| = 0$, and *tilted* otherwise. Oblique photos are called *low oblique* if they do not depict the horizon, and *high oblique* if the horizon is visible.

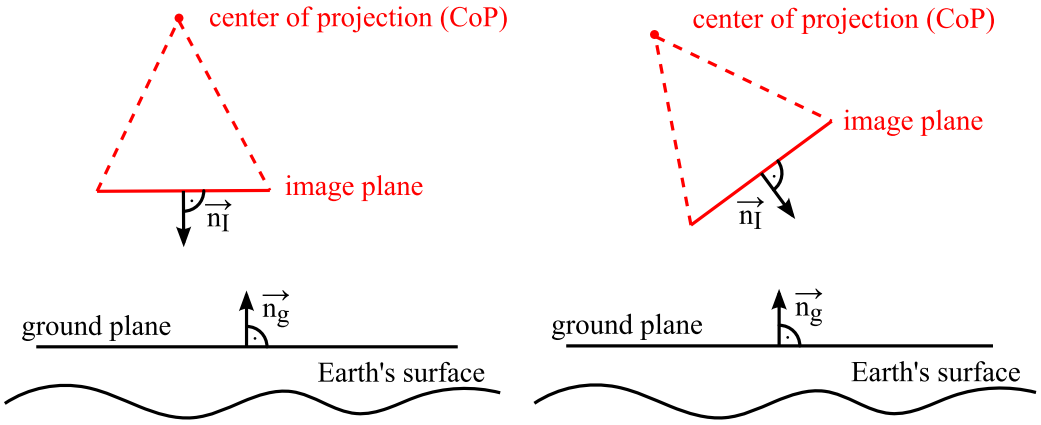

(a) *vertical aerial photograph* **(b)** *oblique aerial photograph*

Figure 2.3: *Aerial images are classified according to [60] as* vertical aerial images *(left) and* oblique aerial images *(right) by the angle φ enclosed between the normal of the image plane $\vec{n}_I$ and the inverse normal of the ground plane $-\vec{n}_g$.*

The two kinds of aerial images have different advantages over each other. It is easier, for instance, to measure horizontal distances and areas in vertical photographs, and they can be used as substitutes or enhancement for conventional schematic maps. Oblique images, on the other hand, provide a more natural perspective and depict structures perpendicular to the ground [60, pp. 29–30]. Because of their different properties, we use vertical aerial

images as input data for generating DEM data and orthophoto textures, whereas oblique aerial images are exclusively used for texturing lateral surfaces in DSM renderings. These two aspects are the subjects of chapter 5 and chapter 6 respectively.

2.3.2 Aerial Image Acquisition

Aerial images are traditionally acquired as vertical photographs from airplanes. Airplanes are capable of keeping approximately constant heights above ground and following fixed paths. This way, a certain overlap between the vertical photographs can be guaranteed, which is important for reconstructing 3D information as described in section 2.5. The camera systems which are employed in traditional aerial photography are usually equipped with sophisticated optical lens systems and mountings in order to capture high resolution images. These systems weigh several tens of kilograms (e. g., [89]), but can be easily carried by airplanes. The acquired photographs are preferably stored in uncompressed data formats on hard disk drives or solid state disks and cannot be accessed until the plane has landed.

Vertical and oblique aerial photographs can also be captured by UAVs [39]. While the flight characteristics and capabilities of acquiring aerial photographs of larger UAVs are similar to those of conventional airplanes, mUAVs are more maneuverable, but may not be able to carry heavy camera systems as payload [82, 84]. Hence, the cameras mounted to mUAVs may provide images at lower resolutions, but this can be compensated by their potentially lower operational altitudes. With mUAVs it is as also possible to capture several images from different perspectives, so that the same points of a surface are depicted in multiple images and stereo matching methods can produce better results, as explained in chapter 5. As smaller UAVs are more prone to drift and may additionally not be capable of following fixed paths at constant altitudes, the images will likely be captured in a less organized manner than in case of traditional aerial photography.

For the purpose of recovering 3D information from photographs, it is essential to have the camera's accurate position and orientation in space. Position and orientation data of airplanes and UAVs are usually available by Global Positioning System (GPS) and inertial measurement units (IMUs) and can be linked to the images. Mapping camera systems borne by airplanes are in fact designed for using data from IMU and GPS devices [89], [42, pp. 150–161].

2.3.3 The AVIGLE Project

The *Avionic Digital Service Platform (AVIGLE)* project [64] is a cooperation of seven partners from the high tech industry and three universities and is funded by the ministry of Innovation, Science and Research of the State of North Rhine-Westphalia, Germany, and the European Union. The goal of the project is amongst others to develop a multi-functional mUAV for civil purposes with a total weight of approximately 10 kg. By design, the aircraft is capable of horizontal and vertical flight, as well as hovering in place, and should operate in heights of up to 300 meters above ground and for about 60 minutes. The payload of $\approx$ 1 kg weight is intended to be either equipment for providing cellular network communications, or a calibrated digital still image camera for capturing high-resolution digital

photographs. Aerial images together with orientation data from the GPS and IMU devices of the mUAV can be transmitted directly to the operators via wireless network technology. This allows to create DSMs for rendering in a virtual 3D environment while the image acquisition is still in progress. Thus, the operators can be immediately provided with a recent overview of the surveyed area in order to direct the aircraft to locations of special interest.

As the development of the aircraft is conducted in parallel to our methods for creating and rendering DSMs during an ongoing image acquisition, and has not finished at the time of writing this dissertation, efforts have been made to simulate the acquisition of aerial images by mUAVs [75]. The simulation of aerial image acquisition basically comprises the preferably photorealistic rendering of 3D models of cities or landscapes, and the provision of individual frames together with their *metadata*. These metadata are the position, orientation and some additional parameters of the virtual camera at the time of image acquisition. In case of the AVIGLE project, aerial images are accessed by means of a database management system which allows to separate the image acquisition process from our methods for rendering and generating DSMs.

2.4 Coordinate Systems

Within this thesis we only employ Cartesian coordinate systems in 2D and 3D, but with different orientations and labels for the axes.

Coordinates from real world space, e. g., locations where images were captured, are assumed to be precise and referenced to a 2D geographic coordinate system. The coordinates are assumed to be provided, for instance, by GPS with eventually applied corrections and accuracy enhancements. We prefer such coordinates in UTM format over WGS84 or similar, because UTM values are already given in a Cartesian coordinate system [60, p. 181]. Height values and altitudes are both assumed to be given relative to a plane of reference based in the xy-plane respectively east-north-plane at $z = 0$ of a 3D coordinate system as depicted in figure 2.4(a). The unit of measurement and scale of the three axes has to be the same, e. g., meter. For convenience, we express all real world coordinates in the virtual world coordinate system Σ, which is shown in figure 2.4(b). The scale and the unit of measurement of Σ are the same as the ones of the real world coordinate system, and Σ is simply referred to as *world coordinate system* throughout this work.

For cameras which are used to capture real world images, as well as virtual cameras, we use the local 3D Cartesian coordinate system Σ'. Σ' is shown in figure 2.4(c), the *center of projection (CoP)* of an image is located at its origin. The basis of Σ' is expressed in Σ by $\vec{r} = (r_x, r_y, r_z)$ (right-vector), $\vec{u} = (u_x, u_y, u_z)$ (up-vector) and $\vec{v} = (v_x, v_y, v_z)$ (view-vector). In contrast to Σ, Σ' has a negative orientation (*left-handed coordinate system*), i. e., the determinant

$$\begin{vmatrix} r_x & u_x & v_x \\ r_y & u_y & v_y \\ r_z & u_z & v_z \end{vmatrix} = (\vec{r} \times \vec{u}) \cdot \vec{v} < 0$$

is negative [1, p. 901]. Due to its positive orientation, Σ is called a *right handed coordinate system*.

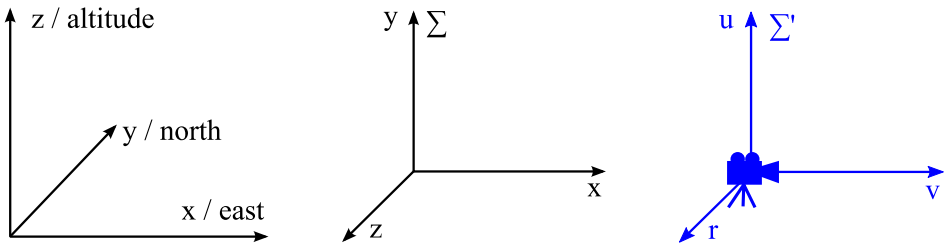

(a) *real world coordinate system*

(b) *(virutal) world coordiante system*

(c) *camera coordinate system*

Figure 2.4: *Illustrations of the different coordinate systems that are used throughout this dissertation. Height values and elevation in the real world coordinate system in (a) are stored at the z-component of coordinates and the ground plane is based in the xy-plane. In the (virtual) world coordinate system in (b), height values and elevation are stored at the y-component and the ground plane is based in the xz-plane. Except for Σ' in (c), theses coordinate systems are right-handed, i. e., their orientation is positive.*

2.5 Basic Principles of Photogrammetry

Photogrammetry is the science of determining the shape, position and orientation of objects in 3D space from 2D images [42, p. 1]. In an image, the objects in 3D space are mapped onto a 2D *image plane* by geometric planar perspective projections (*projections* in short). There are other kinds of projections, e. g., orthographic projections, but they are of less interest in the context of this thesis. The mathematical foundations and detailed information about these different types of projections can be found, for instance, in [29, pp. 229–283] and [1, pp. 89–97].

The depth information of an object is lost during projection and hence a single image is usually not sufficient to reconstruct the 3D positions of the depicted points of an object. But if the same points of an object are present in at least two different images, and if the parameters of the projections for each image are known, the depth information can be recovered. The principle works similar to human stereoscopic vision [60, pp. 44–67].

Under the assumption that optical effects related to lenses, e. g., fraction and distortions, are negligible in calibrated, high quality mapping cameras, these camera systems can be approximately modeled as pinhole cameras. The model of a pinhole camera may also be applied to consumer cameras, but the results are usually less accurate. Recent advances in image processing, however, allow to mitigate this problem by incorporating multiple images of the same objects and statistical methods. An example can be found, for instance, in [72] where images from many different types of cameras are employed for 3D reconstruction.

In section 2.5.1 a mathematical introduction into planar central perspective projections is presented and it is explained, how 3D information can be extracted from 2D images by

effectively reversing projections. The camera parameters which are required for this task are described in section 2.5.2, and section 2.5.3 summarizes the most important properties of images which are appropriate for recovering 3D information.

2.5.1 Perspective Projection

Central perspective projection emulates the effect of foreshortening so that objects that are more distant to the viewer appear smaller than those that are closer. The projection of a 3D object in a 2D image is obtained at the intersections of *projection rays* with the image plane. In the case of central perspective projection, the projection rays emerge from a single *center of projection (CoP)* and pass through each point of the depicted object as illustrated in figure 2.5 [29, p. 230].

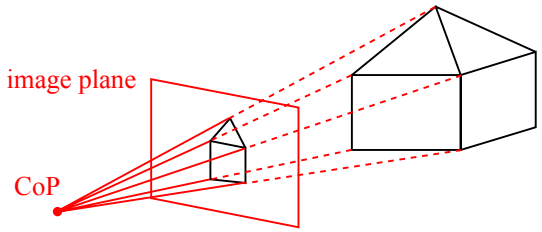

Figure 2.5: *Projection rays intersect at the center of projection (CoP) in case of planar central perspective projections.*

Let the image plane be located at a distance $f > 0$ in front of the CoP. The CoP is located at the origin O' of the local coordinate system of (virtual) camera $\Sigma' = (\vec{r}, \vec{u}, \vec{v})$. Σ' is usually translated by $\vec{t} = (t_x, t_y, t_z)$ and rotated relative to the world coordinate system $\Sigma = (\vec{x}, \vec{y}, \vec{z})$ as shown in figure 2.6(a). The orthonormal basis of Σ is given by

$$\vec{x} = (1, 0, 0) \qquad \vec{y} = (0, 1, 0) \qquad \vec{z} = (0, 0, 1)$$

and the orthonormal basis of Σ' is expressed in Σ by

$$\vec{r} = (v_x, v_y, v_z) \qquad \vec{u} = (u_x, u_y, u_z) \qquad \vec{v} = (v_x, v_y, v_z)$$

In neutral position, i. e., $\vec{t} = (0, 0, 0)$ and with all three rotation angles equal to zero, Σ' is oriented in such a way, that $\vec{r} = \vec{x}$, $\vec{u} = \vec{y}$ and $\vec{v} = -\vec{z}$ as illustrated in figure 2.6(b).

In order to transform locations from Σ to Σ' and to project them onto image planes, 4D homogeneous coordinates can be used. Homogeneous coordinates allow to conveniently represent a sequence of geometric transformations, including translations and projections, as a single matrix [1, pp. 54, 905–906], [29, pp. 213–217]. The transformation of a point $p = (x, y, z) \in \mathbb{R}^3$ to $\hat{p}$ in 4D homogeneous coordinates is achieved by

$$(x, y, z) \mapsto (w \cdot x, w \cdot y, w \cdot z, w)$$

where $w \neq 0$. The additional fourth component is usually set to 1. A point $\hat{p} = (\hat{x}, \hat{y}, \hat{z}, \hat{w})$, $\hat{w} \neq 0$ in 4D homogeneous coordinates is transformed to 3D Cartesian coordinates by

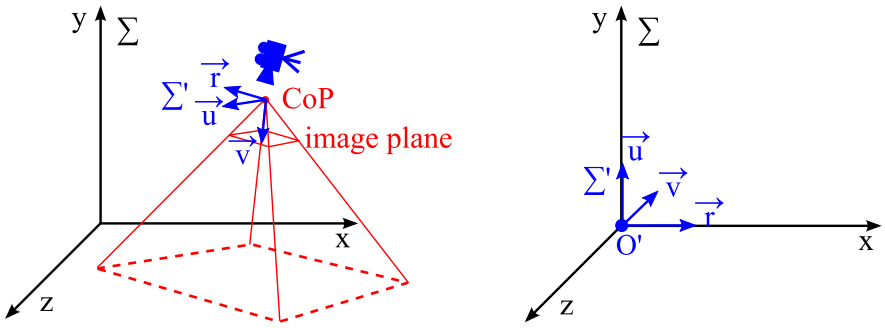

(a) *general position* **(b)** *neutral position*

Figure 2.6: *Illustration of the orientation of the local camera coordinate system Σ' within the world coordinate system Σ in general position (left) and in neutral position (right).*

dividing each component of $\hat{p}$ by $\hat{w}$ and by dropping the fourth component:

$$(\hat{x}, \hat{y}, \hat{z}, \hat{w}) \mapsto \left(\frac{\hat{x}}{\hat{w}}, \frac{\hat{y}}{\hat{w}}, \frac{\hat{z}}{\hat{w}} \right)$$

The division of $\hat{p}$ by $\hat{w}$ is called *homogenization*.

A point $p = (x, y, z)$ can thus be transformed from Σ to $q = (q_r, q_u, q_v)$ in Σ' by multiplying its representation $\hat{p}$ in homogeneous coordinates with a regular 4×4 matrix V, followed by homogenization in order to obtain Cartesian coordinates, as expressed in equation (2.1).

$$\hat{q} = \begin{pmatrix} \hat{q}_r \\ \hat{q}_u \\ \hat{q}_v \\ \hat{q}_w \end{pmatrix} = V \cdot \hat{p} = V \cdot \begin{pmatrix} x \\ y \\ z \\ 1 \end{pmatrix} \quad \Rightarrow \quad q = \left(\frac{\hat{q}_r}{\hat{q}_w}, \frac{\hat{q}_u}{\hat{q}_w}, \frac{\hat{q}_v}{\hat{q}_w} \right) \tag{2.1}$$

Matrix V, which is given in equation (2.2), is composed of a translation T, a rotation R which performs a rigid body transformation of the coordinate axes, and a mirroring operation $-Z$ along the z-axis in Σ.

$$\begin{aligned} V &= \underbrace{\begin{pmatrix} 1 & 0 & 0 & 0 \\ 0 & 1 & 0 & 0 \\ 0 & 0 & -1 & 0 \\ 0 & 0 & 0 & 1 \end{pmatrix}}_{=-Z} \cdot \underbrace{\begin{pmatrix} r_x & r_y & r_z & 0 \\ u_x & u_y & u_z & 0 \\ v_x & v_y & v_z & 0 \\ 0 & 0 & 0 & 1 \end{pmatrix}}_{=R} \cdot \underbrace{\begin{pmatrix} 1 & 0 & 0 & -t_x \\ 0 & 1 & 0 & -t_y \\ 0 & 0 & 1 & -t_z \\ 0 & 0 & 0 & 1 \end{pmatrix}}_{=T} \\ &= \begin{pmatrix} r_x & r_y & r_z & -\vec{t} \cdot \vec{r} \\ u_x & u_y & u_z & -\vec{t} \cdot \vec{u} \\ -v_x & -v_y & -v_z & \vec{t} \cdot \vec{v} \\ 0 & 0 & 0 & 1 \end{pmatrix} \end{aligned} \tag{2.2}$$

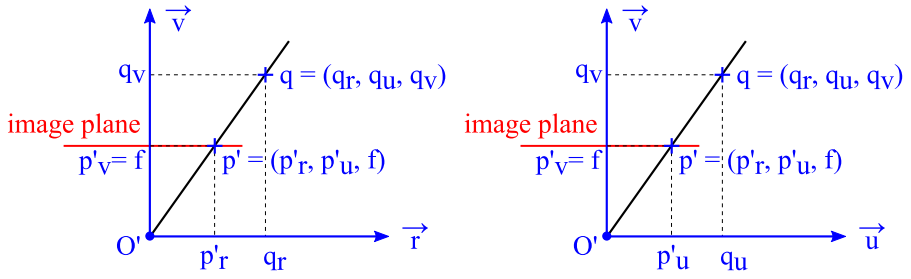

Figure 2.7: *Applying the intercept theorem to the two pairs of similar triangles $\triangle_{O',q,q_r}$ and $\triangle_{O',p',p'_r}$ respectively $\triangle_{O',q,q_u}$ and $\triangle_{O',p',p'_u}$ results in equation (2.4).*

In order to obtain the projection p' of q in the image plane at $v = f > 0$ in Σ', the projection matrix P from equation (2.3) is applied to $\hat{q}$.

$$P = \begin{pmatrix} 1 & 0 & 0 & 0 \\ 0 & 1 & 0 & 0 \\ 0 & 0 & 1 & 0 \\ 0 & 0 & \frac{1}{f} & 0 \end{pmatrix} \tag{2.3}$$

p' and q must satisfy the relations in equations (2.4) which result from applying the intercept theorem to the two pairs of similar triangles $\triangle_{O',q,q_r}$ and $\triangle_{O',p',p'_r}$ respectively $\triangle_{O',q,q_u}$ and $\triangle_{O',p',p'_u}$ as illustrated in figure 2.7.

$$\begin{aligned} p'_v &= f \\ \frac{q_v}{q_r} = \frac{p'_v}{p'_r} = \frac{f}{p'_r} &\Leftrightarrow p'_r = f \cdot \frac{q_r}{q_v} \\ \frac{q_v}{q_u} = \frac{p'_v}{p'_u} = \frac{f}{p'_u} &\Leftrightarrow p'_u = f \cdot \frac{q_u}{q_v} \end{aligned} \tag{2.4}$$

Equation (2.5) confirms that applying P to q in homogeneous coordinates and transforming back to Cartesian coordinates yields $p' = (p'_r, p'_u, p'_v)$ as desired:

$$\begin{aligned} \hat{p}' = \begin{pmatrix} \hat{p}'_r \\ \hat{p}'_u \\ \hat{p}'_v \\ \hat{p}'_w \end{pmatrix} = P \cdot \begin{pmatrix} q_r \\ q_u \\ q_v \\ 1 \end{pmatrix} = \begin{pmatrix} q_r \\ q_u \\ q_v \\ \frac{q_v}{f} \end{pmatrix} \\ \Rightarrow p' = \left(\frac{\hat{p}'_r}{\hat{p}'_w}, \frac{\hat{p}'_u}{\hat{p}'_w}, \frac{\hat{p}'_v}{\hat{p}'_w} \right) = \left(f\frac{q_r}{q_v}, f\frac{q_u}{q_v}, f \right) \end{aligned} \tag{2.5}$$

The transformation matrix V and the projection matrix P are usually combined into a single Matrix M, so that the projection of p in Σ to p' in the image plane at $v = f$ in Σ' can be

expressed as in equations (2.6).

$$\begin{aligned}
\hat{p}' = M \cdot \begin{pmatrix} p_x \\ p_y \\ p_z \\ 1 \end{pmatrix} &= \begin{pmatrix} r_x p_x + r_y p_y + r_z p_z - \vec{t} \cdot \vec{r} \\ u_x p_x + u_y p_y + u_z p_z - \vec{t} \cdot \vec{u} \\ -\left(v_x p_x + v_y p_y + v_z p_z\right) + \vec{t} \cdot \vec{v} \\ \frac{-(v_x p_x + v_y p_y + v_z p_z) + \vec{t} \cdot \vec{v}}{f} \end{pmatrix} \\
\Rightarrow p' = \begin{pmatrix} p'_x \\ p'_y \\ p'_z \end{pmatrix} &= \begin{pmatrix} -f \frac{r_x p_x + r_y p_y + r_z p_z - \vec{t} \cdot \vec{r}}{v_x p_x + v_y p_y + v_z p_z - \vec{t} \cdot \vec{v}} \\ -f \frac{u_x p_x + u_y p_y + u_z p_z - \vec{t} \cdot \vec{u}}{v_x p_x + v_y p_y + v_z p_z - \vec{t} \cdot \vec{v}} \\ f \end{pmatrix} \\
&= f \begin{pmatrix} -\frac{r_x (p_x - t_x) + r_y (p_y - t_y) + r_z (p_z - t_z)}{v_x (p_x - t_x) + v_y (p_y - t_y) + v_z (p_z - t_z)} \\ -\frac{u_x (p_x - t_x) + u_y (p_y - t_y) + u_z (p_z - t_z)}{v_x (p_x - t_x) + v_y (p_y - t_y) + v_z (p_z - t_z)} \\ 1 \end{pmatrix}
\end{aligned} \tag{2.6}$$

where

$$M = P \cdot V = \begin{pmatrix} r_x & r_y & r_z & -\vec{t} \cdot \vec{r} \\ u_x & u_y & u_z & -\vec{t} \cdot \vec{u} \\ -v_x & -v_y & -v_z & \vec{t} \cdot \vec{v} \\ -\frac{v_x}{f} & -\frac{v_y}{f} & -\frac{v_z}{f} & \frac{\vec{t} \cdot \vec{v}}{f} \end{pmatrix}$$

Since projection is not injective, P and hence M are both non-invertible. However, the x- and y-coordinates of p can be expressed in dependency on z as shown in equations (2.7).

$$\begin{aligned}
\hat{p} = V^{-1} \cdot \begin{pmatrix} q_r \\ q_u \\ q_v \\ 1 \end{pmatrix} &\underbrace{=}_{\text{equation (2.4)}} \underbrace{\begin{pmatrix} r_x & u_x & -v_x & t_x \\ r_y & u_y & -v_y & t_y \\ r_z & u_z & -v_z & t_z \\ 0 & 0 & 0 & 1 \end{pmatrix}}_{=V^{-1}} \cdot \begin{pmatrix} q_v \frac{p'_r}{f} \\ q_v \frac{p'_u}{f} \\ q_v \\ 1 \end{pmatrix} \\
&= \begin{pmatrix} r_x q_v \frac{p'_r}{f} + u_x q_v \frac{p'_u}{f} - v_x q_v + t_x \\ r_y q_v \frac{p'_r}{f} + u_y q_v \frac{p'_u}{f} - v_y q_v + t_y \\ r_z q_v \frac{p'_r}{f} + u_z q_v \frac{p'_u}{f} - v_z q_v + t_z \\ 1 \end{pmatrix} = \begin{pmatrix} x \\ y \\ z \\ 1 \end{pmatrix}
\end{aligned} \tag{2.7}$$

Equations (2.7) can be written as

$$\begin{aligned}
x - t_x &= q_v \left(r_x \frac{p'_r}{f} + u_x \frac{p'_u}{f} - v_x \right) \\
y - t_y &= q_v \left(r_y \frac{p'_r}{f} + u_y \frac{p'_u}{f} - v_y \right) \\
z - t_z &= q_v \left(r_z \frac{p'_r}{f} + u_z \frac{p'_u}{f} - v_z \right)
\end{aligned}$$

and dividing the first two equations by the third one results in

$$\begin{aligned}\frac{x - t_x}{z - t_z} &= \frac{r_x p'_r + u_x p'_u - v_x f}{r_z p'_r + u_z p'_u - v_z f} \\ \frac{y - t_y}{z - t_z} &= \frac{r_y p'_r + u_y p'_u - v_y f}{r_z p'_r + u_z p'_u - v_z f}\end{aligned}$$

Therefore

$$\begin{aligned}x &= t_x + (z - t_z)\,\frac{r_x p'_r + u_x p'_u - v_x f}{r_z p'_r + u_z p'_u - v_z f} \\ y &= t_y + (z - t_z)\,\frac{r_y p'_r + u_y p'_u - v_y f}{r_z p'_r + u_z p'_u - v_z f}\end{aligned} \tag{2.8}$$

From equations (2.8) follows that at least two images are needed in order to reconstruct the 3D position of p from its projections p', since the equations depend on the unknown coordinate z. Another possibility to determine z is to incorporate ground control points with known positions, but their registration is an elaborate task (cf. [42, p. 19]).

An image which contains the projection p' of p is usually a rectangular section in a plane. By knowing its size, i. e., the width w and the height h of the image in Σ', the perspective transform matrix P_{image} from equation (2.9) can be used instead of P from equation (2.3).

$$P_{\text{image}} = \begin{pmatrix} \frac{2f}{w} & 0 & 0 & 0 \\ 0 & \frac{2f}{h} & 0 & 0 \\ 0 & 0 & 1 & -f \\ 0 & 0 & 1 & 0 \end{pmatrix} \tag{2.9}$$

This matrix is frequently used in computer graphics for transformations of a symmetric, perspective *view frustum* into a cube with minimum corner $(-1, -1, 0)$ and maximum corner $(1, 1, 1)$, where the far plane f_{far} of the frustum is set to infinity [1, pp. 92–97, 345]. By using the identities from equations (2.10), which are illustrated in figure 2.8, P_{image} can be written as

$$P_{\text{image}} = \begin{pmatrix} \frac{1}{a \cdot \tan\left(\frac{\varphi_{\text{vert}}}{2}\right)} & 0 & 0 & 0 \\ 0 & \frac{1}{\tan\left(\frac{\varphi_{\text{vert}}}{2}\right)} & 0 & 0 \\ 0 & 0 & 1 & -f \\ 0 & 0 & 1 & 0 \end{pmatrix} = \begin{pmatrix} \frac{1}{\tan\left(\frac{\varphi_{\text{hor}}}{2}\right)} & 0 & 0 & 0 \\ 0 & \frac{a}{\tan\left(\frac{\varphi_{\text{hor}}}{2}\right)} & 0 & 0 \\ 0 & 0 & 1 & -f \\ 0 & 0 & 1 & 0 \end{pmatrix}$$

$$a = \frac{w}{h}, \qquad h = 2f \tan\left(\frac{\varphi_{\text{vert}}}{2}\right), \qquad w = 2f \tan\left(\frac{\varphi_{\text{hor}}}{2}\right) \tag{2.10}$$

a denotes the aspect ratio of the image, $f > 0$ is the distance from the CoP to the center of the image located at $\left(\frac{w}{2}, \frac{h}{2}\right) > 0$ and φ_{hor} and φ_{vert} are the horizontal respectively vertical *angles of view*.

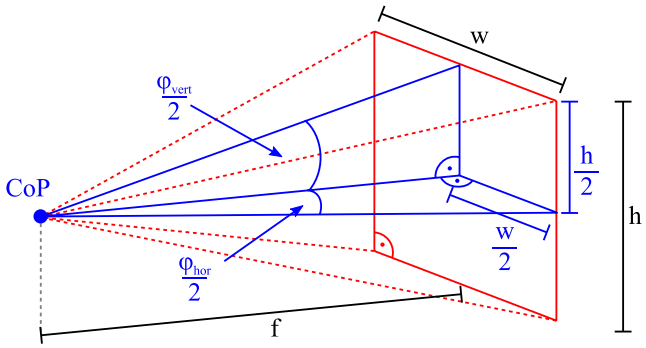

Figure 2.8: *Illustration of the geometry of a view frustum for deriving the horizontal and vertical angles of view φ_{hor} respectively φ_{vert}.*

The advantage of P_{image} over P is that P_{image} is invertible, and its inverse P_{image}^{-1} is given in equation (2.11).

$$\begin{aligned} P_{\text{image}}^{-1} &= \begin{pmatrix} \frac{w}{2f} & 0 & 0 & 0 \\ 0 & \frac{h}{2f} & 0 & 0 \\ 0 & 0 & 0 & 1 \\ 0 & 0 & -\frac{1}{f} & \frac{1}{f} \end{pmatrix} = \begin{pmatrix} a \cdot \tan\left(\frac{\varphi_{\text{vert}}}{2}\right) & 0 & 0 & 0 \\ 0 & \tan\left(\frac{\varphi_{\text{vert}}}{2}\right) & 0 & 0 \\ 0 & 0 & 0 & 1 \\ 0 & 0 & -\frac{1}{f} & \frac{1}{f} \end{pmatrix} \\ &= \begin{pmatrix} \tan\left(\frac{\varphi_{\text{hor}}}{2}\right) & 0 & 0 & 0 \\ 0 & \frac{\tan\left(\frac{\varphi_{\text{hor}}}{2}\right)}{a} & 0 & 0 \\ 0 & 0 & 0 & 1 \\ 0 & 0 & -\frac{1}{f} & \frac{1}{f} \end{pmatrix} \end{aligned} \tag{2.11}$$

We can therefore model the imaging process by using $M_{\text{image}} = P_{\text{image}} \cdot V$ and directly obtain the x- and y-coordinates of a pixel in world space from $p' = (p'_r, p'_u, p'_v)$ by equation (2.12) in a more convenient way.

$$M_{\text{image}}^{-1} \cdot \hat{p}' = V^{-1} \cdot P_{\text{image}}^{-1} \cdot \begin{pmatrix} p'_r \\ p'_u \\ p'_v \\ 1 \end{pmatrix} \tag{2.12}$$

Note that p'_v is in general unknown and not present in a single image, so that x and y will still depend on z as shown in equations (2.13), which are obtained analog to equations (2.8).

$$\text{equation (2.12)} \Rightarrow \begin{cases} x = t_x + (z - t_z)\,\dfrac{wr_x p'_r + hu_x p'_u - 2v_x f}{wr_z p'_r + hu_z p'_u - 2v_z f} \\ y = t_y + (z - t_z)\,\dfrac{wr_y p'_r + hu_y p'_u - 2v_y f}{wr_z p'_r + hu_z p'_u - 2v_z f} \end{cases} \tag{2.13}$$

2.5.2 Camera Parameters

In section 2.5.1, the CoP was assumed to be located at the origin O' of the camera's local coordinate system Σ'. Usually the CoP has an offset (o'_r, o'_u) relative to O' and hence equations (2.8) have to be modified as shown in equations (2.14).

$$\begin{aligned} x &= t_x + (z - t_z)\,\frac{r_x(p'_r - o'_r) + u_x(p'_u - o'_u) - v_x f}{r_z(p'_r - o'_r) + u_z(p'_u - o'_u) - v_z f} \\ y &= t_y + (z - t_z)\,\frac{r_y(p'_r - o'_r) + u_y(p'_u - o'_u) - v_y f}{r_z(p'_r - o'_r) + u_z(p'_u - o'_u) - v_z f} \end{aligned} \tag{2.14}$$

The modification of equations (2.13) for incorporating O' is analog. Manufacturers of high quality camera systems strive for the coincidence of (o'_r, o'_u) with O', i. e., $o'_r = o'_u = 0$ [42, p. 9]. In total, nine image-independent parameters are required for recovering 3D information from 2D images. The three *intrinsic parameters* f, o'_r and o'_u are usually known in advance from the calibration of the camera system or can be determined, e. g., if ground control points with known positions in world space are depicted in the images.

The remaining six parameters are the *extrinsic parameters* and comprise the position and orientation of the camera's local coordinate system Σ' relative to Σ, i. e., $\vec{t} = (t_x, t_y, t_z)$ and the three rotation angles. These parameters are frequently determined by GPS and IMU devices, but other methods can also be used, if the provided data are accurate. The precision of GPS, however, may be insufficient for obtaining precise positions, but in this case, methods like bundle adjustment, for instance, can be used to improve the results [42, pp. 306–307].

Additional parameters of interest for photography-like images are the focal length ϱ, the horizontal and vertical *angle of view*, which is also called *field of view*, and the resolution of the image in terms of pixels per unit in world coordinates. These parameters determine the size of an image and assist in locating positions in world space (see section 2.5.1). The focal length ϱ is frequently stored in the image file created by a digital still image camera, e. g., if the image is stored in the Exif file format [11]. In case of calibrated cameras, the focal length is fixed and is hence known in advance.

Provided that the distance of the depicted objects is large compared to the focal length, the distance from the CoP to the image plane equals ϱ, if the image is sharp. Given the effective sensor size, i. e., the width w_{sensor} and height h_{sensor} of the CCD-sensor[4], φ_{hor} and φ_{vert} can then be determined by means of equations (2.15).

$$\begin{aligned} \varphi_{\text{hor}} &= 2\arctan\left(\frac{w_{\text{sensor}}}{2\varrho}\right) \\ \varphi_{\text{vert}} &= 2\arctan\left(\frac{h_{\text{sensor}}}{2\varrho}\right) \end{aligned} \tag{2.15}$$

The underlying geometry is the same as in figure 2.8 where $f = \varrho$, $w = w_{\text{sensor}}$ and $h = h_{\text{sensor}}$, and these quantities are usually given in millimeters.

[4] With analog images, the sensor size corresponds to the size of the film.

In the context of this work, it is assumed that the employed images are sharp and that the sensor sizes are known. o'_r and o'_u are assumed to be negligible, i. e, $(o'_r, o'_u) \approx O' = (0, 0)$, so that the projection onto the image plane can be considered symmetric around its geometric center. Furthermore, the distances to the depicted objects are assumed to be much larger than ϱ and hence $f = \varrho$ in the corresponding equations in section 2.5.1.

2.5.3 Image Properties

The images which are used within this thesis for generating DSMs are vertical aerial images. These images are captured in traditional aerial photography on a fixed flight path such that they are placed on parallel stripes as sketched in figure 2.9. In order to recover 3D information, the images need to overlap each other along the stripes in direction of flight by at least 50%. Since deviations from the flight path may occur and need to be compensated, overlaps of at least 60% along the direction of flight and 25% – 30% between two adjacent stripes are recommended [42, pp. 145–148]. According to [44], overlaps of aerial images in cities and woodland areas should even be 80% – 90% along the direction of flight and 60% – 70% between the stripes in order to reduce occlusions which would complicate the recovery of 3D information. However, such fixed flight paths may be difficult to follow for small UAVs and the images are likely to have a less organized layout.

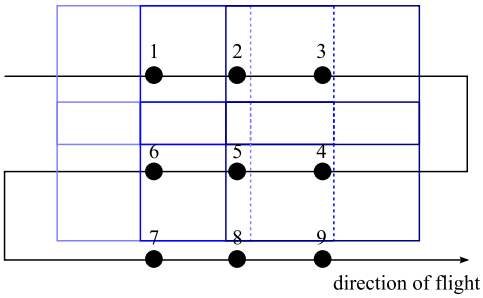

Figure 2.9: *In traditional aerial photography, the images must overlap and their centers are located on stripes along the direction of flight.*

In contrast to real photographs, computer generated images do not suffer from the problem of inaccuracies like lens effects or imprecise position or orientation data. These data are well-suited for developing and testing algorithms, because many sources of potential errors, e. g., image noise or color defects, are eliminated. On the other hand, the data are less realistic and thus can influence the algorithms as well, e. g., like with finding matching feature points in images, if the underlying 3D models of cities or buildings employ repetitive textures. Frequently, only a relatively small amount of artificial textures is used many times on different 3D models in order to reduce the required amount of memory. While these repetitions may not be noticed by the viewer, they can cause algorithms to detect false positive matches of points in different images, although they belong to different objects.

For the remainder of this thesis the additional metadata in table 2.2 of any aerial image are assumed to be available. As the accurate measuring of position and orientation of real

photographs is beyond the scope of this dissertation, it is furthermore assumed that these data have already been corrected by appropriate methods, like bundle adjustment, known ground control points or other existing information, if necessary, and that they are precise.

metadata	semantics
id	a unique identifier for each image
position	position of center of projection given in world coordinates at the moment the image was captured
orientation	three rotation angles (yaw, pitch and roll) of the local camera coordinate system relative to the world coordinate system at the moment the image was captured
focal length	focal length of the camera in millimeters
sensor size	effective width and height of the camera's CCD sensor in millimeters
resolution	width and height of the image in terms of pixels
timestamp	timestamp of the moment when the image was captured

Table 2.2: *The methods presented in this thesis assume that these metadata are available for each (aerial) image, and that the values are precise.*

3 The Flexible Clipmap

In many applications that involve DSM rendering, texture data may have sizes in the gigabyte range and thus often exceed the available physical video memory. For this reason, different techniques for handling very large textures have been developed. However, in many of these applications textures are frequently treated as resources of fixed extension and static or rarely changing content.

Our application relies on texture data of frequently varying content and of time-varying extension, i. e., the size of the textures may change in the course of time. New aerial images are directly processed for generating a single virtually contiguous DEM and matching color textures which can be rendered in a virtual 3D environment. Although the covered areas may be vast and the images may have high resolution, it is desirable to update the content of such a very large virtual texture in real time. Furthermore, any newly acquired image may not only update existing content, but also extend the area covered so far as illustrated in figure 3.1. Related techniques for handling large textures, like common clipmap

Figure 3.1: *Not only the content, but also the extension is altered in the course of time with textures of time-varying extension.*

implementations, are not able to handle such growing textures.

Another issue that arises with textures during rendering is the problem of aliasing. By using perspective projection, a single screen pixel may cover more than one texel of a texture if it is applied to objects distant from the viewer, especially when the object is viewed from an oblique angle (see figure 3.2). The prevalent method for mitigating aliasing is to use pre-filtered versions of the textures, like mipmaps [85]. Special texture sampling and interpolation techniques like trilinear or anisotropic filtering are available in order to conceal transitions between the different *levels of detail (LODs)*. Usually these anti-aliasing techniques are supported by graphics hardware and should be utilized by methods for handling large virtual textures for efficiency reasons.

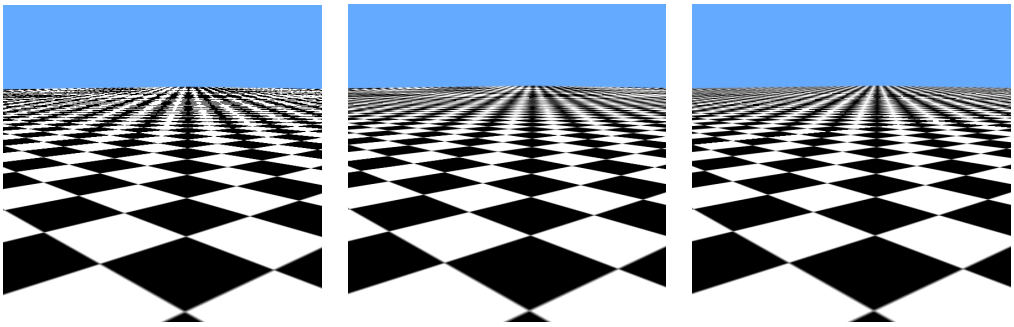

(a) *no anti-aliasing* **(b)** *isotropically filtered mipmap* **(c)** $16\times$ *anisotropically filtered mipmap*

Figure 3.2: *Aliasing becomes apparent on distant textured objects when one screen pixel covers more than one texel. Different anti-aliasing techniques (center and right) are available for reducing this effect.*

In this chapter we present the *Flexible Clipmap (FCM)* to incrementally generate large, virtual textures of time-varying extension and dynamically changing content from multiple input aerial images on-the-fly. Parts of the work on this topic have been previously published in [28]. The resulting virtual textures may contain arbitrary data, but for our purposes we confine their contents to DEM and color texture data. The FCM makes use of a tile-based *clipmap* approach, a spatial indexing data structure and commodity graphics hardware. Its application does not depend on the underlying geometry or a certain kind of polygonal meshes.

3.1 Related Work

If the size of textures to be displayed exceeds the hardware limits, a common and obvious solution is to divide them into smaller, manageable *texture tiles*. For instance, Cline and Egbert proposed a simple division of the texture data, but their approach was limited by a strict dependency on texture coordinates and underlying geometry [13].

A *clipmap*, as introduced in [79], is based on mipmaps [85] and keeps only portions of the entire texture mipmap in video memory. Like mipmaps, the clipmap provides a level of detail (LOD) concept and thus avoids texture aliasing. The lowest level $l = 0$ denotes the level of highest resolution and largest extension of the texture. The clipmap uses a roaming window in video memory to copy only those texels which are visible to the viewer by centering the window around the current view point (*clip center*). As the view point moves, the window is updated by copying new texels using toroidal addressing [79]. This is done for each clipmap level corresponding to a texture of a size greater than a certain *clip size*. Since the extensions of textures of mipmaps and clipmaps become smaller towards higher levels, these parts of a clipmap are small enough to fit entirely into video memory and hence do not need to be clipped. Therefore, the texture data at higher clipmap levels are treated as an ordinary mipmap. However, the original clipmap implementation in [79]

relies on special graphics hardware for loading the texels into video memory. Details about the clipmap are explained in section 3.2.2.

Modern GPU features have eliminated the need for special hardware, and the clipmap concept has been implemented on the GPU in vertex and fragment programs (*shaders*) on commodity hardware making it even more attractive for handling large textures. The *virtual texture* in [23] makes use of texture tiles and can employ shaders for texture mapping. It supports multi-texturing, but does not use toroidal addressing for loading tiles, the texture coordinates are still coupled to the geometry and it requires multiple texturing units, even if only a single texture is mapped.

In [70] a roaming tile cache for each level is used, which is updated using toroidal addressing and texture stacks. Geometry and texture data are kept independent from each other by computing the texture coordinates within a shader. The approaches in [23] and [70], as well as the solution presented in [45] generate complete mipmaps for each tile at each LOD.

Crawfis et al. [16] also employ roaming tile caches for each level, toroidal addressing, texture compression and fragment programs, but they do not generate mipmaps for the tiles. They investigate different methods for clipping and level determination by utilizing fragment programs and arrays of textures to hold the relevant portions of the logical mipmap. Furthermore, they make use of a *tile map* to indicate to the shader the highest available texture resolution, i. e., the lowest LOD, for selecting the optimal clip level. The tile map is implemented by a separate texture and requires additional resources. In addition, the authors propose the usage of more efficient texture arrays, which became available in DirectX 10 hardware [49].

More related work on using large virtual textures on modern GPUs can be found in [5] and [50].

Although the previously mentioned research on texture clipmaps deals with large textures of fixed extension, the proposed approaches do not seem to be capable to update the texture content at a frequent rate. In [78] a method for handling large fixed-size textures of frequently changing content is presented. However, to our knowledge none of the current techniques is able to handle textures of time-varying extension.

3.2 The Flexible Clipmap

The FCM allows to derive from a growing set of images captured at different locations a single virtual texture which can be rendered immediately on any geometric model. It has been developed primarily for being used with aerial images that become directly available after their acquisition, e. g., by transmission over wireless networks as described in chapter 1. For this kind of images, the metadata as listed in table 2.2 must be provided. Though the FCM is not limited to a certain type of input images or to a certain kind of surface onto which the resulting virtual texture can be applied, we will assume for the remainder of this chapter that images are aerial images and that the accompanying metadata are exact. Precise position data for input images can be obtained in a preprocessing step which comprises the adjustment of positions, georeferencing and registration, as well as coordi-

nate transformations from GPS to UTM coordinates for the reasons given in section 2.4. The resulting virtual texture can be viewed as a rectangular section located in a plane like a common texture. Its texels are addressed via normalized texture coordinates in the range $[0, 1] \times [0, 1] \subset \mathbb{R}^2$, independent of the current extension of the FCM.

In addition, corrections of perspective distortion have to be performed, e. g., in order to obtain true orthographic images. Such images depict surfaces from an orthographic point of view and intentionally do not provide any information about (lateral) surfaces which are perpendicular or near-perpendicular to the plane against which the elevation is measured, e. g., frontages of buildings in urban areas or canyon walls. Orthographic images, or *orthoimages* in short, can only be generated if information about the elevation of the underlying surface is available, i. e., if a DEM is given. The latter is generated from the images themselves and hence DEM and orthoimage generation are combined into one logical step which is subject of chapter 5. As a result of the image transformation and warping, the area covered by an input image on the ground plane does not need to be rectangular anymore, but is an arbitrary convex quadrilateral. A 2D minimal enclosing *axis-aligned bounding box (AABB)* of the covered area can be computed efficiently.

3.2.1 Requirements for Handling Spatially Time-Variant Textures

In order to handle textures of time-varying extension, the FCM cannot be confined in advance to a fixed area. Also it may easily become too large to fit entirely into video memory or even main memory, and therefore it has to be partitioned, stored in secondary memory and provided with a LOD concept to avoid texture aliasing. Furthermore, for a frequently changing set of images overlapping the same area, there are different possibilities to decide which of the images (or parts of the images) are the "best" to contribute to the resulting virtual texture. A rating can be based, for instance, on image properties such as timestamp, contrast, brightness, signal-to-noise ratio, degree of perspective distortion, or even content. In any case, whenever "better" images are available, the affected regions within the virtual texture have to be updated. To summarize, the FCM must satisfy the following requirements to address the challenges stated above:

1. Partitioning must be supported, since the virtual texture may have a physical extension which exceeds hardware limits.
2. An LOD concept is required in order to avoid texture aliasing.
3. Efficient updates of the virtual texture must be possible, because updates of the underlying set of images will occur frequently.
4. The virtual texture must have time-varying extension, i. e., it cannot be limited to a fixed extension.

As the FCM may have to be updated during rendering, special attention has to be paid to ensure that the processes for rendering and updating do not excessively interfere with each other as explained in section 7.2.1.

3.2.2 The Clipmap

The first two requirements given in section 3.2.1 can be achieved with texture clipmaps, since they allow to control memory consumption and provide LOD concepts. The structure of a clipmap as presented by Tanner et al. [79] is similar to the one of a mipmap and is illustrated in figure 3.3. At the lowest *clip level* $l = 0$ the clipmap contains texture data at the highest available resolution (cf. [79]). Like with mipmaps, going from clip level l to clip level $l + 1$ the resolution of the texture decreases by a factor of two along each dimension so that each 2×2 neighboring texels are aggregated into one texel. The aggregation scheme depends on the texture data, but a frequently used method for color textures is to calculate the averaged intensities per color component for the resulting texel. At the highest clip level $L - 1$, the clipmap contains a down-sampled version of the entire texture. During texture mapping the minification of a texel in screen space determines the clip level to be used. But in contrast to a mipmap, for each level $l < L - 1$ of a clipmap only a section of the same size of the entire logical texture is kept in video memory. This section is called *active area*, and it is centered around the *clip center*. The *clip area* is a somewhat larger section centered around the clip center which contains the active area and is kept in main memory for updating the active area in video memory as the clip center is moved. Any remaining texture data are stored in secondary memory, e. g., on hard disk, and are loaded when the clip area needs to be updated. Texture data at levels $l \geq L - 1$ can be treated as a standard mipmap, because they are small enough to fit entirely into video memory.

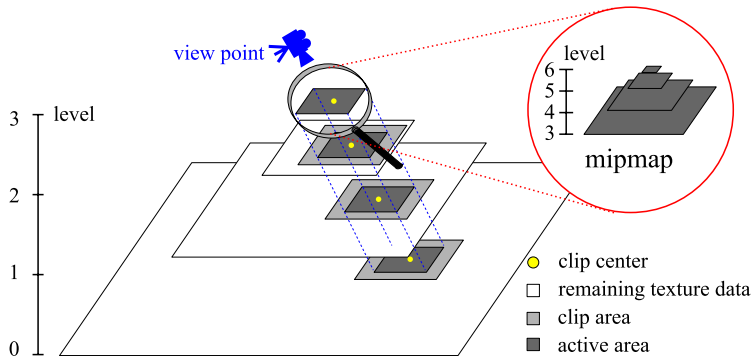

Figure 3.3: *Structure of a clipmap with $L = 4$ clip levels and additional three mipmap levels. The active area (dark gray) and the clip area (light gray) are centered around the clip center (yellow) and are updated as the view point moves.*

The position of the clip center has to be chosen carefully and may be set to the intersection of a ray cast from the position of the virtual camera with the textured surface. This method works well in situations where the angle enclosed between the opposite viewing direction and the normal vector of the textured surface is small. But if this angle is large, the clip center is too far away from the viewer and other heuristics may be more appropriate.

The original clipmap by Tanner et al. relies on special graphics hardware for copying individual texels from the clip area to the border region of the active area [79]. Our FCM implementation is based on a variation of the clipmap similar to the one by Crawfis et al. [16]

which makes use of fragment programs and texture tiles without requiring any special hardware. With this approach, entire texture tiles, or *tiles* in short, are swapped between the active areas and the clip areas instead of replacing individual texels on the border of the roaming window. The principle of a tile-based clipmap is illustrated in figure 3.4. We also adopted the idea by Crawfis et al. of employing a *tile map* and making use of *explicit index-based clipping* [16], but in contrast, we use a special scheme for indexing and generating the required texture tiles. Due to the tiling approach, updates of the virtual texture may be confined to few tiles only, which is helpful for achieving the third requirement stated in section 3.2.1.

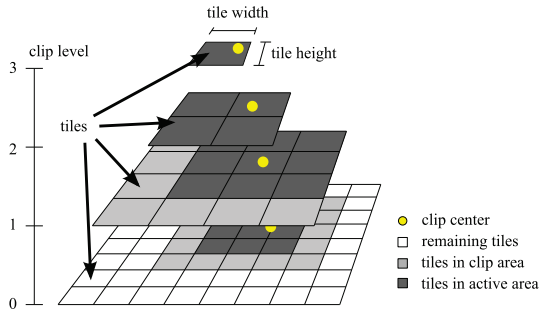

Figure 3.4: *Illustration of tile-based clipmap. The active area consists of at most* 3×3 *texture tiles (dark gray) and the clip area of* 5×5 *tiles of the same size.*

3.2.3 Managing Aerial Images by Spatial Indexes

To satisfy the third requirement from section 3.2.1, we need to be able to efficiently retrieve the aerial images and associated metadata contributing to a certain tile, i. e., the images whose projections cover the area in world space which corresponds to the tile. This can be accomplished by using a spatial indexing data structure. If all aerial images project onto the plane in which the FCM tiles are based, e. g., if only vertical aerial images are employed for creating a virtual texture based in the ground plane, the images can be organized in a 2D spatial index based on their projections. Since our application makes use of aerial images of all kinds of orientations, e. g., in order to use them as projective textures as described in chapter 6, we store the images and their associated metadata in a 3D spatial index. Different types of aerial images can thus be handled in the same way. For an image we use the world coordinates of the 3D axis-aligned bounding box (AABB)[5] of its view pyramid as key. To simplify matters, assume that the FCM is used to create a virtual texture of the ground plane, so that all vertical images project onto that plane.

The view pyramids of the images are determined by the parameters of the associated cameras as follows: In case of vertical aerial images, the top of the pyramid is located at the CoP and the base is formed by the projection of the image onto the ground plane (see figure 3.5a). Oblique aerial images, and in particular high oblique aerial images, do

[5]Throughout this dissertation the term *axis-aligned bounding box*, or AABB in short, refers to the 3D *minimal enclosing* AABB of an object.

not project onto the ground plane if at least one of the four rays emanating from the CoP of the associated camera through one of the corners of the image does not intersect the ground plane. Even if all four rays intersect the ground plane, the resulting projection for this kind of aerial images can be rather distorted. To obtain an appropriate view pyramid for such images, we place a plane oriented perpendicular to the camera's view direction at a predefined distance. The base of the pyramid is then formed by the intersections of the four rays emanating from the CoP with this plane. Figure 3.5 illustrates the view pyramids and AABBs as described above. The AABBs of view pyramids are represented by their minimum corner $c_{\text{min}} = (x_{\text{min}}, y_{\text{min}}, z_{\text{min}})$ and maximum corner $c_{\text{max}} = (x_{\text{max}}, y_{\text{max}}, z_{\text{max}})$, having coordinates given relative to an arbitrary but fixed origin $O = (O_x, O_y, O_z)$. O_z is usually set to $H_{\text{min}} = 0$, and we assume that the height above ground of the center of projection for each image is part of the provided metadata.

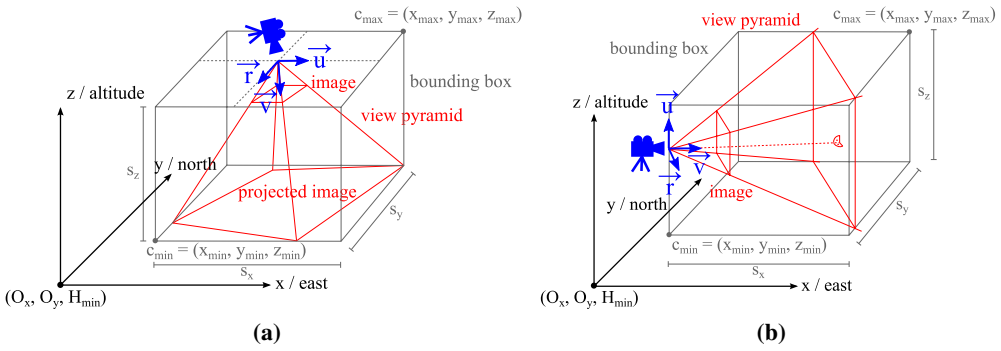

Figure 3.5: *In order to manage the source images that are used to generate the tiles of the FCM, the axis-aligned bounding boxes (gray) of the view pyramids of the associated cameras of the images (red) are stored in a spatial index.*

Since the boxes serve as keys for storing aerial images, and since we have to determine the overlap with a 3D query box as described in section 3.2.5, the spatial index has to support *intersection queries*. Given a 3D box (*query window*), an intersection query on a spatial index returns all items whose keys (i. e., boxes) intersect the query window or are entirely contained inside. When using boxes as keys for associated data, this kind of key can be stored in a spatial index designed for point data, such as the kd-tree by Bentley [9], if the boxes are represented as points in a higher dimensional space. Because multiple representations for boxes in 3D exist, the choice depends on the data, and whether the embedding space is organized (trie-based methods [67, pp. 2–3]) or the data points are organized [37, pp. 24–26]. For example, a 3D AABB can be represented as a point in 6-dimensional space by the six coordinates of its minimum and maximum corner c_{min} and c_{max}. Another possibility is to represent the box by its minimum corner and its extension in each direction $(x_{\text{min}}, y_{\text{min}}, z_{\text{min}}, s_x, s_y, s_z)$. In order to perform intersection queries with a given box Q, Q has to be transformed according to the chosen representation, and the affected objects are located within a certain subspace of the higher dimensional space.

Other types of spatial indexes can directly employ spatially extended objects, like boxes, e. g., the R-tree by Guttman [35] and its variations. R-trees are height-balanced trees related to B-trees, and the data are stored only at the leave nodes (*leaves*). Except for the root node, each node has at least m, but at most $M > m$ entries where $1 < m < M$, $m, M \in \mathbb{N}$. The root may contain less than m, but also at most M entries. An AABB which encloses all children of the assigned subtree is stored at each node. In particular, the root holds an AABB of the entire domain which is covered by the data of the tree. This feature is used by the FCM for handling expansions of the virtual texture and for generating tiles as described in section 3.2.5. The structure of a two-dimensional R-tree is illustrated in figure 3.6. The entries of intermediate nodes are either pointers to other intermediate nodes at the next level or to leaf nodes. At leaf nodes, the entries point to the actual data and their AABBs. Like the leaves of B-trees, the leaf nodes of an R-Tree are split by certain criteria into two nodes if they have to store more than M entries (*overflow*). An entry for the resulting second node is inserted into the same parent node and may result in an overflow of the parent node as well which is handled in the same way. This process ends if either no further split of a node is necessary, or if the root has to be split. In the latter case, the root is replaced by a new one, and the former root together with its new sibling become the only children. Likewise, if nodes contain less than m children due to deletion of data, they are merged and deleted accordingly. After insert or delete operations, the bounding rectangles of the affected node and its ancestors usually need to be adjusted [35].

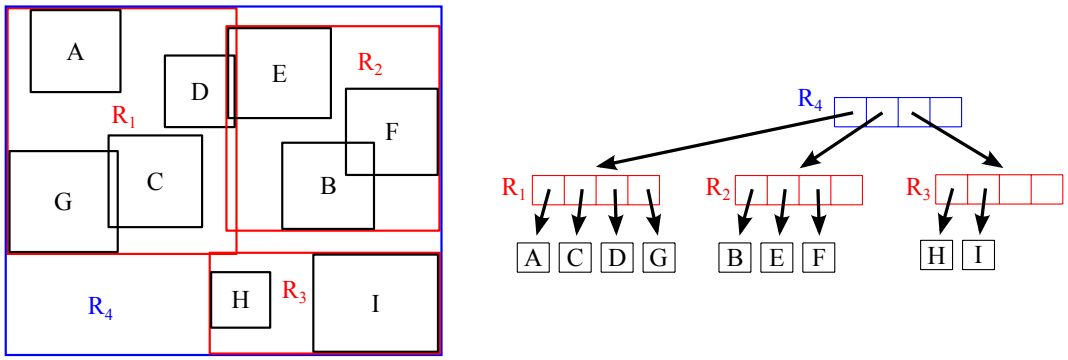

Figure 3.6: *Structure of an R-Tree in 2D: A – I denote data rectangles while R_1 – R_3 are rectangles of leaf nodes at level 1, and R_4 is the rectangle at the root. Note that rectangles may overlap and R_4 is the minimal bounding rectangle that encloses all data rectangles.*

Compared to other spatial indexing structures, R-trees are appropriate for incremental construction by successive insertions [67, pp. 282–286] and some variations of the R-tree, e. g., the R*-tree by Beckmann et. al., do not require periodic global reorganization [6]. The latter aspect is especially desirable, because that data structure does not need to be completely rebuilt after successive insertion of a large number of items, which can degrade the performance of subsequent find operations. This can happen with a standard point kd-tree, for instance, where successive insertions may degenerate the tree structure and decrease its performance [67, p. 58].

For our purposes, we store 3D AABBs in an R*-tree by Beckmann et al. [6] which is a variation of the R-tree. The R*-tree differs from the R-tree in the method for determining node splits, and it utilizes forced reinsertions of existing nodes. Reinserting existing nodes can avoid unnecessary node splits and improves the weight balance of the tree, i. e., it can increase the capacity utilization of the nodes [6]. Further information on the R-tree and the R*-tree can be found in [35] and [6], respectively, and a revised version of the R*-tree is presented in [7]. The wide-ranging topic of spatial indexes is covered in detail in the comprehensive book by Samet [67].

3.2.4 Layout Scheme for Tiles

Since the R*-tree stores at each node an AABB of all elements assigned to the corresponding subtree, the 3D AABB containing the view pyramids of all aerial images is located and maintained at the root node. If only vertical aerial images were inserted into the spatial index, the 2D projection of this AABB onto the ground plane coincides with the rectangular area A currently covered by the FCM. Due to the possible presence of oblique aerial images in the spatial index, which do not contribute to the content of FCM tiles, we keep track of the 2D area covered only by vertical or near-vertical aerial images. Therefore, we store and update an additional 2D bounding rectangle at each R*-tree node. Whenever a vertical aerial image is inserted into the 3D spatial index, we use the 2D projection of its view pyramid's AABB onto the xy-plane to update 2D AABBs at the R*-tree nodes. Hence, the 2D AABB at the root node with minimum and maximum corners $R_{\text{min}} = (R_{x_{\text{min}}}, R_{y_{\text{min}}})$ and $R_{\text{max}} = (R_{x_{\text{max}}}, R_{y_{\text{max}}})$ coincides with the area A covered by the FCM. The total number of clip levels L depends on the extension of A, a previously chosen *tile size* of $T_x \times T_y$ texels, and the desired resolution $(\text{res}_x, \text{res}_y)$ in terms of texels per unit of the virtual texture. The tile resolution preferably matches the resolution of the aerial images so that the quality of the resulting virtual texture is not diminished by further re-sampling. In order to satisfy the fourth requirement from section 3.2.1, the key is to provide the FCM with additional tiles whenever the underlying virtual texture becomes larger. This is accomplished by the following layout scheme for the tiles.

Like with a common mipmap, the L clip levels of the FCM are numbered starting with the most detailed level $l = 0$ to the least detailed level $l = L - 1$. The top-most level $L - 1$ contains a downsampled version of the entire texture and is the first level of the remaining mipmap section (see figure 3.3). Conceptually, we consider the virtual texture as the entire $\mathbb{R}^2$, and the region $\mathbb{R}^2 \backslash A$ is considered as *empty*, i. e., no texture data are available in this area.

Let $O_{xy} = (O_x, O_y)$ denote the projection of the origin of the world coordinate system onto the xy-plane at H_{min}. O_{xy} is used by the spatial index to reference the coordinates of the AABBs in world coordinates (see section 3.2.3). We span a Cartesian grid centered around O_{xy} with spacing $(g_x, g_y) = (T_x/\,\text{res}_x, T_y/\,\text{res}_y)$, where T_d denotes the size of a tile in texels, and res_d its resolution in texels per unit along direction $d \in \{x, y\}$. Starting at the origin, in each quadrant, a cell of size $2^{l+1} \cdot g_x \times 2^{l+1} \cdot g_y$ at level $l + 1$ is formed

by the underlying 2×2 neighboring grid cells from level l. We then proceed with the next level $l + 1$ in the same way in order to build a grid hierarchy, similar to the bottom-up construction of a quadtree. But in contrast to a quadtree, the grid hierarchy does not possess a root, because its domain is unbounded. Therefore, this process is repeated only until A is covered in x- and y-direction by at most two grid cells each, but by at least one in one of the directions, i. e., until A is covered by 1×2, 2×1 or 2×2 grid cells. Each grid cell at level l is identified with exactly one tile at clip level l and indexed as shown in figure 3.7. The at most four remaining cells covering A are also grouped to a single cell at the top-most level $l = L - 1$, but this cell differs from the other ones in that it may contain the origin O_{xy} and provides some sort of root for the grid hierarchy. In this way, the grid hierarchy limited to the area A of the FCM is bounded, which allows to directly address grid cells respectively tiles at a given clip level l via their indices. Direct addressing of tiles is essential for efficiently caching them and updating the active areas and clip areas of the FCM for the purpose of rendering. Furthermore, the FCM fragment program accesses individual tiles by their indices for sampling texture data.

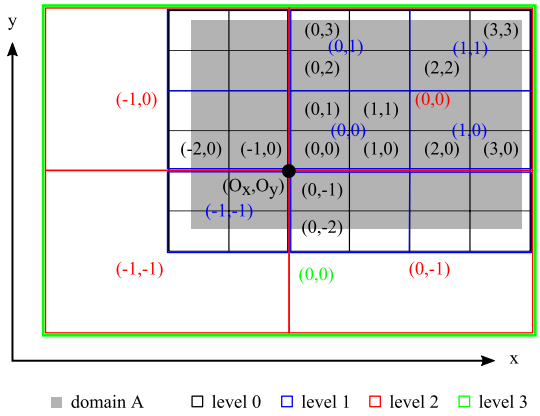

Figure 3.7: *The tiles are indexed at each level starting from the origin* (O_x, O_y)*. Each* 2×2 *tiles from level* l *are grouped into one tile at level* $l + 1$*. At the top-most level (green), only one tile is left that covers the entire domain* A*.*

The top-most grid cell respectively tile at level $L - 1$ requires some special attention, because as a constraint for the FCM, this level must cover A entirely while consisting of exactly 2×2 tiles at the next lower level (*children*). In cases of having only 1×2 or 2×1 children, the missing ones are replaced by the nearest, possibly empty, neighbors in the corresponding direction, i. e., grid cells not covering A may be used. Besides, the top-level tile is indexed $(0, 0)$, because it may be formed of tiles which are not considered as neighboring according to the scheme described above, e. g., if it was formed by the four tiles $(1, -1), (2, -1), (1, 0)$ and $(2, 0)$ at level $L - 2$. In this example, the corresponding parent tiles would be assigned the indices $(0, -1)$, $(1, -1)$, $(0, 0)$ and $(1, 0)$.

Given a certain level $0 \leq l < L$, we can determine the index $n(l, r) = (n_x, n_y)$ of the tile (*tile index*) containing a location $r = (r_x, r_y)$ given in world coordinates by equation (3.1).

$$n(l,r)_d = \begin{cases} \left\lfloor \frac{r_d}{2^l \cdot g_d} \right\rfloor & 0 \leq l < (L-1) \\ 0 & l = (L-1) \end{cases}, \quad d \in \{x, y\} \tag{3.1}$$

Since L depends on the position of R_{min} and R_{max} and hence indirectly on the choice of the origin O_{xy}, the total number of clip levels L cannot be determined directly by the quantity $\hat{L}$ from equation (3.2).

$$\hat{L} = \max_{d \in \{x,y\}} \left(\left\lceil \log_2(R_{d_{\text{max}}} - R_{d_{\text{min}}}) \right\rceil - \lceil \log_2(g_d) \rceil \right) + 1 \tag{3.2}$$

If A would be covered by a common *mipmap*, $\hat{L} - 1$ would indicate the number of mipmap levels at which the corresponding textures would be too small to entirely cover A. Mipmap level $\hat{L} - 1$ would then be the first level that could completely cover A by a texture of size $g_x \cdot \text{res}_x \times g_y \cdot \text{res}_y$. But according to the description above, $L - 2$ is the level l' where the maximum of the differences of the two components of the tile indices $n(l', R_{\text{max}})$ and $n(l', R_{\text{min}})$ equals one as expressed in equation (3.3).

$$\max_{d \in \{x,y\}} \left(n(l', R_{\text{max}})_d - n(l', R_{\text{min}})_d \right) = \max_{d \in \{x,y\}} \left(\left\lfloor \frac{R_{d_{\text{max}}}}{2^{l'} \cdot g_d} \right\rfloor - \left\lfloor \frac{R_{d_{\text{min}}}}{2^{l'} \cdot g_d} \right\rfloor \right) \stackrel{!}{=} 1 \tag{3.3}$$

Therefore the required number of clip levels L is actually determined by checking if $l' = \hat{L}$ from equation (3.2) satisfies equation (3.3). If it does not, l' is incremented and checked again, until a suitable l' is found.

Most important about this indexing scheme is that the tile index $n(l, r)$ does not directly depend on the area A, i. e., the current area of the FCM. This facilitates adding new tiles to the FCM, because each tile at each level has a unique index and conceptually already exists, though it may not contain image information.

3.2.5 Adding and Updating Tiles

Assume that the FCM is used to create a virtual texture for the ground plane. In this case, only vertical or near-vertical aerial images affect the area A covered by the FCM according to the 2D bounding boxes of their projections onto the ground plane, and we only consider this type of aerial images in the following.

Before any aerial images are inserted, A is empty. The insertion of aerial images into the spatial index whose projections onto the ground plane are not completely covered by A triggers an expansion of A and thus of the FCM. This leads to the addition of at least one new clip level if A exceeds the boundaries of the current top-most tile at $L - 1$ as illustrated in figure 3.8. The total number of new clip levels depends on the extension of A. After an expansion of A, the former tile at level $L - 1$ may no longer satisfy the constraint of covering at most 2×2 tiles from the next lower level, and the maximum clip level has to

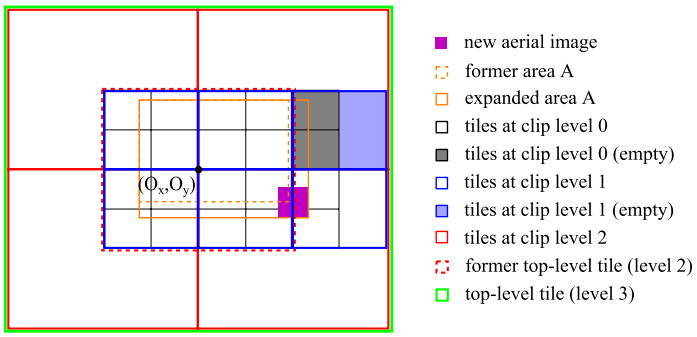

Figure 3.8: *The insertion of a new vertical aerial image (purple) into the spatial index outside the area covered by A (dashed orange) triggers an expansion of the FCM and causes the addition of a new clip level and tiles. Empty tiles (shaded) are not physically created, because no images are contained yet.*

be increased by the number k of new levels, so we denote the former number of clip levels by L' and set $L = L' + k$. However, it is actually not necessary to determine k since L can be recalculated from the new positions of R_{min} and R_{max} which are obtained from the expanded 2D AABB of all (near-)vertical aerial images at the root node of the R*-tree as described in section 3.2.4. Except for the former top-level tile T at $L' - 1$, the indices of all other tiles remain unchanged. Since T is no longer the top-level tile, but a child of another tile, its former index $(0, 0)$ is according to equation (3.1) not necessarily correct any longer, and T is therefore discarded. The former 2×2 children of T may furthermore become assigned to different parent tiles at level $L' - 1$ during the addition of one or more clip levels as illustrated in figure 3.9.

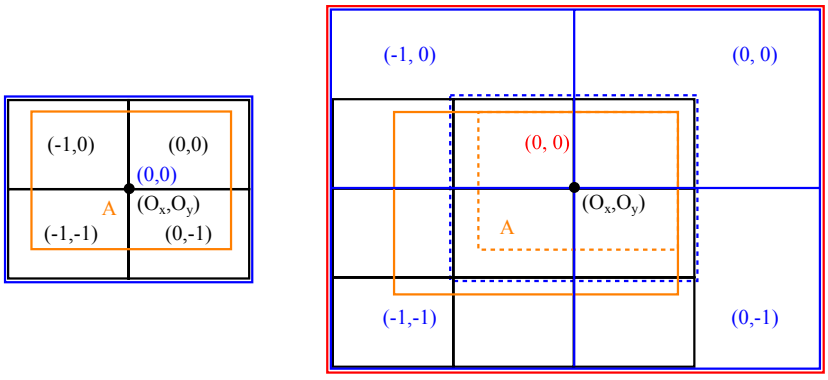

(a) *before expansion* **(b)** *after expansion*

Figure 3.9: *The children of the top-most tile* $(0, 0)$ *at level* $l = 1$ *(left) are assigned to different tiles at level* 1 *after the expansion of A (orange) and the addition of a new top-level tile (red) at* $l = 2$ *(right, red). Note that tile* $(0, 0)$ *at* $l = 1$ *(right, dashed blue) is now relocated and its content must hence be re-created.*

Based on the clip level, two cases for the update and creation process of the content a tile have be to distinguished:

1. creating and updating tiles at the base clip level $l = 0$ directly from the aerial images
2. creating and updating tiles at clip levels $l > 0$ from their 2×2 children

In the first case, a 3D intersection query on the spatial index is used to determine all aerial images whose projections overlap the area of a tile. We create a 3D query box, because 3D boxes are easier to handle by our 3D R*-tree implementation. The intersection query is triggered each time a certain number of aerial images has been inserted into the spatial index. The affected tiles are determined by computing the indices n_1, n_2, n_3 and n_4 at the four corners of the projection of an aerial image onto the ground plane in world space according to equation (3.1). Let

$$n_{\min_d} = \min_{i \in \{1,2,3,4\}} (n_{i_d}), \quad n_{\max_d} = \max_{i \in \{1,2,3,4\}} (n_{i_d}), \quad d \in \{x, y\}$$

Since an aerial image may project onto multiple tiles, all tiles whose indices are in the range $[n_{\min_x}, n_{\min_y}] \times [n_{\max_x}, n_{\max_x}]$ can potentially contain parts of the projected image and must be considered for updating. This is illustrated in figure 3.10. For each considered tile t, the query box Q is constructed from the 2D bounding rectangle of t in the xy-plane, and the z-values of the box are set to $H_{\min}$ and $H_{\max}$. $H_{\min}$ denotes the minimum and $H_{\max}$ the maximum z-value of all bounding boxes of the aerial images currently stored in the R*-tree. Given the index $n = (n_x, n_y)$ of t and the grid spacing $g = (g_x, g_y)$ of the tile grid, the 2D bounding rectangle of t is computed by using equations (3.4).

$$q_{d_{\min}} = n_d \cdot g_d, \quad q_{d_{\max}} = (n_d + 1) \cdot g_d, \quad d \in \{x, y\} \tag{3.4}$$

By using the query box $Q = (q_{x_{\min}}, q_{y_{\min}}, H_{\min}, q_{x_{\max}}, q_{y_{\max}}, H_{\max})$, the result set can also contain non-vertical aerial images. These images can be identified during further processing by the viewing direction of the associated camera, for instance.

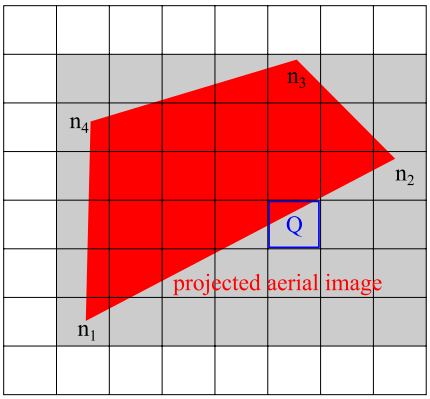

Figure 3.10: *An aerial image may project onto multiple tiles. The indices n_1, n_2, n_3 and n_4 of the tiles containing the four corners of the image's projection (red) determine the range of tiles that potentially contain image data (gray shaded). For each of these tiles, a 3D query box (blue) is created in order to determine all images having projections that overlap the area of the tile.*

A very simple way to generate texture data for each tile t is to project the returned aerial images according to their orientation and camera parameters onto t and to replace existing

texels with values from the images. The problem with this method is that the pixels become projected onto the same plane in world space, although they probably originate from non-planar objects and from images captured from different perspectives. Therefore, the borders of overlapping images will not match each other and the results look similar as depicted in figure 3.11. The solution to this problem is to incorporate information about the surface elevation and to project the images according to the depicted objects in world space as described in section 5.4.

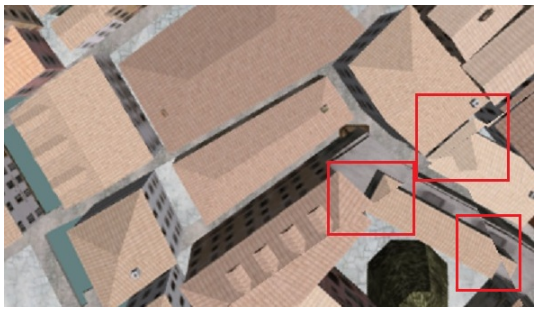

Figure 3.11: *If the aerial images are all projected onto the same plane, their borders may not match each other as can be seen in the regions highlighted by red rectangles.*

As the number of contributing images and hence the costs for updating one tile may increase over time, different selection criteria can be applied to discard images which are not supposed to contribute to the final texture, e. g., if the contrast of the image is below a certain threshold or if it is outdated. Depending on the desired quality of the resulting virtual texture and the application, it may be sufficient to update existing tiles incrementally by processing only the latest images and blending them with the previously generated tiles. The tiles need to be updated in principle as soon as they are covered by a new aerial image, but it may be sufficient to start updating affected tiles only if a certain threshold for the number of new images has been reached or after a certain period of time.

In the second case, tiles at levels $l > 0$ are recursively updated in increasing level order from their children as follows. For each tile t at level l with a given index $(n(l)_x, n(l)_y)$, equation (3.5) denotes the index $n(l+1)$ of the tile's parent at level $l+1$.

$$n(l+1) = \begin{cases} \left(\left\lfloor \frac{n(l)_x}{2} \right\rfloor, \left\lfloor \frac{n(l)_y}{2} \right\rfloor \right) & l < L-2 \\ (0,0) & l = L-2 \end{cases} \tag{3.5}$$

Whenever t is updated, the respective quadrant in its parent tile is replaced by a version of t which is downscaled by a factor of two. Afterwards, the updated parent takes the role of its children, and the process is repeated until the top-most tile has been updated. Note that only quadrants corresponding to updated children are replaced.

The number of updates required at level $l = 0$ depends on the area and locations of new images, the chosen tile size and the resolution of tiles in terms of texels per unit. At levels

> 0, the number of updates depends on the number and locations of updated tiles at the next lower level and is limited in the best case to a single tile update per level. In the worst case, all tiles have to be updated, e. g., if every or every second tile at $l = 0$ is updated.

3.3 Architecture and Implementation Details

In this section we discuss the architecture and some technical details of the FCM. The FCM is implemented in C++ and GLSL 1.50 and is an important part of our framework for DSM rendering which is covered in chapter 7.

3.3.1 Caching

One characteristic of clipmaps is the employment of caching and secondary storage. In the FCM, we keep the $c_x(l) \times c_y(l)$ texture tiles from all L clip areas in a cache in main memory. As described in section 3.2.2, the set is chosen based on the current clip center with the $c_x(l) \times c_y(l)$ neighboring tiles centered around it. This set corresponds to the *clip stack* in [79]. Its content is updated as the virtual view point and thus the clip center moves by a distance greater than some threshold. The quantities c_d, $d \in \{x, y\}$, depend on the clip level l and are limited by user-defined constants C_d, i. e., $c_d(l) \leq C_d$. At the top-most clip level $l = L - 1$, only a single tile exists and hence $c_d(L - 1) = 1$. Likewise, at $l = L - 2$, there are at most 2×2 tiles and hence $c_d(L - 2) = 2$, etc.

The smaller subset of $k_x(l) \times k_y(l)$ tiles with $k_d(l) \leq c_d(l)$, which are also centered around the clip center and visible to the viewer, i. e., the active area, is copied to the *tile texture array* in video memory, which is realized as a 1D texture array, accessible by GPU fragment programs. Similar to $c_d(l)$, the quantities $k_d(l)$ also depend on the clip level l and are limited by user-defined constants $K_d \leq C_d$. K_d and hence C_d should be chosen with respect to the tile size $T_x \times T_y$ in texels so that $T_d \cdot K_d$ are at least as large as the width respectively height of the application's viewport in pixels. Otherwise, the borders between different clip levels may become visible to the viewer during rendering, if the scene is shown from a perpendicular point of view.

The cache of an FCM of L clip levels consists of a *tile level cache* and a *tile buffer*. These two data structures identify individual tiles by means of their clip level l and tile index (n_x, n_y). The tile level cache consists of an array of L 2D *tile arrays* where the 2D tile array at index l corresponds to the clip area at clip level l. Each of the 2D tile arrays can store at most $C_x \times C_y$ tiles. The tile arrays for the two top-most levels hence need to contain only one respectively four tiles. If clip levels are added to the FCM, the tile level cache must be adjusted as well in order to keep it consistent with the clip areas. This requires not only to update the number of 2D tile arrays contained in the tile level cache, but also the sizes of the tile arrays representing the top-most clip areas, because after resizing, they need to store more tiles than they did before. For instance, if the FCM is resized from $L' = 5$ to $L = 6$ levels, the tile array representing the clip area at level $l = L' - 1 = 4$ must be resized from a 1×1 array to a 2×2 array, since $l = L - 1 = 5$ becomes the new top-most clip level and may only need to store a single tile. The transfer of tiles between the cache of the FCM and

secondary memory is performed asynchronously in a separate thread in order not to stall the rendering process as explained in section 7.2.1.

To reduce the transfer of tiles from secondary memory, we additionally keep a certain amount of tiles that have already been loaded during updating, but which are not yet cached, in the tile buffer which resides in main memory. The tile buffer is an unsorted, associative array and is accessed via a textual string which is constructed from the requested clip level l and the tile index (n_x, n_y) according to the pattern `l`l`x`n_x`y`n_y. For instance, the tile having the index $n = (-7, 4)$ at clip level $l = 3$ is accessed via the textual string `l3x-7y4`. This pattern was designed to be short, but human readable, e. g., in order to facilitate debugging during development. Besides, the string is used as the name of the file storing the tile in secondary memory. If the tile buffer overflows, tiles that are currently not marked as being about to be updated and which are not in use otherwise are written back to secondary memory. Figure 3.12 contains a sketch of the components and entities of the FCM.

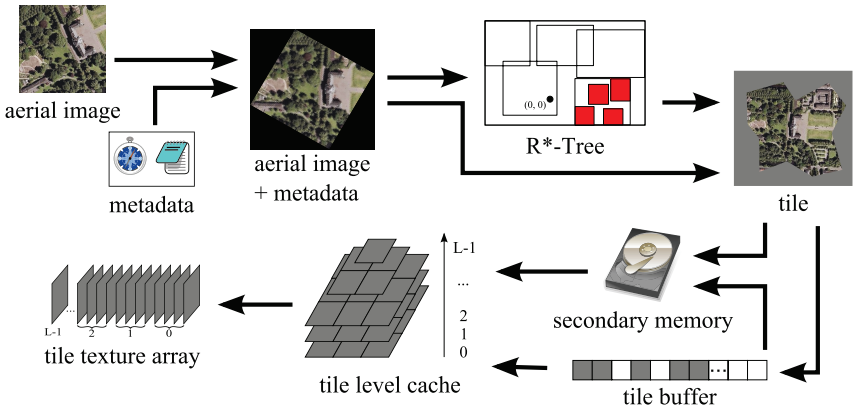

Figure 3.12: *An overview of the architecture of the FCM.*

3.3.2 Tile Arrays

The 2D tile arrays of the tile level cache of the FCM for storing the clip areas are implemented by 1D arrays. In order to access a tile at a certain clip level l within the corresponding 1D array by means of its 2D tile index $n = (n_x, n_y)$, we need to transform n into a 1D array index. Each tile array holds $c_x(l) \times c_y(l)$ tiles from a contiguous rectangular section of the tile grid (cf. section 3.3.1), so that the indices of the tiles in the clip area are in the range $[n_x, n_x + 1, \ldots, n_x + c_x(l) - 1] \times [n_y, n_y + 1, \ldots, n_y + c_y(l) - 1]$. The tile indices in this range can be mapped to $[0, 1, \ldots, c_x(l) - 1] \times [0, 1, \ldots, c_y(l) - 1]$ by using the function $j(n) = (j_x(n_x), j_y(n_y))$ with $j_d(k), d \in \{x, y\}$, as given in equation (3.6).

$$j_d(k) = k \mod c_d(l) \tag{3.6}$$

In this way, we can map the range of tile indices in a 2D tile array to a 1D range of size $c_x(l) \cdot c_y(l)$ by using equation (3.7).

$$f(n) = f(n_x, n_y) = j_y(n_y) \cdot c_x(l) + j_x(n_x) \tag{3.7}$$

In some programming languages, like C/C++, or specific implementations, the result of the modulo operator depends on the signs of the operands and may become negative. We therefore ensure that the components of a tile index n_d are always mapped to positive values by adding an integral multiple μ of the (positive) divisor $c_d(l)$ to n_d, where $\mu > n_d$. The modified versions of equation (3.6) and equation (3.7) as used in our FCM implementation are given in equations (3.8).

$$\begin{aligned} \overline{j_d}(k) &= \left(k + \left(\left\lfloor \frac{|k|}{c_d(l)} \right\rfloor + 1 \right) \cdot c_d(l) \right) \mod c_d(l) \\ \overline{f}(n) &= \overline{f}(n_x, n_y) = \overline{j_y}(n_y) \cdot c_x(l) + \overline{j_x}(n_x) \end{aligned} \tag{3.8}$$

The elements of a 2D array can thus be stored in a 1D array as illustrated in figure 3.13. If the virtual view point and hence the clip center moves, this kind of toroidal addressing allows to directly access and update the entries in the 1D array which correspond to elements from the rows or columns at the border of the 2D array, without relocating the remaining ones.

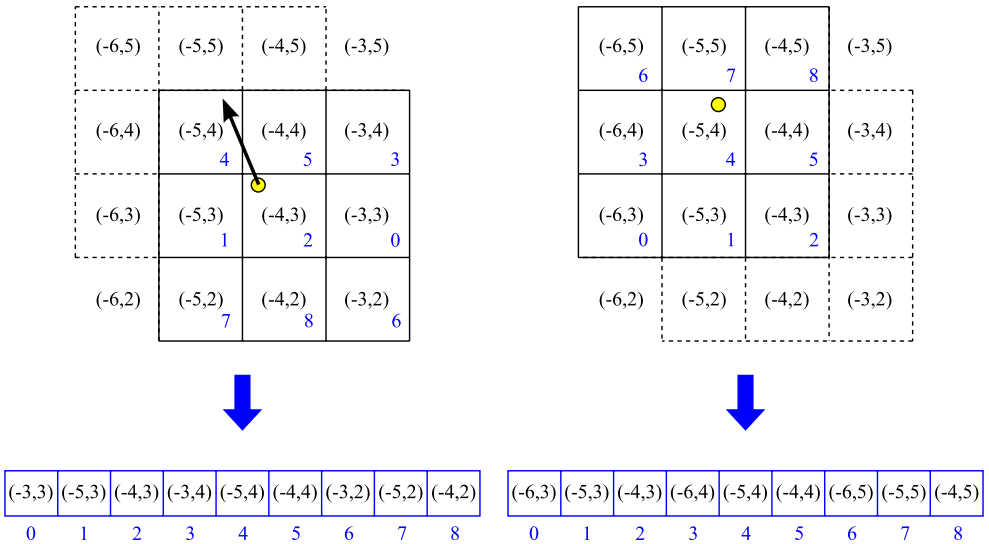

(a) *situation before movement of clip center* **(b)** *situation after movement of clip center*

Figure 3.13: *Equation 3.7 is used to calculate linear array addresses from the tile indices in order to store them in a 1D array (blue). If the clip center (yellow dot) is moved, only tiles at the border of the 2D tile array are replaced.*

We use the same technique to linearize the subset of tiles from the active areas in the tile arrays of the FCM's tile level cache in order to pack the texture data from all clip levels into a single 1D tile texture array in video memory for rendering. Texture arrays consist of textures of the same size and texel format as opposed to arrays of textures which are not restricted in this way. Arrays of textures are furthermore bound to one texture unit per contained texture, whereas one texture array is bound to only one texture unit. Since this eliminates

the need for switching textures and multiple draw calls during rendering, if there are more textures than texture units, texture arrays can yield better rendering performance [54]. At each clip level l, the active area consists of $\nu(l) = k_x(l) \cdot k_y(l)$ tiles. The total number of elements for storing the tiles in the active areas from all clip levels in a 1D tile texture array thus equals $\sum_{l=0}^{L-1} \nu(l)$. The 2D tile indices are linearized by means of the formulas in equations (3.6) and 3.7 where $c_d(l)$ is replaced by $k_d(l)$. The first of the $\nu(l)$ tiles at level l is stored in the tile texture array at offset $\Omega(l) = \sum_{i=0}^{l-1} \nu(i)$. Like the clip areas, the active areas at the top-most clip levels are smaller than those at lower levels, because at level $L-1$ there is only one tile, at $L-2$ are at most four tiles, etc., so that the ranges and offsets within the tile texture array are not constant. As explained in section 3.3.5, the FCM's fragment program for rendering uses the clip level and a 2D tile index $n = (n_x, n_y)$ to access texture data of a tile within the tile texture array. In order to compute the tile's index within the tile texture array in the fragment program, the offsets $\Omega(l)$ are required. Therefore, the offsets are stored in a separate array indexed by l and provided to the fragment program via a uniform variable. Figure 3.14 illustrates the tile texture array as stored in video memory and the array containing the offsets $\Omega(l)$.

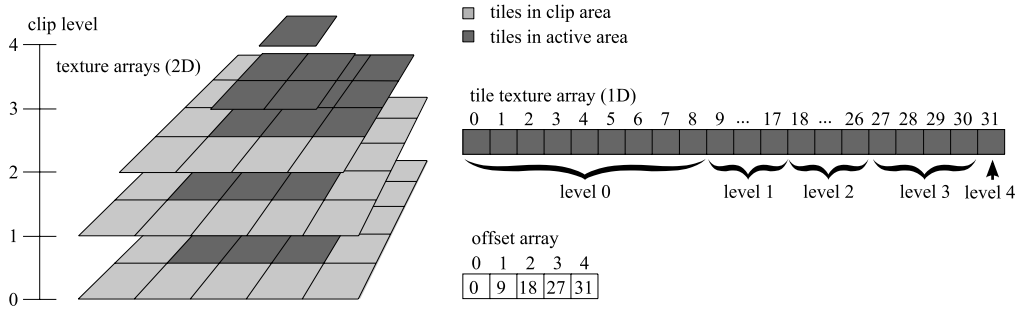

Figure 3.14: *Illustration of the 1D tile texture array and the array for storing the offsets $\Omega(l)$ of the first tile from each clip level l. In this example, the FCM has $L = 5$ clip levels, the clip areas (light gray) have sizes of at most 5×5 tiles and the active areas (dark gray) consist of at most 3×3 tiles. At levels 3 and 4, the sizes of both types of areas are only 2×2 and 1×1, respectively. The two 1D arrays are located in video memory for being accessed by the fragment program for rendering.*

3.3.3 Scheduling Tile Updates

Updating and creating tiles as described in section 3.2.5 is also performed in a separate thread. Tiles at level $l = 0$ are created by a GPU program for DSM synthesis which is subject of chapter 5.

When images are inserted into the spatial index, the tile update process calculates the indices for the tiles at $l = 0$ that are covered by the new images. For each tile that is about to be updated, all images whose projections overlap the tile's area are retrieved from the spatial index as described above. The texture data are then generated by projecting the returned aerial images onto the tile and assigning texel values according to one of the

methods presented in section 5.4. After updating a tile at level $l = 0$, equation (3.5) is used to determine its parent tile and a *tile update job* at level $l = 1$ is inserted into a schedule. A tile update job consists of a sequential number (ID), the clip level of the parent and the indices of the parent and its child. The schedule is implemented as a priority queue, and the jobs are assigned priorities according to the parent level and the ID of a job. Given two distinct tile update jobs j_1 and j_2, the priority of j_1 is considered to be higher than the one of j_2, if

$$(l_1 < l_2) \vee ((l_1 = l_2) \wedge (ID_1 < ID_2))$$

where l_i and ID_i, $i = 1, 2$ are the level and ID of tile update job j_i, respectively.

As soon as no tiles at level $l = 0$ are left for being updated from images, the thread responsible for updating tiles continues to process the jobs from its schedule. A parent tile and its respective child are retrieved from the cache of the FCM and are both locked during updating, i. e., they cannot be accessed by any other process. If a tile is requested for updating, but already locked for other reasons, e. g., because it is about to be copied into video memory by the rendering process, the job is re-scheduled with a greater ID. Updated tiles are unlocked again, marked as updated and stored in the tile buffer of the cache of the FCM, since they are likely to be used for updating their own parents or for being copied to video memory by the rendering process. Updating tiles at $l > 0$ will cause further jobs to be scheduled in the same way, until the top-most tile has been updated and the schedule runs empty.

3.3.4 Tile Map and LOD Calculation

In order to avoid aliasing during rendering, the texture data that determine the final color of a screen pixel have to be selected from tiles at clip level l_{opt}. A single texel of a tile at l_{opt} aggregates a number of texels from levels $< l_{\text{opt}}$ and thus provides a pre-filtered version of the texture data. Therefore we have to calculate the level of detail (LOD) l_{opt} which best avoids texture aliasing, and we have to locate the corresponding tile that contains the texture data within the tile texture array.

Following the idea by Crawfis et al. [16], we use an extra texture, the *tile map*. Each texel in the tile map corresponds to the area of a tile at level 0 in world space. The value of the texel indicates the lowest clip level l_{low} for which a tile is present in the tile texture array in video memory. A value of zero, for instance, means that a tile is available at level 0. Only a rectangular region of $k_x \times k_y$ texels, i. e., the size of the active area, around the location of the clip center in the tile map can have a value of zero. A tile at level $l > 0$ corresponds to $2^l \times 2^l$ texels within the tile map. Note that the example of a tile map shown in figure 3.15 only contains the lowest clip levels available in video memory, but the corresponding FCM has two more clip levels, so that $L = 5$ due to the total size of the area A covered by the FCM. Tiles at higher levels are implicitly present in video memory as well, because they partially contain the more detailed areas, and the top-most tile must always be available. The tile map is recomputed and uploaded into video memory each time the clip center is relocated due to movements of the virtual camera, and its lateral extension (tm_x, tm_y) in

texels must satisfy equation (3.9).

$$\log_2 \left(\min \left(tm_x, tm_y \right) \right) \geq (L - 1) \tag{3.9}$$

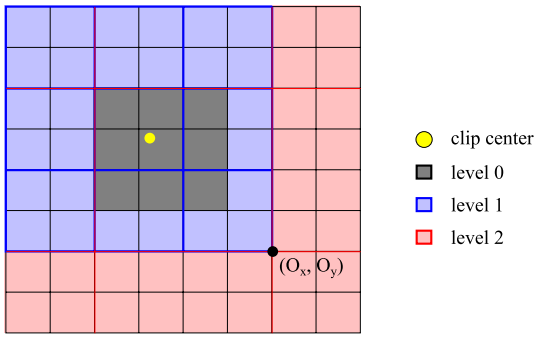

Figure 3.15: *Illustration of a tile map: each grid cell represents a texel and corresponds to a tile at level 0. The color indicates the value of the minimum clip level of a tile that covers the corresponding area of the FCM and which is present in the tile texture array in video memory.*

Aliasing caused by texture sampling is best avoided by the texture data from a tile at clip level l_{opt}. This particular level is computed in the same way as a corresponding mip-map level. The computation is based on the amount of texels that are covered by a single screen space pixel (*minification*) where pixels and texels are assumed to be representable as squares, although they are actually point samples [26]. The minification j corresponds to the number of texels at the base clip level 0 that need to be aggregated into one screen pixel. In this way, the texture is spatially filtered and aliasing is avoided.

If the partial derivatives of the texture coordinates (u, v) with respect to the screen coordinates x and y are assumed to be constant across the area of a single pixel in screen space, its shape in texture space can be approximated by a parallelogram [26]. j can then be determined, for instance, by hypotenuse comparison as presented in [26], i. e., by the length of the greater of the two sides s_a and s_b of the pixel's parallelogram in texture space. As illustrated in figure 3.16, s_a and s_b are given by $s_a^2 = \left(\frac{\partial u}{\partial x}\right)^2 + \left(\frac{\partial v}{\partial x}\right)^2$ and $s_b^2 = \left(\frac{\partial u}{\partial y}\right)^2 + \left(\frac{\partial v}{\partial y}\right)^2$ where $\frac{\partial u}{\partial d}, \frac{\partial v}{\partial d}, d \in \{x, y\}$ denote the changes of the texture coordinates (u, v) along the screen space directions x and y. At clip level l, 2^l texels from the base level 0 are aggregated along each dimension, and we compute $l = l_{\text{opt}}$ according to [26] by means of equations (3.10).

$$\begin{aligned} j &= \max \left(s_a, s_b \right) = 2^l \\ \Rightarrow l &= \log_2 \left(\sqrt{\max \left(s_a^2, s_b^2 \right)} \right) \\ &= \frac{1}{2} \log_2 \left(\max \left(\left(\frac{\partial u}{\partial x} \right)^2 + \left(\frac{\partial v}{\partial x} \right)^2, \left(\frac{\partial u}{\partial y} \right)^2 + \left(\frac{\partial v}{\partial y} \right)^2 \right) \right) \end{aligned} \tag{3.10}$$

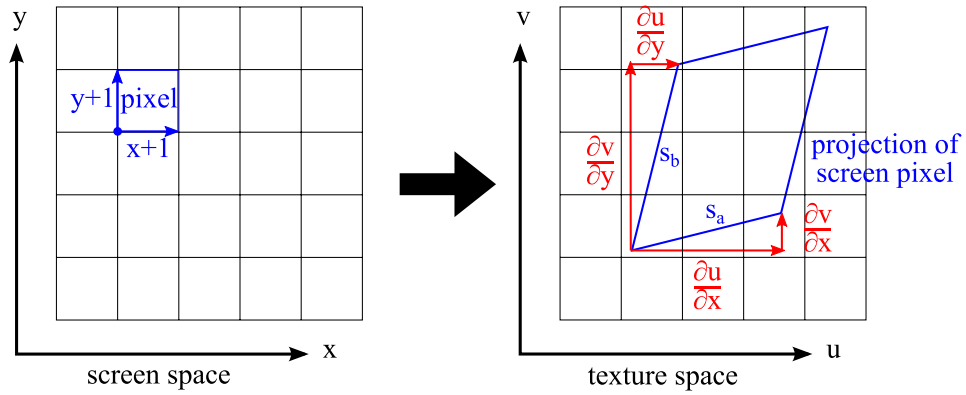

Figure 3.16: *The projected shape of a screen pixel onto a texture (blue) is approximated by a parallelogram in texture space. Its sides are related to the partial derivatives of the texture coordinates (u, v) with respect to the directions x and y in screen space. Illustration following [26].*

The four partial derivatives can be calculated in GLSL fragment programs by applying the built-in functions `dFdx` and `dFdy` to the normalized texture coordinates scaled by the size of the virtual texture in texels.

Though it is computationally more expensive, anisotropic texture filtering, which is supported by current graphics hardware [1, p. 168], yields better visual results, since the resulting images look less blurry as shown in figure 3.2(b) and figure 3.2(c). To take into account the maximum number of samples N_{aniso} along the line of anisotropy [1, pp. 168–170] in order to select an appropriate clip level for texture sampling, equation (3.10) needs to be modified. The modified formula is given in equation (3.11).

$$\sigma_{\text{min}} = \min\left(s_a, s_b\right), \quad \sigma_{\text{max}} = \max\left(s_a, s_b\right) = j,$$
$$r_{\text{aspect}} = \min\left(\frac{\sigma_{\text{max}}}{\sigma_{\text{min}}}, N_{\text{aniso}}\right)$$
$$l = \log_2\left(\frac{\sigma_{\text{max}}}{r_{\text{aspect}}}\right) = \log_2(j) - \log_2(r_{\text{aspect}}) \tag{3.11}$$

The same formula is also used in [16] and [53] for selecting appropriate levels of detail with respect to anisotropic texture filtering.

3.3.5 Rendering

Before a frame is rendered, the FCM checks if the point of view of the virtual camera has changed, and updates its cache if necessary. All tiles from the active area must be uploaded into video memory, i. e., they must be copied into the tile texture array. Since the active areas are subsets of the clip areas, the tiles within the active areas are contained in the tile arrays of the tile level cache. These tiles are retrieved from the cache of the FCM and sent to video memory in descending clip level order. In this way, if some tiles cannot be uploaded on time, at least the tile at top-most level $L - 1$ is likely to be present in video memory.

Furthermore, the FCM checks whether tiles are marked as updated or whether previously any tile could not be transferred to video memory because it was locked for updating or not yet loaded into main memory. Tiles that are not available for the aforementioned reasons are marked as delayed, and a counter for the number of unsuccessful accesses of the corresponding tile will be increased. Subsequent attempts to access a delayed tile for rendering in a later frame are made, if the counter is below some threshold, but not until a predefined timeout has expired. If the threshold for the maximum number of delays is exceeded, the tile is marked as absent and will not be used for rendering again, because it is then considered missing. This avoids further unsuccessful and hence unnecessary attempts to retrieve an absent tile from the cache. Absent tiles are usually tiles which have a valid tile index according to the area A covered by the FCM, but which do not contain any texture data. In this case, the rendering must rely on texture data from the parent tile at the next coarser LOD, if such a level exists.

Texture mapping using the FCM is implemented by a GLSL fragment program. The tile texture array and the tile map have to be bound to one texturing unit each and are accessed by the shader. The texture coordinates (u, v) of the surface to be textured are assumed to be in $[0, 1] \times [0, 1]$ and correspond to the area A covered by the FCM. In this way, whenever the FCM is resized, the texture coordinates can remain unchanged, although the underlying geometry of the textured surface, e. g., a planar quadrilateral mesh, is preferably also scaled in order to reflect the extension of the depicted area.

The actual texture mapping of a surface performed by the fragment program of our FCM implementation comprises the steps listed below.

1. determine the clip level l_f for sampling texture data
2. determine world coordinates p at current fragment
3. compute the 2D tile index $n = (n_x, n_y)$ from p and l
4. transform n into a 1D index to access the tile texture array by using the clip level's offset $\Omega(l)$
5. compute the sampling position (s_u, s_v) sampling the tile's texture data

In the following, we describe each of these steps in detail.

1. At each fragment, the fragment program performs a look-up in the tile map to determine the tile with the lowest clip level l_{low}, i. e., the highest LOD, that is available in the tile texture array, and it furthermore calculates l_{opt} as described in section 3.3.4. The final clip level and LOD l_f, at which the corresponding tile has to be accessed, is computed by $l_f = \max\left(l_{\text{low}}, l_{\text{opt}}\right)$. Since l_f is usually not an integral level, trilinear interpolation between $\lfloor l_f \rfloor$ and $\lceil l_f \rceil$ by means of the fractional part of l_f can be used to obtain smooth transitions of texture data between each two LODs.

2. The corners R_{min} and R_{max} in world coordinates of A are passed to the fragment program via uniform variables. Let (u, v) denote the texture coordinate at the current fragment. The corresponding location $r = (r_x, r_y)$ in world coordinates is computed by

$$\begin{aligned} r_x &= u \cdot (R_{x_{\text{max}}} - R_{x_{\text{min}}}) + R_{x_{\text{min}}} \\ r_y &= v \cdot (R_{y_{\text{max}}} - R_{y_{\text{min}}}) + R_{y_{\text{min}}} \end{aligned}$$

3. The grid spacing of the tile grid (g_x, g_y) is passed as a uniform variable to the fragment program as well. The 2D tile index $n = n(l, r)$ of the tile containing the previously computed position r at clip level $l = l_f$ is then computed by equation (3.1).

4. Using the tile index n, the number of tiles $k(l) = (k_x(l), k_y(l))$ in the 2D tile array from the active area and the array of offsets $\Omega(l)$ where the first tile from the active area is located within the tile texture array, the tile's index within the tile texture array ξ is computed by means of equations 3.6 and 3.7 where $c_d(l)$ is replaced by $k_d(l)$, $d \in \{x, y\}$. The arrays holding $k(l)$ and $\Omega(l)$ are indexed by l and passed via uniform variables to the shader.

5. The position (s_u, s_v) where the tile at index ξ in the tile texture array has to be sampled is calculated by the shader by means of the texture coordinates (u, v) of a fragment according to equations (3.12).

$$\begin{aligned} (G_u, G_v) &= (R_{x_{\text{min}}} \cdot \text{res}_x, R_{y_{\text{min}}} \cdot \text{res}_y) \\ (N_u, N_v) &= ((R_{x_{\text{max}}} - R_{x_{\text{min}}}) \cdot \text{res}_x, (R_{y_{\text{max}}} - R_{y_{\text{min}}}) \cdot \text{res}_y) \\ (F_u, F_v) &= \begin{cases} \left(\left\lfloor \frac{G_u}{2^l} \right\rfloor, \left\lfloor \frac{G_v}{2^l} \right\rfloor \right), & l < L - 1 \\ \left(\left\lfloor \frac{G_u}{2^l} \right\rfloor - \frac{T_x}{2}, \left\lfloor \frac{G_v}{2^l} \right\rfloor - \frac{T_y}{2} \right), & l \geq L - 1 \end{cases} \\ (t_u, t_v) &= \left(\frac{u \cdot N_u}{2^l} + F_u, \frac{v \cdot N_v}{2^l} + F_v \right) \\ (s_u, s_v) &= \left(\frac{t_u \mod T_x}{T_x}, \frac{t_v \mod T_y}{T_y} \right) \end{aligned} \tag{3.12}$$

$(\text{res}_x, \text{res}_y)$ denotes the tile resolution in terms of texels per unit in world coordinates and (T_x, T_y) is the size of the tile's texture in texels. Both quantities are also available in the fragment program. This formula is implemented by the GLSL functions `getTileCoordUniform()` and `getTileCoord()` which can be found at the beginning of the complete source code of our FCM fragment program in listing A.2 in appendix A. The latter function is used for texel-precise texture sampling and hence computes sampling positions (s'_u, s'_v) in the range $[0, T_x - 1] \times [0, T_y - 1]$ instead of $[0, 1] \times [0, 1]$ by omitting the divisions by T_x and T_y.

3.4 Performance Analysis

We analyzed the performance of the FCM in terms of the number of updated tiles per second during continuous addition of aerial images. Aerial images data were created using the

simulation framework in [75] which allows to generate virtual vertical aerial images at locations, orientations, resolutions and frequencies specified by the user from renderings of digital 3D models. The images with added metadata were sent by the simulator over network via TCP to a client application where they were processed by the employed FCM.

3.4.1 Evaluation Setup

The run-time performance of the rendering and the visual quality of the resulting texture map in the FCM depend on the following quantities: the resolution of the incoming aerial images in texels, the number of aerial images per second (*image rate*), the number of tile updates per second (*update rate*), the resolution of the final texture in texels per unit $(\mathrm{res}_x, \mathrm{res}_y)$, the tile size in texels (T_x, T_y), the sizes of the clip areas $(c_x(l), c_y(l))$ and the active areas $(k_x(l), k_y(l))$ in number of tiles at each level l, and capacity of the tile buffer B.

In our evaluation setup, we always used a viewport/screen size of $(V_x, V_y) = (1024, 768)$ pixels, $\mathrm{res}_d = 20$, $K_d = \lceil V_d/T_d \rceil$, $C_d = 2 \cdot K_d$ with $d \in \{x, y\}$ and $B = C_x \cdot C_y$. For each tested configuration of tile sizes, image sizes and average images rates, we simulated a single camera with a vertical field of view of 60° and following exactly the same path at a constant altitude of 50 m above ground, and we performed 10 runs each to obtain means. Means are necessary, because the images received by the client are located at random positions along the path of image acquisition during different runs, as there was no synchronization between the client application and the simulator. In addition, the simulator cannot guarantee to provide a certain update rate, which also strongly depends on the resolution of the aerial images and the network. Tile updates were executed before every frame whenever at least one new aerial image had been received. The simulator and the client application were executed in parallel on a desktop computer with an Intel i7 860 CPU at 2.8 GHz, a NVidia GeForce 470 GTX with 1280 MB dedicated video memory, 6 GB RAM and 64-bit Windows 7 operating system.

3.4.2 Results

The performance of the FCM in terms of updated tiles per second from the setup described in section 3.4.1 for tile sizes of $T_x = T_y = 256$ and $T_x = T_y = 512$ texels and for different image sizes at different averaged image rates is shown in figure 3.17. Error bars indicate the standard deviations. During the evaluation the FCM had at most $L = 8$ clip levels in case of $T_x = T_y = 256$ and $L = 7$ in case of $T_x = T_y = 512$ after the area of A reached its maximum extension. The amount of texture data managed by the FCM thus corresponds to a single 32-bit R8G8B8A8 texture of $2^{15} \times 2^{15}$ texels with a memory size of 4 GB. The most demanding configuration $(4000 \times 3000$ texels@$0.26)$ corresponds to an average data rate of 11.9 MB per second but still achieved tile update rates of 427.59 tiles per second for tile size 256×256 and 150.57 tiles per second for tile size 512×512. The total number of tiles in the tile texture array was only 85 respectively 25. This implies that the average update rates are sufficient to update the entire tile texture array multiple times per second and still permit interactive rendering frame rates.

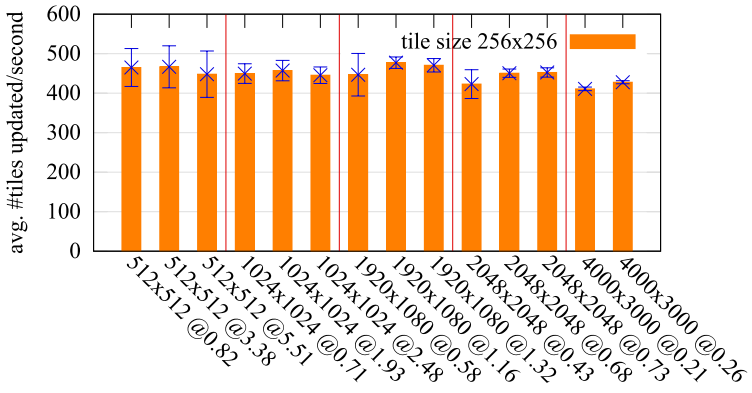

(a) *tile size* 256×256 *texels*

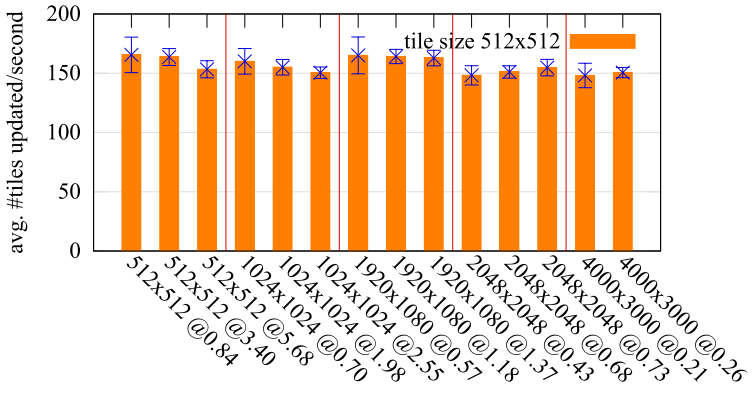

(b) *tile size* 512×512 *texels*

Figure 3.17: *FCM performance in terms of tile updates/second in our evaluation setup.*

3.5 Discussion

Our evaluation has shown that the most important limiting factors in our setup were the simulation of image sources providing high resolution images at high frequency, and the transmission over the network. Therefore the simulator and client were executed in parallel on the same machine using the network loopback device in order to eliminate transmission errors. This prevented us from performing further measurements and determining the limits of the FCM in the given scenario.

A problem arises if the projections of the aerial images cover the entire area of the FCM or even more, e. g., when the images are taken from high altitudes: the updates then would not be confined to few tiles and would affect the entire FCM. However, this issue can be avoided by limiting the number of tiles updated in each frame, which is advisable anyway, because performing many tile updates between two frames would stall the rendering and reduce interactivity.

Another severe issue is caused by the 32-bit floating point precision of the texture coordinates (u, v), because they need to cover the entire $\mathbb{R}^2$ (see section 3.3.5). This also arises in other GPU based clipmap implementations (cf. [23], [78]). By deriving the geometry from the FCM as well, we could drop that constraint and map the texture coordinate range of $[0, 1] \times [0, 1]$ only to the visible portion of the geometry.

Furthermore, the size of the tile map can exceed the hardware limits as the number of clip levels increases (cf. section 3.3). This can be countered by virtualizing the clip stack, as already introduced in [79], by processing only a subset $[L_{\text{min}}, L_{\text{max}}] \subset [0, L - 1]$ of clip levels which are relevant for the viewer at the current view point. Though the tile map requires an additional texture unit, it provides a very easy LOD selection and avoids invalidating entire detail levels, if a single tile is missing (cf. [16]).

4 Digital Surface Model Rendering

Since textured polygonal meshes can be processed and rendered by GPUs at high speed, a widely used rendering technique stores a digital elevation model (DEM) in (grayscale) texture maps (so called *heightmaps* or *heightfields*) and uses them to displace the vertices of a sufficiently tessellated planar polygonal mesh. This technique is known as *displacement mapping* [1, p. 198] and is considered an extension of *bump mapping* [15]. Bump mapping employs textures to perturb the surface normals to modify the perceived smoothness of a surface during lighting computations, without modifying the underlying geometry [1, pp. 183–190].

However, most renderers accept only triangle meshes which can become rather complex and may easily consist of millions of triangles. During mesh generation, particular attention has to be paid to different issues, e. g., to not produce any cracks, to choose appropriate tessellations and to avoid aliasing caused by small or distant triangles.

Furthermore, when a large mesh becomes rasterized, many triangles result in at most a few pixels whose corresponding fragments succeed in passing all of the numerous tests encountered on their way through the rendering pipeline. Therefore it appears to be attractive to bypass the entire process of converting a heightfield into a mesh. Techniques like relief mapping [63] or parallax occlusion mapping [80] can make use of pixel shaders on modern GPUs to perform real-time ray casting on heightfields. This allows to conveniently calculate the displaced sample positions in corresponding color textures for determining the final fragment color. During this ray casting fine-structured details can be added to surfaces without further tessellating the underlying polygonal mesh. In many cases this even allows to reduce the polygonal mesh to a planar quadrilateral which may be tessellated into only two triangles.

In order to speed up the ray casting and to achieve real-time frame rates, many GPU-based heightfield rendering techniques employ *maximum mipmaps* to access the DEM. At each level, a maximum mipmap aggregates 2×2 texels into one texel at the next higher mipmap level by using the maximum of the four texel values instead of their averaged value. As the size of texture maps that can be handled by GPUs is currently limited by manufacturer specific restrictions and ultimately by the amount of available video memory, large DEMs cannot be stored in a single heightfield texture for direct access during GPU-based ray casting.

In this chapter, we present a GPU-based heightfield ray casting technique for single-pass rendering of heightfields of almost arbitrary sizes in real time. The technique employs the Flexible Clipmap (FCM) discussed in chapter 3 and current graphics hardware to speed up the ray casting while alleviating the aforementioned video memory limitations. The speedup

is achieved by taking into account the desired image quality on a per-pixel basis and early ray termination based on level of detail selection: At each intersection of a ray with the surface to be rendered, we check if the corresponding element of the surface becomes projected to less than one screen pixel. In this case, we can stop ray casting, because it would be unnecessary to depict more details about the surface at the current pixel. Additionally, two different refinement methods for improving the appearance of the reconstructed surfaces in our renderings can be employed.

4.1 Related Work

Much research has been done on CPU-based ray casting of heightfields as well as on terrain rendering based on polygonal meshes. Since summarizing these two areas would exceed the scope of this thesis, we confine ourselves to an overview of recent GPU-based heightfield ray casting methods related to our work.

Qu et al. [65] presented one of the first GPU-based ray casting schemes for heightfields which primarily aims at accurate surface reconstruction of heightfields but does not use any sophisticated structures for acceleration.

Relief mapping [57] and parallax (occlusion) mapping [40] are techniques for adding structural details to polygonal surfaces, which have their origin in CPU-based rendering and improve upon the disadvantages of bump mapping [10]. Both techniques have been implemented for GPUs (e. g., [63, 80]) and benefit from programmable graphics pipelines. But as most of these implementations resemble the strategies used in CPU-based ray casting, like iterative and/or binary search to detect heightfield intersections, they are prone to the same kind of rendering artifacts caused by missed intersections in highly spatially variant data sets. An introduction to these closely related techniques can be found for instance in [1, pp. 183–199], and more details are given in the comprehensive state-of-the-art report by Szirmay-Kalos and Umenhoffer [77] which focuses on GPU-based implementations.

Oh et al. [55] accelerate ray casting and achieve real-time frame rates by creating a bounding volume hierarchy (BVH) of the heightfield, which is stored in a maximum mipmap and allows to safely advance along the ray over long distances (see section 4.2.2). They also present a method based on bilinear interpolation of heightfield values to improve the quality of the reconstructed surface obtained from point-sampled data.

The method presented by Tevs et al. [81] also relies on BVHs stored in maximum mipmaps, but uses a different sampling strategy. Their method advances along the ray from one intersection of the projected ray with a texel boundary to the next such intersection, whereas Oh et al. use a constant step size to advance along the ray. In addition, Tevs et al. store in each heightfield texel the height values at the four corners of a quadrilateral encoded as an RGBA value instead of point samples, which allows surface reconstruction on parametric descriptions.

Compared to other techniques which also rely on preprocessed information about the heightfield and acceleration data structures, like for instance relaxed cone step mapping [20, 48, 62], maximum mipmap creation is much faster and can be performed on the GPU [81].

All these methods have in common that they operate on single heightfields of relatively small extents which are intended to add details to surfaces at meso- or microscales instead of representing vast surfaces themselves. Recently Dick et al. [18] have presented a method for ray casting terrains of several square kilometers extent at real-time frame rates. Their method also employs maximum mipmaps to accelerate the ray casting process and a tiling approach to render data sets of several hundred GB size. They also presented a faster hybrid method which uses ray casting or rasterization-based rendering, but requires knowledge of the employed GPU respectively a training phase to decide whether to use rasterization or ray casting [19]. Another hybrid technique is presented in [3].

Our method aims at rendering very large heightfields only by means of GPU ray casting. It has been inspired in large parts by the works of Dick et al. [18] and Tevs et al. [81] as we also employ a tile-based approach and their cell-precise ray traversal scheme. But in contrast to the technique by Dick et al., which creates a complete mipmap for each tile and requires additional rendering passes to determine the visibility of the tiles, our method further accelerates the ray casting process and requires only a single rendering pass by using our tile-based FCM implementation (see chapter 3).

Another concept worth mentioning in the context of DSM rendering and clipmaps is the *geometry clipmap* as introduced by Losasso et al. [47]. Geometry clipmaps and derived GPU-based variations [4, 12] store DEM data in vertex buffers at different resolutions, but according to our knowledge they are only used in the context of mesh-based rendering and not for accelerating ray casting.

4.2 GPU based Single-pass Ray Casting Using Clipmaps

Our FCM implementation can be used to store different DSM data, and in particular elevation information, i. e., a DEM, in order to produce 3D renderings of the underlying surface by means of ray casting. In this section we explain our storage scheme for DSM data and describe the employed ray traversal method, which is basically the same as the one presented in [18]. We discuss how to accelerate ray casting and how to avoid aliasing by using the FCM. Furthermore, we present two refinement methods that can be used to improve the appearance of the reconstructed surfaces.

4.2.1 Clipmaps for DSM Storage

In order to store DSM data, the tiles in our FCM implementation are extended to consist of several textures (*tile layers*) of the same extension for the different types of data of a DSM. For our purposes, two layers are required, one for storing elevation data (*DEM layer*) and one for color information (*color layer*). The layers correspond to textures, and their texel formats are based on the underlying data according to table 2.1 in section 2.2.3. For each layer, the GPU uses one separate texture tile array as described in chapter 3.3.2 to access the texture data of the tiles in the active area.

To use a digital elevation model (DEM) for rendering, in our approach the height values are stored in the DEM layer of FCM tiles at the highest resolution (lowest) level $l = 0$. A texel at level $l > 0$ obtains as value the maximum height value of the corresponding 2×2 subordinate texels at level $l - 1$. This is the same construction scheme as used with maximum mipmaps [18, 55, 81]. If we identify each texel with a bounding box defined by its height value and its grid cell, i. e., the boundaries of the associated square texel in the texture, we obtain a bounding volume hierarchy (BVH) of the underlying DEM as illustrated in figure 4.1. In the method presented by Dick et al. [18], the heightfield is split into tiles as

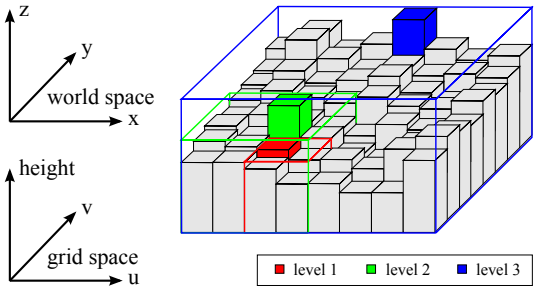

Figure 4.1: *The BVH is derived from the DEM data on a regular grid. Gray boxes correspond to elevation samples at level 0. Bounding boxes on higher levels and their maximum value are highlighted by the same color.*

well, but a separate maximum mipmap is created for each tile. To render vast DSMs, this approach may require either lots of tiles and thus mipmaps to be present in video memory or additional rendering passes, especially if the heightfield is shallow and there is little occlusion between tiles. Furthermore, the tiles located far away from the viewer may contain fine spatial details, e. g., steep summits of distant mountains, which are not only not perceivable from far away but may also expose spatial aliasing artifacts due to minification caused by perspective projection. The latter aspect is the same which motivated the development of mipmaps for texture mapping and also applies to mesh-based rendering techniques which therefore strive to determine an appropriate level of detail (LOD) in order to avoid rasterizing triangles that would become projected to less than one pixel in screen space.

The important difference between the usage of a clipmap and multiple mipmaps is that in case of a clipmap the BVH spans the entire domain at the topmost level. A proper placement of the clip center results in the selection of only those tiles of highest resolution at level $l = 0$ which are closest to the virtual camera and thus potentially have to be rendered in full detail. Compared to level l, at level $l + 1$ the area of the heightfield covered by a tile is four times larger, and the spatial resolution is divided in half along each direction of the grid. Thus the entire domain is spatially pre-filtered and the level of detail of the heightfield decreases with increasing distance towards the viewer. Because higher clipmap levels also correspond to larger bounding boxes, we can exploit this fact to accelerate GPU ray casting in distant parts of the scene as described in section 4.2.2.

4.2.2 Rendering and Accelerated Ray Traversal

The ray casting of DSMs respectively DEMs using the FCM is done on the GPU by means of a vertex and a fragment program. For the mere purpose of ray casting, only the DEM layer of the tiles in the active area is required. The textures containing elevation data are accessed by the GPU via a separate texture tile array in the same way as the texture tile array of an FCM, that is used for texturing a (planar) surface (see section 3.3.5). Given a DSM stored in an FCM of L clip levels, we set the clip center simply by projecting the center of the viewport into the scene. Using this method, the location of the clip center depends on the angle φ_{view} enclosed between the viewer's viewing direction and the opposite surface normal of the plane containing the rendered elevation data. If $\varphi_{\text{view}} = 0$, i. e., the viewer is looking perpendicularly onto the ground plane, the clip center is located in the center of the viewport as desired. If φ_{view} increases, the clip center becomes located in more distant parts of the scene near the horizon. This is undesirable, since the viewer probably wants to see elevated surfaces in parts of the scene closer to her. We therefore control the maximum distance of the clip center from the viewer by confining the maximum angle for computing the distance to the clip center to $70°$, which is an empirical value. In this way, the clip center will remain located within the viewport between its lower border and the horizon of the scene, even if the viewing direction is parallel to the ground plane or directed upwards. This method for placing the clip center is illustrated in figure 4.2. We also ensure that all

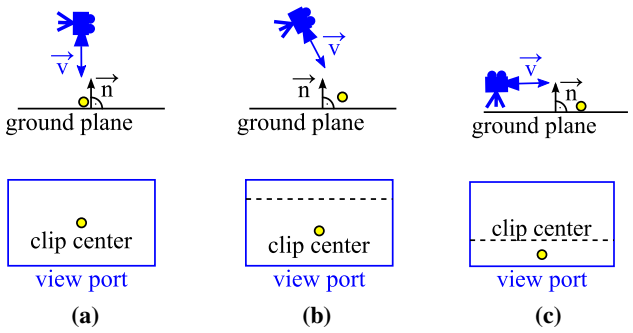

Figure 4.2: *The location of the clip center (yellow dot) in the scene is computed by projecting the geometric center of the viewport into the scene. It depends on the angle enclosed between the opposite surface normal $\vec{n}$ of the ground plane containing the elevation data of the rendered surface and the viewing direction $\vec{v}$. If $\vec{v}$ is (near-)parallel to the ground plane (right image), we ensure that the clip center remains located between the horizon of the scene (dashed line) and the bottom of the viewport.*

tiles in the active areas of all clip levels or at least the highest ones can be stored in video memory by choosing appropriate sizes for the tiles and the active area.

The axis-aligned bounding box (AABB) of the entire DEM, which is associated with the topmost tile, is based in the xy-plane of the world coordinate system. While the extension of this AABB in x- and y-direction can be obtained directly from the box stored at the root node of the FCM's R*-tree, the size in z-direction is determined by the maximum elevation value of that tile. The AABB is used to construct a polygonal box mesh consisting of only

12 triangles which serves as proxy geometry for the ray casting process. A vertex program obtains the dimensions of the box in world space and calculates normalized 3D texture coordinates from the vertex coordinates of the box corners. The clipmap is positioned at the bottom of the box corresponding to the minimum height value $z = H_{min}$ of the DSM. H_{min} and the maximum height value H_{max} are both determined during loading of the topmost clipmap tile into main memory. The texture coordinates on the box range from $(0, 0, 0)$ on its minimum corner to $(1, 1, 1)$ on its maximum corner and are used to setup the rays as described in [43]. By rendering the back faces of the proxy geometry we obtain each ray's exit point e, and we pass the camera position and the geometry of the bounding box in world coordinates to the fragment shader which calculates each ray's normalized direction $\vec{d} = (d_x, d_y, d_z)$ and entry point s to the proxy geometry in normalized 3D texture space[6]. If the camera is located inside the bounding box the entry point s becomes the position of the virtual camera [48]. In order to avoid that faces of a possibly very large proxy geometry are clipped against the far plane of the view frustum of the virtual camera and hence exit points are missing, the box is clipped in advance to fit into the view volume when the virtual camera is moved.

The actual ray traversal is performed by projecting the ray onto a clip level dependent 2D grid with each grid cell corresponding to a texel. For a given clip level $0 \leq l < L$ the extensions of this grid (G_u, G_v) are determined by equation (4.1) with (W, H) being the extensions of the entire DSM in sample points, i. e., texels.

$$(G_u(l), G_v(l)) = \left(\frac{W}{2^l}, \frac{H}{2^l} \right) \tag{4.1}$$

Hence, the grid at level l has the same size a single texture containing the entire DSM at mipmap level l would have. The current height p_z of a location $p = (p_x, p_y, p_z) = s + k \cdot \vec{d}$ is given in grid coordinates. In order to test for intersections with the heightfield, the sampled height values have to be converted from world coordinates to grid coordinates via the height resolution res_z of the DEM. As an alternative, p_z can be transformed into world space for comparing height values and finding intersections of the ray with the surface. During ray traversal we move from one intersection of the projection of the ray onto the xy-plane $\vec{d_p} = (d_x, d_y)$ with a texel boundary to the next such intersection, i. e., from the projected ray's entry point en_p into a grid cell directly to its exit point ex_p as shown in figure 4.3. The only exception is at the first entry point which is the projection of the starting point of a ray s_p.

Ray casting is started at the highest clip level $L - 1$ with the coarsest resolution of the BVH at which the entire DEM is given in a single tile and each pixel corresponds to the maximum value and thus to the bounding box of $2^{L-1} \times 2^{L-1}$ texels at the base level 0. To determine whether a ray hits a bounding box at level l, the clipmap tile containing the grid cell which belongs to the current en_p and ex_p has to be sampled for the associated height value h. The tile is determined by the uniform texture coordinate (u, v) as described

[6] The direction $\vec{d}$ of a ray is noted with an arrow to emphasize its vectorial character and to distinguish it from the previously used variable d.

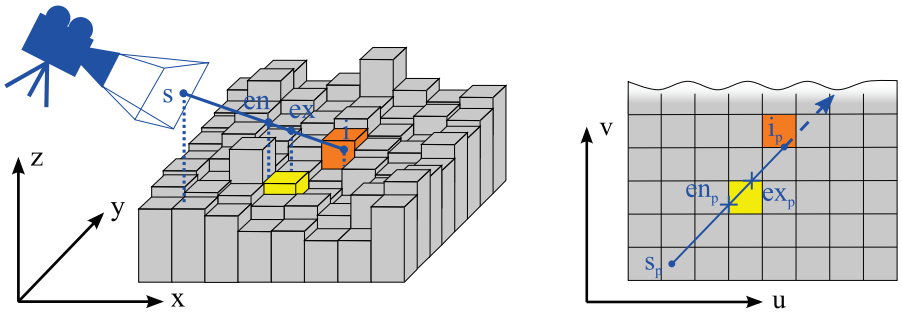

(a) *situation in world space* **(b)** *projection onto grid*

Figure 4.3: *Rays are traversed from one intersection of the projected ray with a texel boundary to the next such intersection. In the depicted situation the projection of the ray enters the yellow box at en_p, exits at ex_p and finally hits the orange box at i.*

in section 3.3.5. Since the direction of the ray is needed to determine this grid cell and the borders where the projected ray enters respectively exits, the sign bits of the components of $\vec{d}$ are stored in the lower three bits of an integer. This bit mask is created once for each ray using bit-wise operations in the fragment shader, and it is evaluated as needed by `switch`-statements to determine the direction of a ray. Details on the implementation are given in section 7.4.1.

When moving along the ray from point en to point ex we hit the box surface in the following two situations:

1. the ray is directed downwards and ex lies below the top of the box at height h
2. the ray is directed upwards and en lies below the top of the box at height h

If a ray hits a bounding box B at the current level l, it may also hit a bounding box contained in B at a lower level of the BVH. Therefore the ray casting process is repeated at the next lower level $l' = l - 1$ from the current position en of the ray, but only if it is possible and reasonable to proceed as described in section 4.2.3. Otherwise the lowest possible level $l = l_{\text{min}}$ has been reached, and the exact intersection i on the bounding box surface is calculated according to equation (4.2).

$$i = \begin{cases} en + \vec{d} \cdot \max\left(\frac{h - en_z}{d_z}, 0\right) & d_z < 0, ex_z < h \\ en & d_z \geq 0, en_z \leq h \end{cases} \tag{4.2}$$

If a ray does not intersect a bounding box B at level l, it cannot intersect any of the bounding boxes contained in B at any lower level either, and we therefore advance along the ray to ex which becomes the entry point en of the next cell. Compared to a ray traversal performed just on level 0, only one instead of $2^l \times 2^l$ samples have to be tested for intersection, which results in a significant speed up of the process [18, 81].

Three different cases for the intersection of a ray with a bounding box are illustrated in figure 4.4. If a ray hits a bounding box B at some level $l > 0$ it does not necessarily have

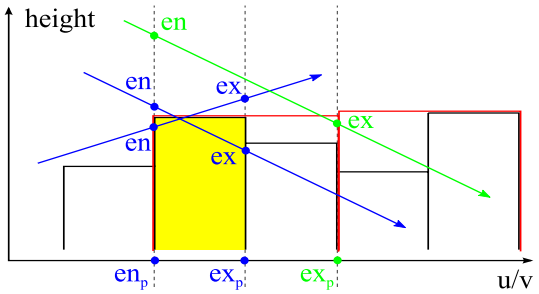

Figure 4.4: *Different situations of intersection of a ray with the height field. The green ray hits the left red box, but none of the black boxes contained.*

to hit any bounding boxes contained in B at level $l-1$, but this cannot be determined without descending to the lower level. In order to avoid using the smaller step size over longer distances, we move up again to level l if we detect that the ray does not hit any bounding box at level $l-1$ (cf. [18, 81]). The level is increased after four steps without intersecting another box, because after four steps the containing box that caused the decrease of the level is safely passed and the ray traversal cannot get stuck by switching alternately between two levels.

The ray casting process is terminated if either a valid intersection point i on a bounding box has been found or if the ray leaves the domain of the DSM. In the latter case, the fragment from which the ray originates is discarded by the shader.

The complete GLSL source code of the vertex and fragment programs is given in appendix A.1.

4.2.3 LOD-determined Ray Termination

Ray casting can be terminated at the current level l, if $l = \max\left(l_{\text{low}}, l_{\text{opt}}\right)$. The termination criterion is designed to speed up ray casting and to avoid aliasing that may be caused if projections of distant or small boxes are smaller than one screen pixel.

At each intersection of the ray with a bounding box we determine the highest resolution available, i. e., the lowest clip level l_{low} of a tile which covers the corresponding area of the DSM and is present in video memory. This is done by transforming the hit point i on the bounding box surface to normalized texture coordinates, followed by a single texel-precise texture lookup in the tile map of the FCM as described in section 3.3.4 and section 3.3.5.

The clip level l_{opt} at the current hit point i is chosen in such a way that aliasing resulting from boxes which cover less than one pixel in screen space is avoided. But instead of using the projection of a single screen pixel into texture space like in section 3.3.4, the size of the corresponding heightfield box in screen space is considered, because a single texel from the DEM layer represents only the top of the box on which i is located. Furthermore, the top may not be visible, e. g., if the viewing direction is nearly parallel to the ground plane of the rendered surface and thus to the top of the box. In this situation, the height of the box has

to be considered as well in order to determine an appropriate LOD based on the number of covered screen pixels.

For this purpose, i is transformed from grid coordinates into world space to obtain $i_{\text{world}} = (i_x, i_y, h)$. Let (Δ_x, Δ_y) denote the spacing of the DEM grid in terms of units per sample in world coordinates and let M denote the combined model, view and projection matrix of the virtual camera. The four corners

$$\begin{aligned}\kappa &= (\lfloor i_x \rfloor, \lfloor i_y \rfloor, h)\\ \lambda &= (\lfloor i_x \rfloor + \Delta_x, \lfloor i_y \rfloor, h)\\ \mu &= (\lfloor i_x \rfloor, \lfloor i_y \rfloor + \Delta_y, h)\\ \nu &= (\lfloor i_x \rfloor, \lfloor i_y \rfloor, 0)\end{aligned}$$

of the box on which i is located are transformed from world space into normalized screen space by means of M. The resulting 2D positions κ', λ', μ' and ν' are used to compute the three sides $\vec{a}, \vec{b}$ and $\vec{c}$ of the box in window coordinates as shown in equations (4.3) where V_x, V_y denote the size of the view port in pixels.

$$\begin{aligned}\vec{a} &= (a_1, a_2) = \big((\lambda'_x - \kappa'_x) \cdot V_x, (\lambda'_y - \kappa'_y) \cdot V_y\big)\\ \vec{b} &= (b_1, b_2) = \big((\mu'_x - \kappa'_x) \cdot V_x, (\mu'_y - \kappa'_y) \cdot V_y\big)\\ \vec{c} &= (c_1, c_2) = \big((\nu'_x - \kappa'_x) \cdot V_x, (\nu'_y - \kappa'_y) \cdot V_y\big)\end{aligned} \tag{4.3}$$

$\vec{a}, \vec{b}$ and $\vec{c}$ correspond to three of the sides of the bounding box of the DEM texel in window coordinates and can be used to form the matrix T_{tex} in equation (4.4).

$$T_{\text{tex}} = \begin{pmatrix} a_1 & a_2 \\ b_1 & b_2 \\ c_1 & c_2 \end{pmatrix} \tag{4.4}$$

T_{tex} allows to transform coordinates from 2D screen space onto a plane in 3D texture space Σ_{tex}. If h was zero, the box would be degenerate and identical to its corresponding texel, since $\vec{c}$ would be 0. In this case, the last row in equation (4.4) can be dropped, and the texture coordinate system would be two-dimensional.

Assuming that the screen pixels are unit squares, they can be transformed to Σ_{tex} using equations (4.5).

$$\vec{r} = T_{\text{tex}} \cdot \begin{pmatrix} 1 \\ 0 \end{pmatrix} = \begin{pmatrix} a_1 \\ b_1 \\ c_1 \end{pmatrix}, \quad \vec{s} = T_{\text{tex}} \cdot \begin{pmatrix} 0 \\ 1 \end{pmatrix} = \begin{pmatrix} a_2 \\ b_2 \\ c_2 \end{pmatrix} \tag{4.5}$$

By means of $\vec{r}$ and $\vec{s}$, we can compute the fraction of one screen pixel that is covered by the box defining Σ_{tex}. This quantity corresponds to the reciprocal of the amount of texels that are covered by one screen pixel in texture space, i. e., the minification j as described in section 3.3.4. The relation becomes directly apparent, if $h = 0$ and the box can be identified with its corresponding texel. In contrast to the texture space in section 3.3.4, Σ_{tex}

corresponds to the projection of a single box instead of an entire texture. Hence, if $|\vec{r}| < 1$ or $|\vec{s}| < 1$, the projection of the box covers less than one pixel and would cause aliasing. The larger of the reciprocals of $|\vec{r}|$ and $|\vec{s}|$ therefore indicates the minification j, which is calculated according to equations (4.6).

$$\begin{aligned} |\vec{r}| &= \sqrt{a_1^2 + b_1^2 + c_1^2}, \quad |\vec{s}| = \sqrt{a_2^2 + b_2^2 + c_2^2} \\ j &= \max\left(\frac{1}{|\vec{r}|}, \frac{1}{|\vec{s}|}\right) = \frac{1}{\min\left(|\vec{r}|, |\vec{s}|\right)} \end{aligned} \tag{4.6}$$

Analog to the LOD computation given in equations (3.10), $j = 2^{l_{\text{opt}}}$, and we compute l_{opt} according to equation (4.7).

$$\begin{aligned} 2^{l_{\text{opt}}} = j &= \frac{1}{\min\left(|\vec{r}|, |\vec{s}|\right)} \\ \Rightarrow l_{\text{opt}} &= -\log_2\left(\min\left(|\vec{r}|, |\vec{s}|\right)\right) \end{aligned} \tag{4.7}$$

Clip level l_{opt} is calculated in screen space at each intersection i of a ray with the heightfield. The different spaces for computing l_{opt} are illustrated in figure 4.5.

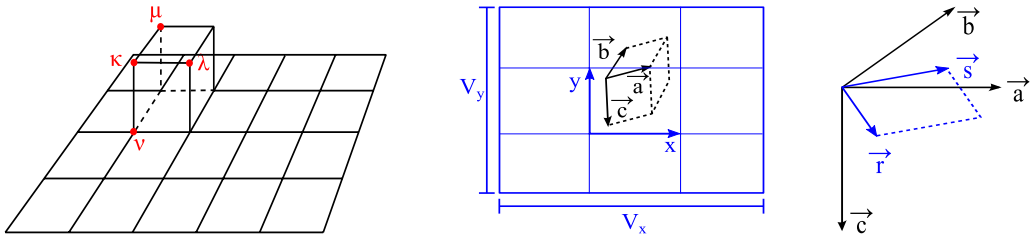

(a) *world space* **(b)** *screen space* **(c)** *texture space*

Figure 4.5: *Illustration of the three different spaces used for computing l_{opt} by means of a bounding box which corresponds to a DEM texel.*

Instead of descending to the full resolution clip level which may cause aliasing, we can terminate ray casting at level $l_{\text{min}} = \max\left(l_{\text{low}}, l_{\text{opt}}\right)$. The two different LODs l_{low} and l_{opt} are visualized in figure 4.6 where each level is encoded by a different color.

Note that this calculation of l_{opt} is different from the one we presented in [27] which is based on the projection of the box surface area containing i into screen space. Both methods are suitable for LOD determination since there are several ways [1, pp. 687–691], but we prefer the approach in equation (4.7), because it is more similar to the LOD selection presented in equation (3.10).

A problem that was left open in [27] is the transition between two LODs which becomes apparent as the virtual camera moves during user interaction or animations. We solved this issue by linearly interpolating between the height values as follows:

Let h denote the height of the grid cell's bounding box for which an intersection i at the clip level l_{min} has been detected. The height value h_p of the parent box is sampled and used

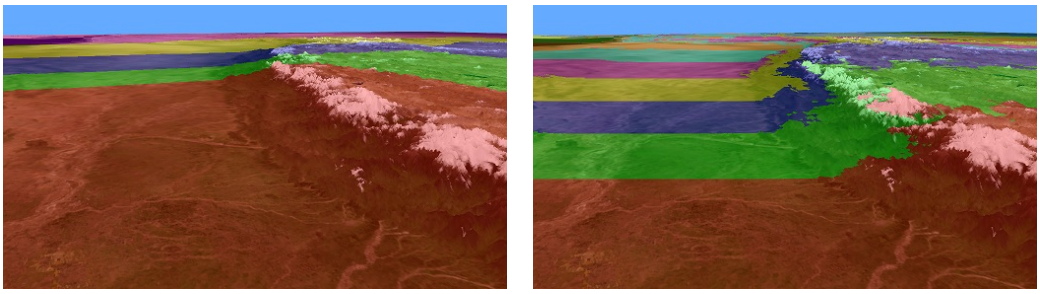

(a) l_{low} **(b)** l_{opt}

Figure 4.6: *The two different LODs l_{low} and l_{opt} are used to terminate the ray traversal and to avoid aliasing. Different colors encode different levels. Their order becomes visible in the right image in the almost planar region on the left. Note that regions of higher elevation are assigned lower levels of detail (right) since they cover more screen pixels.*

together with h and the fractional part τ of l_{min} to compute $\bar{h}$ according to equation (4.8).

$$\bar{h} = h + \tau \cdot (h_p - h), \quad \tau = l_{\text{min}} - \lfloor l_{\text{min}} \rfloor \tag{4.8}$$

The final intersection i is then calculated in equation (4.2) with h being replaced by $\bar{h}$. As desired, the interpolation has no visual effect, if the box has the same height as its parent. Transitions between different LODs are only perceivable during animations and user interaction, especially in areas where the difference $h_p - h$ is large. The interpolation scheme described above makes these transitions less abrupt and is illustrated in figure 4.7.

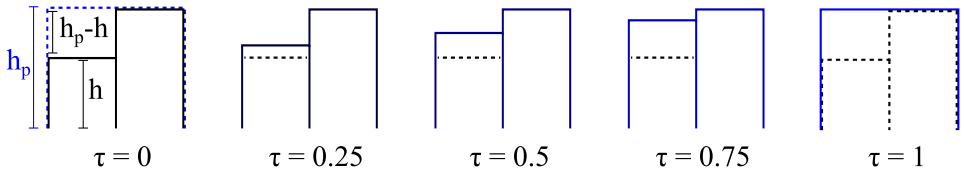

Figure 4.7: *The heights of the cell's bounding box and its parent are linearly interpolated by using the fractional part τ of l_{min} to determine the height value of the final intersection. Actually, the value $\tau = 1$ does not occur, but is included for illustration.*

4.2.4 Refinement of Block-sampled Heightfield Reconstruction

As pointed out by Oh et al. in [55], the point sampled DSMs and their treatment as boxes results in blocky images which from a closeup view remind of models built of bricks (see figure 4.8(a)). Because this effect may be unwanted in most applications, we also implemented two refinement methods to obtain smooth surfaces. Both refinement methods are applied after the intersection i on the bounding box surface has been determined as described in section 4.2.2.

The first method is the one presented by Oh et al. [55] and relies on linear interpolation of two samples obtained from the linearly interpolated heightfield, which are taken at a

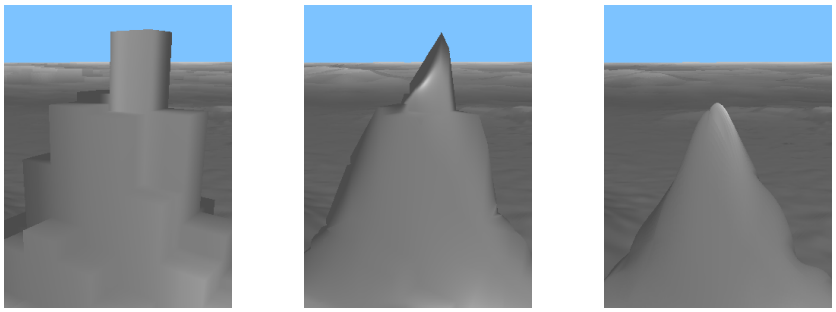

(a) *none* **(b)** *linear* **(c)** *bicubic*

Figure 4.8: *Demonstration of the improvement in surface quality achieved by different refinement methods.*

distance of one half cell from i in forward respectively backward direction along the ray. This method works quite well and has hardly any effect on the overall performance on modern GPUs, but in our implementation, some defects – presumably caused by numerical inaccuracies – on surfaces with steep slopes remain, as shown in figure 4.8(b). Despite these small defects, which are barely noticeable during animations or from farther viewing distances, the surfaces look much smoother.

Our second method uses Hermite bicubic surfaces to improve the reconstruction of the heightfield. Let (i_u, i_v) denote the projection of the point i onto the grid of the heightfield at which ray casting has been terminated. Furthermore let C denote the height value of the cell containing (i_u, i_v) and $SW, S, SE, E, NE, N, NW, W$ the height values of the neighboring cells, starting at the left lower cell and enumerating them in counterclockwise order (see figure 4.9). We interpret the four points given in equations (4.9) as the corners of

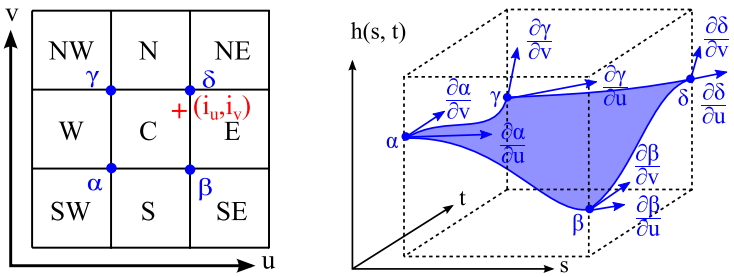

(a) *corners* α, β, γ *and* δ **(b)** *resulting Hermit bicubic patch*

Figure 4.9: *Construction scheme for a Hermite bicubic patch from* 3×3 *heightfield samples surrounding the projection of intersection point* i *on the bounding box (left) and the resulting patch (right).*

a Hermite bicubic surface patch.

$$\begin{aligned}
\alpha &= (\alpha_s, \alpha_t, \alpha_h) = (\lfloor i_u \rfloor, \lfloor i_v \rfloor, \min(SW, S, C, W)) \\
\beta &= (\beta_s, \beta_t, \beta_h) = (\lfloor i_u \rfloor + 1, \lfloor i_v \rfloor, \min(S, SE, E, C)) \\
\gamma &= (\gamma_s, \gamma_t, \gamma_h) = (\lfloor i_u \rfloor, \lfloor i_v \rfloor + 1, \min(W, C, N, NW)) \\
\delta &= (\delta_s, \delta_t, \delta_h) = (\lfloor i_u \rfloor + 1, \lfloor i_v \rfloor + 1, \min(C, E, NE, N))
\end{aligned} \tag{4.9}$$

Each patch is parametrized along the grid axes by $s, t \in [0, 1] \subset \mathbb{R}$, and the height $h(s, t)$ on the surface patch is given in equation (4.10).

$$h(s,t) = \begin{pmatrix} s^3 & s^2 & s & 1 \end{pmatrix} \cdot H \cdot G \cdot H^T \cdot \begin{pmatrix} t^3 & t^2 & t & 1 \end{pmatrix}^T \tag{4.10}$$

$$H = \begin{pmatrix} 2 & -2 & 1 & 1 \\ -3 & 3 & -2 & -1 \\ 0 & 0 & 1 & 0 \\ 1 & 0 & 0 & 0 \end{pmatrix}, \quad G = \begin{pmatrix} \alpha_h & \gamma_h & \frac{\partial \alpha_h}{\partial v} & \frac{\partial \gamma_h}{\partial v} \\ \beta_h & \delta_h & \frac{\partial \beta_h}{\partial v} & \frac{\partial \delta_h}{\partial v} \\ \frac{\partial \alpha_h}{\partial u} & \frac{\partial \gamma_h}{\partial u} & \frac{\partial^2 \alpha_h}{\partial u \partial v} & \frac{\partial^2 \gamma_h}{\partial u \partial v} \\ \frac{\partial \beta_h}{\partial u} & \frac{\partial \delta_h}{\partial u} & \frac{\partial^2 \beta_h}{\partial u \partial v} & \frac{\partial^2 \delta_h}{\partial u \partial v} \end{pmatrix}$$

Superscript T denotes transposed matrices and vectors, and H and G are the *Hermite basis matrix* and *Hermite geometry matrix* respectively. Their derivations can be found, for instance, in [29, pp. 483–488, 516–520]. In [27], we approximated the partial derivatives which define the tangential planes on the patch by using forward respectively backward differences and by making the simplifications in equations (4.11) for the first order derivatives.

$$\begin{aligned}
\frac{\partial \alpha_h}{\partial u} &= \frac{\partial \gamma_h}{\partial u} \approx C - W, & \frac{\partial \beta_h}{\partial u} &= \frac{\partial \delta_h}{\partial u} \approx E - C, \\
\frac{\partial \alpha_h}{\partial v} &= \frac{\partial \beta_h}{\partial v} \approx C - S, & \frac{\partial \gamma_h}{\partial v} &= \frac{\partial \delta_h}{\partial v} \approx N - C
\end{aligned} \tag{4.11}$$

This causes discontinuities at the patch boundaries, although they are hardly perceivable during rendering. However, these discontinuities become apparent in closeup views and for certain viewing angles. To achieve true C^1 continuity between the patches, we compute the first order partial derivatives $\frac{\partial}{\partial u}$ as given in equations (4.12).

$$\begin{aligned}
\frac{\partial \alpha_h}{\partial u} &\approx \frac{C + S - (W + SW)}{2}, & \frac{\partial \beta_h}{\partial u} &\approx \frac{E + SE - (C + S)}{2} \\
\frac{\partial \gamma_h}{\partial u} &\approx \frac{N + C - (NW + W)}{2}, & \frac{\partial \delta_h}{\partial u} &\approx \frac{NE + E - (N + C)}{2}
\end{aligned} \tag{4.12}$$

The computations of the derivatives $\frac{\partial}{\partial v}$ are given in equation (4.13).

$$\begin{aligned}
\frac{\partial \alpha_h}{\partial v} &\approx \frac{C + w - (S + SW)}{2}, & \frac{\partial \beta_h}{\partial v} &\approx \frac{E + C - (SE + S)}{2} \\
\frac{\partial \gamma_h}{\partial v} &\approx \frac{N + NW - (C + W)}{2}, & \frac{\partial \delta_h}{\partial v} &\approx \frac{NE + N - (E + C)}{2}
\end{aligned} \tag{4.13}$$

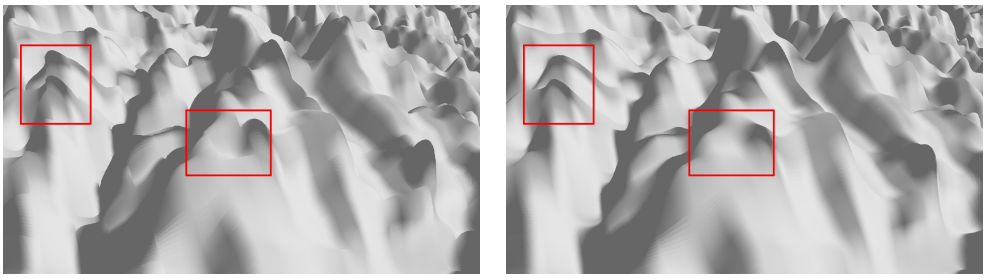

(a) *discontinuities* **(b)** C^1 *continuity*

Figure 4.10: *The simplification made for the first order partial derivatives* $\frac{\partial}{\partial u}$ *and* $\frac{\partial}{\partial v}$ *in equation (4.11) does not lead to desired* C^1 *continuity between patch boundaries. The discontinuities become visible in closeup views and for certain viewing angles (left). By using equations (4.12) and (4.13) to compute the derivatives, the patches possess* C^1 *continuity (right).*

The mixed second order partial derivatives are approximated by equations (4.14).

$$\begin{aligned} \frac{\partial^2 \alpha_h}{\partial u \partial v} &\approx C - W - S + SW, & \frac{\partial^2 \beta_h}{\partial u \partial v} &\approx E - C - SE + S, \\ \frac{\partial^2 \gamma_h}{\partial u \partial v} &\approx N - NW - C + W, & \frac{\partial^2 \delta_h}{\partial u \partial v} &\approx NE - N - E + C \end{aligned} \tag{4.14}$$

The visual difference between the simplified method for computing the first order partial derivatives in equation (4.11) and the method given above is shown in figure 4.10. Although the matrix G at each grid cell respectively texel of the clipmap storing the heightfield is constant, we calculate it directly in the fragment shader as needed.

The pair of parameters (s, t), which corresponds to an intersection of the ray with the bicubic patch instead of the bounding box, is determined by a second ray casting. Starting at i on the bounding box surface, the ray $p = i + k \cdot \vec{d}$ is advanced to its exit point on the box at a fixed step width until it either hits the bicubic patch, i. e., $p_z \leq h(s, t)$, or it leaves the domain of the box without intersection. In the latter case, we treat i as an entry point on the proxy geometry and proceed with the accelerated ray casting process described in section 4.2.2 from the current level. We found a subdivision into 16 steps for traversing the bounding box of a cell to be completely sufficient, independent of the clip level l. Fewer subdivision steps expose defects by missed intersections, whereas increasing the number of subdivision steps only reduces frame rates without further improving the reconstruction of the surface.

Besides their simplicity and the possibility to calculate all the relevant information in the fragment shader, we decided to use Hermite bicubic patches because we wanted to ensure that the surface remains inside the bounding boxes of the BVH. By constructing the patches as described above, we can ensure that they stay completely inside the bounding boxes as we control the defining tangential planes. The direct usage of forward and backward differences according to equations (4.12) and (4.13) avoids any scaling of the tangents and therefore leads to desired C^1 continuity between neighboring patches, because their

tangents have the same direction and magnitude (cf. [29, pp. 517–520]). The most severe drawback of this method is its high computational cost, although we still may achieve interactive frame rates (see section 4.3.2). Furthermore, as this method ensures that the height of each patch is less or equal than the height of its bounding box, and the tangents are not scaled, isolated peaks in the heightfield become clearly flattened as can be seen in figure 4.8(c).

However, both refinement methods presented in this section rely on interpolation of point sampled data on a regular grid, and only serve in making the resulting renderings visually more appealing. Besides, even if it might appear to be sufficient to apply refinement only in cases when the viewer is close to a highly detailed area where the block sampled nature of the data becomes apparent, we refine the surface at all discrete LODs, because the transition between large distant boxes and smooth surfaces is rather disturbing during animations. In addition, the lighting conditions on smooth surfaces and blocks are different due to distinct surface normals.

4.2.5 Sampling Color Textures

The mapping of color information onto the surface obtained by ray casting as described above works on the assumption that the DSM provides a color layer with an orthophoto texture or a similar texture, e. g., a schematic map. As long as the color layer and DEM layer cover the same area in world space and have the same resolution, one heightfield sample corresponds to one color sample. In this case, only texture data on the tops of grid cell bounding boxes of corresponding DEM layer texels are available, but the color value is also used for the lateral faces and hence for the entire box. Therefore the final clip level l_{min} where ray casting has terminated can also be used to perform a texel precise texture lookup in the color layer of the tile that contains the intersection with the DEM.

If the color and DEM layers are of different resolutions, the determination of color values by the FCM can be the same as described in section 3.3.4. Calculating the clip level l_{opt} which best avoids texture aliasing can be integrated into the ray casting procedure or can be performed separately at the final hit point i in the heightfield.

The most severe drawback of using the color from a single texel for the entire box of a heightfield sample is that the lateral faces of elevations do not depict information as expected. By viewing surfaces from oblique angles, a viewer might expect to see details on these faces, e. g., frontages of buildings in urban areas or different layers of rock on canyon walls, which are not available due to the nature of the employed color textures. This problem is illustrated in figure 4.11 and addressed in chapter 6.

4.3 Performance Results

The performance of our technique is demonstrated for renderings of four different data sets of fixed size listed in table 4.1. The data set City 2 was acquired by means of photogram-

(a) *near-perpendicular view* **(b)** *oblique viewing angle*

Figure 4.11: *Orthophoto textures do not contain color information about lateral surfaces. This becomes apparent, for instance, in urban areas if the virtual camera is lowered towards street level (right).*

name	extent [km]	$W \times H$	L	scale	size DEM	size color texture	time [min]
City 1	1.4×1.0	5600×4000	5	1.0	133 MB	99 MB	0:54
City 2	20.9×26.3	83600×105200	9	1.0	31.6 GB	–	3:34
ETOPO1	$\approx 40075.0 \times 19970.0$	21600×10800	7	10.0	1.3 GB	–	9:53
Blue Marble	$\approx 40075.0 \times 19970.0$	86400×43200	9	10.0	19.2 GB	14.4 GB	13:10

Table 4.1: *Properties of the different data sets used to evaluate performance. L denotes the total number of clip levels which have been created, $W \times H$ is the grid size at level 0 respectively the size a single texture would have. Column* time *contains the durations of the virtual camera flights for our evaluation in minutes.*

metric methods from aerial images. City 1 depicts a small area in City 2 in which we have a color texture available that has been derived from orthographic aerial images. The data sets ETOPO1 [2] and Blue Marble [51] depict the entire Earth and are both derived in large parts from SRTM data [52], but ETOPO1 also contains bathymetric data, whereas Blue Marble possesses a color texture derived from satellite images. In addition, we created a fifth data set which contains elevation data of almost the entire surface of Mars and has an extent of 46080×22528 samples. The data from Mars were acquired from the Mars Orbiter Laser Altimeter experiment in the context of the Mars Global Surveyor Mission by NASA [61]. We did not use the Mars data set in our evaluation, because its properties are very similar to those of the ETOPO1 data set. Example renderings of the data sets are shown in figure 4.12.

When being sampled in the fragment shader, the height values are scaled by factors given in column *scale* in order to avoid flattened surfaces. Shallow surfaces do not challenge our ray caster because less mutual occlusions lead to fewer level changes in the BVH during ray traversal.

4.3.1 Evaluation Setup and Results

We used tile sizes of 512×512 texels, active area sizes of 5×5 tiles and clip area sizes of 7×7 for all data sets in our tests. The near and far plane of the virtual camera were set to 1.0 and 2000.0 units, respectively. Heightfield layers consist of single channel 32-bit floating point textures, and color texture layers consist of 24-bit RGB textures. The results were

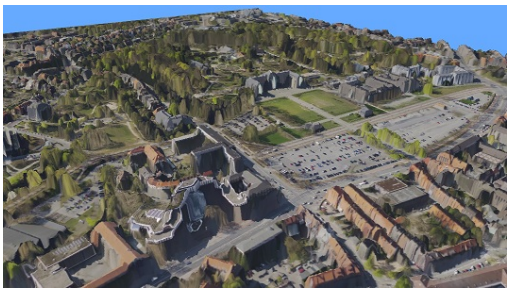

(a) *City 1*

(b) *City 2*

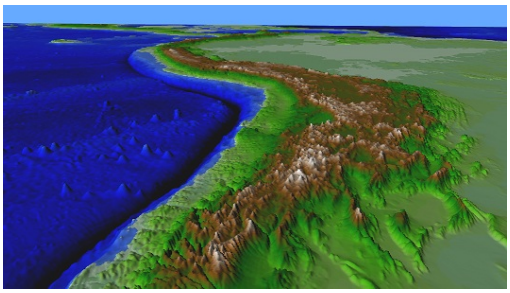

(c) *ETOPO1*

(d) *Blue Marble*

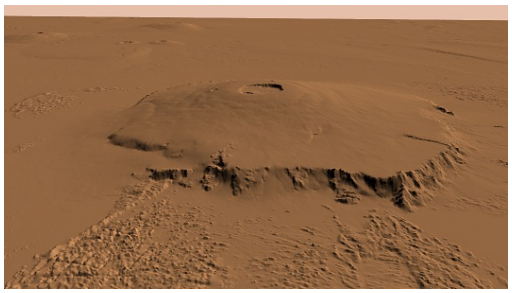

(e) *Mars*

Figure 4.12: *Example renderings of the four data sets which we used in our performance evaluations and the Mars data set. Color textures are only available for City 1 and Blue Marble, ETOPO1 was rendered using a pseudo topographic color map and the rendering of City 2 depicts shadows which were computed by means of secondary ray casting. The colors in the rendering of Olympus Mons on Mars were chosen according to artistic considerations.*

recorded during virtual camera flights along fixed paths over the heightfields on a desktop computer with an Intel i7 860 CPU at 2.8 GHz, 6 GB RAM, NVIDIA GeForce GTX 470 graphics adapter with 1280 MB dedicated video memory and Windows 7 OS (*system A*). To make our results comparable to the results reported in [18], we additionally ran the same tests on a second desktop computer (*system B*) with a hardware configuration more similar to theirs (Intel Q6600 CPU at 2.4 GHz, 4 GB RAM, NVIDIA GeForce GTX 285 with 1024 MB dedicated video memory and Windows 7 OS). Table 4.2 shows the results for different screen resolutions on system A and system B in terms of frames per second (fps). The frame rates take into account the delays caused by updating the tile caches in main memory and video memory as described in section 3.3. The times for rendering the given number of frames are the same on both systems and are denoted by column *time* in table 4.1.

data set	resolution [pixel]	frames	min. [fps]	avg. [fps]
City 1	1024 × 768	5450	6.2	100.9
	1280×1024	3464	5.8	64.1
	1920×1080	2217	5.1	41.0
City 2	1024 × 768	25624	5.6	119.7
	1280×1024	16700	5.6	78.0
	1920×1080	11189	5.1	52.3
ETOPO1	1024 × 768	105747	6.3	178.5
	1280×1024	66869	5.9	112.9
	1920×1080	42907	4.9	72.4
Blue Marble	1024 × 768	121844	3.3	154.2
	1280×1024	75721	4.0	95.8
	1920×1080	50028	1.8	63.3

(a) *System A*

data set	resolution [pixel]	frames	min. [fps]	avg. [fps]
City 1	1024 × 768	3848	5.1	71.2
	1280×1024	2450	4.5	45.3
	1920×1080	1574	5.1	29.1
City 2	1024 × 768	18174	3.6	84.9
	1280×1024	12327	3.6	57.6
	1920×1080	8290	3.3	38.7
ETOPO1	1024 × 768	75790	5.2	127.9
	1280×1024	48027	5.2	81.1
	1920×1080	31134	4.7	52.5
Blue Marble	1024 × 768	95285	2.8	120.6
	1280×1024	63409	2.5	80.3
	1920×1080	43314	1.0	54.8

(b) *System B*

Table 4.2: *Performance results of our rendering technique on two computers with different hardware configuration.*

4.3.2 Performance with Surface Refinement

All values given in table 4.2 were obtained without any of the surface refinement methods described in section 4.2.4. The impact on the rendering speed and the relative loss in performance when using surface refinement in our implementation is shown in table 4.3. These data were acquired from another evaluation of the same camera flight through the City 2 data set on system A and system B, because this data set has high spatial frequencies in the rendered regions and is the most challenging for our ray caster.

4.4 Discussion

The results in table 4.2 show that – in accordance with the results of Dick et al. [18] – very large DSMs can be rendered in real time by using only ray casting and acceleration data structures. Due to its close relation to mipmaps, the FCM proved to be well suited for this

method	1024×768	1280×1024	1920×1080
linear	96.2 (-19.6%)	62.8 (-19.5%)	42.0 (-19.7%)
bicubic	36.8 (-69.3%)	24.3 (-68.8%)	16.6 (-68.3%)

(a) *System A*

method	1024×768	1280×1024	1920×1080
linear	75.4 (-12.4%)	49.8 (-13.5%)	33.7 (-12.9%)
bicubic	36.4 (-57.1%)	17.4 (-69.8%)	11.9 (-69.3%)

(b) *System B*

Table 4.3: *Impact of surface refinement methods on the performance in terms of average frames per second for City 2 data set and the loss compared to unrefined rendering.*

task, because DEM data and color textures can be handled in the same way and the implementation of DEM layers as maximum mipmaps is straightforward. Although the hybrid approach of Dick et al. [19] performs faster rendering, it appears to be less flexible, because it requires to select representative tiles from the data set and views of the scene during its training phase.

As expected, table 4.3 shows that when using bicubic surface refinement the loss in performance is much larger than with the linear method, but even at the highest resolution we still achieve interactive frame rates. The linear method may expose some defects, but offers a good compromise between quality and speed at higher screen resolutions. As expected, when using bicubic surface refinement, the loss in performance is much larger than with the linear method, but even at the highest resolution we still achieve interactive frame rates. Besides, the refinement of the reconstructed surface only pays for coarse resolution DSMs respectively low grid densities where the block structure becomes apparent. The differences in the frame rates between the two city data sets and the two earth data sets result from different grid densities.

As the performance of GPU programs can still be significantly degraded by many conditional code executions, e. g., caused by `if`-statements [36], it is advisable to eliminate branching in dependency on the direction of a ray within the main ray casting loop. An alternative to using `switch`-statements within the ray casting loop as described in section 4.2.2 would be to duplicate the shader code for each of the overall eight possible branches that result from the direction of the ray. This is done, for instance, in [18], and we implemented this technique for test purposes, but we found that the two implementations yield the same performance on the employed graphics hardware.

5 GPU-based DSM Synthesis

In the previous chapter, methods for managing and rendering large DSMs have been presented, but the employed data were previously acquired and static. Our approach is designed to handle DEM and texture data of time-varying extension in order to allow instant updates and rendering, and we can generate these data automatically from aerial photographs by using photogrammetric methods. For this purpose, the source images should be available for processing directly after their acquisition and the DSM creation needs to be as fast as possible.

In this chapter we present a simple GPU-based method for generating DEM data and matching orthophoto textures from multiple vertical aerial photographs. The employed method yields credential results within few seconds and is similar to the approaches presented in [86] and [87]. It relies on a space sweep as presented in [14], and performs the essential steps in the DSM tile generation process in our FCM implementation (see section 3.2.5).

5.1 Methods for Stereo Matching

A dense DEM on a regular grid can be created from a set of aerial images by applying *stereo matching* techniques known from the field of computer vision. According to [76, p. 535], aerial image photogrammetry is the origin of this field of research, and stereo matching is subject of numerous books and publications. A comprehensive summary of the different methods would exceed the scope of this thesis. Hence we confine ourselves to a brief overview of the methods presented in [69] and [76] and describe their basic principles.

Stereo matching usually comprises the processing steps illustrated in figure 5.1 and requires to find regions in the input images, i. e., individual pixels or groups of adjacent pixels, which depict the same points of an object (*features*). In conjunction with the intrinsic and extrinsic camera parameters, the locations within the images allow to calculate the location of the corresponding features in world space (see section 2.5). The distances of these features from the center of projection (CoP) of the containing image are called *depth values* and may be stored in a *depth map*. The depth values of the objects depicted in the input images can be considered as elevations above a plane of reference, and a corresponding depth map can be identified with a digital elevation model (DEM).

As an alternative, the inverse depth of a feature can be computed, because this is frequently a more well-conditioned parameter for cameras [76, p. 49]. The inverse depth of a point in world space is related to its *disparity*, which is the distance between two positions

of that point in a pair of images [76, pp. 539–540]. Analog to depth maps, disparities can be stored in a *disparity map* and are frequently measured in pixels. Depending on the application, depth values and disparities may be referenced to one of the input images used for stereo matching or to an intermediate image of a virtual camera.

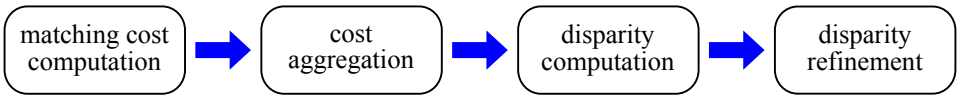

Figure 5.1: *Illustration of the stereo matching process according to [69].*

One method for matching images employs epipolar geometry. Given two images which depict the same object, this method exploits the fact that the same feature depicted in one of the two images is located on the *epipolar line* in the other image (see figure 5.2). This limits the search space where correspondences can be found and thus allows to efficiently find matching features, especially if the images are warped in such a way that epipolar lines coincide with image scan lines (*rectification*). To determine the correspondence for a certain pixel P from image I_1 in image I_2, a *matching cost function* or *error function* C is evaluated at each pixel along the corresponding epipolar line in I_2. C gives a measure of the similarity of pixels, and thus indicates whether the pixels may be related to the same feature. Hence, the pixel with the lowest associated *matching costs* corresponds best to P in I_1, and the pixels are therefore likely to be related to the same feature. By means of the two locations in the two different images, the feature's position in world space can then be computed by using equation (2.13) given in section 2.5.1. More details about epipolar geometry and rectification can be found in [76, pp. 537–540], for instance.

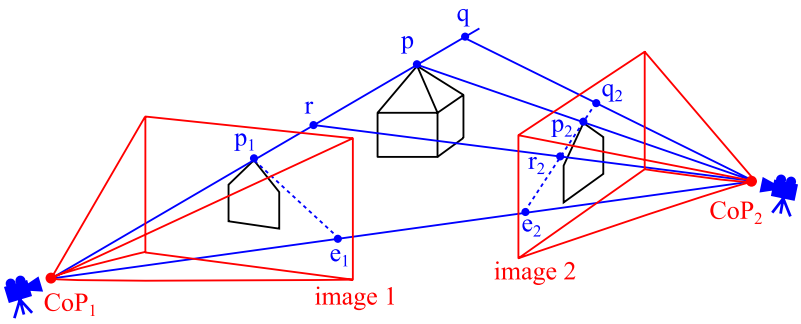

Figure 5.2: *The projection p_2 of point p is located in image 2 on the* epipolar line *(blue, dashed), which starts at e_2 and contains all points on the ray emanating from the center of projection of image 1 (CoP_1) through p, and its projection p_1 in image 1. e_1 and e_2 are the so called* epipoles*, and are given by the intersections of the ray from CoP_1 to CoP_2 with the image planes of image 1 and image 2, respectively.*

Another approach to obtain depth values from a set of two or more images is to choose a plane of reference in world space for measuring elevation, e. g., a plane parallel to one of the image planes or a ground plane, and to sweep the space over a predefined distance by a *sweeping plane*, which is oriented parallel to that plane of reference. Assume that the plane of reference is the xy-plane, and that the sweeping plane is moving along the z-axis.

Each location $r = (r_x, r_y, r_z)$ from a section of interest in the sweeping plane is projected back into the input images by using their associated camera matrices (see section 2.5.1). The similarity between the resulting pixel values for the projections of r into the images is determined by evaluating a matching cost function C as described above. The obtained matching costs at r are stored for the plane's current sweep position. At location (r_x, r_y) in the plane of reference, the z-position z' of the sweeping plane with lowest matching costs then indicates a location in world space for which the related pixels from input images have similar values. Hence, (r_x, r_y, z') is likely the location of the same feature, which is depicted in most of, or even all of the input images. The space sweep[7] approach requires no previous rectification of the input images, and allows to match more than two images [14], [76, p. 559] (see section 5.2).

Finding the minimal matching costs can be achieved in both cases by means of local or global optimization methods. Local optimization methods usually rely on the aggregation of the matching costs over sections (*support windows*) in the disparity image and on choosing the disparity with lowest associated costs. Global optimizations try to optimize an energy function with respect to the costs and some smoothness constraints between the disparities [76, pp. 548–558]. While the latter methods usually yield better results [76, p. 554], the former ones appear to be more appropriate for real-time applications [87]. In image regions with low densities of features, e. g., monochrome or structureless surfaces, and in areas of disparity discontinuities caused by occlusions of the depicted objects, matches are more difficult to find by local methods based on support windows of fixed size and constant shape [41].

Furthermore, if only two images are used for matching, correspondences cannot be detected if a feature is missing or invisible in one of the images. By using $n > 2$ images which depict the same object from slightly different perspectives, better results can be achieved, because more information is available (cf. [76, pp. 558–562]). The results of the matching process may additionally be refined by using robust statistics in order to remove outliers from the resulting set of reconstructed world positions [44]. Another possibility is to cross-check the results of one matching with the results from another matching of the same images, which uses a different image as reference for computing depths respectively disparities [69, 87], [76, p. 550].

5.1.1 Matching Cost Functions

Matching cost functions are a measure of the similarity of two or more values and indicate a likelihood of correspondence [76, p. 546]. The costs can be calculated based on grayscale intensities, intensities for each color component of a pixel, or other photometric quantities, e. g., luminance [76, p. 384]. In order to yield reasonable results from matching cost functions, corresponding pixels in different images must have the same or at least very similar

[7] The *space sweep* is called *plane sweep* in some works from the domain of computer vision, e. g., [76,86,87]. This may not be confused with the term *plane sweep* as used for 2D space sweeps which employ *lines* in order to sweep planes. This latter kind of plane sweep is used, e. g., in the algorithm for computing intersections of 2D line segments as presented in [17, pp. 19–29].

values (*photo consistency*). Usually this requires the depicted object surfaces to be approximately Lambertian, i. e., they need to be ideally diffuse surfaces on which the reflected radiance, and hence the apparent brightness, depends only on the cosine of the angle of irradiance of light. This criterion is not met, for instance, by surfaces showing specular reflections since the reflected radiance depends on the angle of view [1, pp. 110–111].

Let $I_k(u, v)$ denote the pixel value at a discrete location (u, v) in image I_k with $u, v, k \in \mathbb{N}$ and let (u, v) furthermore be valid, i. e., the coordinates are not located outside the image. Given two different images I_0 and I_1, a widespread method is to calculate the *sum of squared differences (SSD)* given in equation (5.1) as a measure of similarity.

$$\mathrm{SSD} = \sum_j \sum_i \left(I_1(i, j) - I_0(i, j)\right)^2 \tag{5.1}$$

The range of the sums for adding up costs depends on the application, but is usually a rectangular region of interest in the images (*support region* or *support window*), or even the entire image. If the two images I_0, I_1 do not have the same size, or if the support windows are located at different positions within the two images, an offset (o_u, o_v) needs to be added to one of the sample positions.

The *sum of absolute differences (SAD)* in equation (5.2) is another popular measure, because of its low computational costs and as it is more robust against outliers [76, p. 384].

$$\mathrm{SAD} = \sum_j \sum_i \left|I_1(i, j) - I_0(i, j)\right| \tag{5.2}$$

Normalized cross-correlation (NCC) as given in equation (5.3) is frequently employed for template matching [34, pp. 869–872] and in the area of signal processing [56, pp. 115–131] for finding similarities between two signals.

$$\begin{aligned} NCC &= \frac{\sum_j \sum_i \left(I_1(i, j) - \bar{I_1}\right)\left(I_0(i, j) - \bar{I_0}\right)}{\sqrt{\sum_j \sum_i \left(I_1(i, j) - \bar{I_1}\right)} \sqrt{\sum_j \sum_i \left(I_0(i, j) - \bar{I_0}\right)}} \\ \bar{I_k} &= \frac{1}{W_k \cdot H_k} \sum_j \sum_i I_k(i, j), \quad k \in \{0, 1\} \end{aligned} \tag{5.3}$$

W_k and H_k denote the width and height of image I_k in pixels, respectively. The values are in $[-1, 1] \subset \mathbb{R}$ where 1 indicates maximal correlation, i. e., highest similarity, and -1 corresponds to total dissimilarity between the two input signals or images. As this measure involves convolution, it is computationally expensive but can be used as well for stereo matching.

More information about matching cost functions can be found, for instance, in [76, pp. 546–548, 384–387].

5.1.2 Cost Aggregation and Support Window Size

Local optimization methods usually aggregate the matching costs over a support window of size $W_x \times W_y$ where $W_x, W_y \in \mathbb{N}$ and $W_x, W_y \geq 1$ [76, p. 548]. A small window size is more likely to produce matching errors, whereas the usage of a large window is less precise, especially if it is placed over areas in an image which contain occluding object boundaries [86]. However, larger windows are accompanied by higher computational costs. As shown in [86], square support windows of power of two sizes for cost aggregation can be efficiently realized by using graphics hardware. By automatically generating mipmaps for each input image, each texel at mipmap level $\lambda \geq 0$ corresponds to a window of size $2^\lambda \times 2^\lambda$. The matching costs can be calculated at different levels and summed up to take advantage of the precision obtained by smaller support windows, and the robustness of larger ones. According to [86–88], large support windows are mainly useful in two-image stereo matching approaches and may not be necessary if multiple images are used. In [33] a comparison of different aggregation schemes is presented, and further methods can be found in [76, pp. 548–551].

5.2 DEM Generation Using Space Sweep

In our application, we obtain DEM values on a regular grid for individual FCM tiles at the base clip level 0 and store them in the DEM layer (see section 4.2.1). For this purpose, we employ a space sweep approach, because it was originally developed in the context of DEM creation from aerial images and appears to be well-suited for this task [14]. The technique is neither restricted to a certain type of input images nor to a particular application of stereo matching, like DEM data generation from aerial images, for instance. Multiple images can be matched without previous rectification and efficient GPU-based implementations can be realized on commodity graphics hardware [87]. It is furthermore possible to sweep the space in multiple directions and to combine the results [30]. A space sweep is also used, for instance, in [32] to obtain an initial depth map in a more complex system for two-image stereo matching.

The space sweep as used in our application is performed as follows: Given a finite set $\{I_0, \ldots, I_{n-1}\}, n \geq 2$ of vertical aerial images which depict the same scene from different points of view, each point of the scene is located at different locations in images I_k, $0 \leq k < n$. Let $M_k = P_k \cdot V_k$ denote the 4×4 matrix composed of the view matrix V_k and the projection matrix P_k of the camera which captured image I_k (see section 2.5.1).

A plane parallel to the xy-plane is moved along the z-axis, where $l \in \mathbb{N}$ and $0 \leq l \leq L$. L is determined for some predefined height resolution Δz by equation (5.4). z_{min} and z_{max} with $z_{\text{min}} \leq z \leq z_{\text{max}}$ may be chosen according to the underlying surface, e. g., if the minimum and maximum elevations are known.

$$L = \left\lceil \frac{z_{\text{max}} - z_{\text{min}}}{\Delta z} \right\rceil \in \mathbb{N} \tag{5.4}$$

In this way, we yield a series of $L+1$ planes Π_l at discrete locations $s_z = l \cdot \Delta z + z_{\text{min}}$ along the z-axis. Let (s_x, s_y) denote a position on a rectangular regular grid with spacing (g_x, g_y) based in the xy-plane. Each discrete sample position $s = (s_x, s_y, s_z)$ is projected into the image plane of each image I_k according to equation (2.6) in section 2.5.1 by using M_k in order to obtain its 2D image coordinates (u_k, v_k). The corresponding pixel value is denoted by $p_k = I_k(u_k, v_k)$ and is probably the result of some sort of interpolation, e. g., bilinear interpolation or nearest neighbor sampling, because s will normally not be mapped to integral pixel positions.

For simplicity, assume that s is not projected outside the boundaries of any image I_k, i. e., all p_k are valid, and that p_k is furthermore a single scalar value like grayscale intensity or luminance. The matching costs $C_k(s)$ for each p_k are calculated according to equation (5.5) as the SAD of p_k and all other values p_i.

$$C_k(s) = \sum_{i=0}^{n-1} |p_i - p_k| \tag{5.5}$$

Since in case of $i = k$ the difference $(p_i - p_k)$ is zero, it does not contribute to the costs and hence does not require any special treatment. The aggregated costs $AC(s)$ in equation (5.6) at sample position s on the current plane Π_l are obtained as the sum of the matching costs $C_k(s)$ for all n images, i. e., the sum of sum of absolute differences (SSAD) for all p_k.

$$\begin{aligned} AC(s) &= \sum_{j=0}^{n-1} C_j(s) = \sum_{j=0}^{n-1} \sum_{i=0}^{n-1} |p_i - p_j| \\ &= \sum_{j=0}^{n-1} \sum_{i=0}^{n-1} |I_i(u_i, v_i) - I_j(u_j, v_j)| \end{aligned} \tag{5.6}$$

In equation (5.6), the costs for matching two pixel values p_k and p_i are summed twice, because $|p_i - p_k| \equiv |p_k - p_i|$. But since we only need to compare the relative costs between image pixels, and since the costs are duplicated for all of them, this duplication does not have any negative effect on the matching process itself[8].

If the corresponding surface is approximately Lambertian, the projection of the same feature from world space into the different images I_k should result in very similar pixel values p_k and the residual error $(p_i - p_j)$ should be almost zero. The plane $\Pi_{l_{\text{best}}}$ containing the best correspondence between the pixels from all images at position (s_x, s_y) in the xy-plane is then given by

$$l_{\text{best}} = \underset{0 \le l \le L}{\arg\min}\, AC(s_x, s_y, l \cdot \Delta z + z_{\text{min}})$$

and the resulting DEM height value is $z_{\text{DEM}} = l_{\text{best}} \cdot \Delta z + z_{\text{min}}$.

[8] Equation 5.6 is in fact convenient for our GLSL implementation, because the corresponding `for`-loops are of fixed lengths and may hence be unrolled by a GLSL compiler, if n is constant.

5.2.1 Input Image Selection

The images employed for DSM creation by stereo matching are returned by the 3D spatial index of the FCM by means of an intersection query (see chapter 3.2.5). If the images are all vertical images, their projections according to the associated camera matrices M_k will be located on the sweeping plane. But oblique aerial images may also be stored in the spatial index and will be returned by a intersection query as well. These images can be easily removed from the set of input images by means of the viewing direction of their associated cameras, so that they are not taken into account for DEM layer generation. However, further changes to the set of input images may be necessary in the following situations:

1. the projection of an image onto the sweeping plane does not overlap the projection of any of the remaining images
2. there are more input images than texture units or video memory available

We call an image which suffers from the first problem a *non-overlapping image* in contrast to an *overlapping image* whose projection onto the sweeping plane has non-empty intersection with at least one other image. As the outlines of these projections are all convex quadrilateral polygons, an image can be identified as non-overlapping if its corresponding polygon does not intersect the polygon of any other image from the set. The intersection test is best performed with image projections on the sweeping plane at z_{min}, i. e., near the ground plane, because the projected areas become smaller as the sweeping plane moves towards the CoPs of the images. Non-overlapping images are removed from a set of input images since they are not suited for stereo matching.

The second situation arises if n images are available, but only $N < n$ textures can be processed at a time by the fragment program. This problem can be solved by splitting the set of input images into multiple sets of $\leq N$ images and by performing the space sweep multiple times per FCM tile at clip level 0, each time with a different subset of images, but without clearing the render targets between the passes.

However, the images need to be redistributed with respect to the mutual overlap of their projections onto the sweeping plane. Otherwise, the resulting subsets might suffer from large numbers of non-overlapping images. These subsets do not need to be disjoint, since an image may be suited for stereo matching with other images that are non-overlapping. This situation is illustrated in figure 5.3 where $n = 3$ images are given, but only $N = 2$ images may be matched at a time. Such layouts of images are the normal case in traditional aerial photography [42, pp. 144–145] and these situations should hence be manageable in our approach. Therefore, we unfortunately cannot simply create a partition of a set of $n > N$ images into $\left\lceil \frac{n}{N} \right\rceil$ disjoint sets.

In order to distribute n images among a number of sets of $N < n$ images, we propose the following proceeding:

For each image I_k, the area of intersection $A_{k,i}$ of its projection with that of another image I_i is computed and stored in a look-up table. The intersection can be obtained by

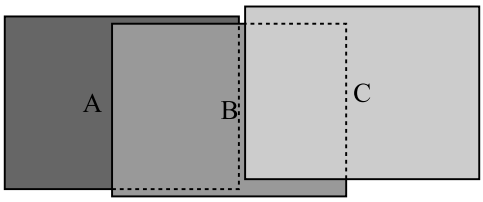

Figure 5.3: *The projection of image B overlaps the ones of images A and C, but A and C are non-overlapping. If only $N = 2$ images can be processed at a time, the two image sets $\{A, B\}$ and $\{B, C\}$ with the common element B must be created.*

clipping the respective bounding polygons against each other, for instance, by using the Sutherland-Hodgman algorithm [29, pp. 124–126]. If $A_{k,i}$ is not empty, the polygon which results from clipping is convex and in particular simple, because it is the intersection of two convex polygons (cf. [17, p. 46, pp. 66–70]). The area A_{poly} of a simple polygon can be calculated according to equation (5.7) where $\chi \geq 3$ is the number of vertices, (s_i, t_i) the respective Cartesian vertex coordinate and $s_\chi = s_0, t_\chi = t_0$.

$$A_{\text{poly}} = \frac{1}{2} \sum_{i=0}^{\chi-1} |s_i t_{i+1} - s_{i+1} t_i| \tag{5.7}$$

A derivation of the formula in equation (5.7) and a proof of its correctness can be found in [58, pp. 20–22], for instance. A series of not necessarily disjoint sets S_j of images is created where each S_j may contain at most N elements. First, all images I_k are marked as `UNUSED`, e. g., by using an array of boolean values indexed by k. Starting with $j = 0$, each S_j is then constructed as follows: An arbitrary image $I_{k'}$, which has not been marked as `USED`, because it has not yet been inserted into any previously created set $S_i, i < j$, is added to the empty set S_j and becomes marked as `USED` afterwards. From the look-up table, successively those images with the largest area of intersection with image $I_{k'}$ are determined in decreasing order and are added to S_j until either $|S_j| = N$, or no more images overlapping $I_{k'}$ which are marked as `UNUSED` are left. The overlapping images are added to S_j regardless of their markers, but are marked as `USED` afterwards. This process is repeated until all images are marked as `USED`. Sets with $|S_j| \leq 1$ are discarded and will not be used as input for DEM generation, since they only contain a single image and thus cannot be used for stereo matching. As the area of intersection of an image I_k with another image can be determined from the look-up table, it is also possible to ignore images whose amount of overlap with $I_{k'}$ is below a certain threshold.

The process described above is guaranteed to terminate after at most n iterations, because during each iteration at least one image becomes marked as `USED`. If we set $N = n$, the algorithm can be used furthermore to remove not sufficiently overlapping images from a set of input images for stereo matching. Although this redistribution of images does no longer allow to compute the matching costs between all n input images, it will create sets of images in which the images have large overlaps and are thus likely to depict the same objects.

5.3 GPU-based Implementation

Our implementation of the space sweep method described in the previous section is similar to the one presented in [87] and relies on OpenGL and GLSL, but employs more modern graphics hardware features. In particular, OpenGL pixel buffers (*P-buffers*) have been superseded by so called *frame buffer objects (FBOs)* which essentially perform the same task of redirecting rendering output into textures in video memory (*render targets*). Since we use multiple input images for matching, we also adopted the idea of using only a certain number of images with lowest matching costs for aggregation, as it is presented in [41]. The resulting DEM and color texture data are stored in the corresponding layers of a single FCM tile at the lowest clip level as described in section 4.2.1 and can be used directly for rendering.

5.3.1 Program Setup

In order to use the GLSL program as described in the next section, it is necessary to set up a virtual orthographic camera which is oriented perpendicular to a rectangular quadrilateral mesh (*quad*). The quad represents the sweeping plane based in the xy-plane in world space and its only purpose is to generate input fragments for the fragment shader at known z-coordinates. Its size is set to $(S_x, S_y) = \left(\frac{T_x}{\mathrm{res}_x}, \frac{T_y}{\mathrm{res}_y}\right)$ where (T_x, T_y) is the size of a single FCM tile in texels and $(\mathrm{res}_x, \mathrm{res}_y)$ denotes the desired resolution of the resulting DEM layer in texels per unit along the respective axis.

The range $[z_{\text{min}}, z_{\text{max}}]$ for the space sweep along the z-direction is obtained by setting $z_{\text{min}} = H_{\text{min}}$ from the box that is associated with the root node of the R*-tree of the FCM (see section 3.2.5). To ensure that z_{max} is not located above any of the CoPs of the employed images, it is set to a value which is somewhat smaller than the smallest of all z-coordinates of the CoPs. If the maximum height H_{max} of the underlying surface is known, z_{max} may also be set to $z_{\text{max}} = H_{\text{max}}$. The number of required rendering passes is equal to the number $L + 1$ of discrete plane positions on the z-axis and is calculated according to equation (5.4) for a desired height resolution Δz.

The z-position of the quad varies from z_{min} to z_{max} and must be located inside the frustum of the virtual orthographic camera. This camera is placed at $\left(\frac{S_x}{2}, \frac{S_y}{2}, (z_{\text{max}} - z_{\text{min}}) + 1\right)$ and looks along the negative z-axis. It is oriented such that its up-vector u and right-vector r are aligned with the y- respectively x-axis as illustrated in figure 5.4; its orthographic projection matrix P_{ortho} is given in equation (5.8).

$$P_{\text{ortho}} = \begin{pmatrix} \frac{2}{S_x} & 0 & 0 & -1 \\ 0 & \frac{2}{S_y} & 0 & -1 \\ 0 & 0 & \frac{2}{z_{\text{max}} - z_{\text{min}}} & -1 \\ 0 & 0 & 0 & 1 \end{pmatrix} \tag{5.8}$$

The input images I_k that contribute to the DEM layer of the FCM tile with index (n_x, n_y) and their associated 4×4 camera matrices M_k are retrieved from the spatial index of the

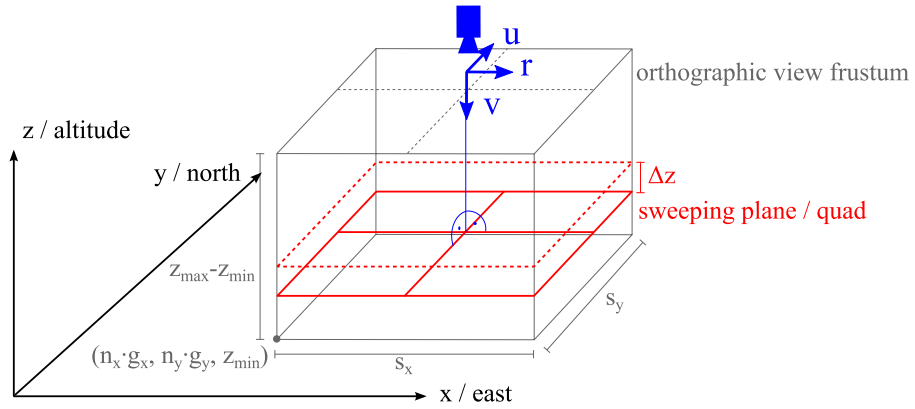

Figure 5.4: *In order to perform a GPU-based space sweep, a virtual orthographic camera is oriented as shown and looks perpendicular onto the center of a quad in order to generate the input fragments for a GLSL shader which calculates DEM values from multiple images.*

FCM as described in section 3.2.5. Images are accessed by the fragment program as textures and may be stored in a texture array of n elements, if they are of the same lateral sizes. The matrices M_k are passed to the shader as the elements of a uniform array of n elements of GLSL data type `mat4`. Both kinds of input data for the shader remain associated with each other by their common index k. Since arrays in fragment programs need to be of fixed size, a `#define` preprocessor directive with the total number N of input images which can be processed at the same time is inserted before the GLSL shader source code. In this way, N is made a constant value within the fragment program, which permits the static allocation of arrays of size N. The number $n \leq N$ of actually employed images is provided as uniform variable.

The camera positions in M_k are referenced to absolute world coordinates. Therefore, the minimum corner $(n_x \cdot g_x, n_y \cdot g_y, z_{\text{min}})$ of the box Q in equation (3.4), which is used to query the spatial index of the FCM, is added to the position of the camera and to the vertices of the quad.

5.3.2 Program Execution

All rendering output is redirected into a frame buffer object (FBO) that matches the predefined FCM tile size in texels. The FBO contains at least one color texture in R8G8B8 or R8G8B8A8 texel format and one *depth texture* in F32 texel format for storing Z-Buffer values.

In each of the $L+1$ rendering passes for the different plane positions at $z = l \cdot \Delta z + z_{\text{min}}$ where $0 \leq l \leq L$, the fragment program must be provided with the texture coordinates (u_k, v_k) for sampling image I_k at each fragment that results from the rasterization of the quad. For efficiency reasons, a vertex program generates homogeneous coordinates $(\hat{u}_k, \hat{v}_k, \hat{z}_k, \hat{w}_k)$ directly from the vertex coordinates (x, y, z) of the quad according to equation (5.9).

$$\begin{pmatrix} \hat{u}_k \\ \hat{v}_k \\ \hat{z}_k \\ \hat{w}_k \end{pmatrix} = \begin{pmatrix} \frac{1}{2} & 0 & 0 & \frac{1}{2} \\ 0 & \frac{1}{2} & 0 & \frac{1}{2} \\ 0 & 0 & \frac{1}{2} & \frac{1}{2} \\ 0 & 0 & 0 & 1 \end{pmatrix} \cdot M_k \cdot \begin{pmatrix} x \\ y \\ z \\ 1 \end{pmatrix} \tag{5.9}$$

These n values are stored in an array indexed by k and are automatically interpolated across the surface of the quad as the array is transferred from the vertex to the fragment program. The normalized texture coordinates (u_k, v_k) for sampling input image I_k are obtained by component-wise division of $(\hat{u}_k, \hat{v}_k)$ by $\hat{w}_k$ in the fragment program:

$$(u_k, v_k) = \left(\frac{\hat{u}_k}{\hat{w}_k}, \frac{\hat{v}_k}{\hat{w}_k} \right)$$

Since the sample positions (u_k, v_k) have to be accessed multiple times within the fragment program, they are computed only once at the beginning of the program and stored in a global array indexed by k. The values sampled from image I_k are usually RGB triples $p'_k = (R_k, G_k, B_k)$ and are converted into grayscale luminance values p_k in CIE XYZ color space[9] according to equation (5.10).

$$p_k = 0.212671 \cdot R_k + 0.715160 \cdot G_k + 0.072169 \cdot B_k \tag{5.10}$$

The numerical constants in equation (5.10) depend to a certain degree on the physical properties for rendering color spectra of the video output device, i. e., the monitor or projector, and are given in [1, p. 215]. The corresponding matching costs C_k are computed for each of the resulting p_k according to equation (5.5) and are stored at index k in an array of size n. Instead of computing the aggregated matching costs according to equation (5.6) by summing up all n values, we may choose to take only the best $\tilde{n} = \left\lfloor \frac{n}{2} \right\rfloor$ of the images into account for matching. This modification has been proposed in [41] in the context of selecting images from a temporal sequence as *better half sequence* and is intended to disregard images in which a feature is occluded. Therefore, the array of matching costs can be sorted in the fragment program, e. g., by using selection sort or insertion sort, and only the $\tilde{n}$ lowest matching costs may be summed up.

In order to find the minimum matching costs and to select the corresponding DEM values, we employ the method presented in [87] which utilizes the Z-Buffer of the graphics hardware. Since we use FBOs, the Z-Buffer values are redirected into the attached depth texture. The current position z of the plane along the z-axis in world coordinates is emitted by the shader as the fragment color, whereas the aggregated matching costs are explicitly assigned to the Z-Buffer value of the fragment. z is available at the vertex coordinates of the quad in the vertex program and is passed on to the fragment program for this purpose. The employed Z-Buffer test is set up to select the fragment with the lowest Z-Buffer value at the current sweeping plane position. In this way, in each rendering pass, i. e., at each different location z of the sweeping plane in space, depth and color values in the FBO are successively replaced by values of new fragments if the new Z-Buffer values emitted by the

[9] CIE is the abbreviation for "Commission Internationale d'Eclairage".

shader are smaller than the existing ones, and the matching costs at the current fragment are thus lower. After $L + 1$ rendering pases, the color texture attached to the FBO contains the elevation values for the area covered by the FCM tile and the data are copied from video memory into the DEM layer of the tile.

A problem arises in parts of a FCM tile which are covered by only a single image so that no matching costs can be computed. We therefore determine at each fragment the number of covering images by checking whether each coordinate pair (u_k, v_k) is within the valid range $[0, 1] \times [0, 1]$. If the coverage is below a certain threshold $TR \in \mathbb{N}, TR \geq 2$, the aggregated matching costs AC for this fragment are set to ∞. Before emitting color and depth values, the shader checks AC and discards fragments if AC is ∞. In this case, neither Z-Buffer nor color values will be generated and any existing data in the FBO will remain unaffected.

5.4 Color Texture Generation

In orthophotos distortions caused by perspective effects are corrected and lateral surfaces, like frontages of buildings, are intentionally not depicted. Orthophotos can be used, for instance, to create or enhance a variety of maps for different applications [42, pp. 410–411]. Moreover, they are employed as color textures in our DSM rendering approach as presented in chapter 4. The generation of an additional orthophoto texture of the same resolution in texels as the DEM layer of a certain tile can be integrated into the previously described DEM creation process. The resulting proceeding is essentially the same as the one outlined in [42, pp. 425–426].

The extension for generating an additional color texture merely requires the fragment shader to output a second color value at each fragment into an additional color texture. This texture should have R8G8B8 or R8G8B8A8 texel format and must be attached to the FBO. Instead of storing only the matching costs C_k in an array, a pair (C_k, k) is stored in order to keep track of the associated image index k. After the array has been sorted in ascending order of C_k, the index of the image with the lowest matching costs k_{min} is stored at the first pair in the array. The RGB value $p'_{k_{\text{min}}}$ from the corresponding image $I_{k_{\text{min}}}$ at sample position $(u_{k_{\text{min}}}, v_{k_{\text{min}}})$ is assigned to the additional fragment color output. Afterwards, these data are copied from video memory to the tile, and the color layer is created in the same way as the DEM layer. As an alternative, the $n' \leq n$ images with lowest matching costs may be sampled, and the component-wise mean of the obtained RGB values may be used to determine the color layer value. Figure 5.5 shows a comparison of the results of these two methods for generating orthophoto textures.

If a region of the tile is covered by only a single aerial image, no elevation data can be derived, and it is in general impossible to determine objects in the input images that are affected by perspective, e. g., skyscrapers, tall trees or mountains. In this case, it may be desirable to rely on using the only available image and to create a color texture layer which is not orthographic, instead of providing no color information at all. Such a texture can be created in a single rendering pass by executing the process for orthophoto texture

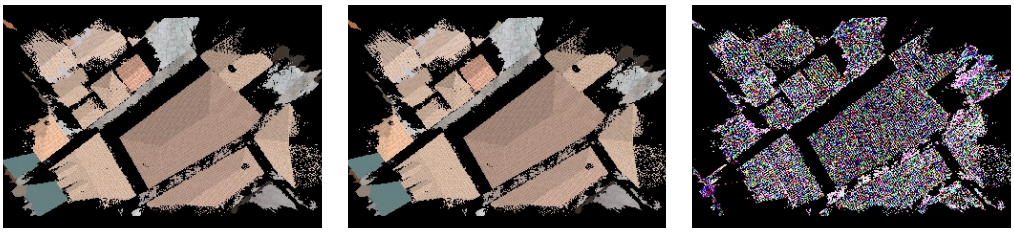

(a) *minimal matching costs* **(b)** *averaged color values* **(c)** *difference image*

Figure 5.5: *A comparison of an orthophoto texture generated by using pixels from the input images with lowest matching costs (left), and by component-wise averaging the color values of the input images (middle). Locations where no DEM data are available remain black. Due to the input data, the differences of the color values are very small and are illustrated in the contrast enhanced difference image (right).*

generation described above only once and by projecting all images onto the quad located at $z = z_{\text{min}}$. In regions where only a single image is available, the sampled color values determine the final color at the corresponding texel in the color texture. If the projections of multiple images overlap, it is possible to use the pixels from one or more images with lowest matching costs. Other possibilities to handle the overlap of multiple pixels at one texel of the color texture are, for instance, blending, averaging or overwriting. Since the perspective distortion of objects depicted in an image increases with their distances from the geometric center of the image, ambiguities at a single texel may also be resolved by using the pixel with smallest geometric distance from the center of its image. These five different possibilities are illustrated in figure 5.6 and have different properties.

Averaging multiple pixels results in severe ghosting and creates fuzzy results. Since the fuzziness tends to increase with the elevation of the underlying surface, this effect might even be useful for visualizing the uncertainty about the elevation in the DSM in regions where no height information could be derived from the input images. Blending multiple pixels tends to blur the results and does not solve the problem of mismatching borders between different images. Considering the minimal matching costs in the plane at $z = z_{\text{min}}$ causes the resulting color texture to look speckled and unclean. Allowing different pixels to overwrite each other is the simplest solution, but also results in mismatching borders and depends on the order of the images (cf. section 3.2.5). Choosing the pixel with smallest distance from the respective center of its image does not eliminate this problem, but has an interesting effect: lateral faces, e. g., like frontages of buildings, tend to vanish in the resulting color texture, and the resulting texture looks almost orthographic in some regions. Since the latter method creates clear images and reduces the amount of lateral surfaces depicted in the resulting texture, we prefer it over the other methods if we have to create non-orthographic color textures.

It is also possible to initialize a color texture layer by means of one of these non-orthographic creation processes and to successively replace values with those obtained during DEM creation. In this way, we can create a color texture layer which provides color information where available, but which is furthermore truly orthographic in regions where DEM data are available.

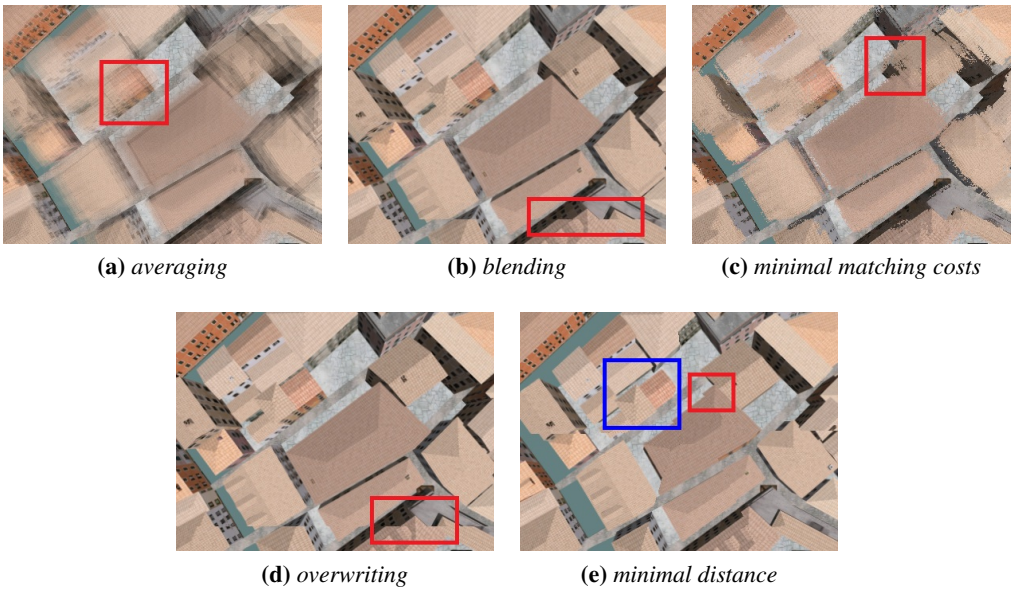

(a) *averaging* **(b)** *blending* **(c)** *minimal matching costs*

(d) *overwriting* **(e)** *minimal distance*

Figure 5.6: *Different methods for resolving ambiguities caused by projecting multiple pixels from different images to one texel in order to create a planar color texture, if no elevation information is taken into account. Properties specific to the methods are highlighted by red and blue rectangles.*

5.5 Improvements of DEM Quality and Results

With the methods for creating DEM data and matching color textures as described above, we can rapidly create all layers of single FCM tiles. Although accuracy is important in our application, we strive for the generation of *credential* DSM data at high speed and therefore do not additionally refine the resulting DEM data by means of statistical analysis for removing outliers, for instance. In the following, we discuss the influence of different improvements for enhancing the quality of the resulting DEM data.

5.5.1 Stereo Matching Errors

As shown in figure 5.7(b), some isolated DEM layer texels exhibit faulty dents or spikes during rendering while their neighboring texels are correct. These outliers may emerge from errors during stereo matching or from ambiguous matching costs and the cost selection by using Z-Buffer tests. In principle, there should be no difference if the space sweep described in section 5.2 starts at z_{min} and the sweeeping plane is moved up to z_{max}, or if the sweeping order is reversed and goes from z_{max} down to z_{min}. But due to the Z-Buffer test, there can be visible differences in the resulting DEM if the matching costs at a fixed image position (u_k, v_k) are equal for two or more different sweeping plane positions. As the Z-Buffer test is set in such a way that only fragments with smaller Z-Buffer values are allowed to replace texels in the render target, the first of a number of different DEM values with equal matching costs will determine the final texel value. If the sweeping plane is moved along the

positive z-axis, faults in the DEM caused by ambiguous matches may show up in renderings as dents respectively spikes, if the sweeping is performed along negative z-direction. An alteration of the Z-Buffer test to let fragments with less or equal matching costs pass would correspond to a reversal of the space sweep order, because the final texel value would then be determined by the last of a number of DEM values with equal matching costs. These stereo matching related errors can be resolved by taking more different images into account in order to obtain unique and better matching costs for each plane position at each single fragment.

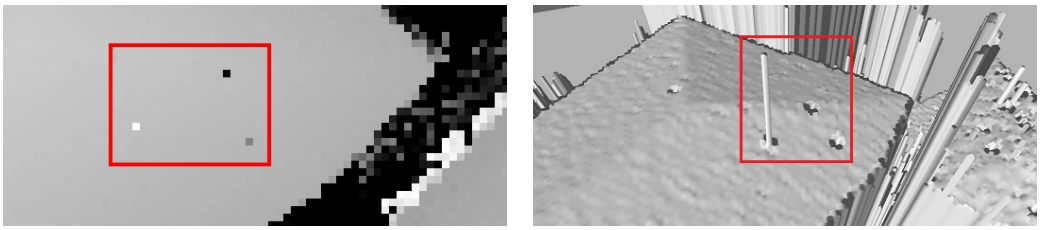

(a) *DEM layer* **(b)** *resulting rendering*

Figure 5.7: *Incorrect results from stereo matching or ambiguous matching costs result in faulty DEM layer texels which become apparent as spikes or dents in renderings as highlighted by the red rectangles. Contrast enhancement was applied to the depicted DEM layer (left) in order to visualize faulty texels. Brighter colors correspond to higher elevations.*

The presence of ambiguous matches may be additionally favored by the kind of employed aerial images. Since we do not yet have a reliable source for providing aerial images as required in our application (cf. section 2.3.3), we create synthetic data from 3D renderings of a virtual city model which has been generated by the software "CityEngine" [24]. The objects depicted in the images are quite artificial, because the underlying 3D models employ only a very limited amount of textures, especially on roofs and frontages, so that lots of repetitive patterns can be found in the renderings. These repetitions can easily lead to equal matching costs for single DEM texels on the sweeping plane at different z-coordinates.

5.5.2 Smoothening DEM Data

Since stereo matching errors and ambiguities may also arise in real-world data, e. g., in image regions depicting large, monochrome and structureless surfaces, we experimented with smoothening the DEM data before they are copied into the corresponding tile layer. For this purpose we use a rather simple technique which utilizes automatic mipmap generation capabilities of graphics hardware and bilinear interpolation.

By enabling automatic mipmap generation for the textures attached to the FBO, the texture data at mipmap level λ correspond to the result of a convolution of the original texture with a box-shaped filter kernel of size $2^\lambda \times 2^\lambda$. If the texture at $\lambda > 0$ is copied back from video memory, we obtain a down-scaled version of the required DEM layer. This smaller version is scaled afterwards by using re-sampling and bilinear filtering in order to get a texture of the original size. As a result, the texture becomes blurred and this technique

is therefore also used in GPU image processing for creating certain effects [1, p. 471]. In this way, we achieve a replacement of DEM texels by averaged values that incorporate neighboring texels and dents and spikes are less prominent as shown in figure 5.8. However, potentially correct edges at steep elevations will be smoothened as well and turn into ramps. This effect is illustrated in figure 5.9 by means of a DEM of an isolated cube obtained from synthetic images.

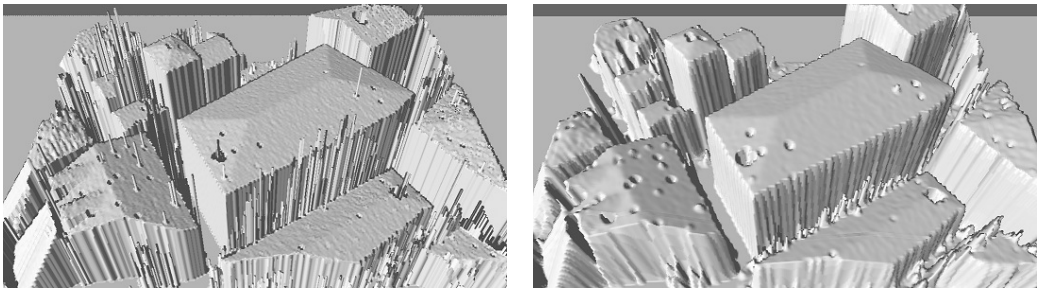

(a) *no smoothening at mipmap level* $\lambda = 0$ **(b)** *smoothening at mipmap level* $\lambda = 1$

Figure 5.8: *Smoothening DEM textures levels incorrect spikes and dents and makes the resulting renderings visually more appealing. The visual effect of defects in the DEM is enhanced by applied shading and lighting.*

With the data employed in our application, we found the usage of smoothening by copying DEM textures at mipmap level $\lambda = 1$ to be a reasonable compromise. Using more sophisticated and adaptive methods for compensating defects would probably further improve the resulting DEM data.

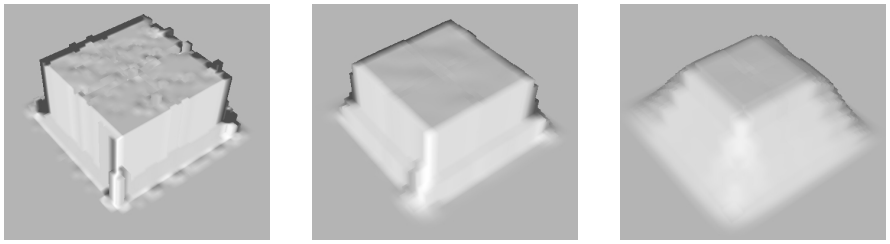

(a) $\lambda = 0$ **(b)** $\lambda = 1$ **(c)** $\lambda = 2$

Figure 5.9: *Smoothening DEM textures by means of simple GPU-based blurring results in an unwanted transformation of edges at steep elevations into ramps.*

5.5.3 Cost Aggregation Over Support Windows

We also implemented the possibility of aggregating matching costs over support windows having power of two size by using mipmaps which are automatically generated by graphics hardware for each input image [86, 87]. For this purpose we compute the matching costs at sample position $s = (s_x, s_y, s_z)$ by means of $C'_k(s)$ from equation (5.11) for a given range

of mipmap levels $[\lambda_{\text{min}}, \lambda_{\text{max}}]$ instead of using $C_k(s)$ from equation (5.5).

$$C'_k(s) = \sum_{\lambda=\lambda_{\text{min}}}^{\lambda_{\text{max}}} \sum_{i=0}^{n-1} |p_i(\lambda) - p_k(\lambda)| \tag{5.11}$$

In equation (5.11), $p_j(\lambda) = I_j(u_j, v_j, \lambda)$ denotes the luminance value which results from sampling image I_j at mipmap level λ at position (u_j, v_j). The aggregated matching costs $AC(s)$ according to equation (5.6) are then calculated by using $C'_k(s)$ instead of $C_k(s)$ in equation (5.5).

With the data in our application, we found that matching cost aggregation over support windows significantly improves the visual quality of renderings of the resulting DEMs, and comparative results are given in section 5.6. However, if the size of the support windows becomes too large, features are missing as illustrated in the resulting DEM renderings in figure 5.10. We found the cost aggregation over support windows up to sizes of 8×8 completely sufficient for our kind of input images.

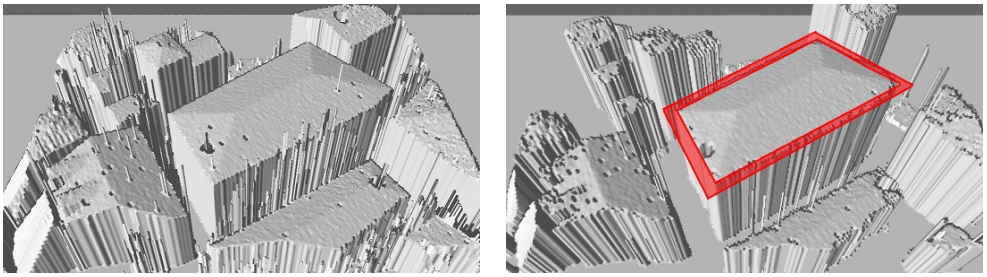

(a) *support window size* 8×8 **(b)** *support window size* 64×64

Figure 5.10: *Using support windows larger than* 8×8 *for cost aggregation results in DEMs where features are missing. In the right image, for instance, the sizes of the roofs are reduced.*

5.5.4 Better Half Sequence

Our implementation also allows to consider only the $\lfloor \frac{n}{2} \rfloor$ input images with lowest matching costs for aggregation (*better half sequence*) [41]. For this purpose, we sort the matching costs of the input images within the fragment program in increasing order by means of a simple selection sort implementation. Figure 5.11(a) shows a rendering of a DEM generated by using the better half sequence method, whereas figure 5.11(b) shows a rendering of a DEM generated by using all images for matching cost aggregation. Both DEMs were created from the same eight input images and costs were aggregated over support windows up to size 8×8. The visual differences are small, but with the employed input images, the results obtained by using all input images for matching cost aggregation depict fewer defects in some regions, e. g., on the side of the main building which is closest to the viewer.

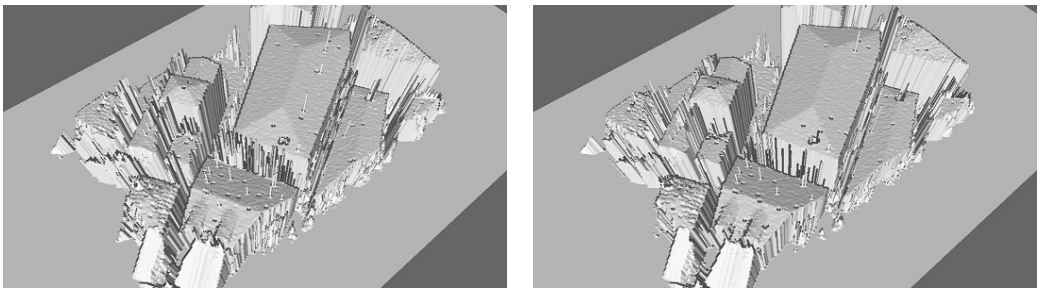

(a) *better half sequence* **(b)** *all images*

Figure 5.11: *A direct comparison of renderings of DEMs of an urban area created from the same set of eight input images, but by using two different matching cost aggregation schemes. The costs were aggregated over support windows of sizes up to* 8×8*.*

5.6 Performance Evaluation and Discussion

The performance and the quality of the output data depend in particular on the number of employed images and the chosen height resolution Δz of the space sweep. Table 5.1 contains exemplary performance results for creating the DEM and color layers of 2×2 neighboring FCM tiles at clip level 0, which were all covered by the same employed images. The results were obtained on a desktop computer with an Intel i7 860 CPU at 2.8 GHz, 6 GB RAM, NVIDIA GeForce GTX 470 graphics adapter with 1280 MB dedicated video memory and Windows 7 OS. The input images had a size of 1920×1080 pixels, and we obtained results for different numbers of images and support window sizes. Column *max. support window size* indicates the maximum size of the support window for cost aggregation according to equation (5.11). The values in table 5.1 are given in seconds and include the time for transferring the images from main memory to video memory. The tile size was set to 512×512 texels and the sweeping plane was moved from $z_{\text{min}} = 0$ to $z_{\text{max}} = 25$ at a step width of $\Delta z = 0.125$ units. This corresponds to $L = 200$ and thus 201 different plane positions and rendering passes. We furthermore measured the runtime using matching cost aggregation of all available images, and the runtime when using better half sequences, i. e., only the $\left\lfloor \frac{n}{2} \right\rfloor$ images with lowest matching costs contribute to cost aggregation. The tile creation was executed in parallel to a process for directly rendering the resulting DEMs. Renderings from the run in which all images were taken into account during cost aggregation are shown in figure 5.12.

5.6.1 Discussion

Table 5.1 shows that the runtime increases with the number of employed images, but the quality increases as well as can be seen in figure 5.12. The additional costs for the aggregation over several support window sizes are moderate, but in case of these particular input images, using support windows significantly increases the quality of the resulting DEMs, even if the number of images increases. As expected, the runtime is higher in case of using

Figure 5.12: *Renderings of the DEMs which were created during a performance evaluation for different numbers n of input images and support window sizes. The depicted DEMs were created by using all images for cost aggregation. The resulting DEM data were not smoothened and shading was applied to enhance the perception of defects, such as spikes and dents.*

max. support window size	all images				better half			
	n = 2	n = 4	n = 6	n = 8	n = 2	n = 4	n = 6	n = 8
1×1	2.32	3.03	4.01	4.90	2.48	3.39	4.65	5.86
2×2	2.20	3.14	4.10	5.07	2.45	3.55	4.74	6.06
4×4	2.38	3.18	4.36	5.23	2.56	3.94	5.09	6.14
8×8	2.26	3.43	4.34	5.49	2.72	3.78	5.11	6.55

Table 5.1: *Performance results of an exemplary DSM synthesis from up to eight different images at different numbers of input images, maximum support window sizes and matching costs aggregations. The values are given in seconds.*

better half sequences for cost aggregation, because it requires the GPU program to sort the aggregated matching costs, and we used a non-optimized selection sort implementation for this task. However, the runtime of the configurations given in table 5.1 was always dominated by the costs for transferring the input images into video memory, which took more than 50% of the total time. Therefore, much more time was required for creating the first of the 2×2 tiles than for creating the remaining three tiles, since they were generated from the same input images. After the input images were transferred to video memory, the creation of one of the remaining tiles never took more than 0.025 seconds. Figure 5.12 furthermore shows that using only two input images is insufficient in our approach. Reasonable results require at least $n = 6$ images and preferably the cost aggregation over support windows of sizes up to 8×8.

The quality of the DEMs which we can generate by means of the method presented in this chapter also depends strongly on the chosen height resolution Δz as shown in figure 5.13. Both DEMs were created from the same eight images and matching costs were aggregated over support windows up to size 8×8, but the DEM in figure 5.13(a) exposes less defects.

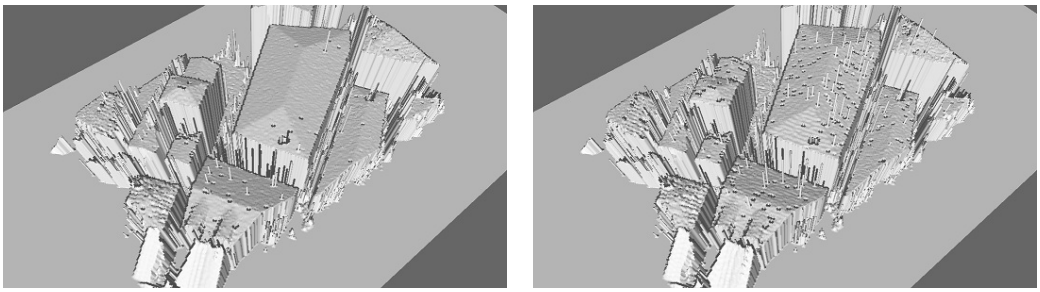

(a) $\Delta z = 0.125$ **(b)** $\Delta z = 0.25$

Figure 5.13: *The chosen height resolution Δz of the space sweep strongly influences the quality of DEMs which can be generated by means of the method presented in this chapter. Both DEMs were created from the same eight input images and use the same support window size of 8×8 without smoothening.*

The DSM creation was executed in parallel to the DSM rendering process on the same computer with a single graphics adapter, and the hardware resources were hence shared between the two processes. We can therefore expect an increase of the performance of the mere DSM creation, if it is executed standalone with exclusive access to the graphics

hardware resources. It is also important to note that all of our results presented in this section were obtained by employing synthetic aerial images. Real images have different properties and would suffer from noise, different illumination conditions, lens distortions and other optical phenomena. The eight input images which were used for creating DEMs of the urban area as presented in this thesis were captured at altitudes from ≈ 78.0 to 95.32 units and are shown in figure 5.14.

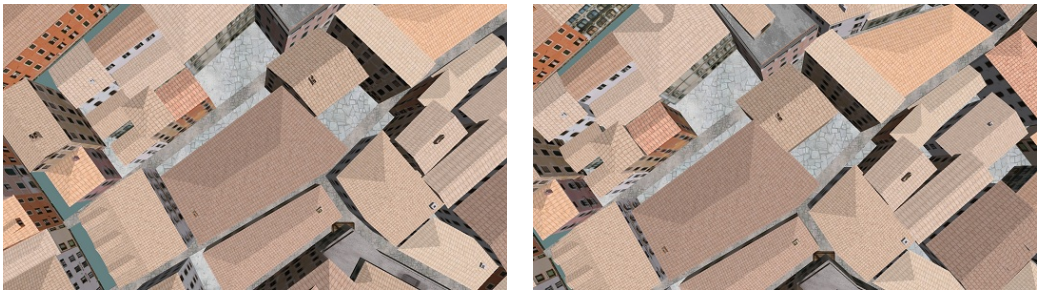

(a) *image 1*

(b) *image 2*

(c) *image 3*

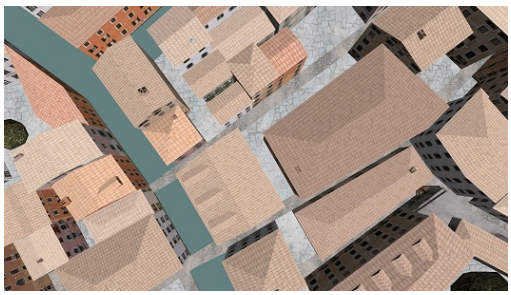

(d) *image 4*

(e) *image 5*

(f) *image 6*

(g) *image 7*

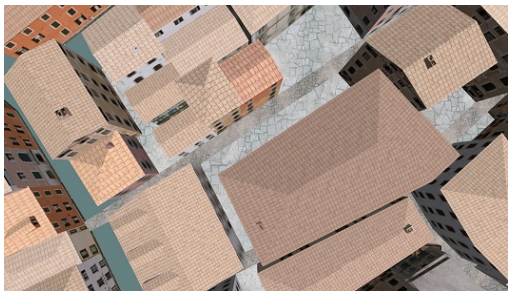

(h) *image 8*

Figure 5.14: *These eight synthetic aerial images at an original resolution of* 1920×1080 *pixels were used to create all DEMs of the urban area as presented throughout this chapter. The depicted city model was created by means of the software "CityEngine" [24].*

6 Texturing Lateral Surfaces

In the previous chapters, we dealt with DSMs that do not contain any color information about *lateral surfaces*, i. e., the faces of elevations which are not parallel to the ground plane. We only employed orthophoto textures derived from vertical aerial photographs, but these images provide no color information about lateral surfaces. Such surfaces, like walls of canyons or frontages of buildings may become visible in renderings of DSMs in virtual 3D environments, and the viewer might expect to see structural details, e. g., different rock layers or windows and doors. Therefore, it is common practice to employ oblique aerial images to overcome this lack of information.

In this chapter, we extend our rendering technique as presented in chapter 4 in order to add color information to lateral surfaces of a DSM. This extension directly employs vertical and oblique aerial images, and benefits from rendering by means of ray casting.

6.1 Complete Color Textures for DSMs

In computer graphics, color information about surfaces is frequently stored in rectangular 2D color textures. Surfaces and *texture space* are usually parametrized by *normalized texture coordinates* $(u, v) \in [0, 1] \times [0, 1] \subset \mathbb{R}^2$. Normalized texture coordinates allow to conveniently transform locations on the surface into texture space and vice versa, independent of their respective physical extensions. Some geometric bodies, like rectangles, spheres or cylinders, possess parametric representations that can be directly used as texture coordinates. If a polygonal mesh is used to represent a surface, the texture coordinates are often given for the vertices of the mesh and interpolated across the associated mesh faces. This method is frequently used if no parametric representation of the surface is available, or in conjunction with manually modeled meshes of complex objects. In some situations, texture coordinates can be computed directly on the GPU from vertex positions, e. g., as described in section 5.3.2.

A simple way to create a color texture of $T_u \times T_v$ texels for a surface with a given parametrization (u, v) is to create a piece-wise linear approximation of the surface by using rectangular patches. These patches are aligned to the tangential planes of the surface at equally spaced distances $\frac{1}{T_u}$ and $\frac{1}{T_v}$ in u- respectively v-direction. Each patch is assigned the color value of the underlying part of the surface and is identified with a texel of the texture. In areas where the piece-wise linear approximation and the sampling rates $\frac{1}{T_u}$ and $\frac{1}{T_v}$ are insufficient, the texture will expose distortions. Figure 6.1 illustrates the creation process of a texture on a sphere and the resulting distortion.

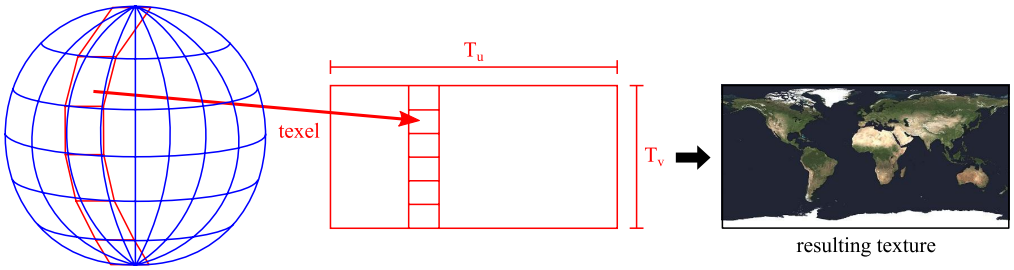

Figure 6.1: *Mapping the surfaces of geometric bodies onto a planar rectangle in order to create a texture can result in distorted images, especially in regions where the approximation by rectangular patches is insufficient, e. g., as in the case of a sphere. Towards the poles, the illustrated image of the Earth's surface is increasingly distorted.*

Orthophoto textures, as employed in our approach, are obtained from a parametrization of the *ground plane* of the underlying DEM, which is a planar rectangular surface. In order to store color information about a complete surface of a DEM in a single texture, the surface has to be parametrized with respect to its elevation. Depending on the range of the elevation, such a texture can require substantially more samples than the corresponding DEM, since the surface area can be much larger than the one of the ground plane. This is illustrated in figure 6.2. Furthermore, the total surface area must be computed in order to find an appropriate texture size (T_u, T_v) and to normalize the parametrization.

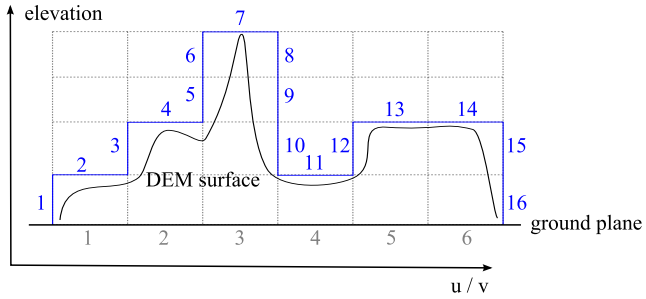

Figure 6.2: *Storing color information about the entire surface of a DEM, including lateral surfaces, may require the creation of large textures. The depicted elevation of the surface, which is illustrated in profile, is sampled at six positions (gray numbers), whereas the entire surface is larger and is sampled at 16 positions (blue numbers).*

Since we strive for fast generation of DSMs, which may in addition change frequently, storing the entire surface in a single texture would be inefficient, and we therefore map colors onto lateral surfaces by means of projective textures.

6.2 Aspects of Projective Texturing

Projective textures can be thought of as virtual video or slide projectors. They can be used to assign color values to surfaces based on an object's position in world space instead of its surface parametrization as described in the previous section. During rendering, the color

values of the corresponding screen pixels are determined by the texels which become projected onto the surface. We already used this approach in chapter 5 in the context of stereo matching by means of a space sweep where aerial images are projected onto the sweeping plane. Another application of projective textures is, for instance, the implementation of complex light effects in virtual environments [1, p. 222]. Shadow mapping uses a similar concept for determining the visibility of locations on a surface from the position of a light source [1, pp. 348–353].

In order to use projective texturing on a DEM, we project oblique aerial images onto lateral surfaces, and vertical aerial images onto surfaces which are parallel to the ground plane. Only images depicting parts of the DEM surface which are currently visible to the viewer in a 3D virtual environment need to be employed as textures. Hence, the selection of aerial images which are appropriate for projective texturing depends on the orientation and position of the virtual camera representing the viewer. The best rendering results can be achieved by projecting images which were captured at positions and with orientations similar to the ones of the virtual camera, because these images are likely to depict the objects which are about to be rendered.

In the context of projective texturing, we call the associated camera of an aerial image $I_k, k \in \mathbb{N}$ *projector* and the *projector matrix* is the camera matrix $M_k = P_k \cdot V_k$, where V_k denotes the camera's view matrix and P_k the projection matrix.

6.2.1 Aerial Image Selection

In our approach, we store all aerial images according to the bounding boxes of the view pyramids of their associated cameras in the spatial index of our FCM implementation (cf. section 3.2.3).

The spatial index assists in selecting aerial images which are appropriate for texturing a DEM as follows: An axis-aligned bounding box (AABB) Q is computed for the view frustum F of the virtual camera in order to perform an intersection query on the spatial index. Thus, images with projectors which are not entirely contained inside Q, but whose frustums may intersect Q are also retrieved. Since Q has usually a larger volume than F, the resulting set of aerial images $S = \{I_0, I_1, \dots I_{n-1}\}$ may contain many elements that are not well-suited for projective texturing. These are in particular all images whose orientations and positions of their associated projectors deviate too much from the ones of the virtual camera. Figure 6.3 illustrates in 2D the relationships of the virtual camera and the projectors, as well as their frustums and the bounding boxes.

Let φ_k denote the angle enclosed by the viewing direction of the projector of an aerial image I_k and the viewing direction of the virtual camera. We remove all images from the initial set S of aerial images for which $|\varphi_k| > \Phi_{\text{max}}$ where $0 < \Phi_{\text{max}} < \frac{\pi}{2}$ is a user-defined threshold. Projectors with $|\varphi_k| \geq \frac{\pi}{2}$ can only depict back sides of objects from the current point of view. The projectors of the remaining images in the modified set S' and the virtual camera thus have similar orientations.

Like with stereo matching, the total number N of projective textures which can be used at a time is limited by the amount of available video memory or the number of texture units

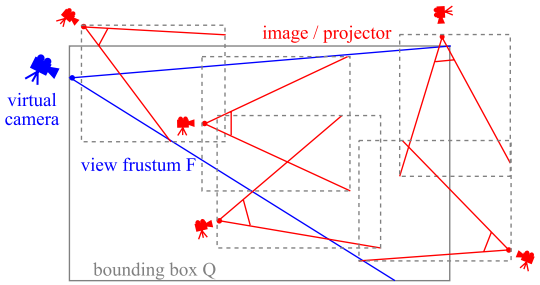

Figure 6.3: *The bounding box Q (gray, solid) of the virtual camera's view frustum F (blue) is used to query the spatial index which stores the aerial images (red) according to the bounding boxes of their view pyramids (gray, dashed).*

(cf. section 5.2.1). Therefore, if the modified set S' of aerial images contains $n' = |S'| > N$ elements after the removal of the aforementioned images, it must be reduced further. Since we want to use images whose projectors are located close to the virtual camera, we sort the images according to the distances d_k of their CoPs from the CoP of the virtual camera. Except for those N images with smallest d_k, we remove all other images from the set S'.

In summary, our algorithm for finding a set $\tilde{S}$ of aerial images which can be used for projective texturing, where $|\tilde{S}| = N$, is as follows:

1. Create AABB Q from the frustum F of the virtual camera.
2. Retrieve from the spatial index of the FCM the set $S = \{I_0, I_1, \ldots, I_{n-1}\}$ of all aerial images having projectors with frustums whose AABBs intersect Q.
3. For each $I_k \in S$, determine the angle φ_k enclosed between the viewing direction of the projector and the viewing direction of the virtual camera.
4. If $|\varphi_k| > \Phi_{\text{max}}$, remove I_k from S.
5. If the modified set S' contains $> N$ elements, sort the elements according to the distances d_k from the CoPs of their associated projectors to the CoP of the virtual camera.
6. Except for those N images with smallest d_k, remove all other images from S' and obtain $\tilde{S}$.

6.2.2 Occlusions Between Lateral Surfaces

Locations on the DEM surface, which are occluded from the point of view of a projector by other elevations as illustrated in figure 6.4, are not visible within the corresponding image. Projecting occluded points on the DEM surface back into images that do not depict them might yield a valid texture coordinate, but the resulting color values must not be used for computing the color at the corresponding screen pixel. This is the same problem as determining the visibility of a point in a scene from the position of a light source in order to render shadows by means of shadow mapping [1, pp. 348–353]. Hence, a solution to

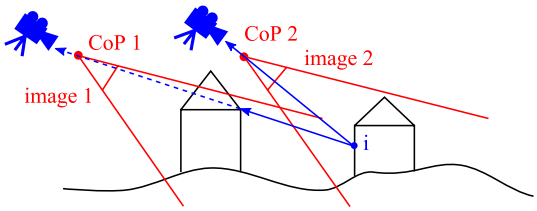

Figure 6.4: *Locations on a DEM surface can be occluded by elevations and may hence not be visible in all projected images. In the depicted situation, i is visible in image 2 but not in image 1, because it is occluded by an elevation. Image 1 depicts the front of that occluding elevation at the corresponding pixel, but not i.*

this problem is the following proceeding: The scene is rendered from the perspective of the projector, and the depth values of locations on the DEM are stored in a depth image, which is called *shadow map* in the context of shadow mapping. When the scene is rendered from the viewer's perspective, locations on the DEM surface that are visible to the viewer are projected into the depth map. If the depth value of a certain location is greater than the value that is stored in the depth map, it is considered invisible from the projector's perspective. The scene needs to be rendered only once per projector and the resulting depth map can be stored and reused.

With our DSM rendering approach, this technique requires one complete ray casting pass per projector, and the depth maps need to be regenerated each time the underlying DEM changes, if new elevation data become available. The video memory consumption is increased by one additional depth map per projected image. In addition, the quality of depth maps depends on their resolution and the technique may expose inaccuracies due to aliasing. More details on the subject of shadow mapping can be found in [1, pp. 348–372], for instance.

Since we use ray casting for DSM rendering, for a projected image I_k the visibility of intersection i of a ray with the DEM surface can be determined by casting a second ray from i to the CoP of I_k. This secondary ray casting can be performed by using the same ray traversal scheme as presented in section 4.2.2. If the second ray intersects the DEM on its way to the CoP, i is not visible in I_k. This method is potentially costly as it requires to cast up to n additional rays for each fragment, where n is the number of projected images. However, the projectors which can definitely not depict i according to their orientations and distances from i and from the virtual camera, can be ignored, and the number of secondary rays may be reduced.

6.2.3 Multiple Projections

A point i on a DEM surface can be depicted in multiple projected images as illustrated in figure 6.5. In this situation, the image whose associated projector is closest to i is probably the best choice for sampling color values, since it potentially depicts more details of the object than images which were captured from greater distances. Furthermore, i is more likely occluded by other elevations in images whose CoP is located at larger distances from i, than in images having CoPs located closer to i.

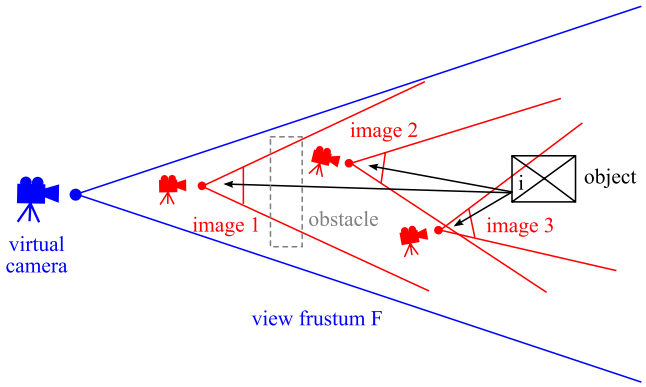

Figure 6.5: *If a point i on a DEM surface is visible in multiple images, the image closest to i (image 3, red) is probably the best choice for determining the final color value at i in the virtual scene, because this image is likely to depict the most details. i may furthermore be occluded in images captured at larger distances (image 1) by an obstacle (gray, dashed), which can be part of the scene that is depicted in those images.*

The image $I_{k'}$ whose CoP is closest to i, can be determined by a fragment program as follows: Let d_k denote the distance from the CoP of image I_k to i. i is projected from world space into each of the images I_k by means of its associated projector matrix. If the resulting 2D image coordinates of the projection of i are contained in the plane section of image I_k, i may be visible in I_k. Image $I_{k'}$ is then determined as the image which contains the projection of i and has the smallest distance $d_{k'}$ among all images containing the projection of i. In order to compute the distances d_k on the GPU, the positions of the CoPs of the projected images can be passed to the fragment program.

6.3 Implementation and Results

Projective texture mapping is implemented by the GLSL fragment program for DSM ray casting as described in chapter 4. The set of aerial images which is used for projective texturing is determined by the application each time the point of view of the virtual camera is modified according to the image selection algorithm presented in section 6.2.1. The images are sorted according to the distances d_k of their respective CoPs from the virtual camera in increasing order, and are provided to the ray casting shader as an array of textures. In addition, the projector matrices and the CoPs of the projected images are passed to the fragment program as uniform arrays of data type `mat4` and `vec3`, respectively. This is the same proceeding which is used to pass vertical aerial images and camera matrices to our GPU programs for stereo matching as presented in chapter 5.

After the intersection i of a ray with the DEM has been determined by ray casting, the fragment program computes the texture coordinate at each fragment for each projected image I_k. If the coordinates are not within the range $[0,1] \times [0,1] \subset \mathbb{R}^2$, the corresponding image is not considered for computing the color value of the fragment. Otherwise, the squared distance ${d_k}^2$ from i to the projector's CoP is computed. If ${d_k}^2$ is the current minimum of all squared distances from i to the CoP of the projected texture I_k, the current

minimum is updated and the sampled color value is assigned to the fragment, but only if the fragment is not occluded in I_k. To determine whether i is not occluded in I_k by any elevation of the DEM surface, we use secondary ray casting from i towards the CoP of I_k.

The GLSL source code of the complete implementation can be found in appendix A in listing A.2 in lines 874 to 917.

6.3.1 Results

Figure 6.6 gives an example of a DSM rendering using projective textures. The maximum enclosing angle between the viewing directions of the associated cameras and the virtual camera was set to $\Phi_{\text{max}} = \frac{\pi}{4}$, and the image projections were confined to areas where elevation data are present.

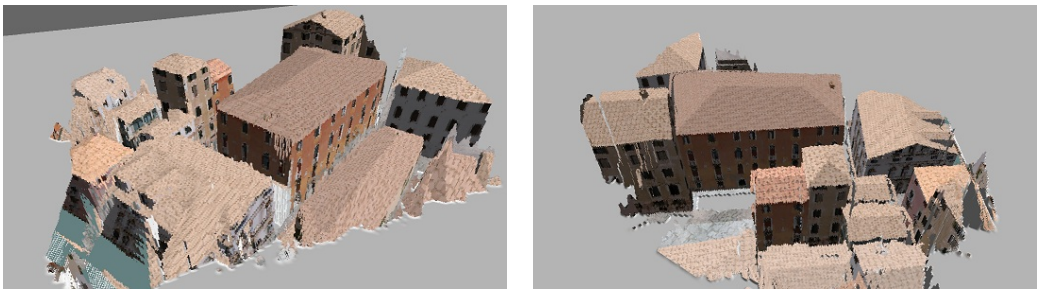

(a) $n = 3$ **(b)** $n = 2$

Figure 6.6: *Examples of renderings of a DEM of an urban area with applied projective textures. The DEM was synthesized from the eight vertical aerial images in figure 5.14, and n oblique aerial images of sizes 1920×1080 pixels were used as projective textures in the depicted scene.*

The performance of our projective texturing approach depends on the number of projected images and the accompanying number of secondary rays that need to be casted in order to test for occlusions. On a computer with the configuration given in section 5.6, we observed during several runs with different DEMs and up to eight active projectors a decrease of the rendering frame rate of about 20% to 50%. However, the frame rate did not drop below interactive rates, even at screen resolutions of 1920×1080 pixels. Furthermore, we observed that the additional color information on lateral surfaces can help to conceal defects in DEMs (see section 5.5.1). An illustration of this effect is shown in figure 6.7.

6.4 Discussion

Using the original aerial images as projective textures in order to provide color information on lateral surfaces of a DEM has several advantages. By employing projective textures, we neither have to create nor to store additional textures, and the set of employed aerial images can be altered without having to update the corresponding DSM layer. The latter aspect is especially important, because our application targets at fast DSM creation from potentially frequently changing sets of images. If a DSM consists only of a DEM layer,

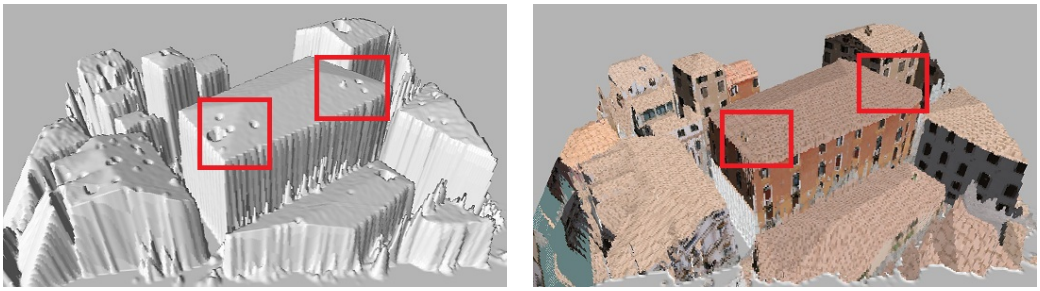

(a) *untextured DEM (shaded)* **(b)** *three projected images*

Figure 6.7: *Applying projective textures to a DEM can conceal defects such as dents or spikes (left), which result from stereo matching errors.*

video memory is not occupied by an additional color texture layer and thus remains available for projective textures. A comparison of DEM renderings using orthophoto textures and by using projective textures is shown in figure 6.8. The six oblique aerial images which were used for projective texturing throughout this chapter are shown in figure 6.9.

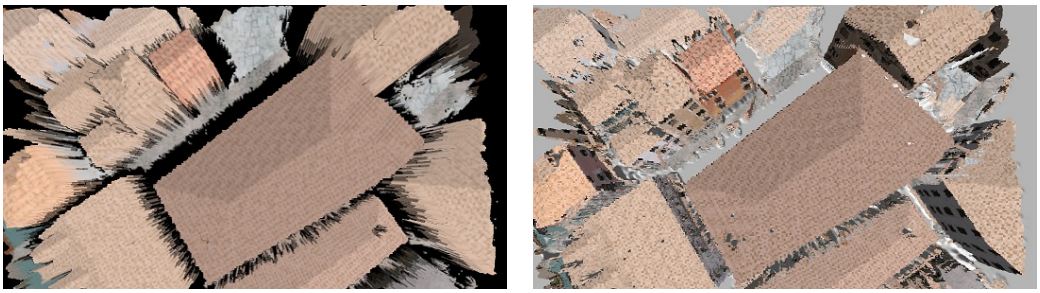

(a) *orthophoto texture* **(b)** *six projective textures*

Figure 6.8: *A comparison of a rendering o the same DEM rendered only with applied orthophoto textures (left), and by using six projective textures, but no orthophoto textures (right).*

The set of projective textures for rendering a scene depends on the viewer's current perspective and must be updated as the virtual camera moves. Transferring large amounts of data from main memory to video memory, however, temporarily degrades the performance of the rendering process. Since the original aerial images may be too large for being directly used as appropriate projective textures, it can be necessary to downscale the images in advance.

We can also enable automatic mipmap generation by graphics hardware for the employed projective textures and compute an appropriate mipmap level for sampling color values. The mipmap level computation can be integrated into the ray casting process, similar to the calculation of clip level l_{opt} which is used for ray termination (see section 4.2.3). In this way, our implementation can provide a simple level-of-detail concept for texturing lateral DEM surfaces.

Although the performance of the technique presented in this chapter appears to be sufficient for our purposes, more detailed investigations might reveal further possibilities for optimization.

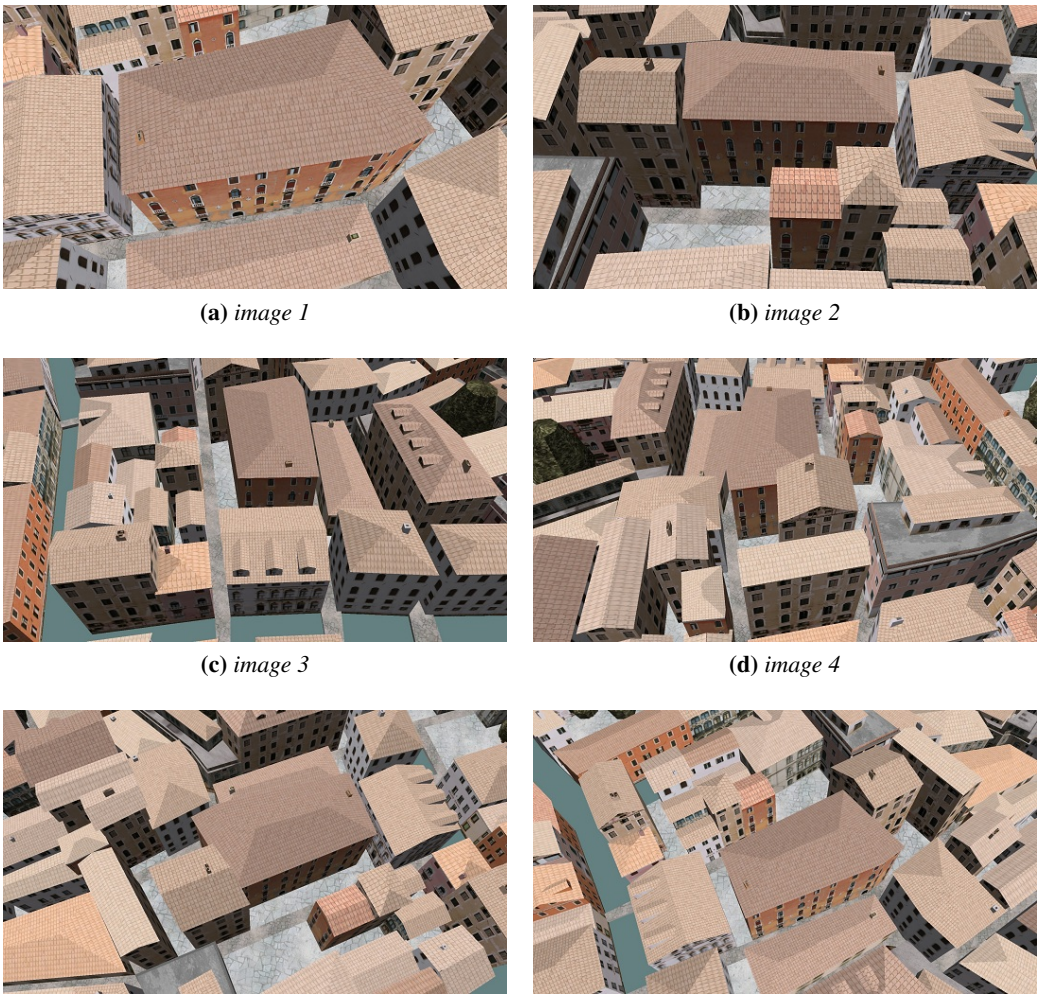

(a) *image 1* **(b)** *image 2*

(c) *image 3* **(d)** *image 4*

(e) *image 5* **(f)** *image 6*

Figure 6.9: *The depicted six oblique aerial images of original sizes of* 1920×1080 *pixels were used for projective texturing on the DEM of an urban area. The DEM was derived from the images shown in figure 5.14 according to the method presented in chapter 5.*

7 Framework Design

In this chapter we present the design and important implementation details about the framework which implements the methods for rendering and generating DSMs as presented in this thesis. The framework is implemented in C++, rendering relies on OpenGL 3.2 and GPU programs (*shaders*) written in GLSL version 1.5. Section 7.1 gives an overview about the organization of the framework, followed by details about the implementation of our Flexible Clipmap in section 7.2. Our implementation of the employed R*-tree is described in section 7.3. Important aspects of the design and the implementation of the two GPU programs for rendering and generating DSM data are presented in section 7.4. This chapter concludes with a brief discussion about further implementation details in section 7.5.

The UML diagrams presented in this chapter are given in UML 2 notation. The names of classes, methods, functions, variables or other programming language constructs are highlighted by using a typewriter font. In favor of readability, we usually omit the parameter lists of methods and functions, but their names are followed by a pair of opening and closing parentheses, e. g., `method()` or `function()`.

7.1 Framework Overview

Our framework is structured by packages as shown in the UML package diagram in figure 7.1. The packages categorize the contained classes and functions according to their domains, and each package corresponds to a C++ `namespace`.

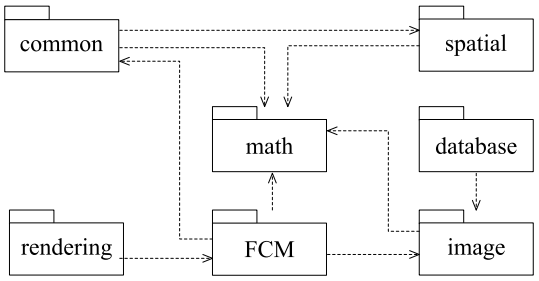

Figure 7.1: *Our framework is structured according to the depicted packages which contain C++ classes and functions for different purposes. Arrows indicate dependencies among the packages.*

In detail, these domains are as follows:

common
This package contains classes and functions for general tasks, e. g., providing base classes

for threads or for asynchronously reading and writing of files.

database
The components from this package provide access to the database management system in order to retrieve and store aerial images and associated metadata.

FCM
Components related to our FCM implementation, like classes for handling tiles, tile layers and caching, are placed in the `FCM`-package.

image
The `image`-package contains classes for processing 2D raster images, i. e., bitmaps, and includes classes and functions for reading and writing different image file formats. In addition, basic image processing functionality for bitmap images of different pixel formats has been implemented and placed in this package.

math
Classes and functions representing mathematical objects and operations, e. g., vectors, matrices and quaternions, are placed in the `math`-package. These classes and functions are used by numerous other components from other packages. For the remainder of this chapter, we avoid to explicitly reference this package in favor of readability.

rendering
This package contains classes for DSM rendering tasks and GPU computations for the stereo matching process (see section 5.3).

spatial
We implemented versatile C++ class templates for the R*-tree and a point kd-tree in order to use these data structures with arbitrary data types for keys and values in 2D and 3D. These two kinds of spatial indexes together with common class templates for geometric primitives like points and boxes are contained in the `spatial`-package.

Due to requirements in the AVIGLE project, we need to access OpenGL via the open source rendering engine "Irrlicht" [38]. We had to add several features available in OpenGL to the engine, e. g., support for 3D textures and GLSL 1.5, because Irrlicht does not support these features at the time of writing this dissertation. Rendering is therefore performed by accessing components of the Irrlicht engine instead of directly calling OpenGL API functions. Classes in our framework which utilize the rendering engine are designed to isolate code which is specific to this engine, and are placed in the `rendering`-package. These classes are prefixed by the letters `Irr`, and usually inherit from an abstract base class which may be from a different package, such as `FCM` or `common`.

7.2 Flexible Clipmap Implementation

The Flexible Clipmap is implemented by several classes and class templates in the `FCM`-package. Figure 7.2 shows the relationships between the most important classes. Attributes and methods, as well as nested classes, some base classes from other packages, enumerations and auxiliary structures, are omitted in favor of clarity.

In our application, an FCM tile is represented by the class `LayeredTile` and may contain up to k layers (see section 4.2.1), but different applications may require different types of FCM tiles. We therefore reduced the dependency of FCM's components related to tiles on a specific type of tile by using C++ templates and by providing an unspecific base class `Tile`. The layers of a tile are represented by the class `TextureTileLayer`, which inherits from the abstract base class `TileLayer`, and class `Image` from the `image`-package. `Cacheable` provides an interface for any kind of data which need to be transferred asynchronously from secondary to main memory, and keeps track of the current location of cached data in main and secondary memory, e. g., FCM tiles and tile layers. While color texture layers are directly handled by the `TextureTileLayer` class, DEM layers are handled by the subclass template `DEMTileLayer`, which additionally stores the maximum and minimum elevation value of its contained data. These values are determined once as the DEM data are loaded or created. The template parameter of `DEMTileLayer` must be set according to the data type of the desired texture format, e. g., `BYTE` for I8 or `float` for F32.

Caching of FCM tiles should work in the same way for all kinds of tiles, hence the template parameter for instantiating the C++ class templates `TileCache`, `TileArray` and `TileLevelCache` must be a subclass of `Tile`. A `TileCache` maintains one `TileLevelCache` object, which in turn maintains L `TileArray` objects, where L denotes the current number of clip levels of the FCM. `TileArray` objects are 2D arrays for storing $c_x(l) \cdot c_y(l)$ tiles from the clip area of the FCM at an associated clip level l in main memory (see section 3.3.2). Class `TileLevelCache` implements the FCM's *tile level cache* as described in section 3.3.2 and contains one `TileArray` object per clip level. The `TileLevelCache` object and its contained `TileArray` objects are resized if the number of clip levels changes. An instance called `LayeredTileCache` of the `TileCache` class template for caching `LayeredTile` objects in our application is obtained via an appropriate C++ `typedef`.

Asynchronous access to secondary memory for loading and writing tile layers is controlled by the class `TileCache`, but is executed by an internally maintained `FileStorage` object. The class `FileStorage` inherits from the abstract class `Thread` class from the `common`-package and executes code in its own thread. In this way, potentially slow accesses to secondary memory do not overly obstruct the execution of other components. Details about the components which are executed in parallel are presented in section 7.2.1.

The numerous parameters for instantiating a `FlexibleClipmap` object, e. g., sizes of the clip area and the active area, tile size and descriptions of the employed tile layers, are combined in the `FCMSettings` structure. `TileLayerDescriptor` objects describe the different tile layers employed by `LayeredTile` objects by providing a collection of the

Figure 7.2: *Overview about the relationships of the most important classes in the FCM-package. Attributes and methods, as well as some less important references to classes from other packages are omitted in favor of clarity.*

properties of the layers, such as texel formats and storage locations in secondary memory, i. e., file system paths and folder names. `TileLayerDescriptor` objects are maintained by instances of `FCMSettings` structures, and are copied to an instance of the `TileLayerConfiguration` class which implements the software engineering design pattern *Singleton* [31, pp. 157–166]. The C++ enumeration `LayerIndex` provides symbolic constants for accessing the different layers of FCM tiles.

The class `FCMState` is responsible for keeping track of the state of the FCM and in particular of its current number of clip levels L. State changes of the FCM are usually triggered by a `TileCreator` object, and are propagated to other components by means of callback objects, which are not depicted in figure 7.2. A `TileCreator` object is responsible for creating new FCM tiles and updating existing ones by means of a `LayerCreator` object, as soon as new aerial images and associated metadata become available. The class `LayerCreator` implements the methods for creating DSM data presented in chapter 5. For this purpose, an instance of this class monitors the `AerialImageIndex` Singleton. The latter maintains an appropriate instantiation of the `RTree` class template, and provides methods for image retrieval. `RTree` is an implementation of the R*-tree by Beckmann et al. [6] by means of C++ class templates and is explained in detail in section 7.3. Since the creation of tiles should not obstruct ongoing rendering, the class `TileCreator` inherits from class `Thread`, so that the creation of tiles is executed in its own thread. Furthermore, the creation of additional tiles directly affects the state of the FCM and its cache. Hence, related `TileCreator` and `FlexibleClipmap` instances need to share the same `FCMState` and `TileCache` objects in order to access the data of FCM tiles in a consistent way.

The classes `TileUpdateSchedule` and `TileUpdateJob` both inherit from more general classes from the `common`-package and are responsible for organizing the order of execution of updating and creating tiles as described in section 3.3.3. Aerial images are delivered to the `AerialImageIndex` Singleton concurrently by an `AerialImageCollector` object. This object also executes code in a separate thread and monitors changes on the database. The communication between the different classes in response to changes of the state of the FCM due to the arrival of new aerial images is explained in detail in section 7.2.2.

Client applications that utilize our FCM implementation need to create one object each of the classes `FCMSettings`, `FlexibleClipmap` and `TileCreator`. An `FCMSettings` object can be created conveniently from FCM configuration settings stored in an XML file. Such an object is the only parameter required by the constructor of class `FlexibleClipmap`. A `TileCreator` object is only required if the FCM needs to handle DSM data of time-varying extension. In order to render a static DSM, the `FCMSettings` object can provide a fixed size for the FCM.

7.2.1 Multithreading

Our implementation makes use of multithreading in order to not overly obstruct the main process which is primarily engaged in rendering at real-time frame rates. The support for

multithreading depends on the operating system, and specific code is isolated in our implementation by the abstract base class `Thread` as shown in figure 7.3.

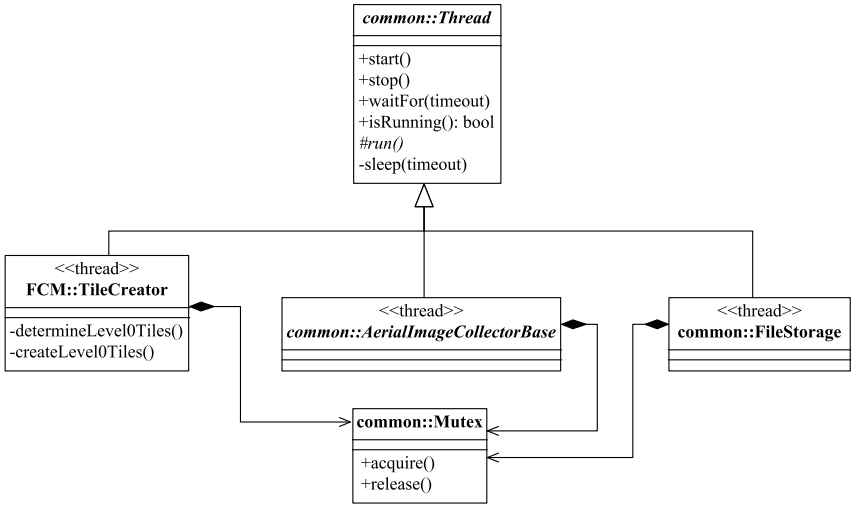

Figure 7.3: *UML class diagram of classes in our FCM implementation which execute code in separate threads. The class `Mutex` is used for synchronizing access to shared code and data via mutual exclusion.*

A class which inherits from class `Thread` must implement the method `run()`. Code within this method is executed in its own thread, as well as the code of other methods which are called directly or indirectly by `run()`. The execution of a thread is initiated by calling `start()` and terminates as soon as `run()` has finished. If a thread needs to run until its termination is explicitly requested by another thread, calling method `stop()` sets an internal state which causes the method `isRunning()` to return `false` on subsequent calls. Hence, loops within the method `run()` should exit if the termination of the thread is requested, so that `run()` can terminate. An example of how to implement such a loop in a fictional class `MyClass` which inherits from `Thread` is given in listing 7.1.

```
1 void MyClass::run()
2 {
3   while (isRunning())
4   {
5     // ...
6   }
7 }
```

Listing 7.1: *Example of an implementation of a loop within the `run()` method of the fictional subclass `MyClass` of class `Thread`. The code within this method is executed in its own thread.*

The method `waitFor()` provides a simple synchronization of `Thread` objects. A caller of `waitFor()` passes a timeout period as parameter and is blocked until either the timeout period expires or the thread terminates. Hence, this method should never be called from method `run()` or any other method of the same object in order to avoid deadlocks. A `Thread` object can be suspended from execution for a given timeout period by calling the

method `sleep()` from the object's `run()`-method or any other method that is directly or indirectly called by `run()`, without causing any deadlock.

Multiple threads may need to access the same methods and data of the same objects, and hence need to be synchronized in order to prevent memory access violations. In our application, we control the access to shared data and code by means of simple mutual exclusion, which is implemented by the `Mutex` class and depends on the operating system.

In the following, we discuss details about the three subclasses of class `Thread` which are shown in figure 7.3, because these classes enable the usage of our FCM implementation for rendering while image acquisition and DSM generation are executed in parallel.

Class `FileStorage`

The class `FileStorage` provides access to secondary memory, because the other threads, e. g., the main thread for rendering, should not be blocked by potentially slow file access operations. Instead of accessing files themselves, other threads can delegate this task to a `FileStorage` object which maintains a queue of `FileStorageOperation` objects as shown in figure 7.4. Classes such as `BitmapImage2D` from the `image`-package can

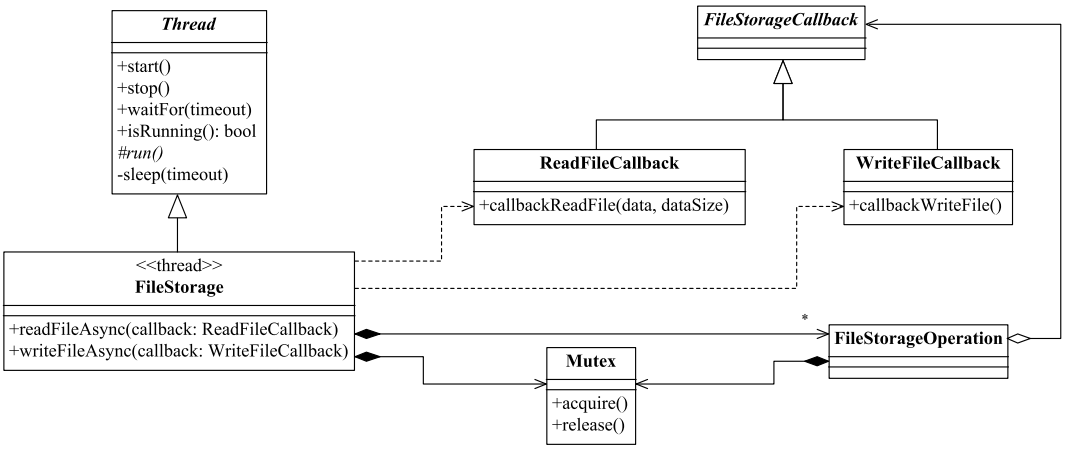

Figure 7.4: *The depicted classes are used for asynchronous file transfer between secondary and main memory.*

inherit from the subclasses `ReadFileCallback` and `WriteFileCallback` of class `FileStorageCallback` and re-implement the callback methods `callbackReadFile()` and `callbackWriteFile()` in order to asynchronously transfer data between secondary and main memory. These callback methods are invoked by `FileStorageOperation` objects after the storage operation is completed. New `FileStorageOperation` objects are inserted into an internally maintained queue of a `FileStorage` object by passing the object which is about to be transferred between main and secondary memory as parameters to the methods `readFileAsync()` or `writeFileAsync()`. The thread associated with the `FileStorage` object will be started automatically, if it is not already

running. The method `run()` of `FileStorage` processes the object's queue and executes until either the queue is empty or the thread is requested to terminate.

In order to avoid unnecessary storage operations on the same files if they are accessed multiple times in a row, e. g., by the cache of the FCM, operations are only enqueued in the follow situations:

- Read operations are only enqueued if the queue does not already contain a read operation or if an already enqueued read operation is followed by an enqueued write operation on the same file.
- Write operations are only enqueued if no write operation is already enqueued or if an existing write operation is succeeded by a read operation on the same file.

This is expressed in the truth table given in table 7.1. The columns *contains read* and *contains write* indicate the existence of an already enqueued read and write operation on the same file, respectively, and column *read first* indicates that a reading operation on the same file is enqueued before writing to the same file.

contains read	contains write	read first	enqueue reading	enqueue writing
true	true	true	true	false
true	true	false	false	true
true	false	true	false	true
false	true	false	true	false
false	false	false	true	true

Table 7.1: *Truth table for situations which require to enqueue a storage operation on the same file at a `FileStorage` object.*

Note that any objects which inherit from one or more of the `FileStorageCallback` subclasses must not be deleted, as long as they are referenced by a `FileStorageOperation` object which is enqueued at a `FileStorage` object, because otherwise the callback would cause a memory access violation.

Class `AerialImageCollector`

The class `AerialImageCollector` is responsible for retrieving aerial images from a database. For this purpose, the images are each identified by a number (*ID*) and a timestamp. Code, which is independent of the underlying database management system (DBMS), such as the method `run()`, is contained in the base class `AerialImageCollectorBase` (see figure 7.5). The method `run()` of `AerialImageCollectorBase` given in listing 7.2 calls virtual methods, which are implemented by derived subclasses and specific to the employed DBMS.

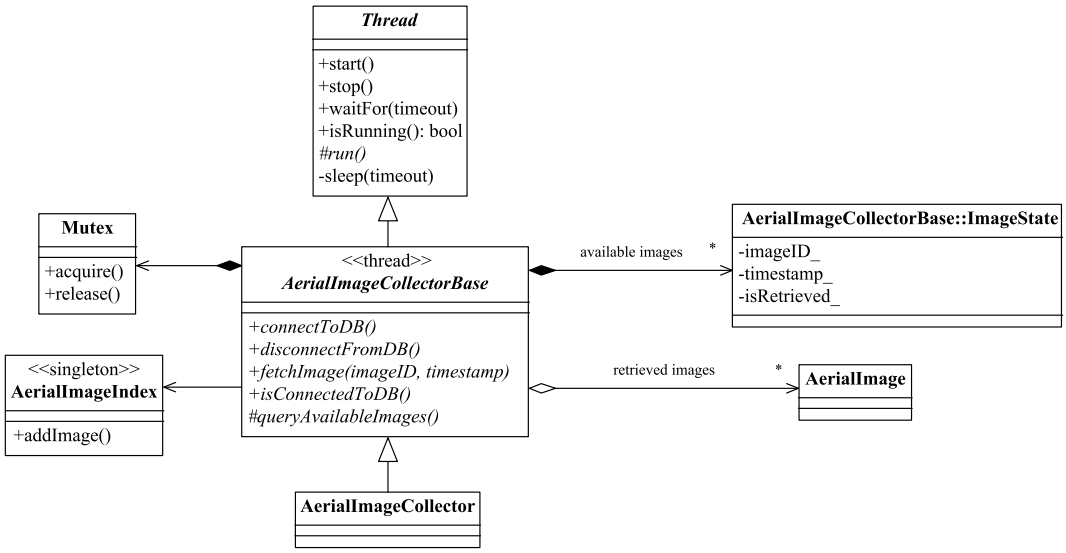

Figure 7.5: *The base class* `AerialImageCollectorBase` *provides an interface for database-specific implementations which are called by the* `run()` *method.*

Listing 7.2: *C++ code of the* `run()` *method of class* `AerialImageCollectorBase`. `availableImages_` *is an attribute for storing the state of retrieval for each of the available aerial images.*

```
1  // This typedef is used in the declaration of AerialImageCollectorBase.
2  //
3  typedef std::set<AerialImageCollectorBase::ImageState> StateSet;
4
5  void AerialImageCollectorBase::run()
6  {
7    StateSet::iterator itNext = availableImages_.end();
8    while (isRunning())
9    {
10     // Attempt to connect to database as long as this thread is running
11     // and no connection has been established.
12       //
13     for (unsigned int i = 0; (isRunning() && (! isConnectedToDB())); ++i)
14     {
15       if (i > 0)
16         sleep(500); // wait 500 ms between each two connection attempts
17       connectToDB();
18     }
19
20     // If the thread is terminated while it attempts to connect to the
21     // database, isRunning() will return false and we go back to the
22     // beginning of the outer while-loop in order to check if the thread
23     // needs to continue to execute.
24       //
25     if (! isConnectedToDB())
26       continue;
27
28     // The set of available images has not yet been completely retrieved.
29     //
30     if (itNext != availableImages_.end())
31     {
32       // Only try to retrieve aerial images if they have not yet been
```

```
33        // marked as retrieved.
34        //
35        const ImageState& is = *itNext;
36        if (! is.isRetrieved_)
37        {
38          // Mark the image if it was successfully retrieved.
39          // Otherwise, assume that something is wrong with the image
40          // (maybe it became deleted meanwhile) and remove it from the
41          // set of available images.
42          //
43          if (fetchImage(is.imageID_, is.timestamp_, false))
44          {
45            // possible since isRetrieved_ is declared as mutable
46            is.isRetrieved_ = true;
47            ++itNext;
48          }
49          else
50            availableImages_.erase(itNext++);
51        }
52        else
53          ++itNext;
54      }
55      else
56      {
57        // If the iterator indicates that the set has been processed,
58        // update the set of images and reset the iterator.
59        //
60        if (queryAvailableImages() > 0)
61          itNext = availableImages_.begin();
62      }
63    }   // while (isRunning()
64
65    disconnectFromDB();
66  } // run()
```

Listing 7.2: *C++ code of the* `run()` *method of class* `AerialImageCollectorBase`. `availableImages_` *is an attribute for storing the state of retrieval for each of the available aerial images.*

Class `TileCreator`

The implementation of the method `run()` in class `TileCreator` basically comprises the processing of its internal schedule for tile creation (cf. section 3.3.3). This class and its most important relationships to other classes are shown in the UML class diagram in figure 7.6. Since tile creation is performed on the GPU, the tile creator creates its own OpenGL *rendering context* by means of an `IrrLayerCreator` object which is directly created at the beginning of method `run()`. The class `IrrLayerCreator` implements the interface of its base class `LayerCreator` and performs the actual texture creation of the different DSM layers as described in section 5.3 and section 5.4 by using components of the "Irrlicht" rendering engine [38]. In this way, the main thread can continue to render, and both threads can act as if they had exclusive access to the graphics hardware. Before the method `run()` of class `TileCreator` returns, the `LayerCreator` object and hence the associated OpenGL rendering context are destroyed.

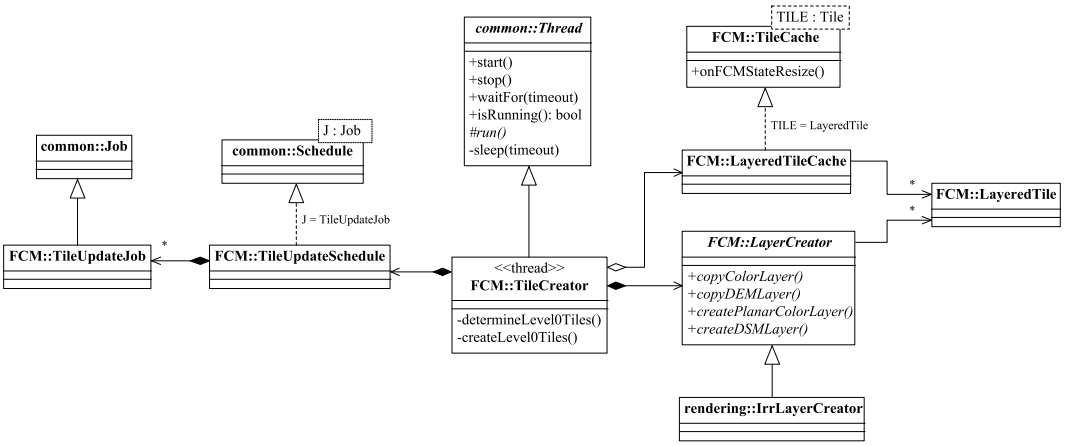

Figure 7.6: *The depicted classes implement the creation of DEM and color texture layers of FCM tiles. Tiles are retrieved by* `TileCreator` *via a* `LayeredTileCache` *object, which in turn manages* `LayeredTile` *objects. The tiles and the schedule are processed in the* `run()` *method of class* `TileCreator`*.*

7.2.2 Communication in Response to the Insertion of Aerial Images

The communication between the affected classes in response to the insertion of an aerial image is illustrated in the communication diagram[10] in figure 7.7. An equivalent sequence diagram of the same communication is given in figure B.2 in appendix B. The involved classes and their methods are shown in figure 7.8. This figure contains additional details about the class hierarchy which are omitted in figure 7.2 in favor of readability.

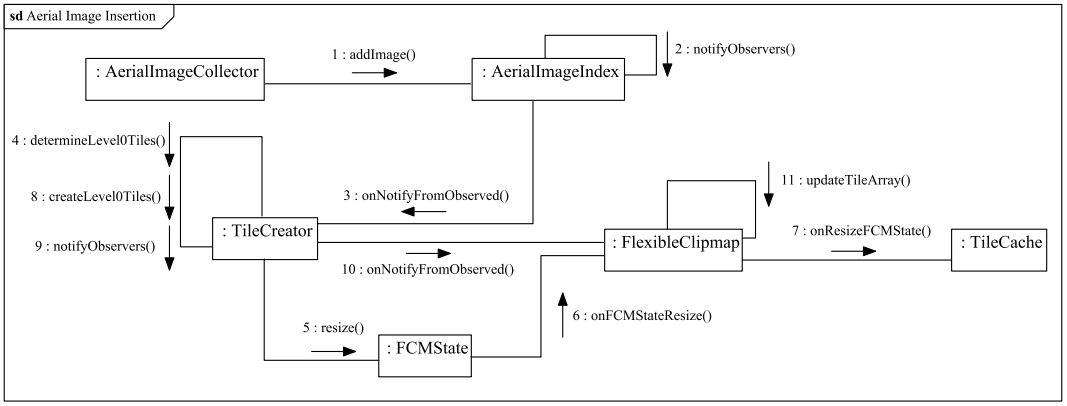

Figure 7.7: *The communication diagram shows the interaction between different objects in response to the insertion of an aerial image at the* `AerialImageIndex` *object by calling* `addImage()`*. Images are retrieved from a database by an* `AerialImageCollector` *object, which executes code in a separate thread.*

The insertion of an `AerialImage` object at `AerialImageIndex` is triggered by an `AerialImageCollector` object. `AerialImageCollector` is connected to the database for storing aerial images, and it monitors the arrival of new images. As soon as

[10] This type of diagram was called *collaboration diagram* in UML versions prior to 1.5 [73, p. 27].

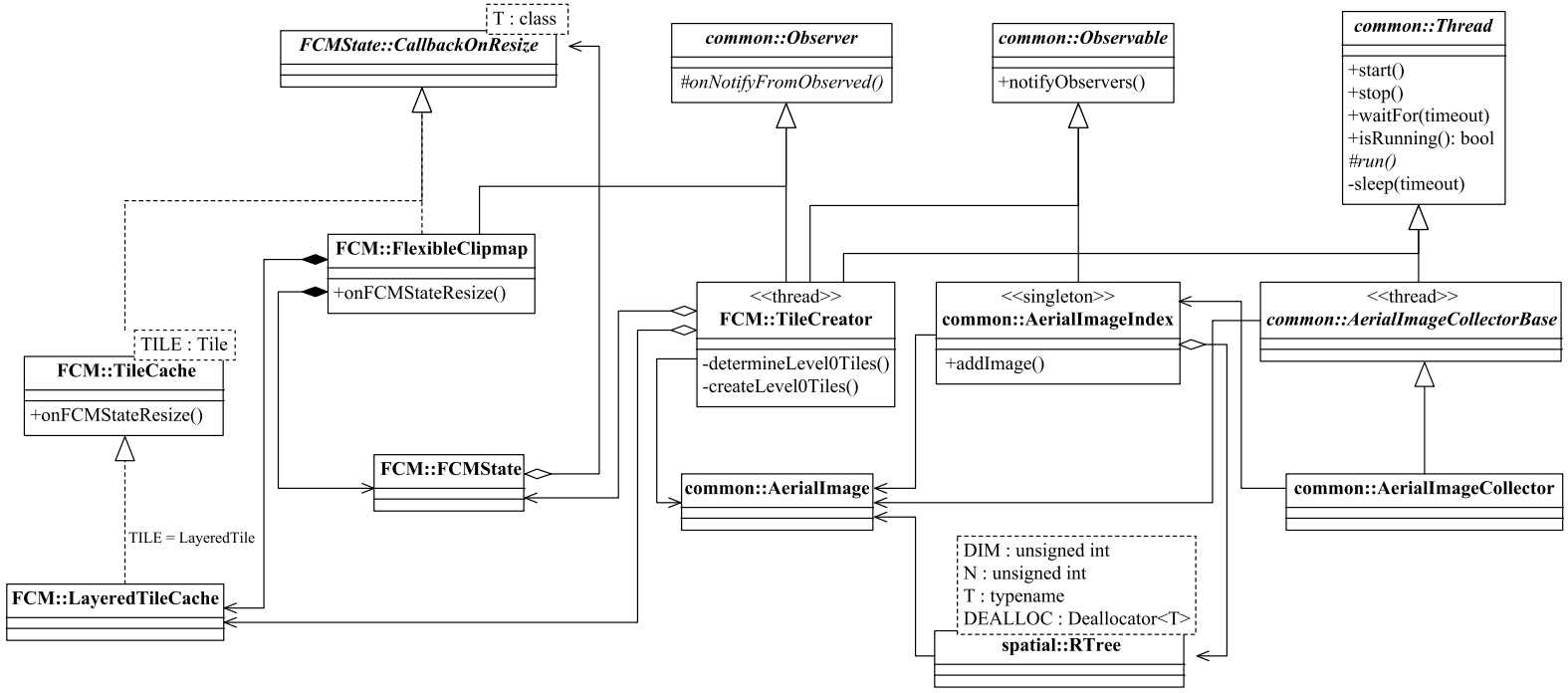

Figure 7.8: *The classes in the depicted diagram are affected by the insertion of new aerial images at the* `AerialImageIndex` *object after* `addImage()` *is called.*

new data are available, they are fetched and inserted into the spatial index maintained by the `AerialImageIndex` object by calling its method `addImage()`. In order to notify the `TileCreator` object about the presence of new aerial images, `AerialImageIndex` and `TileCreator` are implemented by using the *Observer* design pattern [31, pp. 287–300]. Directly after its creation, a `TileCreator` object registers itself as an observer at the `AerialImageIndex` Singleton, which inherits from `Oberservable`. Each time new aerial images are added to the `AerialImageIndex` Singleton, it notifies its registered observers by calling `notifyObservers()`, which in turn calls the observers' specific implementation of the method `onNotifyFromObserved()`. The method `onNotifyFromObserved()` of class `TileCreator` sets an internal flag to indicate the presence of new aerial images. If this flag is present, `determineLevel0Tiles()` is called during the next execution of the method `run()` of `TileCreator`, and the flag is reset. The method `determineLevel0Tiles()` will determine those FCM tiles at the base clip level $l = 0$ which need to be created or updated. Whenever the creation of new tiles causes the addition of additional clip levels as described in section 3.2.5, method `resize()` on the `FCMState` object is called. The `FCMState` object is maintained by the `FlexibleClipmap` object, which registers the method `onFCMStateResize()` as a callback at the `FCMState` object. The callback is invoked in response to changes of the state of the FCM which require to resize it. Since the size of the cache of the FCM must be adjusted as well, the method `onFCMStateResize()` of class `TileCache` is called by `FlexibleClipmap`.

After the eventual resizing of all involved components, the method `run()` of `TileCreator` can proceed with the creation of FCM tiles by calling `createLevel0Tiles()`. This call will also lead to the scheduling of FCM tile creations at clip levels > 0, and each time tiles have been created `TileCreator` calls its method `notifyObservers()`. In this way, objects like `FlexibleClipmap` can register themselves as observers and become notified about the creation of new tiles via calls to their implementations of `onNotifyFromObserved()`. This is required, for instance, by class `FlexibleClipmap` in order to call `updateTileArray()`, which is responsible for initiating the transfer of modified tiles into video memory for rendering.

As shown in figure 7.8, `TileCache` inherits from `CallbackOnResize` and can hence register a callback method at an `FCMState` object as well. This allows to use a `TileCreator` object without having to create a `FlexibleClipmap` object, if no rendering of the created DSM is required. In this case, the required `FCMState` and `TileCache` objects must be directly created by the application, because they are usually managed by the `FlexibleClipmap` object and are only accessed by `FCMState` via references. The `TileCache` object can thus directly register its `onFCMStateResize()` method as a callback at the `FCMState` object and becomes notified about changes of the number of clip levels in order to initiate eventual resizing of its internal tile level cache.

7.3 R*-tree Implementation

The R*-tree by Beckmann et al. [6] is implemented by the C++ class templates shown in figure 7.9.

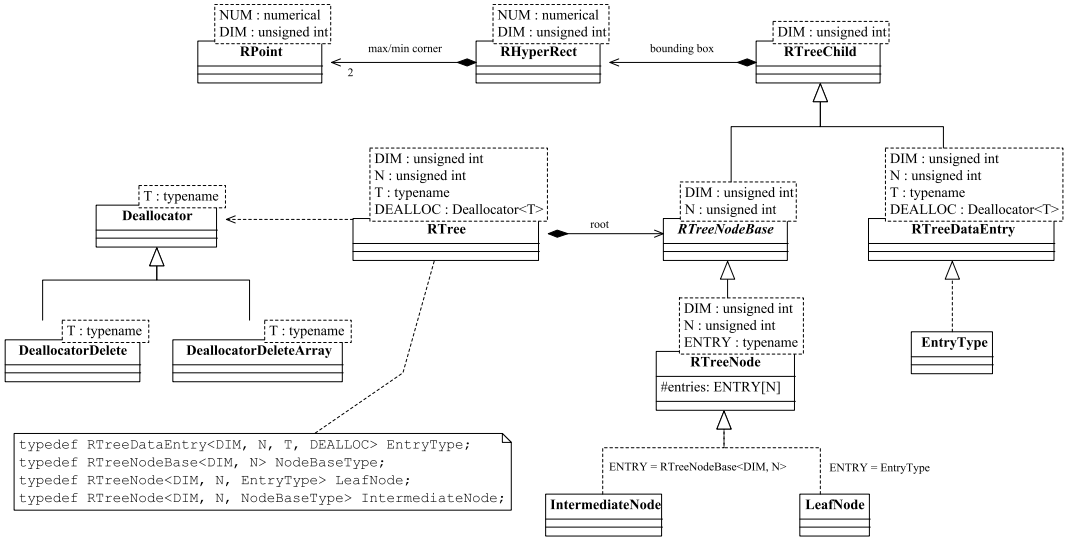

Figure 7.9: *We implemented the R*-tree by the depicted C++ class templates. Note that the classes* `EntryType`, `IntermediateNode` *and* `LeafNode` *are generated by template instantiation in* `RTree` *as indicated by the UML annotation, and that they are available only within instances of that class template.*

The four template parameters of the class template `RTree` representing the R*-tree itself must be used as follows: The parameter `DIM` indicates the dimension of the space and is `DIM = 3` in the context of our work, but `DIM` may have any value ≥ 1. `N` defines the maximal number of entries per node, and the minimal number of entries is set to $m = \lfloor \frac{N}{2} \rfloor$ (cf. section 3.2.3). Specifying the number of entries at compile time allows to use statically allocated arrays in the node classes for storing entries and hence simplifies memory management. The data type which is stored in the R*-tree is indicated by parameter `T` and is a pointer to `AerialImage` objects in our application. Since we want to automatically deallocate memory for objects which are removed from an instance of the class template `RTree`, we pass an appropriate `Deallocator` class template as the fourth template parameter `DEALLOC`. The `Deallocator` class template must be chosen with respect to the allocation method for data stored at the R-*-tree. Therefore, we provide three classes for this task, each one for the most common memory allocation methods used in C++. The base class `Deallocator` does not deallocate any memory and is intended for being used with parameters `T` which are no pointers. `DeallocatorDelete` and `DeallocatorDeleteArray` deallocate memory by using C++ `delete` and `delete[]` operators, respectively. As indicated by the UML annotation in figure 7.9, the four template parameters used by `RTree` are also used for instantiating the `RTreeDataEntry` class template, which represents entries at the leaf nodes of the R*-tree. The meaning of these parameters is the same as with the `RTree` class template, and the instantiated template is made a new

type `EntryType` via a C++ `typedef`, and it is only available within instances of `RTree`. The memory allocated by the actual data of type `T` of an `EntryType` object is deallocated within its destructor by a local deallocator object.

The data are stored in an R*-tree only at its leaf nodes, which are represented by `LeafNode` objects. `IntermediateNode` objects are used for handling intermediate nodes, and both types are instantiations of the `RTreeNode` class template. The template parameter `ENTRY` is set to the data type of the node's entries and is `EntryType` for leaf nodes. In case of intermediate nodes, the entries can be either leaf nodes or other intermediate nodes, and `ENTRY` is set to `RTreeNodeBase`, which is the base class template of all types of nodes. If access to the data is required, the generalized node objects are casted back to pointers of their respective subclasses, based on a node's level within the R*-tree.

Since all nodes and entries must maintain an axis-aligned bounding box (AABB), `RTreeDataEntry` and `RTreeNodeBase` inherit from an instance of the class template `RTreeChild`, which provides amongst others a `RHyperRect<NUM, DIM>` object. The latter represents the actual AABB and consists of two `RPoint<NUM, DIM>` objects, each one for the minimum and the maximum corner. These two class templates provide the basic operations for determining geometric relationships between each other, like containment, overlap, coverage and intersection, for instance. The template parameters `NUM` and `DIM` of `RHyperRect` and `RPoint` must be set to a numerical data type, e. g., `int`, `float` or `double`, and the dimension of space, respectively.

Operations for manipulating the content of the R*-tree, e. g., `insert()`, `find()` and `remove()` as well as operations related to its structure are implemented by methods of the `RTree` class template. The operations described in [35] and [6] for splitting nodes, like *ChooseSplitAxis* and *SplitNode*, are implemented by the class template `RTreeNode`.

7.4 GPU Programs

In this section we discuss the most important details and functions of the GLSL vertex and fragment programs for DSM rendering and DSM synthesis. We employ GLSL version 1.5 in order to have access to texture arrays, i. e., `sampler2Darray` data types. The complete shader source codes can be found in appendix A.

Like C/C++ programs, GLSL shaders can make use of preprocessor definitions [66, pp. 93–97]. Some of these definitions are generated as textual strings at runtime by our FCM components written in C++, e. g., in order to provide constants for allocating arrays of fixed size (cf. section 5.3.1). The resulting strings are inserted in front of the shader source code before the shaders are built by the graphics driver. The additional preprocessor directives are inserted as comments at the beginning of the source code for illustrative purposes. The values of such `#define` directives are chosen according to typical values from our application.

In the GLSL code listings presented in this dissertation, the names of uniform variables contain a trailing underscore, e. g., `worldSize_`. The names of variables of fragment programs qualified as `in`, and the ones of vertex programs qualified as `out`, are prefixed

by an underscore, e. g., `_texCoord0`. Attributes of structures are also suffixed by an underscore, but can be easily distinguished from uniform variables, since they appear outside of `struct` definitions on the right-hand side of an element access operator, i. e., a dot. Furthermore, the world coordinate system that is used by the Irrlicht rendering engine [38] differs from the world coordinate system Σ as presented in section 2.4 by swapped labels of the y- and z-axis. Hence, positions in the ground plane are denoted by `p.xz` instead of `p.xy` and height values are stored at `p.y` instead of `p.z`. In addition, the red and blue color components of RGB color textures are swapped by the rendering engine as well, so that we have to access the components of an RGB color value `texColor` from a texture via `texColor.bgr` instead of `texColor.rgb`.

7.4.1 DSM Rendering

The GPU programs for DSM rendering are associated by subclasses of `FlexibleClipmap`, which contain code specific to rendering by means of a certain API or graphics engine. The vertex program is given in listing A.1 in appendix A. Its task is to transform the vertex coordinates of the polygonal box-shaped mesh, which serves as proxy geometry for ray casting, into screen space, and to compute normalized 3D texture coordinates. The texture coordinate $(0, 0, 0)$ is located at the minimum corner and $(1, 1, 1)$ at the maximum corner. In addition, the vertex program computes the ratios of the two shorter sides to the longest side of the box. If the proxy geometry is not a cube, ray traversal during ray casting would require a non-uniform step width along the different axes. By component-wise multiplication of the direction of the ray with the ratio of the bounding box, we can use a uniform step width for ray traversal.

The function `main()` of the GLSL fragment shader for surface rendering in our FCM implementation and the definition of the employed `RayPosition` structure are given in listing 7.3 . The information that is stored at the current position of a ray in a `RayPosition` structure is indicated by the comments in listing 7.3. In line 969, a preprocessor definition added by the client program determines whether the FCM uses DEM ray casting or not, and the shader either executes the function `rayCasting()` or `planarFCM()`. In the latter case, the FCM can be used for texturing a planar surface as described in chapter 3. Both functions return a `RayPosition` structure which contains the final grid position, and the required clip levels for sampling the color texture layer. The attribute `hit_` indicates whether the grid position is located on the DEM surface. The check in line 983 is used to discard fragments at positions outside the domain of the FCM, e. g., if the ray has left the boundaries of the proxy geometry during ray casting.

If DEM ray casting is employed by using `rayCasting()` in line 978, the texture coordinate which is passed by the vertex program via `_texCoord0` encodes the position where the corresponding ray exits the proxy geometry. The CoP of the virtual camera is transformed by the vertex program into the proxy geometry's normalized texture coordinate system and is passed to the fragment shader via `_camPosTextureCoordinates`. The check in line 971 verifies that the coordinates of the camera position are in range

```
116 struct RayPosition
117 {
118   vec3 pGrid_;         // current grid position
119   float lodBlend_;     // parameter for blending LODs, range [0, 1[
120   uint levelCurrent_; // current clip level at ray position
121   uint levelLowest_;  // lowest clip level available at ray position
122   uint levelIdeal_;   // clip level of least aliasing at ray position
123   uint numSteps_;      // current number of ray casting steps
124   bool hit_;           // indicates whether the ray has hit the DEM surface
125 };  // struct RayPosition
126
```

```
964 void main()
965 {
966   vec3 exit = _texCoord0;
967   RayPosition rp;
968
969 #ifdef FCM_USE_DEM_RAY_CASTING
970   vec3 entry = _camPosTextureCoordinates;
971   if (! isInsideRange(entry, vec3(0.0), vec3(1.0)))
972   {
973     vec3 tmpDir = normalize(entry - exit);
974     entry = getBoxIntersection(exit, tmpDir, vec3(0.0), vec3(1.0));
975   }
976
977   vec3 dir = normalize((exit - entry) * _boxRatio);
978   rp = rayCasting(entry, dir);
979 #else
980   rp = planarFCM(exit);
981 #endif  // FCM_USE_DEM_RAY_CASTING
982
983   if (! rp.hit_)
984     discard;
985
986   fragColor = determineFragmentValues(rp, gl_FragDepth);
987 }   // main()
988
```

Listing 7.3: *The* `main()` *function of the FCM fragment program for DSM rendering and the employed structure* `RayPosition`.

$[0,1] \times [0,1] \subset \mathbb{R}^2$ and that the camera is thus located inside the proxy geometry. In this case, ray casting starts at the position of the camera. Otherwise, the camera is located outside the box, and the corresponding entry points of the ray on the proxy geometry are computed by the function `getBoxIntersection()` in line 974. The direction of the ray is then computed in line 977 and is multiplied component-wise by the ratio of the box.

If the FCM is used without DEM ray casting by calling `planarFCM()` in line 980, the FCM is located in the ground plane at the bottom of the proxy geometry box. In this case, positions for sampling its color texture layers can be thought of as the intersections of rays with a completely flat surface. Hence, `planarFCM()` merely transforms the normalized texture coordinate into the grid coordinate system by multiplying it by the grid size as used for ray casting and determines the optimal clip level that best avoids aliasing as described in section 3.3.4. This transformation into the grid coordinate system allows to handle the

subsequent computation of the final fragment color and the Z-Buffer value by the function `determineFragmentValues()` in line 986 in the same way as with ray casting.

The computation of the final fragment color is controlled by the preprocessor definition `COLORING_MODE`, which causes the function `determineFragmentValues()` to call code for either sampling the color texture layer, sampling projective textures, or applying diffuse shading with optional shadow casting. If no DEM ray casting is employed, sampling the color texture layer is the only available option. The computation of shadows relies on the same occlusion test by means of secondary ray casting, which is also used to determine the visibility of a location on the DEM surface in a projective texture (see section 6.2.2).

The code for initializing ray casting is shown in listing 7.4.

```
807 uint getDirectionCode(const in vec3 dir)
808 {
809   // prevent loss of sign by truncations to zero for small values
810   ivec3 iDir = ivec3(dir * 1.0e8);
811
812   uint dirCode = uint((iDir.x >> 31) & 1);  // sign of x-component (bit 0)
813   dirCode |= uint((iDir.y >> 30) & 2);  // sign of y-component (bit 1)
814   dirCode |= uint((iDir.z >> 29) & 4);  // sign of z-component (bit 2)
815
816   return dirCode;
817 }
818
819 RayPosition rayCasting(const in vec3 p, const in vec3 dir)
820 {
821   RayPosition rp;
822   rp.pGrid_ = (p * g_gridSize);
823   rp.levelCurrent_ = MAX_CLIPLEVEL;
824   rp.levelLowest_ = 0u;
825   rp.levelIdeal_ = 0u;
826   rp.numSteps_ = 0u;
827   rp.hit_ = false;
828
829   // Determine the target octant in space for the ray.
830   // Since the intersection tests with the DEM surface are different
831   // for rays directed upward and downward, use specialized functions.
832   uint dirCode = getDirectionCode(dir);
833   if ((dirCode & 2u) != 0u)
834     castRayDownward(rp, dir, dirCode);
835   else
836     castRayUpward(rp, dir, dirCode);
837
838   return rp;
839 }
840
```

Listing 7.4: *GLSL source code for initializing DEM ray casting.*

After the initialization of a `RayPosition` structure, the direction of the ray is encoded by the bit-mask `dirCode`, which is created by the function `getDirectionCode()`. This bit-mask is used for efficient branching during ray traversal via `switch`-statements. If the x-, y- or z-component of the ray's direction vector are negative, the lower three bits of `dirCode` are set accordingly and thus indicate the octant in 3D space into which the

ray is casted. Since computing the intersection of a ray with the DEM depends on whether the ray is directed upwards or downwards (cf. equation (4.2) in section 4.2.2), the function `rayCasting()` branches accordingly.

The two functions `castRayDownward()` and `castRayUpward()` essentially differ only in the intersection test. `castRayDownward()` is given in listing 7.5.

Listing 7.5: *GLSL source code from the ray casting branch for downward directed rays.*

```
677 void castRayDownward(inout RayPosition rp, const in vec3 dir, const in uint
        dirCode)
678 {
679   uint n = 0u;  // counter for ray casting steps at the current clip level
680   while ((! rp.hit_) && (isInsideRange(rp.pGrid_, vec3(0.0), g_gridSize)))
681   {
682     ++rp.numSteps_;
683     vec4 pNext = getNextCell(rp, dir, dirCode);
684
685     // If an intersection is detected, compute the EXACT hit point
686     // on the box of the grid cell.
687     // The w-component contains the DEM value at the next grid cell.
688     // The y-component is the current height of the ray above the ground
689     // plane.
690     if ((pNext.y - pNext.w) <= EPSILON_HIT)
691     {
692       rp.pGrid_ += dir * max(((pNext.w - rp.pGrid_.y) / dir.y), 0.0);
693
694       // Determine the different clip levels.
695       rp.levelLowest_ = getTileMapEntry(rp.pGrid_);
696       float idealLOD = computeIdealLOD(rp.pGrid_);
697       rp.levelIdeal_ = uint(idealLOD);
698       rp.lodBlend_ = fract(idealLOD);
699
700       // If the corresponding box of the grid cell at the current hit
701       // point is from a clip level greater than the clip level which
702       // would expose the least aliasing, descend one level.
703       // Otherwise, ray casting can terminate, and surface can be
704       // refined.
705       uint bestLevel =
706         max(rp.levelLowest_, min(rp.levelIdeal_, MAX_CLIPLEVEL));
707       if (rp.levelCurrent_ > bestLevel)
708       {
709         --rp.levelCurrent_;
710         n = 0u; // reset counter for ray casting steps at current level
711       }
712 #if (defined(SURFACE_REFINEMENT) && (SURFACE_REFINEMENT ==
        SURFACE_REFINEMENT_LINEAR))
713       else
714         rp.hit_ = refineSurfaceLinear(rp, dir, dirCode);
715 #elif (defined(SURFACE_REFINEMENT) && (SURFACE_REFINEMENT ==
        SURFACE_REFINEMENT_BICUBIC))
716       else
717         rp.hit_ = refineSurfaceBicubic(rp, dir, dirCode);
718 #else
719       else
720         rp.hit_ = true;
721 #endif  // SURFACE_REFINEMENT
722     }
723     else
724     {
725       // the DEM was not hit by the ray => proceed at the next grid cell
```

```
726       rp.pGrid_ = pNext.xyz;
727       ++n;  // increase the number of ray casting steps at this level
728
729       // After four or more ray casting steps at the current clip
730       // level, increase the level again (if possible) in order to
731       // iterate over larger grid cells. Four is an empirical value.
732       //
733       if ((n >= 4u) && (rp.levelCurrent_ < MAX_CLIPLEVEL))
734       {
735         ++rp.levelCurrent_;
736         n = 0u; // reset step counter
737       }
738     }
739   }   // while (
740
741   // fix potential round-off errors which might create "holes" in the ground
742   if (rp.pGrid_.y <= 0.0)
743   {
744     rp.hit_ = true;
745     rp.pGrid_.y = 0.0;
746   }
747 }
748
```

Listing 7.5: *GLSL source code from the ray casting branch for downward directed rays.*

The `while`-loop terminates if the ray has either hit the DEM surface, or if it leaves the domain of the FCM. Based on the current grid position and the direction of the ray, the next grid cell for ray traversal as described in section 4.2.2 is determined by the function `getNextCell()`. This function furthermore computes the position for sampling the DEM layer texture and retrieves the corresponding DEM value, which is stored at the fourth component (w-component) of the returned `vec4`. If the check in line 690 indicates that the ray intersects the DEM, the exact position on the grid cell's box surface is computed and the clip levels are determined according to the description in section 4.2.3. If the current clip level is greater than the clip level which best avoids aliasing, the level is decreased and ray casting continues from the current hit point. Otherwise, the final intersection of the ray with the surface has been found, and ray casting can be terminated. The surface refinement methods as presented in section 4.2.4 are applied only if the corresponding preprocessor definition `SURFACE_REFINEMENT` is present, and if its value is either as in line 712 or as in line 715. This directive is added to the shader source code by class `FlexibleClipmap`, if it is requested by the user of the client application. Since the surface refinement methods may invalidate the final hit point on the box surface of the grid cell, ray casting is resumed from that position if `refineSurfaceLinear()` respectively `refineSurfaceBicubic()` return `false`.

If the DEM is not hit by the ray at the current fragment, the ray is advanced to the next grid cell in line 726, and the counter for ray casting steps at the current level is increased. After four steps without any further intersection of the ray with the DEM, the level is increased again if it is not the top-most level. In this way, the effective size of the grid cell and thus the step width for ray traversal is increased (cf. section 4.2.2).

7.4.2 DSM Synthesis

The complete GPU programs for generating the different DSM layers of FCM tiles as described in chapter 5 are given in listing A.3 and listing A.4 in appendix A. The shaders create the DEM and the color texture layer of an FCM tile simultaneously by emitting two color values. Aerial images which are projected onto the sweeping plane and their associated projector matrices are passed to the programs via the uniform arrays `projectedTextures_` and `mProjectors_`.

The vertex program computes the texture coordinates for each projected image at the vertex positions of the rectangular mesh which represents the sweeping plane. These coordinates are passed on to the fragment program via the array `_texCoords` and are automatically interpolated across the sweeping plane. In the fragment program, the coordinates are transformed from homogeneous coordinates to Cartesian ones. Listing 7.6 shows the structure `ImageInfo` for storing the information about each projected image as indicated by the source code comments. The fragment shader's most important function `computeMatchingCosts()` is given in listing 7.7.

Listing 7.6: *Structure `ImageInfo` for storing information about an aerial image at the current fragment from the fragment program for DSM synthesis.*

```
49 struct ImageInfo
50 {
51   vec4 colorValue_;  // color value from corresponding image
52   float costs_;      // matching costs for image
53   float luminance_;  // luminance value (derived from RGB texel value)
54   uint imageIndex_;  // index of the image
55   bool covers_;      // true if the image covers this fragment
56 };  // struct ImageInfo
57
```

Listing 7.7: *Function `computeMatchingCosts` for computing the aggregated matching costs at each fragment in the fragment program for DSM synthesis.*

```
125 float computeMatchingCosts(out vec4 color)
126 {
127   float summedCosts = 0.0;
128   color = vec4(0.0, 0.0, 0.0, 1.0);
129   ImageInfo info[NUM_PROJECTORS];
130
131   // Determine the coverage by projective images at this fragment and
132   // initialize the ImageInfo structure at the lowest mipmap level for
133   // matching cost aggregation.
134   float mipmapLevel = max(float(minSupportWindowLevel_), 0.0);
135   uint coverage = 0u;
136   for (uint i = 0u; i < NUM_PROJECTORS; ++i)
137   {
138     coverage += initImageInfo(i, mipmapLevel, info);
139     if (info[i].covers_)
140       color = info[i].colorValue_;
141   }
142
143   // Change to (coverage == N) to get visually most appealing results.
144   if (coverage > 1u)
145   {
146     // add costs from previous pass with smallest support window size
```

```
147     for (uint i = 0u; i < NUM_PROJECTORS; ++i)
148     {
149       if (info[i].covers_)
150       {
151         for (uint j = 0u; j < NUM_PROJECTORS; ++j)
152         {
153           if (info[j].covers_)
154             info[i].costs_ += abs(info[i].luminance_ - info[j].luminance_);
155         }
156       }
157     }   // for (i
158
159     // add costs from larger support windows
160     for (int l = (minSupportWindowLevel_ + 1);
161         l <= maxSupportWindowLevel_; ++l)
162     {
163       // update luminances
164       float mipmapLevel = float(l);
165       for (uint i = 0u; i < NUM_PROJECTORS; ++i)
166       {
167         if (info[i].covers_)
168           info[i].luminance_ = getLuminanceUnchecked(i, mipmapLevel);
169       }
170
171       // same as above
172       for (uint i = 0u; i < NUM_PROJECTORS; ++i)
173       {
174         if (info[i].covers_)
175         {
176           for (uint j = 0u; j < NUM_PROJECTORS; ++j)
177           {
178             if (info[j].covers_)
179               info[i].costs_ += abs(info[i].luminance_ - info[j].luminance_);
180           }   // for (j
181         }
182       }   // for (i
183     }   // for (l
184
185 #ifdef USE_BETTER_HALF
186     // sort matching costs in increasing order
187     selectionSort(info, N);
188
189     // use color from image with least matching costs
190     color = info[0].colorValue_;
191
192     // sum up costs
193     uint k = 0u;
194     for (uint i = 0u;
195       ((info[i].costs_ < INFINITY) && (i < (coverage / 2u))); ++i, ++k)
196       summedCosts += info[i].costs_;
197
198     // normalize costs to simplify comparison with threshold
199     summedCosts /= float(k);
200 #else
201     color = vec4(0.0);
202     for (uint i = 0u; (i < N); ++i)
203     {
204       // sum up only valid matching costs (there is at least one valid value)
205       if (info[i].costs_ < INFINITY)
206       {
207         summedCosts += info[i].costs_;
```

```
208         color += info[i].colorValue_;
209       }
210     }
211
212     // normalize costs to simplify comparison with threshold
213     summedCosts /= float(coverage);
214     color /= float(coverage); // use averaged color values
215     color.a = 1.0;  // fix potential round-off errors
216 #endif
217   }   // if (coverage
218   else
219     summedCosts = INFINITY;
220
221   return summedCosts;
222 }
223
```

Listing 7.7: *Function `computeMatchingCosts` for computing the aggregated matching costs at each fragment in the fragment program for DSM synthesis.*

The function `computeMatchingCosts()` returns the aggregated matching costs at the current fragment and additionally assigns a color value to the `out` variable `color`. If all images covering the fragment are taken into account for matching cost computation, the final color value is computed as the averaged pixel value. Otherwise, only those images with lowest matching costs are considered, and the color value is obtained from the image with lowest matching costs. The matching costs can be aggregated over a contiguous range of mipmap levels, which is passed to the shader via `uniform` variables and corresponds to cost aggregation over different support window sizes (cf. section 5.1.2).

The aggregated matching costs are computed in detail as follows. For each projected image, the function initializes one element of an array of `ImageInfo` structures via `initImageInfo()` and simultaneously determines the number of images that cover the current fragment. The function `initImageInfo()` already samples the projected images at the lowest mipmap level given in `mipmapLevel` for cost aggregation. Furthermore, it converts color values into luminance values, which are stored in the attribute `luminance_` of the passed `ImageInfo` structure. If the fragment is not covered by at least two images, the matching costs at the fragment are set to `INFINITY` in line 219. Otherwise, the SAD of the intensities obtained for the images covering the fragment at the lowest mipmap level are computed and are aggregated in the `costs_` attribute in line 154. The coverage of image I_k at the current fragment is indicated by the boolean attribute `covers_`, and projected images not covering that fragment are assigned `INFINITY` as matching costs. If the costs are aggregated over multiple mipmap levels, i. e., over different sizes of support windows, for each additional level the luminance values for the images are updated in the `for`-loop starting at line 161. In lines 172 to 182, the additional costs are computed and aggregated in the same way as at the lowest mipmap level.

After the computation of the matching costs for each projected image for the current fragment, the costs are summed up to obtain the aggregated matching costs. If the GLSL preprocessor definition `USE_BETTER_HALF` exists, the array of `ImageInfo` structures is sorted by the function `selectionSort()` in line 187 in increasing order of matching

costs. Since images whose projections do not cover the current fragment have matching costs of `INFINITY`, which is implemented as a very large constant value, these images do not contribute to the summed costs. In addition, the color value sampled from the image with least matching costs is assigned to the `out` variable `color` and thus determines the final value of the corresponding texel in the color texture layer of the DSM.

If all images are considered for computing matching costs, images with matching costs of `INFINITY` are not taken into account during cost aggregation in line 207, because they do not cover the current fragment. In this case, the final value of the color texture layer is computed in line 208 and line 213 as the averaged color value of pixels from images covering the fragment.

7.5 Further Implementation Details

A detailed class diagram of the most important class `FlexibleClipmap` is presented in figure B.1 in appendix B.

The classes and functions from the packages `common`, `database`, `math` and `rendering` shown in figure 7.1 basically support those classes, which have been presented so far. Classes and functions from the packages `database` and `rendering` are furthermore specific to the underlying database system and rendering engine, respectively, and possess external dependencies on different code libraries, but their implementations are straightforward. The `math`-package essentially comprises classes and functions for representing mathematical objects like vectors, matrices and quaternions, but makes extensive use of C++ templates. These components are thus very versatile, but their implementations are rather lengthy and a little complex. Most of the classes from the `common` package have already been presented, and the remaining ones have straightforward implementations as well. Hence, we do not enter on further details about the implementation of the elements from these four packages. But since processing bitmap images is an important aspect in our application, the relationships of the classes and class templates for image processing from the `image`-package are shown in the UML diagram in figure B.3 in appendix B.

8 Conclusions

This dissertation presents techniques for managing and rendering digital surface models by using texture data of time-varying extension. The FCM has proved useful not only for managing and rendering color texture data, but also for accelerated ray casting of DEM data which are managed in the same way as color textures. Since the FCM allows to handle textures whose extensions may change in the course of time, it can be used for already rendering while the acquisition of the underlying data is still in progress. The bounding volume hierarchy provided by the FCM allows to render elevation data by means of ray casting at real-time frame rates on commodity graphics hardware. Ray casting provides a lot of flexibility, because the data can be rendered without extensive preprocessing and without generating polygonal meshes, which is especially important in the case of frequently changing data as in our application. The methods for surface refinement as presented in this work allow to improve the visual quality of the resulting surface renderings.

Adding color information to renderings of digital elevation models in 3D virtual environments by using orthophoto textures results in a lack of information on lateral surfaces of the elevations. In order to overcome this limitation, we presented a solution based on projective textures. By directly projecting images which depict the lateral faces of surfaces such as oblique aerial images, we can avoid creating large color textures for the entire surface area of a DEM. Since such textures would have to be modified each time the underlying elevation data and images change, projective textures offer more flexibility.

We furthermore presented a simple method for generating DSM data from simulated aerial images captured at low altitudes in an unsorted manner by means of a GPU-based space sweep for stereo matching. With the employed input images, this method allows to obtain credential results within few seconds, while the resulting surface model can be rendered simultaneously. More sophisticated and optimized method can be expected to yield elevation data of even higher quality, although they may be computationally more expensive. The DSM creation process and projective texturing rely on a 3D spatial index such as an R^*-tree which supports intersection queries, in order to efficiently retrieve the required input images. In conjunction with the caching techniques of the FCM, this allows to create, manage and render DSMs of almost arbitrary sizes.

Our approach mainly targets at the rendering of DSMs and their creation by means of aerial photographs, which are captured at low altitudes by small unmanned aerial vehicles and are directly transferred to a ground station by wireless networks in order to provide instant feedback about the underlying surface. Since we do not yet have a reliable source of such images available, our results are currently based on simulated aerial images. This is not a limitation for our methods for managing and rendering DSMs by using textures

of time-varying extension as presented in chapters 3 and 4, because these techniques are independent of the employed image acquisition technique. Other applications in which time-varying data about surfaces are directly available for rendering may benefit from the managing and rendering capabilities of the FCM as well. The technique for texturing the rendered surfaces by means of projective textures as presented in chapter 6 is also independent of the source of images, but strongly relies on accurate position and orientation information about the employed images. In the case of simulated aerial images, these metadata are perfectly accurate, and the resulting renderings therefore barely expose displacements of the textures on the surfaces. The position and orientation data of real aerial images are probably less precise and hence might require preprocessing by means of bundle adjustment or similar techniques, in order to improve the accuracy of these metadata. The accuracy of the metadata of real aerial images could probably also influence the quality of the results of the stereo matching approach as presented in chapter 5, and adjustments of the technique for such images might be necessary.

The runtime performance of our techniques appears to be completely sufficient for our intended applications, but might be further improved by careful optimizations. It would also be interesting to obtain direct comparisons with competitive rendering techniques which are based on rasterization of polygonal meshes. For instance, our FCM implementation could be extended in such a way that it can be used like a Geometry Clipmap [47] for handling triangular meshes of time-varying extension. As tessellation shaders become more available on commodity graphics hardware, the FCM might also be useful for directly rendering DSMs that are represented by bicubic patches stored in texture data instead of using ray casting with applied bicubic surface refinement (see chapter 4.2.4). However, these extensions and further comparisons were not required in the context of our application in the AVIGLE project and have thus been omitted in favor of the development of the techniques presented in this work.

The space sweep approach for stereo matching produces a dense set of 3D points as required for DSM synthesis, but other techniques for stereo matching, like feature-based methods, would also be worthwhile to investigate. We would also have liked to extensively evaluate our DSM creation process for a wider range of input data, but unfortunately had no such data available at the time of writing this thesis.

A GPU Programs

The GPU programs listed in this appendix were developed and tested on a desktop computer with a NVidia GeForce 470 GTX graphics adapter, 64-bit Windows 7 operating system and NVidia graphics drivers version 306.92.

A.1 Flexible Clipmap Shaders

The following GLSL vertex and fragment programs are employed by our Flexible Clipmap implementation for rendering DSMs by means of ray casting according to chapter 4.

Listing A.1: *The complete GLSL vertex program of our FCM implementation.*

```
#version 150

uniform mat4 modelMatrix_;
uniform mat4 viewMatrix_;
uniform mat4 projectionMatrix_;
uniform vec3 worldOffset_;
uniform vec3 worldSize_;
uniform vec3 cameraPosition_;

in vec3 vertexPos;
in vec3 vertexNormal;
in vec2 vertexTexCoord0;
in vec4 vertexColor;

out vec3 _texCoord0;         // exit point of a ray on proxy geometry
out mat4 _modelViewProj;
out vec3 _camPosTextureCoordinates; // camera position in texture coordinates
out vec3 _boxRatio;

vec3 getBoundingBoxRatio()
{
  vec3 ratio = worldSize_;
  if ((ratio.x >= ratio.y) && (ratio.x >= ratio.z))
  {
    ratio.yz /= ratio.x;
    ratio.x = 1.0;
  }
  else if ((ratio.z >= ratio.x) && (ratio.z >= ratio.y))
  {
    ratio.xy /= ratio.z;
    ratio.z = 1.0;
  }
  else
  {
    ratio.xz /= ratio.y;
    ratio.y = 1.0;
```

```
37    }
38    return ratio;
39  }
40
41  void main()
42  {
43    _texCoord0 = (vertexPos - worldOffset_) / worldSize_;
44    _camPosTextureCoordinates = (cameraPosition_ - worldOffset_) / worldSize_;
45    _boxRatio = getBoundingBoxRatio();
46
47    _modelViewProj = projectionMatrix_ * viewMatrix_ * modelMatrix_;
48    gl_Position = _modelViewProj * vec4(vertexPos, 1.0);
49  }
```

Listing A.1: *The complete GLSL vertex program of our FCM implementation.*

Listing A.2: *The complete GLSL fragment program of our FCM implementation.*

```
1  // The following defines are added by the class <code>FlexibleClipmap</code>
2  // according to program settings after the file containing this code is read.
3  // The given values are only for illustrative purposes.
4  /*
5  #version 150
6
7  #define NUM_CLIPLEVELS
8  #define TILE_SIZE vec2(512.0, 512.0)
9  #define SAMPLES_PER_UNIT vec3(4.0, 4.0, 4.0)
10 #define MAX_FILTERING_ANISOTROPY 16.0
11 #define EPSILON_HIT 0.0
12 #define MAX_NUM_PROJECTORS  8u
13 #define COLORING_MODE COLOR_MODE_SHADED_WITH_SHADOWS
14 #define FCM_USE_DEM_RAY_CASTING
15 #define SURFACE_REFINEMENT SURFACE_REFINEMENT_LINEAR
16
17 // Indicates the scaling factor for different texel formats of textures storing
18 // DEM layers: I8 ~ BYTE = 255.0, F32 ~ float = 1.0
19 //
20 #define SAMPLE_SCALE
21
22 // These two arrays only change as the number of clip levels of the FCM
23 // changes. Hence their content is generated in form of GLSL code by class
24 // <code>FlexibleClipmap</code> and the shader is rebuilt each time the number
25 // of clip levels changes.
26 //
27 uniform vec2 numTilesAtLevel_[NUM_CLIPLEVELS] = vec2[NUM_CLIPLEVELS]();
28 uniform int tileArrayOffsets_[NUM_CLIPLEVELS] = int[NUM_CLIPLEVELS]();
29 */
30 #line 30
31
32 #define COLOR_MODE_TEXTURING  1
33 #define COLOR_MODE_TEXTURING_PROJECTIVE 2
34 #define COLOR_MODE_SHADED 3
35 #define COLOR_MODE_SHADED_WITH_SHADOWS 4
36
37 #define SURFACE_REFINEMENT_LINEAR 1
38 #define SURFACE_REFINEMENT_BICUBIC 2
39
40 #ifndef FCM_USE_DEM_RAY_CASTING
41 #undef MAX_NUM_PROJECTORS
42 #undef SURFACE_REFINEMENT
43 #endif
```

```
44
45 // ### in/out variables ###
46
47 in vec3 _texCoord0;  // uniform texture coordinate on proxy geometry
48 in mat4 _modelViewProj; // combined model, view and projection matrix
49
50 // Position of camera relative to the left lower corner of the proxy geometry
51 // box.
52 //
53 in vec3 _camPosTextureCoordinates;
54
55 // Ratios of the two shorter sides of the proxy geometry box and its longest
56 // side. Required for facilitating ray traversal.
57 //
58 in vec3 _boxRatio;
59
60 out vec4 fragColor;  // the final fragment color
61
62
63 // ### uniform variables ###
64
65 // The current size of the rendering window; required for LOD calculations.
66 uniform vec2 windowSize_;
67
68 // Offset and size of the grid/proxy geometry in world coordinates.
69 uniform vec3 worldOffset_;
70 uniform vec3 worldSize_;
71
72 uniform sampler2D tileMap_;
73
74 #ifndef MAX_NUM_PROJECTORS
75 uniform sampler2DArray colorLayerArray_;
76 #endif
77
78 #ifdef FCM_USE_DEM_RAY_CASTING
79 // only relevant if DEM ray casting is used
80 uniform sampler2DArray demLayerArray_;
81 uniform float heightScaling_;
82
83 uniform vec3 dirLight_;
84 uniform vec3 surfaceColorAmbient_;
85 uniform vec3 surfaceColorDiffuse_;
86
87 #ifdef MAX_NUM_PROJECTORS
88 // only relevant if projective texturing is used
89 uniform int numProjectors_;
90 uniform sampler2D projectiveTextures_[MAX_NUM_PROJECTORS];
91 uniform mat4 mProjectors_[MAX_NUM_PROJECTORS];
92 uniform vec3 projectionCenters_[MAX_NUM_PROJECTORS];
93 #endif  // MAX_NUM_PROJECTORS
94
95 #endif  // FCM_USE_DEM_RAY_CASTING
96
97
98 // ### global variables and constants ###
99
100 vec3 g_gridSize = (worldSize_ * SAMPLES_PER_UNIT);
101 vec3 g_gridOffset = (worldOffset_ * SAMPLES_PER_UNIT);
102 const uint MAX_CLIPLEVEL = ((NUM_CLIPLEVELS > 0u) ? (NUM_CLIPLEVELS - 1u) :
      0u);
103
```

```
104 #ifdef MAX_NUM_PROJECTORS
105 const mat4 g_mScaleProjector = mat4(
106   0.5, 0.0, 0.0, 0.0, // 1st row
107   0.0, 0.5, 0.0, 0.0,
108   0.0, 0.0, 0.5, 0.0,
109   0.5, 0.5, 0.5, 1.0);
110
111 uint N = min(uint(numProjectors_), MAX_NUM_PROJECTORS);
112 #endif  // MAX_NUM_PROJECTORS
113
114
115 // ### structures ###
116 struct RayPosition
117 {
118   vec3 pGrid_;        // current grid position
119   float lodBlend_;    // parameter for blending LODs, range [0, 1[
120   uint levelCurrent_; // current clip level at ray position
121   uint levelLowest_;  // lowest clip level available at ray position
122   uint levelIdeal_;   // clip level of least aliasing at ray position
123   uint numSteps_;     // current number of ray casting steps
124   bool hit_;          // indicates whether the ray has hit the DEM surface
125 };  // struct RayPosition
126
127
128 // ## functions ##
129
130 /**
131  * Returns the texel coordinate and the index of a tile within the tile array
132  * at the given grid location at the given clip level.
133  *
134  * @param   level   Clip level where the tile is located.
135  * @param   pGrid   Grid position of a location.
136  */
137 ivec3 getTileCoord(const in uint level, const in vec2 pGrid)
138 {
139   if (level >= NUM_CLIPLEVELS)
140     return ivec3(-1);
141
142   ivec3 pTile;  // xy = uniform texture coordinate, z = tile array index
143   float k = float(1u << level);   // 2^level
144
145   // Compute the offset of the area covered by the FCM at the grid position
146   // in texels. The offset is different at top-most clip level, since the
147   // tile at that level covers the entire area of the FCM.
148   vec2 offset = floor(g_gridOffset.xz / k);
149   if ((level + 1u) >= NUM_CLIPLEVELS)
150     offset -= vec2(0.5 * TILE_SIZE);
151
152   // Compute the coordinates of the grid position at the tile in texels.
153   vec2 coord = (pGrid / k) + offset;
154   pTile.xy = ivec2(mod(coord, TILE_SIZE));
155
156   // Compute the index of the tile in the tile array.
157   vec2 tileID = floor(coord / TILE_SIZE);
158   vec2 n = numTilesAtLevel_[level];
159
160   // GLSL appearently uses the mathematical modulus function
161   // mod(a, b) = a - floor(a / m) * m
162   // instead of the symmetrical one which is
163   // mod(a, b) = a - div(a, m) * m
164   // where div(x, y) = sign(x) * sign(y) * floor(abs(x) / abs(y))
```

```
165   // as used in C/C++. Therefore the expression below can be simplified.
166   //
167   //vec2 i = floor(abs(tileID) / n.xy);
168   //vec2 r = mod(((tileID + (i + vec2(1.0)) * n.xy)), n.xy);
169   vec2 r = mod(tileID, n);
170
171   pTile.z = tileArrayOffsets_[level] + int(r.y * n.x + r.x);
172   return pTile;
173 }
174
175 /**
176  * Returns the uniform texture coordinate and the index of a tile within the
177  * tile array at the given grid location at a given clip level.
178  *
179  * THE COMPUTATIONS OF THIS FUNCTION ARE THE SAME AS IN FUNCTION getTileCoord()
180  * EXCEPT FOR THE MARKED TWO LINES.
181  */
182 vec3 getTileCoordUniform(const in uint level, const in vec2 pGrid)
183 {
184   vec3 pTile;
185   float k = float(1u << level);
186
187   vec2 offset = floor(g_gridOffset.xz / k);
188   if ((level + 1u) >= NUM_CLIPLEVELS)
189     offset -= vec2(0.5 * TILE_SIZE);
190
191   vec2 coord = (pGrid / k) + offset;
192   pTile.xy = (mod(coord, TILE_SIZE) / TILE_SIZE); // division, no casting
193
194   vec2 tileID = floor(coord / TILE_SIZE);
195   vec2 n = numTilesAtLevel_[level];
196   vec2 r = mod(tileID, n);
197
198   // cast to float
199   pTile.z = float(tileArrayOffsets_[level]) + (r.y * n.x + r.x);
200   return pTile;
201 }
202
203 /**
204  * Returns the entry of the tile map at the given grid location. The tile map
205  * contains the lowest clip level at which a tile is available in video memory.
206  */
207 uint getTileMapEntry(const in vec3 pGrid)
208 {
209   vec2 coord = (pGrid + g_gridOffset).xz;
210   ivec2 tileID = ivec2(floor(coord / TILE_SIZE));
211
212   // Multiply value by 255.0 to obtain the original BYTE value.
213   float texValue = texelFetch(tileMap_, tileID + ivec2(256), 0).b * 255.0;
214
215   uint mapEntry = uint(ceil(texValue + 0.5)); // avoid round-off errors
216   if (mapEntry >= 255u)
217     mapEntry = MAX_CLIPLEVEL;
218
219   return mapEntry;
220 }
221
222 /** Returns true if all components of r are within the given range. */
223 bool isInsideRange(const in vec2 r, const in vec2 lower, const in vec2 upper)
224 {
225   return all(greaterThanEqual(r, lower)) && all(lessThanEqual(r, upper));
```

```
226 }
227
228 /** Returns true if all components of r are within the given range. */
229 bool isInsideRange(const in vec3 r, const in vec3 lower, const in vec3 upper)
230 {
231   return all(greaterThanEqual(r, lower)) && all(lessThanEqual(r, upper));
232 }
233
234 /**
235  * Compute the ideal clip level for texture sampling based on the distortion
236  * of one pixel in screen coordinates if no DEM ray casting is used.
237  */
238 float computeIdealLODPlanar(const in vec3 pGrid)
239 {
240   vec2 ddx = dFdx(pGrid.xz);
241   vec2 ddy = dFdy(pGrid.xz);
242   float lddx = dot(ddx, ddx);
243   float lddy = dot(ddy, ddy);
244
245   float level;
246   if (MAX_FILTERING_ANISOTROPY <= 1.0)
247     level = log2(max(lddx, lddy)) * 0.5;  // = log2(sqrt(max()))
248   else
249   {
250     float pMax = sqrt(max(lddx, lddy));
251     float pMin = sqrt(min(lddx, lddy));
252     float aspect = min((pMax / pMin), MAX_FILTERING_ANISOTROPY);
253     level = log2(pMax / aspect);
254   }
255
256   return max(level, 0.0);
257 }
258
259 RayPosition planarFCM(const in vec3 p)
260 {
261   RayPosition rp;
262   rp.numSteps_ = 1u;
263   rp.pGrid_ = (p * g_gridSize);
264   rp.hit_ = ((p.y <= 0.0) && isInsideRange(rp.pGrid_, vec3(0.0), g_gridSize));
265   if (rp.hit_)
266   {
267     rp.levelLowest_ = getTileMapEntry(rp.pGrid_);
268     float idealLOD = computeIdealLODPlanar(rp.pGrid_);
269     rp.levelIdeal_ = uint(idealLOD);
270     rp.lodBlend_ = fract(idealLOD);
271     rp.levelCurrent_ =
272       max(rp.levelLowest_, min(rp.levelIdeal_, MAX_CLIPLEVEL));
273   }
274
275   return rp;
276 }
277
278 #ifdef FCM_USE_DEM_RAY_CASTING
279 /**
280  * Determines where a ray given by a point r on the box (specified by boxMin
281  * and boxMax) and a direction vector dir will intersect the box a second time.
282  */
283 vec3 getBoxIntersection(const in vec3 r, const in vec3 dir,
284             const in vec3 boxMin, const in vec3 boxMax)
285 {
286   vec3 hit = r;
```

```
287   hit.x = (dir.x >= 0.0) ? boxMax.x : boxMin.x;
288   hit.y = (dir.y >= 0.0) ? boxMax.y : boxMin.y;
289   hit.z = (dir.z >= 0.0) ? boxMax.z : boxMin.z;
290
291   vec3 k = (hit - r) / dir;
292   if ((k.x <= k.y) && (k.x <= k.z))
293     hit.yz = r.yz + dir.yz * k.x;
294   else if ((k.y <= k.x) && (k.y <= k.z))
295     hit.xz = r.xz + dir.xz * k.y;
296   else
297     hit.xy = r.xy + dir.xy * k.z;
298
299   return hit;
300 }
301
302 /** Texel-precise sampling of DEM at the given clip level and grid position. */
303 float sampleDEM(const in uint level, const in vec2 pGrid)
304 {
305   ivec3 tileCoord = getTileCoord(level, pGrid);
306
307   // sample height value and scale according to data type & program settings
308   float h = texelFetch(demLayerArray_, tileCoord, 0).r
309     * SAMPLE_SCALE * heightScaling_;
310
311   // transform from world coordinates into grid coordinates
312   return (((h - worldOffset_.y) * g_gridSize.y) / worldSize_.y);
313 }
314
315 /**
316  * Sample the DEM layer at the given clip level and grid position using
317  * bilinear intrepolation.
318  */
319 float sampleDEMFiltered(const in uint level, const in vec2 pGrid)
320 {
321   vec3 pTile = getTileCoordUniform(level, pGrid);
322
323   // sample height value and scale according to data type & program settings
324   float h = texture(demLayerArray_, pTile, 0).r
325     * SAMPLE_SCALE * heightScaling_;
326
327   // transform from world coordinates into grid coordinates
328   return (((h - worldOffset_.y) * g_gridSize.y) / worldSize_.y);
329 }
330
331 /** Compute surface normal by means of simple forward differences. */
332 vec3 getSurfaceNormal(const in vec3 pGrid, const in uint level)
333 {
334   float center = sampleDEMFiltered(level, pGrid.xz);
335   float right = sampleDEMFiltered(level, pGrid.xz + vec2(1.0, 0.0));
336   float upper = sampleDEMFiltered(level, pGrid.xz + vec2(0.0, 1.0));
337
338   return normalize( vec3((center - right), 1.0, (center - upper)) );
339 }
340
341 /** Compute the ideal LOD of the DEM surface at the given grid position. */
342 float computeIdealLOD(const in vec3 pGrid)
343 {
344   const vec3 du = vec3(1.0 / SAMPLES_PER_UNIT.x, 0.0, 0.0);
345   const vec3 dv = vec3(0.0, 0.0, 1.0 / SAMPLES_PER_UNIT.z);
346
347   // transform from grid into world coordinates
```

```
348   vec3 pWorld = (floor(pGrid) / SAMPLES_PER_UNIT) + worldOffset_;
349   pWorld.y *= heightScaling_;
350
351   // transform into screen space
352   vec4 r = _modelViewProj * vec4(pWorld, 1.0);
353   vec4 s = _modelViewProj * vec4(pWorld + du, 1.0);
354   vec4 t = _modelViewProj * vec4(pWorld + dv, 1.0);
355   vec4 u = _modelViewProj * vec4(pWorld.x, 0.0, pWorld.z, 1.0);
356
357   // transform to normalized device coordinates in the range [0, 1]
358   r.xyz = (r.xyz / r.w) * 0.5 + vec3(0.5);
359   s.xyz = (s.xyz / s.w) * 0.5 + vec3(0.5);
360   t.xyz = (t.xyz / t.w) * 0.5 + vec3(0.5);
361   u.xyz = (u.xyz / u.w) * 0.5 + vec3(0.5);
362
363   // three corners of grid cell's bounding box
364   vec2 a = (s - r).xy * windowSize_;
365   vec2 b = (t - r).xy * windowSize_;
366   vec2 c = (u - r).xy * windowSize_;
367
368   // the two sides of the parallelogram
369   float l1 = a.x * a.x + b.x * b.x + c.x * c.x;
370   float l2 = a.y * a.y + b.y * b.y + c.y * c.y;
371
372   float minification = sqrt(min(l1, l2));
373   float level = -log2(minification);
374
375   return max(level, 0.0);
376 }
377
378
379 // ### functions for ray casting ### //
380
381 vec3 getNextCellRU(const in float k, const in vec3 pGrid, out vec2 samplePos)
382 {
383   samplePos = pGrid.xz;
384   return (floor(pGrid / k) + 1.0) * k;
385 }
386
387 vec3 getNextCellLU(const in float k, const in vec3 pGrid, out vec2 samplePos)
388 {
389   vec3 pNext = vec3((ceil(pGrid.x / k) - 1.0) * k, 0.0,
390     (floor(pGrid.z / k) + 1.0) * k);
391   samplePos = vec2(pNext.x, pGrid.z);
392   return pNext;
393 }
394
395 vec3 getNextCellRL(const in float k, const in vec3 pGrid, out vec2 samplePos)
396 {
397   vec3 pNext = vec3((floor(pGrid.x / k) + 1.0) * k, 0.0,
398     (ceil(pGrid.z / k) - 1.0) * k);
399   samplePos = vec2(pGrid.x, pNext.z);
400   return pNext;
401 }
402
403 vec3 getNextCellLL(const in float k, const in vec3 pGrid, out vec2 samplePos)
404 {
405   vec3 pNext = vec3(ceil(pGrid / k) - 1.0) * k;
406   samplePos = pNext.xz;
407   return pNext;
408 }
```

```
409
410 /**
411  * Returns the grid position on the boundary of the next cell at the current
412  * grid position stored in the given RayPosition struct in direction dir.
413  * The w-component of the returned vec4 contains the DEM height in grid
414  * coordinates at the next cell.
415  */
416 vec4 getNextCell(const in RayPosition rp, const in vec3 dir, const in uint
        dirCode)
417 {
418   float k = float(1u << rp.levelCurrent_);  // = 2^level
419
420   vec4 pNext;
421   vec2 samplePos; // position for sampling DEM layer at the next cell
422   switch (dirCode)
423   {
424     case 2u:
425     case 0u: // only bit 1 is set => (dir.x >= 0.0) && (dir.z >= 0.0)
426       pNext.xyz = getNextCellRU(k, rp.pGrid_, samplePos);
427       break;
428
429     case 3u:
430     case 1u: // bit 0 is set => dir.x < 0.0
431       pNext.xyz = getNextCellLU(k, rp.pGrid_, samplePos);
432       break;
433
434     case 6u:
435     case 4u: // bit 2 is set => dir.z < 0.0
436       pNext.xyz = getNextCellRL(k, rp.pGrid_, samplePos);
437       break;
438
439     case 7u:
440     case 5u: // bit 0 and bit 2 are set
441       pNext.xyz = getNextCellLL(k, rp.pGrid_, samplePos);
442       break;
443   }   // switch (dirCode
444
445   float h1 = sampleDEM(rp.levelCurrent_, samplePos);
446
447   // Use blending between DEM LODs only if no surface refinement is employed.
448 #ifndef SURFACE_REFINEMENT
449   if (rp.levelCurrent_ == max(rp.levelLowest_, min(rp.levelIdeal_,
          MAX_CLIPLEVEL)))
450   {
451     float h2 = sampleDEM(min((rp.levelCurrent_ + 1u), MAX_CLIPLEVEL),
            samplePos);
452     pNext.w = mix(h1, h2, rp.lodBlend_);
453   }
454   else
455 #endif
456   pNext.w = h1;
457
458   // Compute the exact position on the boundary of the next grid cell.
459   vec3 t = ((pNext.xyz - rp.pGrid_) / dir);
460   if (abs(t.x) <= abs(t.z))
461     pNext.yz = rp.pGrid_.yz + (dir.yz * t.x);
462   else
463     pNext.xy = rp.pGrid_.xy + (dir.xy * t.z);
464
465   return pNext;
466 }
```

```
467
468
469 // ### functions for surface refinement ###
470
471 #ifdef SURFACE_REFINEMENT
472 #if (SURFACE_REFINEMENT == SURFACE_REFINEMENT_LINEAR)
473 bool refineSurfaceLinear(inout RayPosition sample, const in vec3 dir, const in
        uint dirCode)
474 {
475   float k = (1u << sample.levelCurrent_); // = 2^level
476
477   vec2 dir_proj = normalize(dir.xz);
478   float maxComp = max(abs(dir.x), abs(dir.z));
479   if (abs(dir.y) > (2 * maxComp))
480     return true;
481
482   float delta_proj = (k * 0.5) / maxComp;
483   float delta = delta_proj / maxComp;
484
485   vec2 samplePos = sample.pGrid_.xz + dir_proj * delta_proj;
486   vec3 pB = sample.pGrid_ + dir * delta;
487   float hB = sampleDEMFiltered(sample.levelCurrent_, samplePos);
488
489   if (hB < pB.y)
490   {
491     sample.pGrid_ = getNextCell(sample, dir, dirCode).xyz;
492     return (! isInsideRange(sample.pGrid_, vec3(0.0), g_gridSize));
493   }
494
495   samplePos = sample.pGrid_.xz - dir_proj * delta_proj;
496   vec3 pA = sample.pGrid_ - (dir * delta);
497   float hA = sampleDEMFiltered(sample.levelCurrent_, samplePos);
498
499   float a = abs(hA - pA.y);
500   float b = abs(hB - pB.y);
501
502   sample.pGrid_ = mix(pA, pB, a / (a + b));
503   return true;
504 }
505 #elif (SURFACE_REFINEMENT == SURFACE_REFINEMENT_BICUBIC)
506 /**
507  * +----+----+----+  0: alpha
508  * | NW | N  | NE |  1: beta
509  * +----2----3----+  2: gamma
510  * | W  | .p | E  |  3: delta
511  * +----0----1----+
512  * | SW | S  | SE |
513  * +----+----+----+
514  *
515  * Hermite bicubic geometry matrix (transposed!!!):
516  *
517  * [   alpha      gamma      ddv(alpha)      ddv(gamma)     ]
518  * [   beta       delta      ddv(beta)       ddv(delta)     ]
519  * [ ddu(alpha) ddu(gamma) ddu(ddv(alpha)) ddu(ddv(gamma)) ]
520  * [ ddu(beta)  ddu(delta) ddu(ddv(beta))  ddu(ddv(delta)) ]
521  */
522 mat4 getHermiteBicubicGeometryMatrix(const in vec2 r, const in uint level)
523 {
524   float k = (1u << level);  // = 2^level
525
526   float samples[9]; // 0 = SW, 1 = S, 2 = SE, 3 = W, ..., 8 = NE
```

```
527   for (int i = 0; i < 9; ++i)
528   {
529     vec2 off = vec2(mod(i, 3) - 1, (i / 3) - 1) * k;
530     samples[i] = sampleDEM(level, r + off);
531   }
532
533   float s = min(samples[4], samples[1]);
534   float w = min(samples[4], samples[3]);
535   float n = min(samples[4], samples[7]);
536   float e = min(samples[4], samples[5]);
537
538   mat4 G_y; // first index: column, second index: row
539   G_y[0][0] = min(min(s, w), samples[0]); // alpha
540   G_y[0][1] = min(min(s, e), samples[2]); // beta
541   G_y[1][0] = min(min(w, n), samples[6]); // gamma
542   G_y[1][1] = min(min(e, n), samples[8]); // delta
543
544   s = samples[4] + samples[1];  // C + S
545   e = samples[5] + samples[4];  // E + C
546   n = samples[7] + samples[4];  // N + C
547   w = samples[4] + samples[3];  // C + W
548
549   // ddu(alpha) = 0.5 * (C + S - (W + SW))
550   G_y[0][2] = 0.5 * (s - (samples[3] + samples[0]));
551   // ddv(alpha) = 0.5 * (C + w - (S + SW))
552   G_y[2][0] = 0.5 * (w - (samples[1] + samples[0]));
553   // ddu(ddv(alpha)) = C - W - S + SW
554   G_y[2][2] = (samples[4] - samples[3] - samples[1] + samples[0]);
555
556   // ddu(beta) = (E + SE) - s
557   G_y[0][3] = 0.5 * ((samples[5] + samples[2]) - s);
558   // ddv(beta) = e - (SE + S)
559   G_y[2][1] = 0.5 * (e - (samples[2] + samples[1]));
560   // ddu(ddv(beta)) = E - C - SE + S
561   G_y[2][3] = (samples[5] - samples[4] - samples[2] + samples[1]);
562
563   // ddu(gamma) = n - (NW + W)
564   G_y[1][2] = 0.5 * (n - (samples[6] + samples[3]));
565   // ddv(gamma) = (N + NW) - w
566   G_y[3][0] = 0.5 * ((samples[7] + samples[6]) - w);
567   // ddu(ddv(gamma)) = N - NW - C + W
568   G_y[3][2] = (samples[7] - samples[6] - samples[4] + samples[3]);
569
570   // ddu(delta) = (NE + E) - n
571   G_y[1][3] = 0.5 * ((samples[8] + samples[5]) - n);
572   // ddv(delta) = (NE + N) - e
573   G_y[3][1] = 0.5 * ((samples[8] + samples[7]) - e);
574   // ddu(ddv(delta)) = NE - N - E + C
575   G_y[3][3] = (samples[8] - samples[7] - samples[5] + samples[4]);
576
577   return G_y;
578 }
579
580 bool refineSamplingBicubic(inout RayPosition rp, const in vec3 dir, const in
        uint dirCode)
581 {
582   const uint NUM_STEPS = 16u;
583   float k = float(1u << rp.levelCurrent_);  // = 2^level
584
585   // Same as getNextCell(), but computes an with additional offset on the
586   // next cell's boundary.
```

```
587   vec3 pNext;
588   vec2 samplePos;
589   vec2 off; // offset for mapping map (u, v) to [0.0, 1.0] x [0.0, 1.0]
590   switch (dirCode)
591   {
592     case 0u:
593     case 2u:  // (dir.x >= 0.0) && (dir.z >= 0.0)
594       pNext = getNextCellRU(k, rp.pGrid_, samplePos);
595       off = floor(rp.pGrid_.xz / k);
596       break;
597
598     case 1u:
599     case 3u:  // dir.x < 0.0
600       pNext = getNextCellLU(k, rp.pGrid_, samplePos);
601       off.x = ceil(rp.pGrid_.x / k) - 1.0;
602       off.y =  floor(rp.pGrid_.z / k);
603       break;
604
605     case 4u:
606     case 6u:  // dir.z < 0.0
607       pNext = getNextCellRL(k, rp.pGrid_, samplePos);
608       off.x = floor(rp.pGrid_.x / k);
609       off.y = ceil(rp.pGrid_.z / k) - 1.0;
610       break;
611
612     case 5u:
613     case 7u:  // (dir.x < 0.0) && (dir.z < 0.0)
614       pNext = getNextCellLL(k, rp.pGrid_, samplePos);
615       off = ceil(rp.pGrid_.xz / k) - 1.0;
616       break;
617   }   // switch (dirCode
618
619   // Compute the exact position on the boundary of next grid cell.
620   vec2 t = ((pNext.xz - rp.pGrid_.xz) / dir.xz);
621   if (abs(t.x) <= abs(t.y))
622     pNext.yz = rp.pGrid_.yz + (dir.yz * t.x);
623   else
624     pNext.xy = rp.pGrid_.xy + (dir.xy * t.y);
625
626   // Get the Hermite geometry matrix for DEM.
627   mat4 g_y = getHermiteBicubicGeometryMatrix(samplePos, rp.levelCurrent_);
628   float delta = length(pNext - rp.pGrid_) / NUM_STEPS;
629
630   bool hit = false;
631   for (uint n = 0u; n < NUM_STEPS; ++n)
632   {
633     // Map grid position at current level to [0.0, 1.0] x [0.0, 1.0].
634     // Cannot use fract() here, because when looking along negative
635     // directions, the border would contain the fraction of an integral
636     // value which is 0.0, but it must be equal to 1.0.
637     //
638     vec2 uv = (rp.pGrid_.xz / k) - off;
639
640     // Result of Hermite base matrix after multiplication with vectors
641     // [u^3, u^2, u, 1] and [v^3, v^2, v, 1], respectively.
642     //
643     //a = vec4(2.0 * uuu - 3.0 * uu + 1.0, 3.0 * uu - 2.0 * uuu,
644     //         uuu - 2.0 * uu + uv.x, uuu - uu);
645     //b = vec4(2.0 * vvv - 3.0 * vv + 1.0, 3.0 * vv - 2.0 * vvv,
646     //         vvv - 2.0 * vv + uv.y, vvv - vv);
647     //
```

```
648     vec2 i1 = uv * uv;
649     vec2 i2 = i1 * uv;
650     vec2 i3 = vec2(2.0) * i2 - vec2(3.0) * i1;
651     vec2 i4 = i2 - i1;
652     vec4 a = vec4(i3.x + 1.0, -i3.x, i4.x - i1.x + uv.x, i4.x);
653     vec4 b = g_y * vec4(i3.y + 1.0, -i3.y, i4.y - i1.y + uv.y, i4.y);
654
655     float h = dot(a, b);
656     if ((rp.pGrid_.y - h) <= EPSILON_HIT)
657     {
658       n = NUM_STEPS;
659       hit = true;
660       rp.pGrid_.y = h;
661     }
662     else
663       rp.pGrid_ += dir * delta;
664   }   // for (n
665
666   if (! hit)
667     rp.pGrid_ = pNext;
668
669   if (! isInsideRange(rp.pGrid_, vec3(0.0), g_gridSize))
670     hit = true;
671   return hit;
672 }
673 #endif  // (SURFACE_REFINEMENT ==
674 #endif  // SURFACE_REFINEMENT
675
676 /** Performs ray casting for rays directed downwards, i.e., dir.y < 0. */
677 void castRayDownward(inout RayPosition rp, const in vec3 dir, const in uint
        dirCode)
678 {
679   uint n = 0u;  // counter for ray casting steps at the current clip level
680   while ((! rp.hit_) && (isInsideRange(rp.pGrid_, vec3(0.0), g_gridSize)))
681   {
682     ++rp.numSteps_;
683     vec4 pNext = getNextCell(rp, dir, dirCode);
684
685     // If an intersection is detected, compute the EXACT hit point
686     // on the box of the grid cell.
687     // The w-component contains the DEM value at the next grid cell.
688     // The y-component is the current height of the ray above the ground
689     // plane.
690     if ((pNext.y - pNext.w) <= EPSILON_HIT)
691     {
692       rp.pGrid_ += dir * max(((pNext.w - rp.pGrid_.y) / dir.y), 0.0);
693
694       // Determine the different clip levels.
695       rp.levelLowest_ = getTileMapEntry(rp.pGrid_);
696       float idealLOD = computeIdealLOD(rp.pGrid_);
697       rp.levelIdeal_ = uint(idealLOD);
698       rp.lodBlend_ = fract(idealLOD);
699
700       // If the corresponding box of the grid cell at the current hit
701       // point is from a clip level greater than the clip level which
702       // would expose the least aliasing, descend one level.
703       // Otherwise, ray casting can terminate, and surface can be
704       // refined.
705       uint bestLevel =
706         max(rp.levelLowest_, min(rp.levelIdeal_, MAX_CLIPLEVEL));
707       if (rp.levelCurrent_ > bestLevel)
```

```
708       {
709         --rp.levelCurrent_;
710         n = 0u; // reset counter for ray casting steps at current level
711       }
712 #if (defined(SURFACE_REFINEMENT) && (SURFACE_REFINEMENT ==
      SURFACE_REFINEMENT_LINEAR))
713       else
714         rp.hit_ = refineSurfaceLinear(rp, dir, dirCode);
715 #elif (defined(SURFACE_REFINEMENT) && (SURFACE_REFINEMENT ==
      SURFACE_REFINEMENT_BICUBIC))
716       else
717         rp.hit_ = refineSurfaceBicubic(rp, dir, dirCode);
718 #else
719       else
720         rp.hit_ = true;
721 #endif  // SURFACE_REFINEMENT
722     }
723     else
724     {
725       // the DEM was not hit by the ray => proceed at the next grid cell
726       rp.pGrid_ = pNext.xyz;
727       ++n;  // increase the number of ray casting steps at this level
728
729       // After four or more ray casting steps at the current clip
730       // level, increase the level again (if possible) in order to
731       // iterate over larger grid cells. Four is an empirical value.
732       //
733       if ((n >= 4u) && (rp.levelCurrent_ < MAX_CLIPLEVEL))
734       {
735         ++rp.levelCurrent_;
736         n = 0u; // reset step counter
737       }
738     }
739   }   // while (
740
741   // fix potential round-off errors which might create "holes" in the ground
742   if (rp.pGrid_.y <= 0.0)
743   {
744     rp.hit_ = true;
745     rp.pGrid_.y = 0.0;
746   }
747 }
748
749 /**
750  * Performs ray casting for rays directed upwards, i.e., dir.y >= 0.
751  * Except for the computation of the intersection with the DEM, this function
752  * is essentially the same as castRayDownward().
753  */
754 void castRayUpward(inout RayPosition rp, const in vec3 dir, const in uint
      dirCode)
755 {
756   uint n = 0u;
757   while ((! rp.hit_) && (isInsideRange(rp.pGrid_, vec3(0.0), g_gridSize)))
758   {
759     ++rp.numSteps_;
760     vec4 pNext = getNextCell(rp, dir, dirCode);
761
762     if ((rp.pGrid_.y - pNext.w) <= EPSILON_HIT)
763     {
764       rp.levelLowest_ = getTileMapEntry(rp.pGrid_);
765       float idealLOD = computeIdealLOD(rp.pGrid_);
```

```
766       rp.levelIdeal_ = uint(idealLOD);
767       rp.lodBlend_ = fract(idealLOD);
768       uint bestLevel =
769         max(rp.levelLowest_, min(rp.levelIdeal_, MAX_CLIPLEVEL));
770
771       if (rp.levelCurrent_ > bestLevel)
772       {
773         --rp.levelCurrent_;
774         n = 0u;
775       }
776 #ifdef SURFACE_REFINEMENT
777 #if (SURFACE_REFINEMENT == SURFACE_REFINEMENT_LINEAR)
778       else
779         rp.hit_ = refineSurfaceLinear(rp, dir, dirCode);
780 #elif (SURFACE_REFINEMENT == SURFACE_REFINEMENT_BICUBIC)
781       else
782         rp.hit_ = refineSurfaceBicubic(rp, dir, dirCode);
783 #endif
784 #else
785       else
786         rp.hit_ = true;
787 #endif  // SURFACE_REFINEMENT
788     }
789     else
790     {
791       rp.pGrid_ = pNext.xyz;
792       ++n;
793
794       if ((n >= 4u) && (rp.levelCurrent_ < MAX_CLIPLEVEL))
795       {
796         ++rp.levelCurrent_;
797         n = 0u;
798       }
799     }
800   }   // while
801 }
802
803 /**
804  * Creates a bit-mask which indicates the negative components of the given
805  * direction vector.
806  */
807 uint getDirectionCode(const in vec3 dir)
808 {
809   // prevent loss of sign by truncations to zero for small values
810   ivec3 iDir = ivec3(dir * 1.0e8);
811
812   uint dirCode = uint((iDir.x >> 31) & 1);  // sign of x-component (bit 0)
813   dirCode |= uint((iDir.y >> 30) & 2);  // sign of y-component (bit 1)
814   dirCode |= uint((iDir.z >> 29) & 4);  // sign of z-component (bit 2)
815
816   return dirCode;
817 }
818
819 RayPosition rayCasting(const in vec3 p, const in vec3 dir)
820 {
821   RayPosition rp;
822   rp.pGrid_ = (p * g_gridSize);
823   rp.levelCurrent_ = MAX_CLIPLEVEL;
824   rp.levelLowest_ = 0u;
825   rp.levelIdeal_ = 0u;
826   rp.numSteps_ = 0u;
```

```
827   rp.hit_ = false;
828
829   // Determine the target octant in space for the ray.
830   // Since the intersection tests with the DEM surface are different
831   // for rays directed upward and downward, use specialized functions.
832   uint dirCode = getDirectionCode(dir);
833   if ((dirCode & 2u) != 0u)
834     castRayDownward(rp, dir, dirCode);
835   else
836     castRayUpward(rp, dir, dirCode);
837
838   return rp;
839 }
840
841 /**
842  * Determines whether the given grid location is occluded by other elevations
843  * along the given direction. This function is used for casting shadows and
844  * for determining the visibility of fragments in projective textures.
845  */
846 bool isOccluded(const in vec3 pGrid, const in vec3 dir)
847 {
848   RayPosition sample;
849   sample.pGrid_ = pGrid;
850   sample.levelCurrent_ = 0u;  // only for getting to next grid cell
851   sample.levelLowest_ = 0u;
852   sample.levelIdeal_ = 0u;
853   sample.numSteps_ = 0u;
854   sample.hit_ = false;
855
856   // Do not directly start at the give location, but advance one cell
857   // before checking for occlusion. Otherwise, the initial location would
858   // be considered as an intersection of the ray with the DEM.
859   uint dirCode = getDirectionCode(dir);
860   sample.pGrid_ = getNextCell(sample, dir, dirCode).xyz;
861   sample.levelCurrent_ = MAX_CLIPLEVEL;
862
863   if ((dirCode & 2u) == 0u)
864     castRayUpward(sample, dir, dirCode);
865   else
866     castRayDownward(sample, dir, dirCode);
867   return sample.hit_;
868 }
869
870
871 // ### functions for computing color values ###
872
873 #ifdef MAX_NUM_PROJECTORS
874 bool projectiveTexturing(const in vec3 pWorld, const in vec3 pGrid, inout vec3
      color)
875 {
876   if (pWorld.y <= 0.1)
877     return false;
878
879   bool isValid = false;
880   float minDistSq = 1.0e8;
881   for (uint i = 0u; (i < N); ++i)
882   {
883     // Compute texture coordinate in projected images.
884     vec4 tmp = g_mScaleProjector * mProjectors_[i] * vec4(pWorld, 1.0);
885     tmp.xy /= tmp.w;
886     tmp.y = 1.0 - tmp.y;
```

```
887     vec2 projTexCoord = tmp.xy;
888
889     // Vector pointing from DEM intersection towards CoP of projetor.
890     vec3 dirProj = (projectionCenters_[i] - pWorld);
891
892     // If the projective texture coordinate is valid...
893     if (isInsideRange(projTexCoord, vec2(0.0), vec2(1.0)))
894     {
895       // ...compute distance from CoP of projector to DEM intersection...
896       float distSq = dot(dirProj, dirProj);
897
898       // ...and check if the distance is smaller than the current minimum.
899       // Only perform the occlusion test, if the distance is smaller,
900       // since the test is computationally expensive.
901       //
902       if ((distSq <= minDistSq) &&
903         (! isOccluded(pGrid, normalize(dirProj))))
904       {
905         // If the tests are passed, update fragment color and current
906         // minimal distance.
907         //
908         minDistSq = distSq;
909         color = texture(projectiveTextures_[i], projTexCoord).bgr;
910         isValid = true;
911         //color = getLevelColor(i + 1u);
912       }
913     } // if (insideRange
914   } // for (i
915
916   return isValid;
917 }
918 #endif  // MAX_NUM_PROJECTORS
919 #endif // FCM_USE_DEM_RAY_CASTING
920
921 vec4 determineFragmentValues(const in RayPosition rp, out float zBuffer)
922 {
923   vec4 color = vec4(0.0, 0.0, 0.0, 1.0);
924
925   // transform grid position to world space
926   vec3 pWorld = (floor(rp.pGrid_) / SAMPLES_PER_UNIT) + worldOffset_;
927
928 #ifdef FCM_USE_DEM_RAY_CASTING
929   // compute surface normal + dot-product with directional light source
930   vec3 n = getSurfaceNormal(rp.pGrid_, rp.levelCurrent_);
931   float nDotL = clamp(dot(n, -dirLight_), 0.0, 1.0);
932
933   // use diffuse shading by default
934   color.rgb = clamp(nDotL * surfaceColorDiffuse_ + surfaceColorAmbient_, 0.0,
        1.0);
935
936 #if (defined(COLORING_MODE) && (COLORING_MODE == COLOR_MODE_TEXTURING))
937   vec3 pTile = getTileCoordUniform(rp.levelCurrent_, rp.pGrid_.xz);
938   color.rgb = texture(colorLayerArray_, pTile).bgr;
939 #elif (defined(COLORING_MODE) && (COLORING_MODE ==
      COLOR_MODE_TEXTURING_PROJECTIVE))
940   projectiveTexturing(pWorld, rp.pGrid_, color.rgb);
941 #elif (defined(COLORING_MODE) && (COLORING_MODE ==
      COLOR_MODE_SHADED_WITH_SHADOWS))
942   if (isOccluded(rp.pGrid_, -dirLight_))
943     color.rgb = surfaceColorAmbient_;
944 #endif  // (COLORING_MODE && (COLORING_MODE ==
```

```
945 #else
946   vec3 pTile = getTileCoordUniform(rp.levelCurrent_, rp.pGrid_.xz);
947   color.rgb = texture(colorLayerArray_, pTile).bgr;
948 #endif  // FCM_USE_DEM_RAY_CASTING
949
950   // Compute the correct depth value at the fragment for correct "interaction"
951   // with polygonal data, i.e., occlusion, depth-values and depth-tests.
952   //
953   // transform world position to normalized device coordinate
954   vec4 pNDC = _modelViewProj * vec4(pWorld, 1.0);
955   pNDC.xyz = (pNDC.xyz / pNDC.w) * 0.5 + vec3(0.5);
956   zBuffer = pNDC.z;
957
958   return color;
959 }
960
961
962 // ### main fucntion ###
963
964 void main()
965 {
966   vec3 exit = _texCoord0;
967   RayPosition rp;
968
969 #ifdef FCM_USE_DEM_RAY_CASTING
970   vec3 entry = _camPosTextureCoordinates;
971   if (! isInsideRange(entry, vec3(0.0), vec3(1.0)))
972   {
973     vec3 tmpDir = normalize(entry - exit);
974     entry = getBoxIntersection(exit, tmpDir, vec3(0.0), vec3(1.0));
975   }
976
977   vec3 dir = normalize((exit - entry) * _boxRatio);
978   rp = rayCasting(entry, dir);
979 #else
980   rp = planarFCM(exit);
981 #endif  // FCM_USE_DEM_RAY_CASTING
982
983   if (! rp.hit_)
984     discard;
985
986   fragColor = determineFragmentValues(rp, gl_FragDepth);
987 }   // main()
988
```

Listing A.2: *The complete GLSL fragment program of our FCM implementation.*

A.2 DSM Synthesis Shaders

The following GLSL vertex and fragment programs are employed by our implementation for creating DSM layers as described in chapter 5.

```
//#version 150
//
//#define NUM_PROJECTORS 8u

#line 5

// Required to unroll loops when using NVidia graphics adapters and drivers
// up to version 306.92 (or greater?).
#pragma optionNV(unroll all)

const mat4 g_mScaleProjector = mat4(
  0.5, 0.0, 0.0, 0.0, // 1st row
  0.0, 0.5, 0.0, 0.0,
  0.0, 0.0, 0.5, 0.0,
  0.5, 0.5, 0.5, 1.0);


uniform mat4 modelMatrix_;
uniform mat4 viewMatrix_;
uniform mat4 projectionMatrix_;
uniform mat4 mProjectors_[NUM_PROJECTORS];
uniform int numActiveProjectors_;


in vec3 _vertexPos;
in vec3 _vertexNormal;
in vec2 _vertexTexCoord0;
in vec4 _vertexColor;


out vec4 _texCoords[NUM_PROJECTORS];
out vec3 _worldPos;

void main()
{
  mat4 modelViewMatrix = viewMatrix_ * modelMatrix_;
  mat4 modelViewProjMatrix = projectionMatrix_ * modelViewMatrix;

  uint N = min(uint(numActiveProjectors_), NUM_PROJECTORS);
  for (uint i = 0u; i < NUM_PROJECTORS; ++i)
  {
    if (i < N)
      _texCoords[i] = g_mScaleProjector * mProjectors_[i] * vec4(_vertexPos,
          1.0);
    else
      _texCoords[i] = vec4(0.0, 0.0, 0.0, 1.0);
  }

  gl_Position = modelViewProjMatrix * vec4(_vertexPos, 1.0);
  _worldPos = _vertexPos;
}
```

Listing A.3: *The complete GLSL vertex program for DSM synthesis by means of a space sweep.*

Listing A.4: *The complete GLSL fragment program for DSM synthesis by means of a space sweep.*

```
// The following defines are generated by the class <code>LayerCreator</code>
// according to client program settings.
/*#version 150

#define NUM_PROJECTORS 8
#define CREATION_MODE CREATE_DEM_AND_COLOR
//#define USE_BETTER_HALF*/
#line 8

// Required to unroll loops when using NVidia graphics adapters and drivers
// up to version 306.92 (or greater?).
#pragma optionNV(unroll all)

#define CREATE_DEM_AND_COLOR 0
#define CREATE_COLOR_PLANAR 1

// ### in/out variables ###

in vec4 _texCoords[NUM_PROJECTORS]; // coordinates in projective textures
in vec3 _worldPos;  // fragment's position in world space

out vec4 _demValue;
out vec4 _fragColor;


// ### uniform variables ###

// must be casted to uint because Irrlicht 1.7.2 cannot handle uniform uint
uniform int numActiveProjectors_;

uniform int minSupportWindowLevel_;
uniform int maxSupportWindowLevel_;
uniform float costsThreshold_;
uniform float minDEMHeight_;
uniform sampler2D projectedTextures_[NUM_PROJECTORS];

// ### global variables and constants ###

uint N = min(uint(numActiveProjectors_), NUM_PROJECTORS);
vec2 g_texCoords[NUM_PROJECTORS];

// values for transforming RGB values to CIE XYZ luminance
const vec3 g_LuminanceFactors = vec3(0.212671, 0.715160, 0.072169);

const float INFINITY = 1.0e8;

// ### structures ###

struct ImageInfo
{
  vec4 colorValue_;  // color value from corresponding image
  float costs_;      // matching costs for image
  float luminance_;  // luminance value (derived from RGB texel value)
  uint imageIndex_;  // index of the image
  bool covers_;      // true if the image covers this fragment
};  // struct ImageInfo


// ### functions ###

```

```
61  /** Returns true if all components of v are within the given range. */
62  bool isInsideRange(const in vec2 v, const in vec2 lower, const in vec2 upper)
63  {
64    return (all(greaterThanEqual(v, lower)) && all(lessThanEqual(v, upper)));
65  }
66
67  /** Selection sort for sorting the first R elements of the given array. */
68  void selectionSort(inout ImageInfo arr[NUM_PROJECTORS], const in uint R)
69  {
70    for (uint i = 0u; i < R; ++i) // (R - 1u) would be sufficient
71    {
72      uint minIndex = i;
73      for (uint j = i + 1u; j < R; ++j)
74      {
75        if (arr[j].costs_ < arr[minIndex].costs_)
76          minIndex = j;
77      } // for (j
78
79      // swap elements
80      ImageInfo tmp = arr[i];
81      arr[i] = arr[minIndex];
82      arr[minIndex] = tmp;
83    } // for (i
84  }
85
86  /**
87   * Returns the luminance of the projective texture at the given index which
88   * projects onto this fragment. For efficiency reasons, no check for is
89   * performed whether the projector's texture coordinate is valid.
90   */
91  float getLuminanceUnchecked(const in uint index, const float mipmapLevel)
92  {
93    vec3 clr = textureLod(projectedTextures_[index],
94      g_texCoords[index], mipmapLevel).bgr;
95    return dot(clr, g_LuminanceFactors);
96  }
97
98  /**
99   * Initialize the ImageInfo structure for this fragment at the given index
100  * with all information available.
101  */
102 uint initImageInfo(const in uint index, const float mipmapLevel, out ImageInfo
        info[NUM_PROJECTORS])
103 {
104   // projective texture covers this fragment, if index is valid and
105   // texture coordinates are within the range [0, 1] x [0, 1]
106   info[index].covers_ = ((index < N) &&
107     isInsideRange(g_texCoords[index], vec2(0.0), vec2(1.0)));
108   if (info[index].covers_)
109   {
110     info[index].imageIndex_ = index;
111     info[index].colorValue_ = textureLod(projectedTextures_[index],
112       g_texCoords[index], mipmapLevel).bgra;
113     info[index].luminance_ = // convert RGB value to luminance
114       dot(info[index].colorValue_.rgb, g_LuminanceFactors);
115     info[index].costs_ = 0.0;
116     return 1u;  // for computing the total coverage at the fragment
117   }
118
119   info[index].colorValue_ = vec4(0.0, 1.0, 0.0, 1.0);
120   info[index].luminance_ = 0.0;
```

```
121   info[index].costs_ = INFINITY;
122   return 0u;
123 }
124
125 float computeMatchingCosts(out vec4 color)
126 {
127   float summedCosts = 0.0;
128   color = vec4(0.0, 0.0, 0.0, 1.0);
129   ImageInfo info[NUM_PROJECTORS];
130
131   // Determine the coverage by projective images at this fragment and
132   // initialize the ImageInfo structure at the lowest mipmap level for
133   // matching cost aggregation.
134   float mipmapLevel = max(float(minSupportWindowLevel_), 0.0);
135   uint coverage = 0u;
136   for (uint i = 0u; i < NUM_PROJECTORS; ++i)
137   {
138     coverage += initImageInfo(i, mipmapLevel, info);
139     if (info[i].covers_)
140       color = info[i].colorValue_;
141   }
142
143   // Change to (coverage == N) to get visually most appealing results.
144   if (coverage > 1u)
145   {
146     // add costs from previous pass with smallest support window size
147     for (uint i = 0u; i < NUM_PROJECTORS; ++i)
148     {
149       if (info[i].covers_)
150       {
151         for (uint j = 0u; j < NUM_PROJECTORS; ++j)
152         {
153           if (info[j].covers_)
154             info[i].costs_ += abs(info[i].luminance_ - info[j].luminance_);
155         }
156       }
157     }   // for (i
158
159     // add costs from larger support windows
160     for (int l = (minSupportWindowLevel_ + 1);
161         l <= maxSupportWindowLevel_; ++l)
162     {
163       // update luminances
164       float mipmapLevel = float(l);
165       for (uint i = 0u; i < NUM_PROJECTORS; ++i)
166       {
167         if (info[i].covers_)
168           info[i].luminance_ = getLuminanceUnchecked(i, mipmapLevel);
169       }
170
171       // same as above
172       for (uint i = 0u; i < NUM_PROJECTORS; ++i)
173       {
174         if (info[i].covers_)
175         {
176           for (uint j = 0u; j < NUM_PROJECTORS; ++j)
177           {
178             if (info[j].covers_)
179               info[i].costs_ += abs(info[i].luminance_ - info[j].luminance_);
180           }   // for (j
181         }
```

```
182       }   // for (i
183     }   // for (l
184
185 #ifdef USE_BETTER_HALF
186     // sort matching costs in increasing order
187     selectionSort(info, N);
188
189     // use color from image with least matching costs
190     color = info[0].colorValue_;
191
192     // sum up costs
193     uint k = 0u;
194     for (uint i = 0u;
195       ((info[i].costs_ < INFINITY) && (i < (coverage / 2u))); ++i, ++k)
196       summedCosts += info[i].costs_;
197
198     // normalize costs to simplify comparison with threshold
199     summedCosts /= float(k);
200 #else
201     color = vec4(0.0);
202     for (uint i = 0u; (i < N); ++i)
203     {
204       // sum up only valid matching costs (there is at least one valid value)
205       if (info[i].costs_ < INFINITY)
206       {
207         summedCosts += info[i].costs_;
208         color += info[i].colorValue_;
209       }
210     }
211
212     // normalize costs to simplify comparison with threshold
213     summedCosts /= float(coverage);
214     color /= float(coverage); // use averaged color values
215     color.a = 1.0;  // fix potential round-off errors
216 #endif
217   }   // if (coverage
218   else
219     summedCosts = INFINITY;
220
221   return summedCosts;
222 }
223
224 void createDSM(out float fragDepth, out vec4 dsmValue, out vec4 color)
225 {
226   // Compute the SAD to rate the quality of matching. The smaller the SAD,
227   // the better the matching. The SAD is output as depth value of the
228   // fragment in order to make subsequent Z-Buffer tests consider only
229   // fragments that have better quality, i.e., lower SADs.
230   float matchingCosts = computeMatchingCosts(color);
231   if (matchingCosts >= costsThreshold_)
232   {
233     // must be < 1.0; otherwise the fragment would be discarded
234     fragDepth = 0.999999;
235     dsmValue.rgba = vec4(vec3(minDEMHeight_), 1.0);
236     color = vec4(0.0, 0.0, 0.0, 1.0);
237     return;
238   }
239
240   fragDepth = matchingCosts;
241   dsmValue.rgba = vec4(vec3(_worldPos.y), 1.0);
242 }
```

```
243
244 /**
245  * Create a color texture layer based on the pixels which have the least
246  * geometric distance from the centers of their images. and without using
247  * elevation data
248  */
249 vec4 createPlanarColorLayerLeastDistance()
250 {
251   float minDist = INFINITY;
252   vec4 color = vec4(0.0, 0.0, 0.0, 1.0);
253   for (uint i = 0u; (i < N); ++i)
254   {
255     if (isInsideRange(g_texCoords[i], vec2(0.0), vec2(1.0)))
256     {
257       vec2 delta = (g_texCoords[i] - vec2(0.5));
258       float dSq = dot(delta, delta);
259       if (dSq < minDist)
260       {
261         minDist = dSq;
262         color = texture(projectedTextures_[i], g_texCoords[i]).bgra;
263       }
264     }
265   }   // for (i
266
267   return color;
268 }
269
270 /**
271  * Transform all coordinates in projective textures from homogeneous
272  * coordinates to Cartesian coordinates.
273  */
274 void transformTextureCoordinates()
275 {
276   for (uint i = 0u; i < NUM_PROJECTORS; ++i)
277   {
278     vec4 tmp = (_texCoords[i] / _texCoords[i].w);
279     tmp.y = 1.0 - tmp.y;  // flip horizontally due to Irrlicht
280     g_texCoords[i] = tmp.xy;
281   } // for (i
282 }
283
284
285 // ### main function ###
286
287 void main()
288 {
289   transformTextureCoordinates();
290
291 #if (defined(CREATION_MODE) && (CREATION_MODE == CREATE_DEM_AND_COLOR))
292   createDSM(gl_FragDepth, _demValue, _fragColor);
293 #elif (defined(CREATION_MODE) && (CREATION_MODE == CREATE_COLOR_PLANAR))
294   _demValue = vec4(vec3(_worldPos.y), 1.0);
295   _fragColor = createPlanarColorLayerLeastDistance();
296 #else
297   _demValue = vec4(0.0, 0.0, 0.0, 1.0);
298   _fragColor = vec4(1.0, 1.0, 0.0, 1.0);
299 #endif
300 }
```

Listing A.4: *The complete GLSL fragment program for DSM synthesis by means of a space sweep.*

B Additional UML Diagrams

The class diagram in figure B.1 contains details about the interface of class `FlexibleClipmap`. Methods which contain the word *upload* call virtual methods which are implemented by derived subclasses, like `IrrFlexibleClipmap`, in order to initiate the transfer of texture data from main memory to video memory. The two structures `ClipLevelInfo` and `TileArrayInfo` are both declared as `private` in class `FlexibleClipmap` and store information about a clip level such as the number of tiles, sizes of active area and clip area, etc., and the state of presence of a tile in the tile array, respectively. The method `update()` is responsible for initiating updates of the active areas and clip areas as the virtual camera is moved and must therefore be called before a frame is rendered. This method takes the current position of the virtual camera and the clip center as parameters.

Figure B.2 illustrates the communication between the affected objects in our FCM implementation in response to the insertion of an aerial image at the `AerialImageIndex` object. The depicted communication is the same as shown in the communication diagram in figure 7.7 in chapter 7.

Figure B.3 shows the relationships of the classes in the `image`-package of our FCM implementation. The components of this package provide basic raster image processing functionality such as filtering, re-sampling, loading and storing different file formats and converting between different pixel formats.

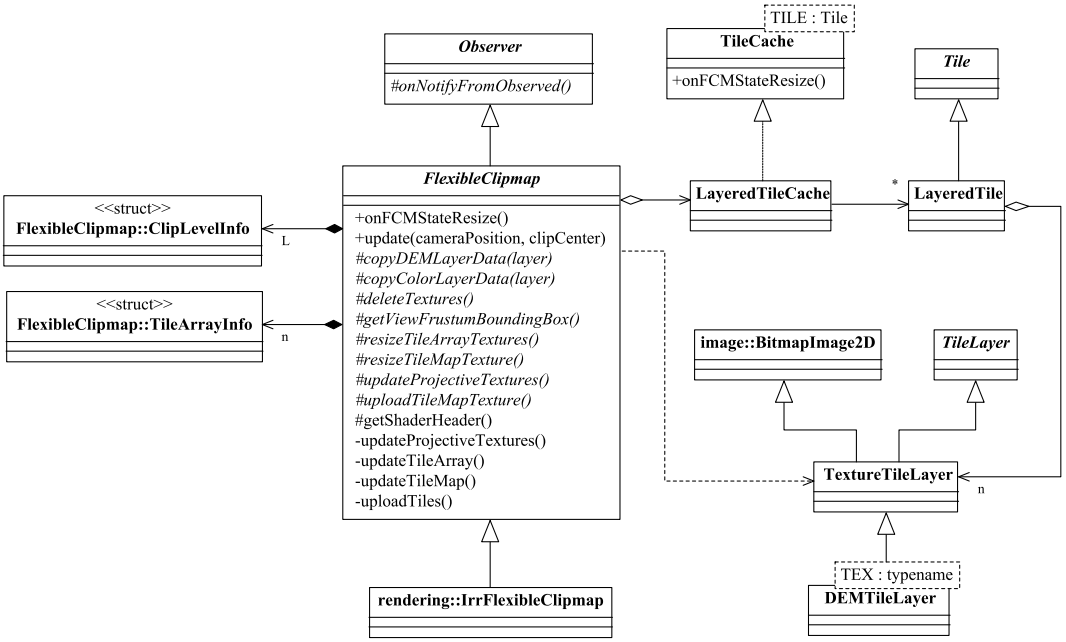

Figure B.1: *Details about the class* `FlexibleClipmap` *from our FCM implementation.*

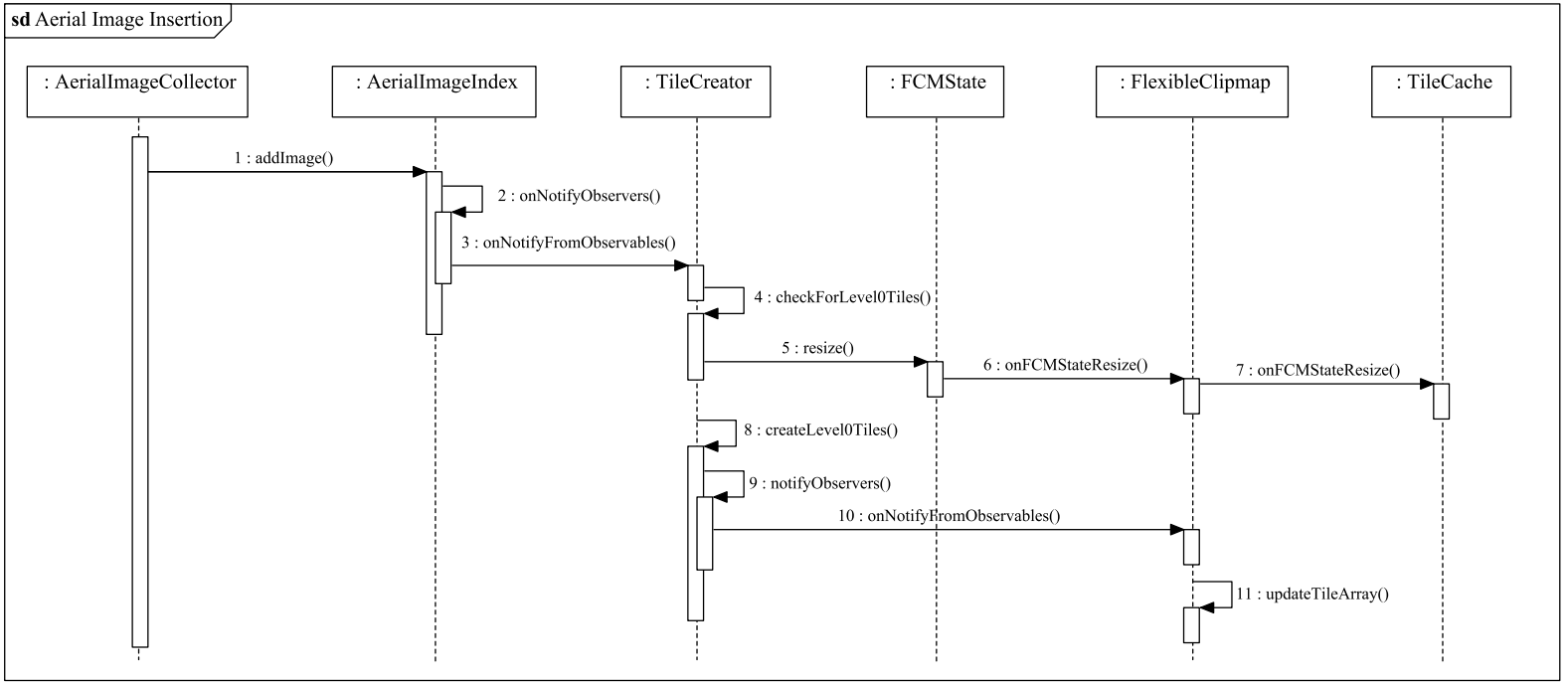

Figure B.2: *A sequence diagram showing the communication of affected objects in response to the insertion of an aerial image at the* `AerialImageCollector` *object.*

Figure B.3: *Relationships between the classes in the* `image`*-package for image processing.*

Bibliography

[1] Tomas Akenine-Möller, Eric Haines, and Nathaniel Hoffman. *Real-Time Rendering*. A K Peters, 3rd edition, 2008.

[2] C. Amante and B. W. Eakins. ETOPO1 1 Arc-Minute Global Relief Model: Procedures, Data Sources and Analysis. In *NOAA Technical Memorandum NESDIS NGDC-24*, page 19 et seqq., 2009.

[3] Lucas Ammann, Olivier Génevaux, and Jean-Michel Dischler. Hybrid Rendering of Dynamic Heightfields Using Ray-Casting and Mesh Rasterization. In *Proceedings of Graphics Interface 2010*, GI '10, pages 161–168. Canadian Information Processing Society, 2010.

[4] Arul Asirvatham and Hugues Hoppe. *GPU Gems 2*, chapter Terrain Rendering Using GPU-Based Geometry Clipmaps. Addison-Wesley Longman, 2005.

[5] Sean Barrett. Sparse Virtual Textures. http://silverspaceship.com/src/svt/, 2008.

[6] Norbert Beckmann, Hans-Peter Kriegel, Ralf Schneider, and Bernhard Seeger. The R*-tree: An Efficient and Robust Access Method for Points and Rectangles. In *SIGMOD '90: Proceedings of the ACM SIGMOD International Conference on Management of Data*, volume 19(2), pages 322–331. ACM, 1990.

[7] Norbert Beckmann and Bernhard Seeger. A Revised R*-tree in Comparison with Related Index Structures. In *Proceedings of the 2009 ACM SIGMOD International Conference on Management of Data*, SIGMOD '09, pages 799–812. ACM, 2009.

[8] H. Bendea, F. Chiabrando, F. Giulio Tonolo, and D. Marenchino. Mapping of Archaeological Areas Using a Low-Cost UAV: The Augusta Bagiennorum Test Site. In *Proceedings of XXI CIPA Symposium*, 2007.

[9] Jon Louis Bentley. Multidimensional Binary Search Trees Used for Associative Searching. *Communications of the ACM*, 18(9):509–517, September 1975.

[10] James F. Blinn. Simulation of Wrinkled Surfaces. In *SIGGRAPH '78: Proceedings of the 5th Annual Conference on Computer Graphics and Interactive Techniques*, pages 286–292. ACM, 1978.

[11] Camera & Imaging Products Association (CIPA). CIPA DC-008-Translation-2010, Exchangeable Image File Format for Digital Still Cameras: Exif Version 2.3. http://www.cipa.jp/english/hyoujunka/kikaku/pdf/DC-008-2010_E.pdf, April 2010.

[12] Malte Clasen and Hans-Christian Hege. Terrain Rendering using Spherical Clipmaps. In *EuroVis06 Joint Eurographics - IEEE VGTC Symposium on Visualization*, pages 91–98. Eurographics Association, 2006.

[13] David Cline and Parris K. Egbert. Interactive Display of Very Large Textures. In *VIS '98: Proceedings of the Conference on Visualization '98*, pages 343–350. IEEE Computer Society Press, 1998.

[14] Robert T. Collins. A Space-Sweep Approach to True Multi-Image Matching. In *Proceedings of the 1996 Conference on Computer Vision and Pattern Recognition (CVPR '96)*, CVPR '96. IEEE Computer Society, 1996.

[15] Robert L. Cook. Shade Trees. In *SIGGRAPH '84: Proceedings of the 11th Annual Conference on Computer Graphics and Interactive Techniques*, pages 223–231. ACM, 1984.

[16] Roger Crawfis, Eric Noble, Michael Ford, Frederic Kuck, and Eric Wagner. Clipmapping on the GPU. Technical report, Ohio State University, Columbus, OH, USA, 2007.

[17] Mark de Berg, Marc van Kreveld, Mark Overmars, and Otfried Schwarzkopf. *Computational Geometry: Algorithms and Applications*. Springer, 2nd edition, 2000.

[18] Christian Dick, Jens Krüger, and Rüdiger Westermann. GPU Ray-Casting for Scalable Terrain Rendering. In *Proceedings of Eurographics 2009 - Areas Papers*, pages 43–50, 2009.

[19] Christian Dick, Jens Krüger, and Rüdiger Westermann. GPU-Aware Hybrid Terrain Rendering. In *Proceedings of IADIS Computer Graphics, Visualization, Computer Vision and Image Processing 2010*, pages 3–10, 2010.

[20] Jonathan Dummer. Cone Step Mapping: An Iterative Ray-Heightfield Intersection Algorithm. http://www.lonesock.net/files/ConeStepMapping.pdf, 2006.

[21] Henri Eisenbeiss. Applications of Photogrammetric Processing Using an Autonomous Model Helicopter. *Revue Francaise de Photogrammetrie et de Teledetection*, Symposium ISPRS Commission Technique I "Des capteurs a l'Imagerie", 2007.

[22] Henri Eisenbeiss and Li Zhang. Comparison of DSMs Generated from Mini UAV Imagery and Terrestrial Laser Scanner in a Cultural Heritage Application. In *ISPRS Commission V Symposium 'Image Engineering and Vision Metrology'*, pages 90 – 96, 2006.

[23] Anton Ephanov and Chris Coleman. Virtual Texture: A Large Area Raster Resource for the GPU. In *Interservice/Industry Training, Simulation, and Education Conference (I/ITSEC) 2006*, pages 645–656, 2006.

[24] esri. Esri CityEngine. http://www.esri.com/software/cityengine/, 2012.

[25] Jurgen Everaerts. The Use of Unmanned Aerial Vehicles (UAVS) for Remote Sensing and Mapping. In *XXIth ISPRS Congress*, volume XXXVII, part 2, pages 1187 – 1192, 2008.

[26] Jon P. Ewins, Marcus D. Waller, Martin White, and Paul F. Lister. MIP-Map Level Selection for Texture Mapping. *IEEE Transactions on Visualization and Computer Graphics*, 4(4):317–329, 1998.

[27] Dirk Feldmann and Klaus Hinrichs. GPU based Single-Pass Ray Casting of Large Heightfields Using Clipmaps. In *Digital Proceedings of Computer Graphics International (CGI)*, 2012.

[28] Dirk Feldmann, Frank Steinicke, and Klaus Hinrichs. Flexible Clipmaps for Managing Growing Textures. In *Proceedings of International Conference on Computer Graphics Theory and Applications (GRAPP)*, 2011.

[29] James D. Foley, Andries van Dam, Steven K. Feiner, and John F. Hughes. *Computer Graphics: Principles and Practice*. Addison-Wesley, 2nd edition, 1995.

[30] David Gallup, Jan-Michael Frahm, Philippos Mordohai, Qingxiong Yang, and Marc Pollefeys. Real-Time Plane-Sweeping Stereo with Multiple Sweeping Directions. In *Proceedings of the 2007 IEEE Computer Society Conference on Computer Vision and Pattern Recognition*, CVPR '07. IEEE Computer Society, 2007.

[31] Erich Gamma, Richard Helm, Ralph Johnson, and John Vlissides. *Entwurfsmuster – Elemente wiederverwendbarer objektorientierter Software*. Addison-Wesley, Programmer's Choice edition, 2004.

[32] Indra Geys, Thomas P. Koninckx, and Luc Van Gool. Fast Interpolated Cameras by Combining a GPU based Plane Sweep with a Max-Flow Regularisation Algorithm. In *Proceedings of the 3D Data Processing, Visualization, and Transmission, 2nd International Symposium*, 3DPVT '04, pages 534–541. IEEE Computer Society, 2004.

[33] Minglun Gong, Ruigang Yang, Liang Wang, and Mingwei Gong. A Performance Study on Different Cost Aggregation Approaches Used in Realtime Stereo Matching. *International Journal of Computer Vision*, 2007.

[34] Rafael C. Gonzalez and Richard E. Woods. *Digital Image Processing*. Pearson Education Inc., Pearson International edition, 2008.

[35] Antonin Guttman. R-trees: A Dynamic Index Structure for Spatial Searching. In *SIGMOD '84: Proceedings of the ACM SIGMOD International Conference on Management of Data*, pages 47–57. ACM, 1984.

[36] Mark Harris and Ian Buck. *GPU Gems 2*, chapter GPU Flow-Control Idioms. Addison-Wesley Longman, 2005.

[37] Klaus Hinrichs. *The Grid File System: Implementation and Case Studies of Applications*. PhD thesis, ETH Zürich, 1985.

[38] Irrlicht. The Irrlicht Engine. http://irrlicht.sourceforge.net/, 2012.

[39] Jürgen Roßmann and Malte Rast. High-Detail Local Aerial Imaging Using Autonomous Drones. In *12th AGILE International Conference on Geographic Information Science*, 2009.

[40] Tomomichi Kaneko, Toshiyuki Takahei, Masahiko Inami, Naoki Kawakami, Yasuyuki Yanagida, Taro Maeda, and Susumu Tachi. Detailed Shape Representation with Parallax Mapping. In *In Proceedings of the ICAT 2001*, pages 205–208, 2001.

[41] Sing Bing Kang, Richard Szeliski, and Jinxiang Chai. Handling Occlusion in Dense Multi-view Stereo. Technical report, Microsoft Research, September 2001.

[42] Karl Kraus. *Photogrammetrie Band 1: Geometrische Informationen aus Photographien und Laserscanneraufnahmen*. de Gruyter, 7th edition, 2004.

[43] Jens Krüger and Rüdiger Westermann. Acceleration Techniques for GPU-based Volume Rendering. In *Proceedings IEEE Visualization 2003*, 2003.

[44] Charles Lemaire. Aspects of the DSM Production with High Resolution Images. In *The International Archives of the Photogrammetry, Remote Sensing and Spatial Information Sciences*, volume XXXVII, part B4, Beijing, 2008.

[45] Zeyu Li, Hui Li, Anxiang Zeng, Lian Wang, and Yongwen Wang. Real-Time Visualization of Virtual Huge Texture. In *ICDIP '09: Proceedings of the International Conference on Digital Image Processing*, pages 132–136. IEEE Computer Society, 2009.

[46] Zhilin Li, Qing Zhu, and Christopher Gold. *Digital Terrain Modeling: Principles and Methodology*. CRC Press, 2004.

[47] Frank Losasso and Hugues Hoppe. Geometry Clipmaps: Terrain Rendering Using Nested Regular Grids. *ACM Transactions on Graphics (TOG)*, 2004.

[48] Microsoft. DirectX SDK Documentation: RaycastTerrain Sample. http://www.microsoft.com/en-us/download/details.aspx?id=6812, 2008.

[49] Mircosoft. Direct3D 10 API Features. http://msdn.microsoft.com/en-us/library/windows/desktop/bb172268(v=vs.85).aspx, 2007.

[50] Martin Mittring and Crytek GmbH. Advanced Virtual Texture Topics. In *SIGGRAPH '08: ACM SIGGRAPH 2008 Classes*, pages 23–51. ACM, 2008.

[51] NASA. Visible Earth: Earth – The Blue Marble. http://visibleearth.nasa.gov/view.php?id=54388, 1997.

[52] NASA. Shuttle Radar Topography Mission. http://www2.jpl.nasa.gov/srtm/, 2000.

[53] NVIDIA Corporation. OpenGL Extension No. 187: EXT_texture_filter_anisotropic. http://www.opengl.org/registry/specs/EXT/texture_filter_anisotropic.txt, 1999.

[54] NVIDIA Corporation. White Paper: Texture Arrays Terrain Rendering. http://developer.download.nvidia.com/whitepapers/2007/SDK10/TextureArrayTerrain.pdf, 2007.

[55] Kyoungsu Oh, Hyunwoo Ki, and Cheol-Hi Lee. Pyramidal Displacement Mapping: a GPU based Artifacts-free Ray Tracing through an Image Pyramid. In *VRST '06: Proceedings of the ACM Symposium on Virtual Reality Software and Technology*, pages 75–82. ACM, 2006.

[56] Jens-Rainer Ohm and Hans Dieter Lüke. *Signalübertragung*. Springer, 10th edition, 2007.

[57] Manuel M. Oliveira, Gary Bishop, and David McAllister. Relief Texture Mapping. In *SIGGRAPH '00: Proceedings of the 27th Annual Conference on Computer Graphics and Interactive Techniques*, pages 359–368. ACM Press/Addison-Wesley Publishing Co., 2000.

[58] Joseph O'Rourke. *Computational Geometry in C*. Cambridge University Press, 2nd edition, 1998.

[59] John D. Owens, David Luebke, Naga Govindaraju, Mark Harris, Jens Krüger, Aaron E. Lefohn, and Tim Purcell. A Survey of General-Purpose Computation on Graphics Hardware. *Computer Graphics Forum*, 26(1):80 – 113, March 2007.

[60] David P. Paine and James D. Kiser. *Aerial Photography and Image Interpretation*. John Wiley & Sons, 3rd edition, 2012.

[61] PDS Geoscience Node, NASA. Mars Global Surveyor: MOLA MEGDRs. http://pds-geosciences.wustl.edu/missions/mgs/megdr.html, April 2007.

[62] Fábio Policarpo and Manuel M. Oliveira. *GPU Gems 3*, chapter Relaxed Cone Stepping for Relief Mapping. Addison-Wesley Professional, 2007.

[63] Fábio Policarpo, Manuel M. Oliveira, and João L. D. Comba. Real-time Relief Mapping on Arbitrary Polygonal Surfaces. In *Proceedings of the 2005 Symposium on Interactive 3D Graphics and Games*, I3D '05, pages 155–162. ACM, 2005.

[64] The AVIGLE Project. AVIGLE – Avionic Digital Service Platform. http://www.avigle.de, 2012.

[65] Huamin Qu, Feng Qiu, Nan Zhang, Arie Kaufman, and Ming Wan. Ray Tracing Height Fields. In *Procedings of Computer Graphics International*, pages 202–207, 2003.

[66] Randi J. Rost and Bill Licea-Kane. *OpenGL Shading Language*. Addison-Wesley, 2010.

[67] Hanan Samet. *Foundations of Multidimensional and Metric Data Structures*. Morgan Kaufmann, 2006.

[68] M. Sauerbier and Henri Eisenbeiss. UAVs for the Documentation of Archaeological Excavation. *Proceedings of the ISPRS Commission V Mid-Term Symposium 'Close Range Image Measurement Techniques'*, 2010.

[69] Daniel Scharstein and Richard Szeliski. A Taxonomy and Evaluation of Dense Two-Frame Stereo Correspondence Algorithms. *International Journal of Computer Vision*, 47(1-3):7–42, April 2002.

[70] Antonio Seoane, Javier Taibo, and Luis Hernández. Hardware-Independent Clipmapping. In *Journal of WSCG 2007*, pages 177 – 183. Eurographics Association, 2007.

[71] Dave Shreiner. *OpenGL Programming Guide*. Pearson Education, 7th edition, 2010.

[72] Noah Snavely, Steven M. Seitz, and Richard Szeliski. Photo Tourism: Exploring Photo Collections in 3D. *ACM Transactions on Graphics (TOG)*, 25(3):835–846, July 2006.

[73] Harald Sörrle. *UML 2 für Studenten*. Pearson Studium, 1st edition, 2005.

[74] Sven Strothoff, Dirk Feldmann, Frank Steinicke, Tom Vierjahn, and Sina Mostafawy. Interactive Generation of Virtual Environments Using MUAVs, 2011.

[75] Sven Strothoff, Frank Steinicke, Dirk Feldmann, Jan Roters, Klaus Hinrichs, Tom Vierjahn, Markus Dunkel, and Sina Mostafawy. A Virtual Reality-based Simulator for Avionic Digital Service Platforms. In *Proceedings of Joint Virtual Reality Conference (Additional Material)*, 2010.

[76] Richard Szeliski. *Computer Vision: Algorithms and Applications*. Springer, http://szeliski.org/Book/drafts/SzeliskiBook_20100903_draft.pdf, draft edition, September, 3rd 2010.

[77] László Szirmay-Kalos and Tamás Umenhoffer. Displacement Mapping on the GPU - State of the Art, 2006.

[78] Javier Taibo, Antonio Seoane, and Luis Hernández. Dynamic Virtual Textures. In *Journal of WSCG 2009*, pages 25 – 32. Eurographics Association, 2009.

[79] Christopher C. Tanner, Christopher J. Migdal, and Michael T. Jones. The Clipmap: a Virtual Mipmap. In *SIGGRAPH '98: Proceedings of the 25th Annual Conference on Computer Graphics and Interactive Techniques*, pages 151–158. ACM, 1998.

[80] Natalya Tatarchuk. Dynamic Parallax Occlusion Mapping with Approximate Soft Shadows. In *SIGGRAPH '06: ACM SIGGRAPH 2006 Courses*, pages 63–69. ACM, 2006.

[81] Art Tevs, Ivo Ihrke, and Hans-Peter Seidel. Maximum Mipmaps for Fast, Accurate, and Scalable Dynamic Height Field Rendering. In *I3D '08: Proceedings of the 2008 Symposium on Interactive 3D Graphics and Games*, pages 183–190. ACM, 2008.

[82] United States Secretary of Defense. Unmanned Aircraft Systems Roadmap 2005 – 2030. www.fas.org/irp/program/collect/uav_roadmap2005.pdf, 2005.

[83] Alan Watt. *3D Computer Graphics*. Pearson Education Ltd., 3rd edition, 2000.

[84] Roland E. Weibel and R. John Hansman. Safety Considerations for Operation of Different Classes of UAVs in the NAS. In *AIAA's 4th Aviation Technology, Integration and Operations (ATIO) Forum*. AIAA, 2004.

[85] Lance Williams. Pyramidal Parametrics. In *SIGGRAPH '83: Proceedings of the 10th Annual Conference on Computer Graphics and Interactive Techniques*, pages 1–11, 1983.

[86] Ruigang Yang and Marc Pollefeys. Multi-Resolution Real-Time Stereo on Commodity Graphics Hardware. In *Proceedings of the 2003 IEEE Computer Society Conference on Computer Vision and Pattern Recognition*, CVPR '03, pages 211–217. IEEE Computer Society, 2003.

[87] Ruigang Yang and Marc Pollefeys. A Versatile Stereo Implementation on Commodity Graphics Hardware. *Real-Time Imaging*, 11(1):7–18, February 2005.

[88] Ruigang Yang, Greg Welch, and Gary Bishop. Real-Time Consensus-Based Scene Reconstruction Using Commodity Graphics Hardware. In *Proceedings of the 10th Pacific Conference on Computer Graphics and Applications*, PG '02. IEEE Computer Society, 2002.

[89] Z/I Imaging. Z/I DMC II 250 Camera System Datasheet. http://www.ziimaging.com/media/ZI_DMC250_DS_en.pdf, 2011.

List of Acronyms

AABB	axis-aligned bounding box
API	application programming interface
BVH	bounding volume hierarchy
CCD	charge-coupled device
CoP(s)	center(s) or projection
DEM	digital elevation model
DSM	digital surface model
FCM	Flexible Clipmap
FBO	frame buffer object
GPS	Global Positioning System
GPU	graphics processing unit
GLSL	OpenGL Shading Language
IMU	inertial measurement unit
LOD	level of detail
(m)UAV	(miniature) unmanned aerial vehicle
SAD	sum of absolute differences
UML	Unified Modeling Language
UTM	Universal Transverse Mercator (coordinate system)
XML	Extensible Markup Language